SPLITTING OF CARBON DIOXIDE ON $Ba_2Ca_{0.66}Nb_{1.34-x}Fe_xO_6$ FOR CLEAN FUEL PRODUCTION

By

Harriet Kildahl

A thesis submitted to the University of Birmingham for the

Degree of Doctor of Philosophy

School of Chemical Engineering

College of Engineering and Physical Sciences

The University of Birmingham

February 2022

Abstract

Limiting warming to 1.5 °C, in line with the Paris Climate Agreement, requires rapid emissions reductions across all sectors of the economy by 2050. However, there are sectors, often called the hard-to-decarbonise sectors, for which electrification and efficiency improvements alone will be insufficient. The production of carbon-neutral drop-in fuels could help to decarbonise aviation, shipping, and freight, while a carbon-neutral chemical precursor could reduce the chemical industry's reliance on crude oil. This precursor could be carbon monoxide, which is already widely used in the chemical sector. Kerosene, diesel, and petrol can be synthesised from carbon monoxide and hydrogen *via* the Fischer Tropsch process. A thermochemical cycle based on $Ba_2Ca_{0.22}Nb_{1.34-x}Fe_xO_6$ (BCNF), a double perovskite, can convert carbon dioxide into carbon monoxide.

BCNF perovskites with varying iron content (x = 0, 0.34, 0.66 and 1) were synthesised and characterised before being thermally cycled between reduction under nitrogen and oxidation under carbon dioxide. The presence of iron was found to be crucial to the formation of oxygen vacancies and the ability to split carbon dioxide, where $Ba_2Ca_{0.22}Nb_{0.34}FeO_6$ (BCNF1) was the only compound capable of splitting carbon dioxide. Optimising the reaction conditions for BCNF1 increased the CO production from 160 μmol/g to 447 μmol/g. Reacting over the perovskite as a powder increased yields to around 730 μmol/g. Increasing the mass of powder used from 1g to 18g, increased the CO yield further to 859 μmol/g. This makes BCNF1 one of the most successful materials in the literature while reacting at lower temperatures than other thermochemical materials. This is partly due to the low activation energy of the CO_2 splitting reaction of 46.62

kJ/mol, which is one of the lowest recorded in the literature. Additionally, BCNF1 powder has been proven to be thermally stable over 10 cycles, without experiencing the sintering and grain growth seen in BCNF1 pellets.

Next, BCNF1 was scaled up to 100g to understand the redox activity at a larger scale. BCNF1 was found to split 10.1 % of CO_2 at 800 °C, with 100 % selectivity to CO. This conversion yield was used to perform a techno-economic analysis for an industrial CO production facility based on BCNF1. Such a facility was found to produce CO at well below the market price. A 150 m^3/hr facility can be profitable with electricity prices up to $0.39/kWh, allowing for short-term fluctuations in electricity prices without affecting profitability. At an electricity price of $0.15/kWh, CO can be produced at $0.26/kg, which is significantly cheaper than other carbon-neutral methods of carbon monoxide production including electrolysis. Finally, the sector coupling between the iron and steel sector and a thermochemical CO production facility is presented. The TC-BF-BOF system allows for the production of low emission steel through a closed carbon loop. If this system was applied to the BF-BOF facilities in the UK, steel sector emissions could be reduced by 88 %. Additionally, with an initial investment of £720 million, UK wide emissions could be lowered by 2.9 %. This investment would be completely repaid in 22 months due to significant savings from the replacement of expensive metallurgical coal. Finally, recommendations for future research are made.

Acknowledgements

Firstly, I gratefully acknowledge funding from the Birmingham Centre for Energy Storage and UK EPSRC for partial financial support to the work under EP/S016627/1 and EP/R024006/1. I am extremely thankful to my two supervisors, Prof Yulong Ding and Dr Hui Cao for their guidance and kindness and for providing exactly the support I needed in their own way. I am particularly grateful for their understanding, care, and compassion through navigating a global pandemic with pre-existing conditions.

I would like to thank Jie Chen, Chyntol Kanhimbe and Jonathon Goldfinch for their unwavering help and kindness throughout the years, my time in the lab would certainly not have run as smoothly without you. I would also like to thank Guozhan Jiang and Shiva Jethwa for their invaluable help with the GC.

To my mum and dad, thank you for raising me in an environment where my love of learning was allowed to flourish. Thank you for loving me and supporting me in pursuing my passions. À ma Tatine, merci pour ton amour.

Finally, to my partner Patrick, your daily acts of love and support mean more than I can put into words.

Table of Contents

Chapter 1 – Introduction 1
1.1 Background 1
1.2 Aims and Objectives 6
1.3 Layout of the Thesis 7
1.4 References 9
Chapter 2 – Literature Review 12
2.1 The History of Thermochemical Cycles 12
2.2 Materials for Thermochemical Cycles 14
2.2.1 Ferrites 16
2.2.1.1 Iron Oxide 16
2.2.1.2 Manganese Ferrites 17
2.2.1.3 Nickel Ferrites 18
2.2.1.4 Cobalt Ferrites 19
2.2.1.5 Other Ferrites and Mixed Metal Ferrites 21
2.2.2 Volatile Metal Oxides 23
2.2.3 Ceria 25
2.2.4 Perovskites 34
2.3 Ideal Thermochemical Materials 37
2.4 References 38
Chapter 3 – Thermochemical splitting of carbon dioxide by lanthanum manganites – understanding the mechanistic effects of doping 49
3.1 Abstract 49
3.2 Introduction 50
3.3 The Reduction Reaction 53
3.3.1 Alkaline Earth Metals 53
3.3.2 Lanthanides 59
3.3.3 Transition Metals 62
3.3.4 Other B-site Metals 68
3.4 The Oxidation Reaction 70
3.4.1 Alkaline Earth Metals 73
3.4.2 Lanthanides 73
3.4.3 Transition Metals 74
3.4.4 Other B-site Metals 75
3.4.5 Supported Perovskites 75
3.5 Concluding Remarks 92
3.6 References 93
Chapter 4 – Carbon Dioxide Decomposition Through Gas Exchange in Barium Calcium Iron Niobates 103
4.1 Abstract 103
4.2 Introduction 104
4.3 Experimental 106
4.3.1 Material Synthesis 106
4.3.2.Material Characterisation 106
4.3.3 Temperature Programmed Experiments 107

4.4 Results and Discussion 108
4.4.1 Material Characterisation 108
4.4.2 Reduction and Oxidation 113
4.4.3 Perovskite Stability 116
4.5 Conclusion 120
4.6 References 120
Chapter 5 – Thermochemical Splitting of Carbon Dioxide on $Ba_2Ca_{0.66}Nb_{0.34}FeO_6$ at moderate temperatures: the Influences of Reduction and Oxidation Conditions, and CO_2 Diffusion 123
5.1 Abstract 123
5.2 Introduction 124
5.3 Methodology 126
5.3.1 Material Synthesis 126
5.3.2 Material Characterisation 127
5.3.3 Reduction Temperature and Time 127
5.3.4 Oxidation Temperature 128
5.3.5 Oxidation Kinetics 128
5.3.6 Material Shape/Form 128
5.3.7 Thermal Cycling 129
5.4 Results and Discussion 129
5.4.1 Reduction Reaction 129
5.4.2 Oxidation Reaction 131
5.4.2.1 Diffusion Effect 132
5.4.2.2 Reaction Extent 135
5.4.2.3 Oxidation Kinetics 137
5.4.3 Material Shape/Form 137
5.4.4 Thermal Cycling 138
5.5 Conclusions 142
5.6 References 143
Chapter 6 – Carbon Monoxide Production by Thermochemical CO_2 Splitting – A Techno-Economic Assessment 148
6.1 Abstract 148
6.2 Introduction 150
6.3 Methodology 152
6.3.1 Perovskite Synthesis 152
6.3.2 Kinetics 152
6.3.3 Lab-Based Scale-Up 153
6.3.4 Gas Chromatography 153
6.4 Results & Discussion 154
6.4.1 Kinetics 154
6.4.2 100g Scale-Up 157
6.4.3 Industrial Plant Scale-Up 159
6.5 Conclusion 163
6.6 References 164
6.7 Supplementary Information 167
Chapter 7 – Thermochemical Sector Coupling with Blast Furnace – Basic Oxygen Furnace Steel Production for Cost Effective Decarbonisation 169

7.1 Abstract 169
7.2 Introduction 170
7.3 Blast Furnace – Basic Oxygen Furnace 173
7.4 Thermochemical Cycle 176
7.5 Thermochemical Blast Furnace – Basic Oxygen Furnace Coupling 176
7.5.1 Mass Flows 177
7.5.2 Energy Flows 181
7.6 Decarbonisation of the UK Steel Industry 183
7.7 Advantages of the TC-BF-BOF System 185
7.8 Conclusions 186
7.9 References 186
Chapter 8 – Conclusions and Recommendations for Future Research 190
8.1 Conclusions 190
8.2 Recommendations for Future Research 193
8.3 References 194

List of Tables

Table 2.1. Oxygen Evolution and Carbon Monoxide Production from Nickel Ferrites. 18

Table 2.2. Oxygen Evolution and Carbon Monoxide Production from Cobalt Ferrites. 20

Table 2.3. Oxygen Evolution and Carbon Monoxide Production from Mixed Metal Ferrites. 23

Table 2.4. Oxygen Evolution and Carbon Monoxide Production from Ceria-based Compounds. 30

Table 2.5. Oxygen Evolution and Carbon Monoxide Production from Perovskites. 36

Table 3.1. Temperature Required for Various Reduction Reactions of Iron and Manganese. 66

Table 3.2. Manganese Oxidation State and Oxygen Production Volumes of $La_{0.5}Sr_{0.5}Mn_{1-x}B_xO_3$ (B = Al, Mg & Ga). 68

Table 3.3. The Effect of Reduction Temperature on Carbon Monoxide Yield. 72

Table 3.4. Activation Energy of Carbon Dioxide Splitting for various Transition Metal Doped Perovskites. 74

Table 3.5. Thermochemical Conversion Results from the Lanthanum Manganite Family of Perovskites. 77

Table 4.1. Helium Pycnometry Results showing Density, Pore Volume and Porosity. 109

Table 4.2. Indexed XRD data for BCNF1, BCNF0.66, BCNF0.34 and BCNF0 with d Spacing and Intensity. 111

Table 4.3. Enthalpy Calculations of the Perovskites Calculated from Simultaneous Thermal Analysis. 116

Table 5.1. Pore Diameter, $\lambda /(2*r_a)$, and Type of Diffusion Present in 10mm Pellets Oxidised between 600 and 800 °C. 133

Table 6.1. Carbon Monoxide Yields of Several Perovskites Undergoing Thermochemical Cycles. 151

Table 6.2. Activation Energy of the Perovskite Oxidation Reaction under Carbon Dioxide. 157

Table 6.3. Three Scenarios of the Scale-Up of a BCNF1 based Facility for the Production of CO. 160

Table 6.4. Cost of CO Production per kg for Different Technologies with Variable Electricity Price 162

Supplementary Table 6.1. Phase-Boundary Controlled Models Against which the Experimental Results were Tested for Best Fit. 167

List of Figures

Figure 2.1. Oxygen Evolution in the Second Thermochemical Cycle as a Function of Ceria Content and Dopant Element. 28

Figure 2.2. Carbon Monoxide Production in the Second Thermochemical Cycle as a Function of Ceria Content and Dopant Element. 30

Figure 2.3. Crystal Structure of a Typical Perovskite ABO_3. 35

Figure 3.1. Components of the Lanthanum Manganite Perovskite Family. 52

Figure 3.2.(a) Oxygen Evolution and Carbon Monoxide Production of $La_{1-x}Sr_xMnO_3$ with Varying Strontium Content, with Reduction and Oxidation Temperatures, Reduction under Ar/N_2 and Oxidation under 40-100 % CO_2 (b) The Effect of Strontium Content on the Enthalpy of Reduction in $La_{1-x}Sr_xMnO_3$. 54

Figure 3.3.(a) Gas Production Volumes of $La_{1-x}E_xMnO_3$ with E = Ca, Sr, and Ba, Showing Different Dopant Concentrations and Reactions at Varying Temperatures. Column 1: Ca-doped Oxygen Evolution, Column 2: Ca-doped CO Production, Column 3: Sr-doped Oxygen Evolution, Column 4: Sr-doped CO Production, Column 5: Ba-doped Oxygen Evolution, Column 6: Ba-doped CO Production. Reduction under Ar and oxidation under 40-50 % CO_2 (b) Mn-O_6 Octahedra in Rhombohedral Crystal Structure (c) Tilted Mn-O_6 Octahedra in Octahedral Crystal Structure. 57

Figure 3.4. Effect of Lanthanide Ionic Radii on Oxygen Evolution ($La_{0.5}Ln_{0.5}MnO_3$) and Reduction Enthalpy ($LnMnO_3$). 60

Figure 3.5. (a) Distribution of the Five Transition Metal d Orbitals when in an Octahedral Bonding Arrangement, Molecular Orbital Arrangement of (b) Mn^{3+} high spin, (c) Mn^{3+} low spin and (d) Mn^{4+}. 63

Figure 3.6. (a) Distribution of Transition Metal d Orbital Electrons into the e_g and t_{2g} orbitals in $LaTO_3$ (T = Cr, Fe, Co and Ni) (b) Oxygen Evolution and Carbon Monoxide Production with Variation in the Transition Metal, Reduction under Ar/N_2 and Oxidation under 40-100 % CO_2. 65

Figure 3.7. Oxygen Evolution and Carbon Monoxide Production of the Mixed Transition Metal Perovskites, when Reduced under Ar/N_2 and Oxidised under 10-50 % CO_2. 67

Figure 3.8. Doping of the B-site with Non-Redox Active Metals at Different Temperatures, with Oxygen Evolution and Carbon Monoxide Production when Reduced under Ar and Oxidised under 5-50 % CO_2. 70

Figure 3.9. (a-d) Mechanism of Carbon Dioxide Splitting on Lanthanum 71

Manganites, (e) Energy Changes during the CO_2 Splitting Reaction on the Perovskite Surface Showing the Absorption of CO_2 onto a Perovskite Surface with Oxygen Vacancies, Decomposition of CO_2 into CO and Filling of Oxygen Vacancies and the Desorption of CO from the Perovskite Surface.

Figure 4.1. (a) Experimental Workflow, (b) Visual Representation of the As-synthesised Pellets, (1) BCNF1, (2) BCNF0.66, (3) BCNF0.34 and (4) BCNF0. 108

Figure 4.2. SEM Images of As-prepared, After Reduction and After Re-oxidation of BCNF0, BCNF0.34, BCNF0.66 and BCNF1. 109

Figure 4.3. Micro Computer Tomography Reconstructed Images of (a) BCNF0, (b) BCNF0.34, (c) BCNF0.66, and (d) BCNF1. 110

Figure 4.4. X-ray Diffraction Patterns of As-synthesised BCNF1, BCNF0.66, BCNF0.34 and BCNF0. 111

Figure 4.5. Crystal Structures of (a) BCNF0, (b) BCNF0.34, (c) BCNF0.66 and (d) BCNF1. 112

Figure 4.6. EDX Scans of As-synthesised BCNF1, BCNF0.66, BCNF0.34 and BCNF0. 113

Figure 4.7. Average Mass Change of the Four Perovskites During Reduction and Reoxidation. 114

Figure 4.8. XRD Scans of (1) BCNF0, (2) BCNF0.34, (3) BCNF0.66 and (4) BCNF1 with (a) As-prepared, (b) After Reduction and (c) After Re-oxidation. 117

Figure 4.9. Mass Change of BCNF1 during Five Cycles of Reduction and Reoxidation. 120

Figure 5.1. (a) Oxygen Evolution from the Reduction Reaction Performed between 600-900 °C for 24 hours. The Reduction Reaction at 800 °C was repeated due to the lower than expected result. (b) Oxygen Evolution from the Reduction Reaction reformed at 700 °C for between 6 and 36 hours. 130

Figure 5.2. (a) XRD Plots and (b) SEM images of the Perovskite Pellets Before Reduction and After Reduction at Different Temperatures. 131

Figure 5.3. Carbon Monoxide Production from the Oxidation Reaction Performed between 600-800 °C for 24 Hours. 132

Figure 5.4. Effective Diffusion Coefficient plotted against Carbon Monoxide Production at Oxidation Temperatures between 600 and 800 °C. 135

Figure 5.5. Elemental Analysis from EDX showing the presence of carbon. 136

Figure 5.6. Carbon Monoxide Production plotted Against the Percentage of the Pellets Involved in the Oxidation Reaction at Different Oxidation Temperatures. 136

Figure 5.7. (a) Carbon Monoxide Production of BCNF1 Pellets between 1 and 24 Hours of Oxidation, (b) Conversion of Carbon Dioxide to Carbon Monoxide over Various Time Domains between 1 and 24 Hours. 137

Figure 5.8. Reduction Reaction at 700 °C for 24 Hours and Oxidation Reaction at 800 °C for 24 Hours for different Shape of Material, 10mm Pellet, 5mm Pellet, 1g of Powder in a Ceramic Boat and 0.5g of Powder in a Ceramic Boat. 138

Figure 5.9. Thermal Cycling of BCNF1 over 10 Cycles for (a) 10mm Pellets, (b) 1g Powder. 140

Figure 5.10. SEM Images of BCNF1 (a) 10mm Pellet before Thermal Cycling, (b) 10mm Pellet after 5 Cycles, (c) 10mm Pellet after 10 Cycles, (d) Powder after 10 Cycles at 30x Magnification, (e) Powder after 10 Cycles at 3000x Magnification. 141

Figure 5.11. Oxygen Evolution and Carbon Monoxide Production of 18g of BCNF1 Reacted in a Ceramic Boat under Optimum Conditions. 142

Figure 6.1. Image of the 100g Scale-Up rig with 1” reactor 153

Figure 6.2.(a) Carbon Monoxide Production at 700 °C, 750 °C and 800 °C between 1 and 24 hours, (b) Carbon Dioxide Conversion at 700 °C, 750 °C, and 800 °C between 1 and 24 hours relative to maximum conversion (800 °C, 24 hours). 155

Figure 6.3. Hancock & Sharp plot, obtained by plotting $ln(-ln(1-Xa))$ against $ln(t)$, where Xa is the conversion and t is the time in seconds. 155

Figure 6.4.(a) Rate constants at Various Oxidation Temperatures, (b) Arrhenius plot. 156

Figure 6.5. CO_2 Conversion to CO in (a) Cycle 1 between 0 and 11 hours, (b) Cycles 2-5 between 12 and 23 hours. 158

Figure 6.6.(a) Annual Costs, Sales and Profits for Three Scenarios, (b) Effect of Electricity Prices on Profits in the Three Scenarios. 161

Supplementary Figure 6.1. Gas Chromatography Calibration Curves for (a) CO_2, (b) CO, (c) N_2. 167

Figure 7.1. The TC-BF-BOF System with Mass Flows for the Production 181

of 1 Tonne of Liquid Steel.

Figure 7.2. The TC-BF-BOF System with Energy Flows for the Production of 1 Tonne of Liquid Steel. 178

Abbreviations

Activation Energy (Ea)

Barium Calcium Iron Niobates (BCNF)

$Ba_2Ca_{0.66}Nb_{0.34}FeO_6$ (BCNF1)

$Ba_2Ca_{0.66}Nb_{0.68}Fe_{0.66}O_6$ (BCNF0.66)

$Ba_2Ca_{0.66}NbFe_{0.34}O_6$ (BCNF0.34)

$Ba_2Ca_{0.66}Nb_{1.34}O_6$ (BCNF0)

Basic Oxygen Furnace Gas (BOF Gas)

Blast Furnace (BF)

Blast Furnace-Basic Oxygen Furnace (BF-BOF)

Carbon Capture, Use and Storage (CCUS)

Carbon Dioxide (CO_2)

Carbon Monoxide (CO)

Coke Oven Gas (COG)

CO_2 Equivalents (CO_{2eq})

Concentrated Solar Power (CSP)

Density Functional Theory (DFT)

Direct Air Capture (DAC)

Direct Reduced Iron-Electric Arc Furnace (DRI-EAF)

Energy Dispersive X-ray (EDX)

Fischer Tropsch (FT)

Gas Chromatography (GC)

High Temperature Solid Oxide Electrolysis Cell (HTSOEC)

Hydrogen (H_2)

Hydrogen Direct Reduced Iron (HDRI)

International Energy Agency (IEA)

International Panel on Climate Change (IPCC)

Lanthanum Strontium Manganites (LSMO)

Low Temperature Solid Oxide Electrolysis Cell (LTSOEC)

Microcomputer tomography (Micro CT)

Oxidation Product Gas (OPG)

Oxide Ion Diffusivity (D^*)

Reduction Product Gas (RPG)

Scanning Electron Microscopy (SEM)

Scenario 3 (S3)

Surface Oxygen Exchange Coefficient (k^*)

Synthesis Gas (syngas)

Technology Readiness Levels (TRL)

Thermochemical Cycle (TC)

Thermochemical Cycle Coupled with Blast Furnace-Basic Oxygen Furnace (TC-BF-BOF)

Thermochemical Splitting of CO_2 by BCNF1 (TC-BCNF1)

Tonne of Hot Metal (thm)

Tonne of Liquid Steel (tls)

X-ray Diffraction (XRD)

Yttrium Stabilised Zirconium (YSZ)

Chapter 1 – INTRODUCTION

1.1 Background

To meet the Paris Climate Agreement goal of limiting warming to 1.5 °C, the remaining carbon budget is estimated to be as little as 300 Gt of CO_2 equivalents (CO_{2eq}) [1]. This requires rapid decarbonisation on a global scale, reaching net-zero emissions by 2050. Progress is being made – renewables made up 82 % of total energy capacity installations in 2020, up from 72 % in 2019 [2,3]. The continued growth of renewables along with electrification and efficiency improvements will make up a large proportion of the progress towards net-zero in the coming decades. However, there are sectors, known as the hard-to-decarbonise sectors, for which these methods of emissions reduction will not be enough to lower emissions to close to zero by 2050. These sectors include aviation, shipping, freight, the petrochemicals industry, and other extractive industries, particularly the iron and steel sector. These industries are characterised by extremely high capital investments and long natural lifetimes of equipment. This poses a risk of trillions of dollars in stranded assets if the transition is not managed correctly, but also gigatonnes of entrenched emissions if these assets are allowed to continue operating as usual. Each of these industries has its own unique challenges, for example, freight trucks will have many owners during their million-mile lifetimes before frequently being used in ports for the remaining years of their lives [4].

Many solutions have been proposed to help decarbonise these industries such as electric aircraft for short-haul flights [5], electric heavy-duty trucks [6] and hydrogen-powered ships [7]. However, most of these solutions suffer from low Technology Readiness Levels (TRL), low energy densities and require substantial investment to bring to market at scale.

For example, a ship using 1000 m^3 of heavy fuel oil would require over 8178 m^3 of hydrogen (H_2), at 700 bar, to deliver the same power [7]. Most importantly, waiting for these technologies to mature while existing infrastructure continues to emit at the same rate will make limiting warming to 1.5 °C almost impossible. Immediate, large scale emissions reduction in these sectors is needed while waiting for these zero-carbon solutions to come to fruition. Therefore, drop-in carbon-neutral fuels could be used as a bridging technology while research continues. Carbon neutral drop-in fuels have a few main advantages including immediate emissions reduction once deployed, lower investment requirements and compatibility with existing infrastructure. The concentration of the drop-in fuel could also be gradually increased as supply allows. These fuels could include kerosene for aviation, diesel for freight and diesel or heavy bunker fuel for container ships.

There are currently two main routes of producing drop-in fuels namely from biomass or synthetic fuels, also known as e-fuels or power-to-fuel. Biomass relies upon nature's carbon capture, namely photosynthesis, to take carbon dioxide (CO_2) from the atmosphere and fix the carbon as glucose. This plant matter is then either burnt to produce electricity and heat or converted to fuels such as bio-ethanol. Biomass requires large areas of the globe to be set aside to grow crops, which could displace food crops leading to increased hunger, and requires large volumes of water to grow the crops. According to the International Energy Agency (IEA) net-zero roadmap, 102 EJ of biomass-based energy will be used a year by 2050, requiring a landmass the size of India and Pakistan combined [8]. For example, if all the agricultural and forestry residues, along with all biomass from industrial and municipal waste and all cover crops (crops grown in winter, not the principal crop) in Europe were converted to jet fuel each year, it would supply

only 19% of European jet fuel demand [9]. However, in reality, this would likely only be between 2 and 5%, due to collection and transportation. Additionally, mono-crops, planting only one crop in a large area which is common in biomass practices, can lead to increased soil degradation [10]. Finally, there is often a geographical divide between the place where crops can be optimally grown and where the fuel is needed, meaning that millions of tonnes of biomass would need to be transported.

On the other hand, power-to-fuels technology aims to replicate photosynthesis artificially, taking carbon dioxide from the atmosphere and converting it into a useful form. Carbon monoxide (CO) would be an ideal chemical building block, particularly when combined with hydrogen as synthesis gas (syngas), as it can be converted into fuels such as kerosene and diesel and can also be used as a feedstock for the petrochemical industry, reducing the need for crude oil. The conversion from syngas to fuels is performed *via* the Fischer Tropsch (FT) process, a catalytic upgrading to higher-order olefins (hydrocarbons with more than one carbon atom) [11]. Iron and cobalt catalysts are frequently used, with catalyst choice, reaction conditions and the ratio of CO to H_2 determining the products produced [12]. Alkanes, carbon chains with single carbon-carbon bonds are produced according to Equation 1.1, while alkenes, carbon chains with one carbon=carbon double bond, follow Equation 1.2 and methanol follows Equation 1.3

$$nCO + (2n + 1)H_2 \rightarrow C_nH_{2n+2} + nH_2O \quad (1.1)$$

$$nCO + 2nH_2 \rightarrow C_nH_{2n} + nH_2O \quad (1.2)$$

$$CO + 2H_2 \rightarrow CH_3OH \quad (1.3)$$

Fuels produced from syngas, where the CO is obtained from atmospheric CO_2, release the same amount of CO_2 once the fuels are burnt in use. This essentially closes the carbon cycle, allowing useful work to be produced while maintaining the existing carbon stock

and decoupling economic activity from greenhouse gas emissions. Additionally, synthetic fuels generally generate less soot, particulate matter, and SO_x emissions, leading to improved air quality and human health [13].

There are currently a few methods of producing carbon monoxide from carbon dioxide. Most simply is the thermal decomposition of CO_2 at extremely high temperatures (>2500 °C), requiring large amounts of energy [14]. Second is the electrolysis of CO_2 which suffers from high costs and cannot produce a pure stream of CO, being around 90 % selective [15]. The final option is the thermochemical splitting of CO_2 over a material, commonly a metal oxide or perovskite [16–19]. In a thermochemical cycle, oxygen is released in the first step, while CO is produced in the second step, requiring heat to power the cycle. If this heat is supplied by carbon-neutral sources of energy, such as renewable electricity powering an electric heater, waste heat from existing industrial processes or concentrated solar power (CSP), the carbon monoxide produced is net carbon neutral.

The carbon dioxide can be obtained from various sources. Firstly, the thermochemical plant could be co-located with existing industry or thermal power plants to utilise the high carbon dioxide concentrations in the flue gases, also known as a point source of emissions. Secondly, this technology could also be used with waste pyrolysis plants, capturing carbon dioxide from the waste gases rather than the carbon dioxide being slowly emitted from landfill. Thirdly, as the energy transition proceeds, less fossil-fuelled thermal plants will be operational for use as point sources but direct air capture (DAC) of carbon dioxide should begin at a commercial scale [20]. Where possible, the thermochemical plant should be located near to the carbon source to reduce the need for transporting the gas. Importantly, the only requirement for a CO_2 source for thermochemical splitting is the absence of oxygen in the gas. For the best economics of

the system, carbon dioxide that can be obtained for free produces carbon monoxide at the lowest possible cost.

The synthetic fuels produced from carbon monoxide from a thermochemical cycle may initially be more expensive than that of the fossil fuel equivalent. For example, methanol produced by a solar-powered thermochemical cycle with FT synthesis costs $1.22/kg [21] whereas fossil-based methanol costs $0.51/kg [22]. There are a few factors that can reduce the cost over time. In the short term, companies that pay more for a carbon-neutral fuel will be able to sell their products or services at a higher price as consumers become more climate and carbon-conscious [23]. Secondly, as carbon taxes begin to be introduced across the globe and the price of emitting a tonne of carbon increases, the use of a carbon-neutral fuel will become more attractive [24], potentially even becoming cheaper than the fossil fuel alternative if the full negative externalities of burning fossil fuels are considered. Additionally, oxygen produced during the thermochemical cycle can be sold for profit, and since the oxygen and carbon monoxide are produced in separate steps of the reaction, separation is not required, reducing costs. Furthermore, in a future grid with an overcapacity of renewables, a thermochemical plant may be able to act as demand response, taking electricity from the grid when demand is lower than supply [25]. This could enable the plant to get paid when electricity prices go negative.

Although synthetic fuels produced from the splitting of CO_2 by a thermochemical cycle are originally intended as a transition technology, once the carbon-free alternatives to the hard-to-decarbonise sectors are available at scale there should be a diminishing demand for carbon-neutral fuels. There may be a few small industries that still require these fuels, such as classic cars requiring net-zero compatible petrol. However, at this stage, the

technology could be used to produce liquid fuels for underground storage as a source of negative emissions and carbon sequestration, particularly with injection into old oil fields.

There is great scope for synthetic fuels produced from captured carbon dioxide to aid in the race to net zero. The first industrial-scale thermochemical plant has been demonstrated in Zurich [13]. The system involves three components, a DAC plant, a solar-powered thermochemical reactor, and a gas-to-liquid unit of mature FT technology. A 1GW solar thermal plant can produce 95,000 litres of kerosene a day, enough for a round-trip from London to New York on an Airbus A350, at a cost of €1.2-2.0 per litre (jet fuel currently costs around €0.80 per litre [26]). Most importantly, producing enough synthetic kerosene to completely decarbonise the aviation sector would require an area of 45,000 km^2 for the solar plants, equivalent to 0.5 % of the Sahara Desert. Demonstration plants have also been used to produce solar-powered diesel [27], petrol [28], dimethyl ether [29] and many other commodity chemicals [30,31].

In conclusion, the decarbonisation of the hard-to-decarbonise sectors with synthetic fuels produced from the thermochemical splitting of carbon dioxide is possible. High carbon dioxide to carbon monoxide conversion yields can increase solar-to-fuel efficiency and decrease costs. A large number of thermochemical materials have been researched in the literature which will be discussed in Chapters 2 and 3. However, these materials frequently require extremely high temperatures of between 1400 °C and 1500 °C. Therefore, a material with high CO_2 conversion at lower temperatures is highly sought after to further improve efficiencies. This thesis will focus on a promising family of materials for the thermochemical splitting of CO_2, the barium calcium iron niobates (BCNF).

1.2 Aims and Objectives

- Synthesise and investigate the optimal composition of barium calcium iron niobate perovskites for thermochemical CO_2 splitting.
- Optimise the reduction and oxidation reaction conditions to improve fuel yields.
- Investigate the kinetics and enthalpy of the oxidation reaction and the activation energy of CO_2 splitting.
- Develop and build a rig for the scale up of the BCNF system to enable the conversion of CO_2 to be measured.
- Perform a techno-economic assessment of a BCNF-based thermochemical plant for the industrial production of carbon-neutral carbon monoxide.
- Apply the BCNF-based thermochemical cycle to the decarbonisation of the steel industry through sector coupling.

1.3 Layout of the Thesis

This is an alternative format thesis and includes published and publishable work. To give an overview of the materials that have been researched in the literature for the thermochemical splitting of CO_2, the literature review in Chapter 2 covers iron oxide and the ferrites, the volatile metal oxides, ceria, and perovskites. The BCNF materials covered in this thesis have a perovskite structure but very little is known about them. However, there is a large literature base on another perovskite family, the lanthanum strontium manganites (LSMO). Chapter 3, therefore, investigates the various methods of increasing the CO yields of these materials, with a focus on the mechanisms behind the reduction and oxidation reactions. This gives some insight into how the BCNF perovskite functions. This LSMO-based chapter is in a publishable format and therefore cannot be easily incorporated into the literature review and has therefore been given its own chapter.

Chapter 4 is the beginning of the experimental work. Chapter 4 is a published work, while Chapters 5, 6 & 7 are of publishable standard and have been included in a publishable format. Chapter 4 explores four different compositions of BCNF in the reduction and oxidation reaction, with a focus on understanding the relationship between iron content and CO_2 splitting ability. Chapter 5 utilises the most successful material from Chapter 4, $Ba_2Ca_{0.66}Nb_{0.34}FeO_6$ (BCNF1) and attempts to improve the CO yields by optimising the reduction and oxidation reaction conditions. Chapter 6 investigates the kinetics of the oxidation reaction, culminating in the calculation of the activation energy of the CO_2 splitting reaction. The chapter then covers the scale-up of BCNF1 in a 100g reactor, and the CO_2 to CO conversion rate is measured with gas chromatography (GC). Finally, the industrial scale-up for a BCNF-based thermochemical CO production facility is considered, with a techno-economic assessment culminating in the refinement of a cost of CO production in dollars per kg. Chapter 7 proposes the sector coupling of the iron and steel industry with a BCNF-based thermochemical CO plant. The iron and steel sector is an optimal sector for coupling due to the high temperatures employed, use of carbon monoxide and extremely high CO_2 emissions. The chapter culminates in the calculation of the emissions reduction potential of the UK steel industry if such coupling was utilised. Finally, Chapter 8 presents the conclusions of the current research and suggests areas for future research.

1.4 References

[1] Masson-Delmotte, V., P. Zhai, A. Pirani, S. L. Connors, C. Péan, S. Berger, N. Caud, Y. Chen, L. Goldfarb, M. I. Gomis, M. Huang, K. Leitzell, E. Lonnoy, J.B.R. Matthews, T. K. Maycock, T. Waterfield, O. Yelekçi RY and BZ (eds. . Climate change 2021: the physical science basis. 2021. doi:10.1080/03736245.2010.480842.

[2] IRENA. Renewable Energy Capacity Highlights. 2021.

[3] IRENA. Renewable Energy Capacity Highlights. 2020.

[4] Lee H, Pham HT, Kim C, Lee K. A Study on emissions from drayage trucks in the port city-focusing on the port of Incheon. Sustain 2019;11:1–15. doi:10.3390/su11195358.

[5] Moua L, Roa J, Xie Y, Maxwell D. Critical Review of Advancements and Challenges of All-Electric Aviation. Int Conf Transp Dev 2020 2020.

[6] ICCT, Moultak M, Lutsey N, Hall D. Transitioning to zero-emission heavy-duty freight vehicles. Int Counc Clean Transp 2017:53.

[7] Gray N, McDonagh S, O'Shea R, Smyth B, Murphy JD. Decarbonising ships, planes and trucks: An analysis of suitable low-carbon fuels for the maritime, aviation and haulage sectors. Adv Appl Energy 2021;1:100008. doi:10.1016/j.adapen.2021.100008.

[8] IEA. Net Zero by 2050: A Roadmap for the Global Energy Sector. Int Energy Agency 2021:224.

[9] O'Malley J, Pavlenko N, Searle S. Estimating sustainable aviation fuel feedstock availability to meet growing European Union demand - International Council on Clean Transporation. Int Counc Clean Transp 2021.

[10] Hetherington K. Agribiopolitics: The health of plants and humans in the age of monocrops. Environ Plan D Soc Sp 2020;38:682–98. doi:10.1177/0263775820912757.

[11] Fischer F, Tropsch H. Process for the production of paraffin-hydrocarbons with more than one carbon atom. U.S Patent 1746464, 1930.

[12] Ng DKS, Ng KS, Ng RTL. Integrated Biorefineries. vol. 4. Elsevier; 2017. doi:10.1016/B978-0-12-409548-9.10138-1.

[13] Schäppi R, Rutz D, Dähler F, Muroyama A, Haueter P, Lilliestam J, et al. Drop-in fuels from sunlight and air. Nature 2022;601:63–8. doi:10.1038/s41586-021-04174-y.

[14] Mellor JW. A Comprehensive Treatise on Inorganic and Theoretical Chemistry Vol. VII - Ti, Zr, Hf, Th, Ge, Sn, Pb, Inert Gases. vol. VII. 1927.

[15] Jouny M, Luc W, Jiao F. General Techno-Economic Analysis of CO2 Electrolysis Systems. Ind Eng Chem Res 2018;57:2165–77. doi:10.1021/acs.iecr.7b03514.

[16] Kubicek M, Bork AH, Rupp JLM. Perovskite oxides-a review on a versatile material class for solar-to-fuel conversion processes. J Mater Chem A 2017;5:11983–2000. doi:10.1039/c7ta00987a.

[17] Scheffe JR, Steinfeld A. Oxygen exchange materials for solar thermochemical splitting of H_2O and CO_2: A review. Mater Today 2014;17:341–8. doi:10.1016/j.mattod.2014.04.025.

[18] Hu J, Galvita V V., Poelman H, Marin GB. Advanced chemical looping materials for CO_2 utilization: A review. Materials (Basel) 2018;11:1187, 1–32. doi:10.3390/ma11071187.

[19] Bhosale RR, Takalkar G, Sutar P, Kumar A, AlMomani F, Khraisheh M. A decade of ceria based solar thermochemical H2O/CO2 splitting cycle. Int J Hydrogen Energy 2018;44:34–60.

[20] McQueen N, Gomes KV, McCormick C, Blumanthal K, Pisciotta M, Wilcox J. A review of direct air capture (DAC): scaling up commercial technologies and innovating for the future. Prog Energy 2021;3:032001. doi:10.1088/2516-1083/abf1ce.

[21] Kim J, Henao CA, Johnson TA, Dedrick DE, Miller JE, Stechel EB, et al. Methanol production from CO 2 using solar-thermal energy: Process development and techno-economic analysis. Energy Environ Sci 2011;4:3122–32. doi:10.1039/c1ee01311d.

[22] Methanex. Methanol Price Sheet. 2022.

[23] Roheim CA, Asche F, Santos JI. The elusive price premium for ecolabelled products: Evidence from seafood in the UK market. J Agric Econ 2011;62:655–68. doi:10.1111/j.1477-9552.2011.00299.x.

[24] aus dem Moore N, Brehm J, Gruhl H. Driving Innovation? Carbon Tax Effects in the Swedish Transport Sector. SSRN Electron J 2022. doi:10.2139/ssrn.3995632.

[25] Tan H, Yan W, Ren Z, Wang Q, Mohamed MA. A robust dispatch model for integrated electricity and heat networks considering price-based integrated demand response. Energy 2022;239:121875. doi:10.1016/j.energy.2021.121875.

[26] IATA. Jet Fuel Price Monitor 2022. https://www.iata.org/en/publications/economics/fuel-monitor/.

[27] Graves C, Ebbesen SD, Mogensen M, Lackner KS. Sustainable hydrocarbon fuels by recycling CO2 and H 2O with renewable or nuclear energy. Renew Sustain Energy Rev 2011;15:1–23. doi:10.1016/j.rser.2010.07.014.

[28] Borugadda VB, Kamath G, Dalai AK. Techno-economic and life-cycle assessment of integrated Fischer-Tropsch process in ethanol industry for bio-diesel and bio-gasoline production. Energy 2020;195:116985. doi:10.1016/j.energy.2020.116985.

[29] Michailos S, McCord S, Sick V, Stokes G, Styring P. Dimethyl ether synthesis via captured CO2 hydrogenation within the power to liquids concept: A techno-economic assessment. Energy Convers Manag 2019;184:262–76. doi:10.1016/j.enconman.2019.01.046.

[30] Ali M, Koo HM, Kasipandi S, Han GY, Bae JW. Direct synthesis of liquid fuels and aromatics from syngas over mesoporous FeZrOx catalyst mixed with Mo/ferrierite. Fuel 2020;264:116851. doi:10.1016/j.fuel.2019.116851.

[31] Panzone C, Philippe R, Chappaz A, Fongarland P, Bengaouer A. Power-to-Liquid catalytic CO2 valorization into fuels and chemicals: Focus on the Fischer-Tropsch route. J CO2 Util 2020;38:314–47. doi:10.1016/j.jcou.2020.02.009.

Chapter 2 – LITERATURE REVIEW

2.1 The History of Thermochemical Cycles

The idea behind a thermochemical cycle was to find a group of chemical reactions driven by thermal energy and capable of producing hydrogen which could perform more efficiently and at a lower cost than the process of turning thermal energy into electricity and then electrolysing water. The key to the cyclic nature of the reactions is that the original reactant must be reformed in subsequent steps. In 1966 Funk & Reinstrom implemented the first published thermochemical cycle to produce low-cost hydrogen for use in ammonia fertilisers [1]. Around 1974, General Atomic developed the Sulphur-Iodine cycle, which involved the production of HI and H_2SO_4, the thermal decomposition of H_2SO_4 at 830 °C and finally the decomposition of HI into iodine and hydrogen at 300-450 °C [2,3]. The extremely corrosive nature of HI and H_2SO_4 at high temperatures required careful engineering of the reactor. Then, in 1976 the Cu-Cl cycle was developed, which consisted of the electrolysis of CuCl and hydrochloric acid at room temperature into hydrogen and $CuCl_2$ [4]. The cycle was completed by heating the $CuCl_2$ with steam at 600 °C to reform CuCl and HCl and release oxygen. The electrolysis step has the benefit of only requiring 0.6-1.0V, while conventional water electrolysis requires 1.23V [5].

The ZnO/Zn cycle was established in 1977. Firstly, ZnO is reduced to Zn at 2050 °C, which then decomposes water at 1215 °C, reforming ZnO [6]. This water decomposition occurs at much lower temperatures than the direct thermal decomposition of water which requires between 2000 °C and 2500 °C. The high temperature required for the reduction of ZnO was lowered by the carbothermic reduction of ZnO, reducing ZnO with a carbon

source, requiring only 950 °C and lowering the energy consumption of the cycle [7]. The hybrid sulphur cycle, also called the Westinghouse cycle, was also developed in the 1970s [8,9]. SO_2 is combined with water at below 100 °C to give sulphuric acid and hydrogen. The regeneration steps occur at over 800 °C and involve the decomposition of sulphuric acid to SO_3 and water followed by the splitting of SO_3 to SO_2.

The iron oxide process, first documented in 1977, incorporates the reaction of FeO with water to form Fe_3O_4 and hydrogen at 175 °C [10]. The Fe_3O_4 is then reduced back to FeO at 2225 °C. Modern reactors can perform this reduction reaction in two minutes at 1700 °C under 0.1bar of pressure [11]. The UT-3 cycle was proposed in 1978 and involved Fe, Ca and Br [12]. In the four-step cycle, $CaBr_2$ is reacted with water to give CaO and HBr at 700-750 °C. The CaO is then reacted with bromine at 500-600 °C to reform the $CaBr_2$ and release oxygen. Next Fe_3O_4 is reacted with the HBr produced in the first step to form $FeBr_2$, water and bromine at 200-300 °C. Finally, the $FeBr_2$ is reacted with water to reform the Fe_3O_4 and HBr, and produce hydrogen at 550-600 °C. In the bench-scale UT-3 plant created in 1984 up to 2 litres per hour of hydrogen was produced [13].

At the same time as these water splitting reactions were being developed, attention began to turn to CO_2 splitting as a non-fossil fuel source of carbon, thanks in part to the 1973 oil crisis [14]. The first published carbon dioxide splitting cycle was described in 1974 and involved the reaction between a metal sulphite and CO_2, producing carbon monoxide and metal sulphate. The metal sulphite is regenerated by the decomposition of the sulphate to metal oxide followed by the reaction with SO_2 [15]. Large-scale screening of potential cycles in 1977 found that the reaction between CO_2 and cadmium was promising but proceeded slowly [14]. In 1980, research was published detailing a cerium-based cycle, where CeO_2 reacts with $Na_4P_2O_7$ at 950 °C and, in the absence of water, is able to

split CO_2 to CO [16]. These discoveries started decades of research on the thermochemical splitting of CO_2, to which cerium oxide played a large part. The potential cycles and materials have varied greatly over the years, but one trend is clear: modern thermochemical cycles employ two-step reactions to reduce energy and space requirements and improve round-trip efficiency.

2.2 Materials for Thermochemical Cycles

Modern thermochemical cycles rely on a basic redox reaction, employing the reduction of a material followed by oxidation under carbon monoxide. Reduction requires heat to proceed, and oxygen evolution can be improved by low oxygen partial pressures. Oxidation generally occurs at lower temperatures than those required for reduction. In stoichiometric thermochemical materials, reduction occurs according to Equation 2.1, where one mole of oxygen atoms (or half a mole of diatomic oxygen) is released per mole of material reduced. Once a CO_2 flow is introduced, the original material is reformed through the incorporation of an oxygen atom taken from the CO_2, forming one mole of CO per mole of reduced material that undergoes oxidation (Equation 2.2). Importantly, stoichiometric materials generally undergo a reversible change in the crystal structure.

$$MO_x \rightarrow MO_{x-1} + \frac{1}{2}O_2 \tag{2.1}$$

$$MO_{x-1} + CO_2 \rightarrow MO_x + CO \tag{2.2}$$

Conversely, non-stoichiometric materials undergo reduction and oxidation following Equations 2.3 and 2.4 without significant structural changes in the crystal lattice. During reduction, oxygen is released from the crystal lattice forming local defects called oxygen vacancies. The reduction extent is based on the degree of non-stoichiometry (δ), with one mole of material releasing δ moles of oxygen atoms. For example, if one mole of CeO_2

was reduced to $CeO_{1.96,}$ 0.02 moles of oxygen gas would be released. Once a CO_2 flow is introduced, the material splits CO_2 to CO, using the oxygen atoms to fill the oxygen vacancies, reforming the original material.

$$MO_y \rightarrow MO_{y-\delta} + \frac{\delta}{2} O_2 \quad (2.3)$$

$$MO_{y-\delta} + \delta CO_2 \rightarrow MO_y + \delta CO \quad (2.4)$$

The literature on thermochemical cycles is inconsistent on reaction conditions, including temperatures and gas employed, as well as how gas production is measured. Some researchers measure mass change during the reaction via thermogravimetric analysis, while others weigh the sample before and after the reaction to determine the change in mass and concurrent gas production. Additionally, the units of gas production measurement are inconsistent. While μmol/g seems to be becoming the unit of choice, some researchers are still using ml/g. To aid in comparison, gas production has been standardised to μmol/g in the following research. Another difficulty in comparing results is that in many cases it is unclear whether the gas productions are measured once the reaction is completed, i.e. reaches equilibrium since arbitrarily stopping an experiment after a certain amount of time is not an accurate representation of the activity of a material. One of the challenges of thermochemical cycles is susceptibility to sintering during thermal cycling, where the high temperatures employed lead to agglomeration and a decrease in porosity, resulting in decreased yields. In an attempt to ascertain the influence of sintering, where possible, oxygen evolution and carbon monoxide production are reported from the second thermochemical cycle, indicated by * in the following tables. The second cycle results are thought to provide a more accurate representation of the thermochemical activity of the material.

2.2.1 Ferrites

2.2.1.1 Iron Oxide

Iron oxide is a non-volatile stoichiometric metal oxide, meaning an oxygen atom is lost from every unit cell of the crystal structure during reduction. The most common form of iron oxide is Fe_2O_3; the reduction and oxidation reactions of this material are shown in Equations 2.5 and 2.6, respectively.

$$3Fe_2O_{3(s)} \rightarrow 2Fe_3O_{4(s)} + \frac{1}{2}O_{2(g)} \quad (2.5)$$

$$2Fe_3O_{4(s)} + CO_{2(g)} \rightarrow 3Fe_2O_{3(s)} + CO_{(g)} \quad (2.6)$$

For every three moles of Fe_2O_3 reacted, one mole of carbon monoxide is formed. Iron oxide is cheaply available ($40/kg) however requires temperatures above 1400 °C during reduction [17]. It is possible to increase the efficiency of the reduction reaction by lowering the temperatures used, which can be accomplished by using low oxygen partial pressures (pO_2) in the reduction step [18]. A reduction temperature of 1300 °C is possible at 10^{-11}atm pO_2 while 1000 °C is possible at 10^{-15} atm pO_2. Early work focused on variations of Fe_3O_4. For example, cation-excess magnetite ($Fe_{3+\delta}O_4$, δ=0.127) can split carbon dioxide into carbon in 100 % conversion at 290 °C [19]. This is due to the donation of O^{2-} from the CO_2 to the cation-excess magnetite, which in turn donates electrons to the carbon to maintain charge neutrality. The cation-excess magnetite is formed by heating Fe_3O_4 to 290 °C in a hydrogen flow to allow extra iron to become present in the interstices of the lattice. However, cation-excess magnetite must be stored under a nitrogen atmosphere to avoid oxidation in air. More recently, the Fe_2O_3/Fe_3O_4 pair was found to release 1024 μmol/g of O_2 and produce 34 μmol/g of carbon monoxide during reduction at 1400 °C and oxidation at 1000 °C [20]. Other metals have been doped into the iron

oxide in an effort to improve CO yields and stability, as described in the following sections. It is thought that doping introduces defect structures which may aid in reduction through the addition of an element with a different valence than Fe, also called aliovalence. Doping may also increase the strain in the lattice which may affect the reactivity.

2.2.1.2 Manganese Ferrites

Conversely, ferrites are non-stoichiometric oxides. Oxygen-deficient Mn(II)ferrite ($Mn_{0.97}Fe_{2.02}O_{3.92}$) is produced by heating stoichiometric Mn(II)ferrite to 300 °C under hydrogen [21]. The oxygen-deficient ferrite was able to decompose carbon dioxide into carbon or CO at 300 °C however the rate was much slower than oxygen-deficient magnetite, showing that the concentration of Fe^{2+} ions influences the rate of conversion. Another manganese ferrite is Mangano-Wüstite, $Fe_{0.67}Mn_{0.32}O$ [22]. At 400 °C, 23 % of the CO_2 injected was decomposed to CO, 88 % of which was then decomposed to carbon. After 200 hours, only 18 % of the initial CO_2 was present, although the benefit of this high yield is offset by the slow reaction rate. For $Fe_{2-x}Mn_xO_4$ $(0.2 \geq x \geq 1)$, as the manganese content increases, oxygen evolution decreases but CO production increases [23,24]. $MnFe_2O_4$ produced 105 μmol/g of CO in the first cycle, decreasing to 78 μmol/g by the third cycle, showing that these materials are susceptible to sintering. $MnFe_2O_4$ was supported on yttrium stabilised zirconia (YSZ), with 10 wt% of the ferrite [25]. This supported ferrite was able to produce 73 μmol/g of oxygen and 148 μmol/g of CO after 5 cycles. Doping iron oxide with manganese decreases the enthalpy of reduction, although varying concentrations of manganese all have similar enthalpies of around 160 kJ/kg [26–28]. The enthalpy for the reduction of

Mn_2O_3 to Mn_3O_4 is 205 kJ/kg, much lower than iron oxide, suggesting the reduction reaction of manganese oxide is more favourable [29,30].

2.2.1.3 Nickel Ferrites

In comparison to manganese ferrites, where there are opposing trends of oxygen and carbon monoxide production, in nickel ferrites, the higher the nickel content, the higher the oxygen evolution and carbon monoxide production, as seen in Table 2.1. For example, $NiFe_2O_4$ produces 222 μmol/g of oxygen and 375 μmol/g of CO [24]. However, in the second thermochemical cycle these values drop to 64 μmol/g and 128 μmol/g, respectively [31]. This same drop in reactivity is seen between the first and second cycles for all other unsupported nickel ferrites in the literature when the nickel content is 1 or below, suggesting extreme susceptibility to sintering. However, $Ni_{1.8}Fe_{1.2}O_4$ produced 420 μmol/g consistently over twenty full cycles, suggesting that the higher concentration of nickel aids in sintering resistance during repeated cycling [32]. To improve the cyclability of $NiFe_2O_4$, the ferrite was supported on four different supports (SiO_2, ZrO_2, MgO and YSZ) [33]. MgO was found to be the most successful support, producing 211 μmol/g in the second thermochemical cycle, which is higher than the unsupported ferrite. On the other hand, SiO_2 and ZrO_2 led to decreases in yield, while YSZ had very little effect [25,33].

Table 2.1. Oxygen Evolution and Carbon Monoxide Production from Nickel Ferrites (data from second thermochemical cycle, % value next to a supported ferrite indicates weight or molar % of ferrite in total material)*

Material	Oxygen Evolution (μmol/g)	Carbon Monoxide Production (μmol/g)	Reference
$Ni_{1.8}Fe_{1.2}O_4$	Not given	420*	[32]
$NiFe_2O_4$	222	375	[24]
	64*	128*	[31]
$Ni_{0.8}Fe_{2.2}O_4$	128	200	[24]

	29*	42*	[31]
$Ni_{0.6}Fe_{2.4}O_4$	90	100	[24]
	22*	30*	[31]
$Ni_{0.5}Fe_{2.5}O_4$	81	76	[24]
	12*	20*	[31]
$Ni_{0.4}Fe_{2.6}O_4$	75	70	[24]
	11*	14*	[31]
$Ni_{0.2}Fe_{2.8}O_4$	62.5	56.2	[24]
	10*	10*	[31]
$NiFe_2O_4/SiO_2$ (19%)	71*	24*	[33]
$NiFe_2O_4/ZrO_2$ (19%)	83*	69*	[33]
$NiFe_2O_4/ZrO_2$ (61 %)	Not given	180*	[32]
$NiFe_2O_4$/MgO (19%)	121*	211*	[33]
$NiFe_2O_4$/YSZ (10%)	65*	138*	[25]

2.2.1.4 Cobalt Ferrites

There is a large variation in the results reported for cobalt ferrites by different research groups, as seen in Table 2.2. Two groups report decreasing oxygen evolution with decreasing cobalt content [34,35], while a third reports increasing oxygen production [20]. However, all three groups report increasing carbon monoxide production with increasing cobalt content. The highest production for $CoFe_2O_4$ is reported as 241 μmol/g of O_2 and 469 μmol/g in the second cycle [35]. The activation energy of the oxidation reaction under CO_2 was found to be 52.1 kJ/mol for this material [36]. When $CoFe_2O_4$ is actively reduced under hydrogen, an exceptional carbon monoxide yield of 6800 μmol/g is achieved [37], although the overall energy implications of this has yet to be calculated since the production of hydrogen requires energy. $CoFe_2O_4$ was tested with various supports including varying concentrations of YSZ and SiO_2, ZrO_2, Al_2O_3 and CoO [25,36,38,39]. YSZ and Al_2O_3 are found to lower yields, while the SiO_2 supported material produces 408 μmol/g of CO, despite an activation energy of CO_2 splitting of 133 kJ/mol, well over double the unsupported material [25,36,38]. CoO and ZrO_2 are also

successful supports, producing 333 μmol/g and 233 μmol/g of CO in the second cycle, respectively [39].

Table 2.2. Oxygen Evolution and Carbon Monoxide Production from Cobalt Ferrites (data from second thermochemical cycle, % value next to a supported ferrite indicates weight or molar % of ferrite in total material)*

Material	Oxygen Evolution (μmol/g)	Carbon Monoxide Production (μmol/g)	Reference
$CoFe_2O_4$	222	145	[20]
	241*	469*	[35]
	80*	140*	[34]
	146	284	[38]
	Reduced under H_2	6800	[37]
$Co_{0.8}Fe_{2.2}O_4$	38*	73*	[34]
	116*	225*	[35]
	274	114	[20]
$Co_{0.6}Fe_{2.4}O_4$	30*	39*	[34]
	59*	113*	[35]
	340	51	[20]
$Co_{0.5}Fe_{2.5}O_4$	15*	14*	[34]
	53*	94*	[35]
	503	43	[20]
$Co_{0.4}Fe_{2.6}O_4$	18*	18*	[34]
	47*	75*	[35]
	532	40	[20]
$Co_{0.2}Fe_{2.8}O_4$	11*	7*	[34]
	22*	75*	[35]
	862	37	[20]
$CoFe_2O_4$/YSZ (5%)	Not given	18	[36]
$CoFe_2O_4$/YSZ (10%)	93*	191*	[25]
	Not given	40	[36]
$CoFe_2O_4$/YSZ (20%)	Not given	64	[36]
$CoFe_2O_4$/YSZ (30%)	Not given	73	[36]
$CoFe_2O_4$/YSZ (50%)	Not given	16	[36]
$CoFe_2O_4/SiO_2$ (30%)	248	408	[38]
$CoFe_2O_4$/CoO (75.8%)	Not given	333*	[39]
$CoFe_2O_4/ZrO_2$ (75.8%)	Not given	223*	[39]

$CoFe_2O_4/Al_2O_3$ (75.8%)	Not given	93*	[39]

2.2.1.5 Other Ferrites and Mixed Metal Ferrites

Magnesium ferrites and other mixed-metal ferrites including zirconium and copper have also been studied, as seen in Table 2.3. $Mg_xFe_{3-x}O_4$ with $x \leq 1$ is unsuccessful at all Mg contents, with the highest CO yields in the second cycle of only 79 µmol/g for $MgFe_2O_4$ [23,40]. However, $Mg_{1.2}Fe_{1.8}O_4$ has exceptionally high O_2 and CO yields of 951 µmol/g and 688 µmol/g, respectively [41]. In addition, the CO yield after four cycles is 614 µmol/g, showing that this material is incredibly resistant to sintering. This replicates the finding from $Ni_{1.8}Fe_{1.2}O_4$ where a Ni content above 1 had high CO yields and extreme resistance to sintering [32]. This suggests that the incorporation of another metal atom in Fe_3O_4 with an Fe content below 2 is sufficient to induce resistance to the sintering that plagues other ferrites. Mixed nickel and magnesium ferrites have higher yields than magnesium ferrites, with the highest CO production obtained for $Ni_{0.9}Mg_{0.1}Fe_2O_4$ of 231 µmol/g in the second cycle [42].

Another mixed metal ferrite, zirconium cobalt ferrites, also demonstrate high CO yields, both unsupported and with SiO_2 supports [38]. The most successful of these ferrites is $Co_{0.8}Zr_{0.2}Fe_2O_4/SiO_2$, producing 536 µmol/g of CO. Finally, copper-cobalt ferrites were actively reduced under hydrogen and $Cu_{0.2}Co_{0.8}Fe_2O_4$ produced the most carbon monoxide, with yield decreasing with increasing copper content [37]. Interestingly the yield with any concentration of copper is higher than when there is no copper present, suggesting that the incorporation of copper in cobalt ferrites is beneficial for CO_2 splitting. Another copper-based mixed metal ferrite is $(Ni_{1-x}Cu_x)Fe_2O_4$ where x = 0.25, 0.5 and 0.75 [43]. As the copper content increases and nickel content decreases, the

temperature at which the oxidation reaction proceeds decreases, again suggesting that the presence of copper in the ferrite is favourable for CO_2 splitting. This is thought to be because the presence of copper causes an increase in the reduction of Fe^{3+} and Fe^{2+} to Fe^0 [37]. The x = 0 material had 7.2 % of iron atoms in the Fe^0 state whereas the x = 0.2 material had 13.4 % of iron in this state. This deeper reduction provides more opportunities for re-oxidation through the splitting of CO_2.

Table 2.3. Oxygen Evolution and Carbon Monoxide Production from Mixed Metal Ferrites (data from second thermochemical cycle, % value next to a supported ferrite indicates weight or molar % of ferrite in total material)*

Material	Oxygen Evolution (μmol/g)	Carbon Monoxide Production (μmol/g)	Reference
$Cu_{0.2}Co_{0.8}Fe_2O_4$	Reduced under H_2	9000	[37]
$Cu_{0.4}Co_{0.6}Fe_2O_4$	Reduced under H_2	8200	[37]
$Cu_{0.6}Co_{0.4}Fe_2O_4$	Reduced under H_2	7600	[37]
$Co_{0.8}Zr_{0.1}Fe_2O_4$	207	373	[38]
$Co_{0.9}Zr_{0.1}Fe_2O_4/SiO_2$ (30%)	308	517	[38]
$Co_{0.85}Zr_{0.15}Fe_2O_4/SiO_2$ (30%)	297	437	[38]
$Co_{0.8}Zr_{0.2}Fe_2O_4/SiO_2$ (30%)	302	536	[38]
$Co_{0.7}Zr_{0.3}Fe_2O_4/SiO_2$ (30%)	308	503	[38]
$Ni_{0.9}Mg_{0.1}Fe_2O_4$	134*	231*	[42]
$Ni_{0.7}Mg_{0.3}Fe_2O_4$	92*	151*	[42]
$Ni_{0.5}Mg_{0.5}Fe_2O_4$	107*	171*	[42]
$Ni_{0.3}Mg_{0.7}Fe_2O_4$	95*	180*	[42]
$Ni_{0.1}Mg_{0.9}Fe_2O_4$	93*	155*	[42]
$Mg_{1.2}Fe_{1.8}O_4$	951	688	[41]
$MgFe_2O_4$	58*	79*	[40]
	60.2*	79.1*	[23]
$Mg_{0.8}Fe_{2.2}O_4$	27.2*	29.5*	[23]
	27*	28*	[40]
$Mg_{0.6}Fe_{2.4}O_4$	12.4*	16.8*	[23]
	12*	14*	[40]
$Mg_{0.5}Fe_{2.5}O_4$	12.7*	17.6*	[23]

	12*	14*	[40]
$Mg_{0.4}Fe_{2.6}O_4$	13.9*	18.6*	[23]
	13*	13*	[40]
$Mg_{0.2}Fe_{2.8}O_4$	15.8*	16.1*	[23]
	14*	10*	[40]
$MgFe_2O_4$/YSZ (10%)	55*	130*	[25]

2.2.2 Volatile Metal Oxides

Volatile metal oxides have a boiling temperature of the reduced metal that is lower than the reduction temperature of the metal oxide, meaning that the gaseous product metal must be quenched to prevent it from recombining with the oxygen-containing product gases [44]. The reduction and oxidation of zinc oxide, the most frequently researched volatile metal oxide, can be seen in Equations 2.7 and 2.8, respectively. The reduction reaction occurs at 2000 °C, producing gaseous metallic zinc. Metallic zinc is liquid above 420 °C and gaseous above around 910 °C. The zinc can then be used to split CO_2 at 425 °C, reforming the original zinc oxide [45,46].

$$ZnO_{(s)} \rightarrow Zn_{(g)} + \frac{1}{2}O_{2(g)} \tag{2.7}$$

$$Zn_{(s)} + CO_{2(g)} \rightarrow ZnO_{(s)} + CO_{(g)} \tag{2.8}$$

The reaction rate of the CO_2 splitting reaction by Zn is extremely rapid, regardless of the reaction temperature [47]. Oxidation at 535 °C has the fastest reaction rate, with maximum conversion achieved in a matter of seconds. However, oxidation at 375 °C has the highest overall conversion, despite having slightly lower kinetics. The heating rate also plays a role, with 20 °C/min having the fastest kinetics but 15 °C/min having higher overall conversion. Additionally, a CO_2 concentration of 50 % relative to the Zn concentration has the fastest kinetics, with CO_2 concentrations of 30 % or lower leading

to incomplete conversion. Finally, the temperature of maximum CO_2 formation can be lowered by increasing the ratio of inert gas (often N_2) to metal. For example, at a 1000:1 ratio, this temperature is 550 °C, while it is 500 °C for a 10,000:1 ratio.

Focusing briefly on the SnO_2/SnO redox pair, the optimum temperature for CO_2 splitting is 800 °C, where there is 100% conversion of the tin back to SnO_2 [48]. However, at around 600 °C, disproportionation of the SnO produced during reduction occurs, following Equation 2.9.

$$2SnO_{(s)} \rightarrow SnO_{2(s)} + Sn_{(l)} \quad (2.9)$$

This is unfavourable for CO_2 splitting due to the melting of Sn which decreases the surface area of the powder and therefore decreases reactivity. However, disproportionation can be minimised by fast heating rates during the oxidation reaction, maximising the concentration of the reactive Sn^{2+} species. A heating rate of 20 °C/min reaches full conversion in half the time than when the heating rate is 10 °C/min [49]. As the CO_2 concentration relative to the SnO is increased, the reaction rate and conversion increase [47,49]. The activation energy for SnO oxidation is estimated to be 86-88 kJ/mol [47].

Other volatile metal oxides and their reduction temperatures include MgO at 3440 °C [7,50], ZrO_2 at 2725 °C [51], and GeO_2 at 1830 °C [48]. These extremely high reduction temperatures require a large amount of energy and the large temperature swing between reduction and oxidation is also inefficient. One way to reduce the reduction temperature is through carbothermal reduction with a solid carbon source. For example, the carbothermal reduction of SnO_2 reduces the reduction temperature from 2060 °C to 650 °C [7,51]. However, this requires a large supply of solid carbon that will be used up and

may increase the carbon emissions of the thermochemical cycle if the carbon source is not carefully selected.

Research has also been undertaken into how to collect the gaseous metal after reduction, including condensation onto a cold solid medium of silica. Maintaining this solid at 250 °C produces the highest yield of metallic zinc and allows for rapid enough cooling to inhibit re-oxidation of the gaseous metal. The ratio of CO to CO_2 also has an effect, since higher CO_2 concentrations lead to more oxidation; a ratio of 9:1 can give almost 100 % pure zinc upon cooling. The thermochemical reactions of the volatile metal oxides can be used for fuel or metal production; however, in either case, quenching of the gaseous metal involves a large energy penalty.

2.2.3 Ceria

Ceria, or cerium oxide (CeO_2), is an attractive compound for the thermochemical splitting of carbon dioxide due to a combination of changes in oxygen stoichiometry as a response to changes in temperature without a change in the crystal structure, a high melting temperature of 2525 °C and a high catalytic activity towards carbon dioxide [52]. In the reduction step, ceria is heated to between 1400 °C and 1600 °C to induce oxygen non-stoichiometry. This causes the formation of oxygen vacancies in the crystal lattice, a defect structure where the charge is accommodated by the surrounding cerium atoms. The average oxygen evolution in the second cycle of CeO_2 in the literature is 77 μmol/g [53–62]. The oxidation reaction generally occurs between 1000 °C and 1400 °C, with an average carbon monoxide production in the second cycle of 139 μmol/g. X-ray Diffraction (XRD) of CeO_2 shows a peak shift towards smaller angles after reduction and a shift back to the original peak positions after oxidation [60]. This is evidence of the redox reaction, as the average oxidation state after reduction is decreased and the ionic

radius of Ce^{3+} is larger than Ce^{4+}, shifting the diffraction peaks to lower angles. Density functional theory (DFT) has found that the CO_2 molecule adsorbs parallel to an oxygen vacancy, resulting in a bent CO_2 molecule with longer CO bonds and an O-C-O angle of 136.9 °, compared to the usual 180 ° [63]. The reduced ceria takes on the negative charge from the oxygen, splitting CO_2 to CO and filling the oxygen vacancy.

Ceria can be made to undergo redox reactions isothermally. At 1500 °C, the flow rates of sweep gas and CO_2 can be manipulated to reduce or oxidise ceria [64]. A sweep gas (N_2 or Ar) flow of 150 $mLmin^{-1}g^{-1}$ is ideal for reduction while a CO_2 flow of 50 $mLmin^{-1}g^{-1}$ leads to oxidation. In this case, the total thermodynamic efficiency for the splitting of CO_2 is 12% [65]. After 102 cycles of reduction and oxidation with the above gas flows, the production of CO was twice that of O_2, meaning all oxygen vacancies are used for fuel production [64]. More rapid CO production is possible with higher CO_2 flow rates, but at the expense of efficiency, since the sensible heating of the gases is a major thermal loss.

The most common and successful dopant of ceria is zirconium. The most effective zirconium-doped ceria is $Ce_{0.85}Zr_{0.15}O_2$, with an average oxygen evolution of 153 μmol/g and carbon monoxide yield of 269 μmol/g in the second cycle, showing significantly higher yields than undoped ceria. This is likely due to a combination of factors which increase or decrease yields. Firstly, zirconium has a lower molecular weight than cerium, meaning that an increase in the zirconium content increases the relative number of cerium active sites per gram of material [56]. However, the presence of zirconium decreases the absolute number of cerium active sites, through the replacement of Ce atoms with Zr. Secondly, Zr^{4+} is smaller than Ce^{4+}, which drives the formation of oxygen vacancies. Thirdly, doping with Zr increases the oxygen partial pressure at which the material will undergo reduction, meaning less oxygen has to be removed from the reactor for reduction

to occur [66]. Additionally, doping with zirconium decreases the enthalpy of reduction from 467 kJ/mol to 273 kJ/mol, leading to more facile oxygen vacancy formation [66]. Finally, doping with 10 % Zr decreases the activation energy of CO_2 splitting from 235 kJ/mol to 162 kJ/mol, in line with the higher capacity for CO production [67]. Another explanation for the higher yields with zirconium doping, is that since zirconium is known to have good oxide ion conductivity, doping could allow oxygen vacancies to migrate easily within the crystal structure, allowing new vacancies to be formed or filled during reduction or oxidation, respectively [68].

However, doping with zirconium leads to a drastic decrease in the reaction rate. For example, 90% oxidation of CeO_2 was obtained in 6 minutes, whereas $Ce_{0.85}Zr_{0.15}O_2$ needed 45 minutes to reach the same degree of oxidation [60]. Additionally, the entropy of the reduction reaction is also lower, reducing the driving force of the reaction [66]. Finally, most zirconium-doped ceria experience sintering during thermal cycling, decreasing fuel yields. However, it was found that $Ce_{0.75}Zr_{0.25}O_2$ synthesised via a Pechini synthesis retains its porous morphology through repeated cycling [54]. This is in direct contrast to $Ce_{0.75}Zr_{0.25}O_2$ synthesised via either the co-precipitation of hydroxides, the hydrothermal-assisted synthesis method, or the sol-gel synthesis, which all exhibited agglomeration and macroscopic sintering after cycling. Additionally, the Pechini material had an activation energy of CO_2 splitting of 88.1 kJ/mol.

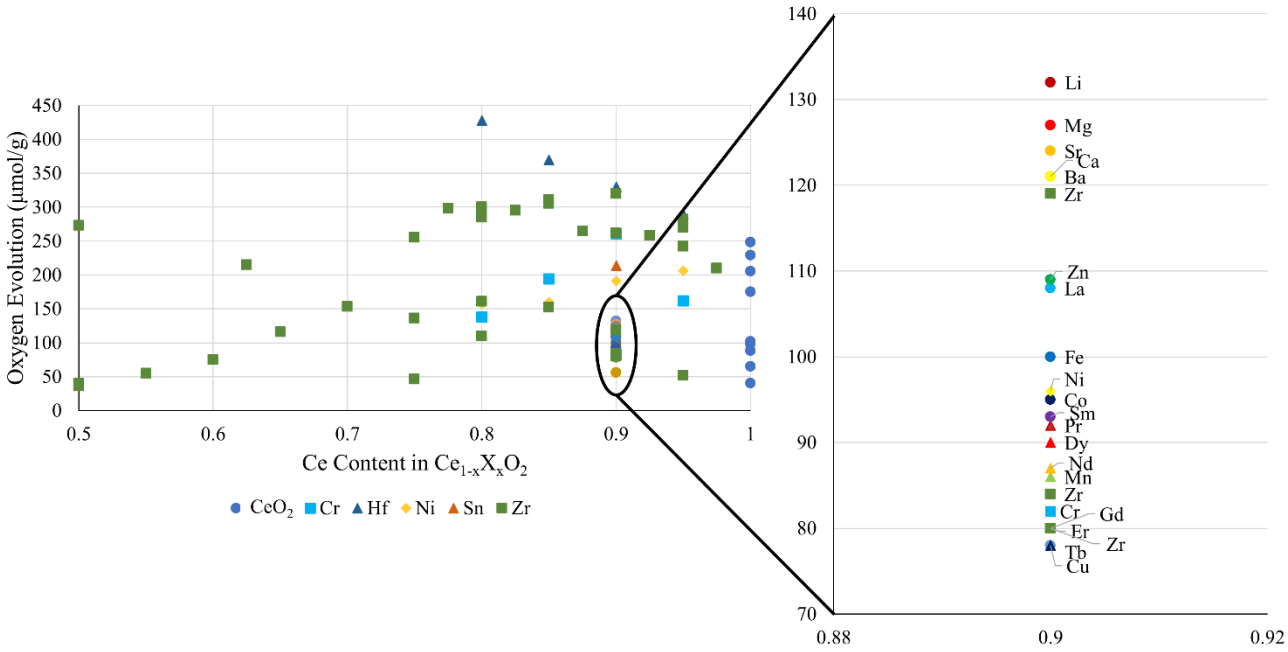

Figure 2.1. Oxygen Evolution in the Second Thermochemical Cycle as a Function of Ceria Content and Dopant Element (data obtained from [53–60,62,69–74])

Twenty-two other dopants have been used in the literature, as outlined in Table 2.4. Chromium, hafnium and nickel are particularly successful, with average oxygen and CO yields in the second cycle of 142 µmol/g and 167 µmol/g, 180 µmol/g and 354 µmol/g, and 139 µmol/g and 162 µmol/g, respectively [58,60,62,67]. Hafnium doping is particularly attractive as the ratio of CO to O_2 is almost exactly two, showing that all oxygen vacancies created during reduction are filled during oxidation. The optimum concentration of hafnium is 20 %, producing 428 µmol/g of carbon monoxide in the second cycle, outperforming all zirconium-doped ceria [58]. Conversely, there are many dopants which produce between 35 and 115 µmol/g of oxygen, as seen in the inset in Figure 2.1, showing either very little change from undoped ceria or even reducing yields. However, there are a few main trends in oxygen evolution volumes in this group of dopants. The alkali earth elements are generally the most successful, such as magnesium, calcium, and barium, while the lanthanides are in the middle, with no relationship

between lanthanide size and oxygen evolution. Finally, the least successful dopants are the first row transition metals, particularly copper and manganese. The same is seen with carbon monoxide yields, with many materials producing between 80 and 125 μmol/g (Figure 2.2 inset). Importantly, some dopants may be beneficial for either reduction or oxidation, rather than both reactions. For example, although doping with titanium leads to a substantial increase in oxygen evolution (537 μmol/g in the first cycle), a concurrent increase in CO production is not seen (32 μmol/g in the first cycle) [69]. Double doping has also been attempted where one of the dopants is zirconium or silver [57,59,71,73–77]. One of the most successful of these materials is $Ce_{0.837}Zr_{0.15}Sm_{0.013}O_2$ producing 140 μmol/g of O_2 and 272 μmol/g of CO in the second cycle [57]. On the other hand, materials containing iron, magnesium or manganese were found to be severely sintered, meaning the materials could not be fully oxidised [75]. $Ce_{0.4}Zr_{0.5}La_{0.08}Pr_{0.02}O_2$, a triple-doped ceria, produced 139 μmol/g and 288 μmol/g of O_2 and CO, despite only containing 40 % of the redox-active component, cerium [59].

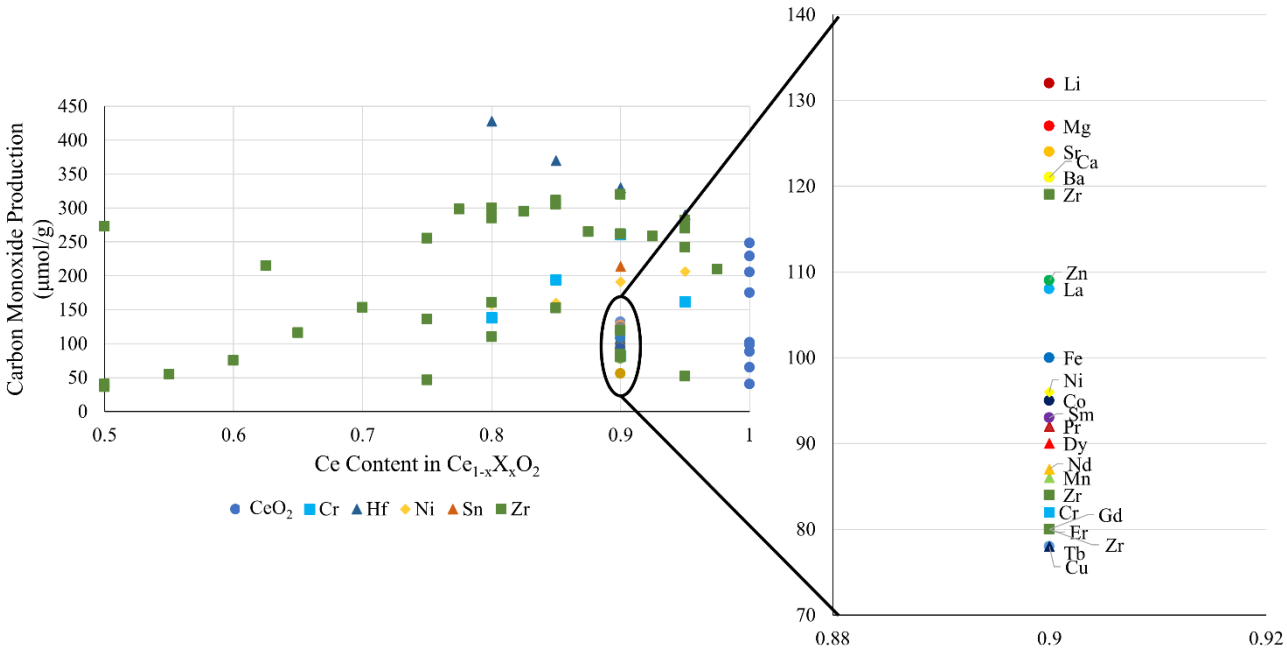

Figure 2.2 Carbon Monoxide Production in the Second Thermochemical Cycle as a Function of Ceria Content and Dopant Element (data obtained from [70–74,53–60,62,69])

Table 2.4. Oxygen Evolution and Carbon Monoxide Production from Ceria-based Compounds (data from second thermochemical cycle)*

Material	Oxygen Evolution (µmol/g)	Carbon Monoxide Production (µmol/g)	Reference
CeO_2	91*	175*	[53]
	50*	102*	[54]
	24*	40*	[55]
	115	238	[77]
	100*	205*	[56] [57]
	Not given	127	[67]
	231	134	[70]
	127*	248*	[58]
	24*	65*	[59]
	188*	229*	[60]
	45*	88*	[61]
	44*	98*	[62]
$Ce_{0.9}Ba_{0.1}O_2$	76*	121*	[79]
$Ce_{0.9}Ca_{0.1}O_2$	63*	121*	[79]
$Ce_{0.9}Co_{0.1}O_2$	41*	95*	[62]

$Ce_{0.95}Cr_{0.05}O_2$	177*	162*	[60]
$Ce_{0.9}Cr_{0.1}O_2$	188*	261*	[60]
	Not given	133	[67]
	73*	82*	[62]
$Ce_{0.85}Cr_{0.15}O_2$	162*	194*	[60]
$Ce_{0.8}Cr_{0.20}O_2$	108*	138*	[60]
$Ce_{0.9}Cu_{0.1}O_2$	38*	78*	[62]
$Ce_{0.9}Dy_{0.1}O_2$	51*	90*	[61]
$Ce_{0.9}Er_{0.1}O_2$	74*	80*	[61]
$Ce_{0.9}Fe_{0.1}O_2$	50*	100*	[62]
$Ce_{0.9}Gd_{0.1}O_2$	54*	80*	[61]
$Ce_{0.95}Hf_{0.05}O_2$	135*	290*	[58]
$Ce_{0.9}Hf_{0.1}O_2$	182*	330*	[58]
$Ce_{0.85}Hf_{0.15}O_2$	195*	370*	[58]
$Ce_{0.8}Hf_{0.2}O_2$	208*	428*	[58]
$Ce_{0.75}Hf_{0.25}O_2$	414	101	[70]
$Ce_{0.9}La_{0.1}O_2$	Not given	142	[67]
	56*	108*	[61]
$Ce_{0.9}Li_{0.1}O_2$	71*	132*	[79]
$Ce_{0.9}Mg_{0.1}O_2$	75*	127*	[79]
$Ce_{0.9}Mn_{0.1}O_2$	39*	86*	[62]
$Ce_{0.95}Ni_{0.05}O_2$	171*	206*	[60]
$Ce_{0.9}Ni_{0.1}O_2$	165*	191*	[60]
	42*	96*	[62]
$Ce_{0.85}Ni_{0.15}O_2$	160*	160*	[60]
$Ce_{0.8}Ni_{0.20}O_2$	160*	158*	[60]
$Ce_{0.9}Nd_{0.1}O_2$	46*	87*	[61]
$Ce_{0.9}Pr_{0.1}O_2$	48*	92*	[61]
$Ce_{0.9}Sm_{0.1}O_2$	84*	93*	[61]
$Ce_{0.9}Sn_{0.1}O_2$	110*	214*	[79]
$Ce_{0.9}Sr_{0.1}O_2$	63*	124*	[79]
$Ce_{0.9}Tb_{0.1}O_2$	56*	78*	[61]
$Ce_{0.9}Ti_{0.1}O_2$	Not given	136	[67]
$Ce_{0.8}Ti_{0.2}O_2$	536	32	[70]
$Ce_{0.9}V_{0.1}O_2$	Not given	139	[67]
$Ce_{0.9}W_{0.1}O_2$	Not given	125	[67]
$Ce_{0.9}Y_{0.1}O_2$	Not given	142	[67]

$Ce_{0.9}Zn_{0.1}O_2$	47*	109*	[62]
$Ce_{0.975}Zr_{0.025}O_2$	110*	210*	[56]
$Ce_{0.95}Zr_{0.05}O_2$	125*	242*	[56]
	130*	270*	[58]
	192*	282*	[60]
	27*	52*	[80]
$Ce_{0.925}Zr_{0.075}O_2$	127*	258*	[56]
$Ce_{0.9}Zr_{0.1}O_2$	40*	84*	[62]
	86*	119*	[81]
	42*	80*	[80]
	Not given	180	[67]
	162*	320*	[58]
	194*	262*	[60]
$Ce_{0.875}Zr_{0.125}O_2$	130*	265*	[56]
$Ce_{0.85}Zr_{0.15}O_2$	155*	305*	[56]
	217*	311*	[60]
	158*	307*	[57]
	81*	152*	[80]
$Ce_{0.825}Zr_{0.175}O_2$	145*	295*	[56]
$Ce_{0.8}Zr_{0.2}O_2$	56*	110*	[80]
	152*	300*	[56]
	105*	161*	[75] [76]
	242	470	[58]
	200*	285*	[60]
$Ce_{0.775}Zr_{0.225}O_2$	145*	298*	[56]
$Ce_{0.75}Zr_{0.25}O_2$	128*	255*	[56]
	97*	152	[54]
	373	382	[70]
	39*	46*	[81]
	71*	136*	[80]
$Ce_{0.7}Zr_{0.3}O_2$	83*	153*	[80]
$Ce_{0.65}Zr_{0.35}O_2$	62*	116*	[80]
$Ce_{0.6}Zr_{0.4}O_2$	39*	75*	[80]
$Ce_{0.625}Zr_{0.375}O_2$	110*	215*	[56]
$Ce_{0.55}Zr_{0.45}O_2$	34*	55*	[80]
$Ce_{0.5}Zr_{0.5}O_2$	53*	36*	[81]
	149*	273*	[59]

	28*	40*	[80]
$Ce_{0.9}Ag_{0.05}Co_{0.05}O_2$	71*	133*	[71]
$Ce_{0.9}Ag_{0.05}Cr_{0.05}O_2$	80*	151*	[71]
$Ce_{0.9}Ag_{0.05}Cu_{0.05}O_2$	71*	125*	[71]
$Ce_{0.9}Ag_{0.05}Dy_{0.05}O_2$	366	144	[72]
$Ce_{0.9}Ag_{0.05}Er_{0.05}O_2$	415	134	[72]
$Ce_{0.9}Ag_{0.05}Fe_{0.05}O_2$	59*	94*	[71]
$Ce_{0.9}Ag_{0.05}Gd_{0.05}O_2$	312	125	[72]
$Ce_{0.9}Ag_{0.05}La_{0.05}O_2$	320	158	[72]
$Ce_{0.9}Ag_{0.05}Mn_{0.05}O_2$	56*	89*	[71]
$Ce_{0.9}Ag_{0.05}Nd_{0.05}O_2$	191	153	[72]
$Ce_{0.9}Ag_{0.05}Ni_{0.05}O_2$	73*	132*	[71]
$Ce_{0.9}Ag_{0.05}Pr_{0.05}O_2$	548	153	[72]
$Ce_{0.9}Ag_{0.05}Sm_{0.05}O_2$	195	126	[72]
$Ce_{0.9}Ag_{0.05}Tb_{0.05}O_2$	212	139	[72]
$Ce_{0.9}Ag_{0.05}Zn_{0.05}O_2$	84*	133*	[71]
$Ce_{0.9}Ag_{0.05}Zr_{0.05}O_2$	72*	128*	[71]
$Ce_{0.5}Zr_{0.25}Hf_{0.25}O_2$	79*	63*	[73]
$Ce_{0.75}Zr_{0.2}Ca_{0.05}O_2$	125*	250*	[76]
$Ce_{0.7}Zr_{0.2}Ca_{0.1}O_2$	138*	226*	[76]
$Ce_{0.75}Zr_{0.2}Co_{0.05}O_2$	115*	167*	[74]
$Ce_{0.75}Zr_{0.2}Cr_{0.05}O_2$	102*	164*	[74]
$Ce_{0.7}Zr_{0.2}Fe_{0.1}O_2$	103*	121*	[75]
$Ce_{0.75}Zr_{0.2}Fe_{0.05}O_2$	147*	155*	[74]
$Ce_{0.6}Zr_{0.2}Hf_{0.2}O_2$	56*	75*	[73]
$Ce_{0.78}Zr_{0.2}Mg_{0.02}O_2$	222*	194*	[75]
$Ce_{0.75}Zr_{0.2}Mg_{0.05}O_2$	106*	160*	[75]
	103*	194*	[76]
$Ce_{0.7}Zr_{0.2}Mg_{0.1}O_2$	123*	221*	[76]
	106*	210*	[75]
$Ce_{0.75}Zr_{0.2}Mn_{0.05}O_2$	88*	147*	[74]
$Ce_{0.7}Zr_{0.2}Mn_{0.1}O_2$	115*	117*	[75]
$Ce_{0.75}Zr_{0.2}Ni_{0.05}O_2$	107*	203*	[74]
$Ce_{0.7}Zr_{0.2}Ni_{0.1}O_2$	102*	113*	[75]
$Ce_{0.75}Zr_{0.2}Zn_{0.05}O_2$	201*	176*	[74]
$Ce_{0.837}Zr_{0.15}Gd_{0.013}O_2$	120*	237*	[57]
$Ce_{0.837}Zr_{0.15}Sm_{0.013}O_2$	140*	272*	[57]

$Ce_{0.837}Zr_{0.15}Y_{0.013}O_2$	123*	238*	[57]
$Ce_{0.825}Zr_{0.15}Gd_{0.025}O_2$	139*	270*	[57]
$Ce_{0.825}Zr_{0.15}La_{0.025}O_2$	140*	270*	[57]
$Ce_{0.825}Zr_{0.15}Sm_{0.025}O_2$	152*	279*	[57]
$Ce_{0.825}Zr_{0.15}Y_{0.025}O_2$	137*	260*	[57]
$Ce_{0.775}Zr_{0.15}Gd_{0.075}O_2$	108*	198*	[57]
$Ce_{0.775}Zr_{0.15}La_{0.075}O_2$	128*	257*	[57]
$Ce_{0.775}Zr_{0.15}Sm_{0.075}O_2$	118*	232*	[57]
$Ce_{0.775}Zr_{0.15}Y_{0.075}O_2$	113*	220*	[57]
$Ce_{0.75}Zr_{0.15}La_{0.1}O_2$	113*	228*	[57]
$Ce_{0.7}Zr_{0.15}Hf_{0.15}O_2$	60*	100*	[73]
$Ce_{0.65}Zr_{0.15}Gd_{0.2}O_2$	87*	164*	[57]
$Ce_{0.65}Zr_{0.15}La_{0.2}O_2$	90*	182*	[57]
$Ce_{0.65}Zr_{0.15}Sm_{0.2}O_2$	77*	150*	[57]
$Ce_{0.65}Zr_{0.15}Y_{0.2}O_2$	74*	123*	[57]
$Ce_{0.8}Zr_{0.1}Hf_{0.1}O_2$	66*	132*	[73]
$Ce_{0.9}Zr_{0.05}Hf_{0.05}O_2$	100*	144*	[73]
$Ce_{0.4}Zr_{0.5}La_{0.08}Pr_{0.02}O_2$	139*	288*	[59]

2.2.4 Perovskites

Another class of materials capable of the thermochemical splitting of carbon dioxide are perovskites which have an ABO_3 structure [82]. Most perovskites are based on a cubic structure with the B-site element located at the centre of the cube while the A site element occupies the corners of the cube as can be seen in Figure 2.3. The oxygen atoms are found at the centre of each of the vertices. When perovskites are used in thermochemical cycles, they are non-stoichiometric. The reduction and oxidation reactions of perovskites are shown in Equations 2.10 and 2.11, respectively.

$$ABO_{3(s)} \rightarrow ABO_{3-\delta(s)} + \frac{\delta}{2} O_{2(g)} \quad (2.10)$$

$$ABO_{3-\delta(s)} + \delta CO_{2(g)} \rightarrow ABO_{3(s)} + \delta CO_{(g)} \quad (2.11)$$

Perovskites are promising thermochemical catalysts due to their low price, high adaptability and high thermal stability [83]. Since around 90 % of metallic elements can

be stably incorporated into a perovskite structure, there are thousands of different combinations of elements, more so when doping is involved [84]. The largest family of perovskites capable of splitting CO_2 are the lanthanum strontium manganites. This family will be discussed in detail in Chapter 3. Therefore, this section will focus on other perovskite materials capable of carbon dioxide splitting.

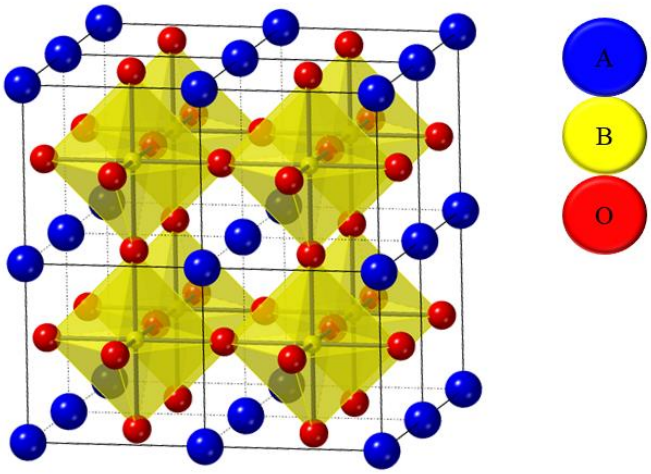

Figure 2.3. Crystal Structure of a Typical Perovskite ABO_3

$Ba_{0.5}Sr_{0.5}FeO_3$ was reduced at 1000 °C and was found to release 582 µmol/g of oxygen in the first cycle [85]. However, during the first oxidation reaction, only 136 µmol/g of CO was produced. The yields during the second cycle were 31 µmol/g of O_2 and 78 µmol/g of CO, showing serious degradation, likely due to sintering during the first reduction reaction. Another perovskite that has been studied is $MgMnO_3$, which was able to release 408 µmol/g of oxygen at 1200 °C [86]. However, this perovskite was unable to split CO_2 to CO. Double perovskites are perovskites with the formula $A_2B_2O_6$. Two of these double perovskites were reduced under hydrogen before the CO_2 splitting reaction. La_2NiFeO_6 was able to produce 2140 µmol/g of CO, while $Sr_2FeNi_{0.4}Mo_{0.6}O_6$ produced 2239 µmol/g [87,88]. This result cannot be directly compared with materials reduced under argon or

nitrogen. However, $Cu_{0.2}Co_{0.8}Fe_2O_4$ reduced under hydrogen was able to produce 9000 μmol/g, suggesting that these double perovskites are not optimal CO_2 splitting materials.

Table 2.5 Oxygen Evolution and Carbon Monoxide Production from Perovskites (data from the second thermochemical cycle)*

Material	Oxygen Evolution (μmol/g)	Carbon Monoxide Production (μmol/g)	Reference
$Ba_{0.5}Sr_{0.5}FeO_3$	31*	78*	[85]
La_2NiFeO_6	Reduced under H_2	2140	[87]
$Sr_2FeNi_{0.4}Mo_{0.6}O_6$	Reduced under H_2	2239	[88]

The focus of this thesis is $Ba_2Ca_{0.66}Nb_{1.34-x}Fe_xO_6$ [89]. Previous research found that the perovskite was able to split CO_2 after reduction under argon for 12 hours at 700 °C, and 24 hours under CO_2 at the same temperature. The higher the iron content, the higher the carbon deposition on the surface of the perovskite. Indeed, the perovskite with no iron (x = 0) had no evidence of carbon deposition and is therefore unlikely to have split CO_2, as expected since iron is the only redox-active element in the material. This family of perovskites have also been used for other applications, such as gas sensors. $BaCa_{0.33}Nb_{0.34}Fe_{0.33}O_3$ was found to exhibit a decrease in total impedance in the presence of 1500 ppm of CO_2 with a linear relationship, when plotted on the log scale, between impedance and carbon dioxide [90]. The presence of iron was again found to be necessary for the activity of the sensor. In BaCa0.33Nb0.76-xFexO3 (x = 0.17, 0.25, 0.5), as the concentration of iron increases, the change in impedance was found to increase [91].

This family has also been found to be mixed ionic electronic conductors. $Ba_2(Ca_{0.79}Fe_{0.21})(Nb_{0.71}Fe_{0.29})O_6$ has high bulk and grain-boundary conductivity and a low activation energy of 0.43 eV [92]. $Ba_2(Ca_{0.79}Nb_{0.66}Ta_{0.55})O_6$ also showed bulk and grain-

boundary conductivity, although it was lower than the iron containing $Ba_2(Ca_{0.79}Fe_{0.21})(Nb_{0.71}Fe_{0.29})O_6$, showing that the presence of iron increases the conductivity [93]. $Ba_3Ca_{1.18}Nb_{1.82}O_9$ is found to be a protonic conductor, with an activation energy of proton migration of 0.54 eV but has no electronic conductivity [94]. In general, the higher conductivity of these materials is thought to correlate with higher thermochemical activity, since the movement of oxygen vacancies can aid in reduction or oxidation.

2.3 Ideal Thermochemical Materials

Based on the literature presented here there are several factors which make up an ideal thermochemical material. Firstly, it has been demonstrated by many materials that high oxygen evolution yields do not necessarily lead to high carbon monoxide yields. Therefore, materials with high CO yields should be prioritised over those with high oxygen yields for further research. Secondly, an ideal material will operate at the lowest possible temperatures. This is for a few reasons, including lower energy requirements for heating both the material and the gas flow, and because lower temperatures can be achieved with technologies such as concentrated solar power (CSP) and industrial waste heat. Additionally, a material with as small a temperature difference as possible between the reduction and oxidation temperatures is ideal as this lowers the energy required during cycling and improves the overall efficiency of the cycle. Finally, one of the most important factors is resistance to sintering and good cyclability. A resistance to sintering reduces the reactivity loss that comes with agglomeration and increasing particle size combined with decreasing porosity which slows gas diffusion. This should ensure that a material is able to consistently produce high CO yields over the thousands of cycles needed to commercialise this technology on a large scale. Optimising these factors will

ensure as large as possible carbon monoxide production from as little as possible energy, increasing the solar-to-fuel efficiency.

2.4 References

[1] Funk JE, Reinstrom R. Energy requirements in the production of hydrogen from water. I&EC Process Des Dev 1966;5:336–42.

[2] Besenbruch, G. General Atomic sulfur-iodine thermochemical water-splitting process. Am Chem Soc, Div Pet Chem, Prepr 1982;27:48–53.

[3] Wong B, Buckingham RT, Brown LC, Russ BE, Besenbruch GE, Kaiparambil A, et al. Construction materials development in sulfur-iodine thermochemical water-splitting process for hydrogen production. Int J Hydrogen Energy 2007;32:497–504. doi:10.1016/j.ijhydene.2006.06.058.

[4] Dokiya M, Kotera Y. Hybrid cycle with electrolysis using Cu-Cl system. Int J Hydrogen Energy 1976;1:117–21.

[5] Coutanceau C, Baranton S, Audichon T. Hydrogen Production From Water Electrolysis. Hydrog. Electrochem. Prod., Academic Press; 2018, p. 17–62. doi:10.1016/B978-0-12-811250-2.00003-0.

[6] Bilgen E, Ducarroir M, Eoex M, Sibieude F. Use of solar energy for direct and two-step water decomposition cycles. Int J Hydrogen Energy 1977;2:251–7.

[7] Levêque G, Abanades S. Investigation of thermal and carbothermal reduction of volatile oxides (ZnO, SnO_2, GeO_2, and MgO) via solar-driven vacuum thermogravimetry for thermochemical production of solar fuels. Thermochim Acta 2015;605:86–94. doi:10.1016/j.tca.2015.02.015.

[8] Brecher LE, Wu CK. Electrolytic decomposition of water. US Patent 3888750, 1975.

[9] Liberatore R, Lanchi M, Turchetti L. Hydrogen production by the solar-powered hybrid sulfur process: Analysis of the integration of the CSP and chemical plants in selected scenarios. AIP Conf. Proc., vol. 1734, 2016, p. 120006,1-8. doi:10.1063/1.4949208.

[10] Nakamura T. Hydrogen production from water utilizing solar heat at high temperatures. Sol Energy 1977;19:467–75.

[11] Charvin P, Abanades S, Flamant G, Lemort F. Two-step water splitting thermochemical cycle based on iron oxide redox pair for solar hydrogen production. Energy 2007;32:1124–33. doi:10.1016/j.energy.2006.07.023.

[12] Kameyama H, Yoshida K. Br-Ca-Fe water decomposition cycles for hydrogen production. Proc. 2nd World Hydrog. Energy Conf., 1978, p. 829–50.

[13] Nakayama T, Yoshioka H, Furutani H, Kameyama H, Yoshida K. Mascot - a bench-scale plant for producing hydrogen by the UT-3 thermochemical decomposition cycle. Int J Hydrog Energy 1984;9:187–90.

[14] Childress T. Closed Cycle CO2 Processes. Georgia Institute of Technology, 1977.

[15] Chulten R. German Patent 2, 257, 375. 2, 257, 375, 1974.

[16] Bamberger CE, Robinson PR. Thermochemical splitting of water and carbon dioxide with cerium compounds. Inorganica Chim Acta 1980;42:133–7. doi:10.1016/S0020-1693(00)88898-2.

[17] Block T, Schmücker M. Metal oxides for thermochemical energy storage: A comparison of several metal oxide systems. Sol Energy 2016. doi:10.1016/j.solener.2015.12.032.

[18] Scheffe JR, Steinfeld A. Oxygen exchange materials for solar thermochemical splitting of H_2O and CO_2: A review. Mater Today 2014;17:341–8. doi:10.1016/j.mattod.2014.04.025.

[19] Tamaura Y, Tahata M. Complete reduction of carbon dioxide to carbon using cation-excess magnetite. Nature 1990;346:255–6. doi:10.1038/346255a0.

[20] Takalkar GD, Bhosale RR. Application of cobalt incorporated Iron oxide catalytic nanoparticles for thermochemical conversion of CO2. Appl Surf Sci 2019;495:143508. doi:10.1016/j.apsusc.2019.07.250.

[21] Tabata M, Nishida Y, Kodama T, Mimori K, Yoshida T, Tamaura Y. CO_2

decomposition with oxygen-deficient Mn(II) ferrite. J Mater Sci 1993;28:971–4. doi:10.1007/BF00400881.

[22] Tabata M, Kato H, Kodama T, Yoshida T, Tsuji M, Tamaura Y. CO_2 decomposition with mangano-wüstite. J Mater Sci 1994;29:999–1003. doi:10.1007/BF00351423.

[23] Takalkar G, Bhosale RR. Thermochemical CO2 splitting using a sol-gel–synthesized Mg-ferrite–based redox system. Int J Energy Res 2019;43:6983–93. doi:10.1002/er.4716.

[24] Bhosale RR, Kumar A, AlMomani F, Ghosh U, Sutar P, Takalkar G, et al. Effectiveness of Ni incorporation in iron oxide crystal structure towards thermochemical CO2 splitting reaction. Ceram Int 2017;43:5150–5. doi:10.1016/j.ceramint.2017.01.034.

[25] Leonard J, Reyes N, Allen KM, Randhir K, Li L, AuYeung N, et al. Effects of Dopant Metal Variation and Material Synthesis Method on the Material Properties of Mixed Metal Ferrites in Yttria Stabilized Zirconia for Solar Thermochemical Fuel Production. Int J Photoenergy 2015;2015. doi:10.1155/2015/856385.

[26] Carrillo AJ, Serrano DP, Pizarro P, Coronado JM. Manganese oxide-based thermochemical energy storage: Modulating temperatures of redox cycles by Fe-Cu co-doping. J Energy Storage 2016;5:169–76. doi:10.1016/j.est.2015.12.005.

[27] André L, Abanades S, Cassayre L. High-temperature thermochemical energy storage based on redox reactions using Co-Fe and Mn-Fe mixed metal oxides. J Solid State Chem 2017;253:6–14. doi:10.1016/j.jssc.2017.05.015.

[28] Block T, Schmücker M. Metal oxides for thermochemical energy storage: A comparison of several metal oxide systems. Sol Energy 2016;126:195–207. doi:10.1016/j.solener.2015.12.032.

[29] Agrafiotis C, Roeb M, Sattler C. Exploitation of thermochemical cycles based on solid oxide redox systems for thermochemical storage of solar heat. Part 4: Screening of oxides for use in cascaded thermochemical storage concepts. Sol

Energy 2016;139:695–710. doi:10.1016/j.solener.2016.04.034.

[30] Ehrhart B, Coker E, Siegel N, Weimer A. Thermochemical cycle of a mixed metal oxide for augmentation of thermal energy storage in solid particles. Energy Procedia 2014;49:762–71. doi:10.1016/j.egypro.2014.03.082.

[31] Takalkar G, Bhosale RR, AlMomani F. Sol-gel synthesized NixFe3−xO4 for thermochemical conversion of CO2. Appl Surf Sci 2019;489:693–700. doi:10.1016/j.apsusc.2019.05.285.

[32] Huang J, Fu Y, Zhao Y, Zhang J, Li S, Li S, et al. Anti-sintering non-stoichiometric nickel ferrite for highly efficient and thermal-stable thermochemical CO2 splitting. Chem Eng J 2021;404:127067. doi:10.1016/j.cej.2020.127067.

[33] Huang J, Liu W, Hu W, Metcalfe I, Yang Y, Liu B. Phase interactions in Ni-Cu-Al2O3 mixed oxide oxygen carriers for chemical looping applications. Appl Energy 2019;236:635–47. doi:10.1016/j.apenergy.2018.12.029.

[34] Takalkar G, Bhosale RR, AlMomani F, Khraisheh M. Thermocatalytic splitting of CO2 using sol-gel synthesized Co-ferrite redox materials. Fuel 2019;257:115965. doi:10.1016/j.fuel.2019.115965.

[35] Bhosale RR, Alxneit I, Van Den Broeke LLP, Kumar A, Jilani M, Gharbia SS, et al. Sol-gel synthesis of nanocrystalline Ni-ferrite and Co-ferrite redox materials for the rmoche mical production of solar fuels. Mater Res Soc Symp Proc 2014;1675:203–8. doi:10.1557/opl.2014.866.

[36] Allen KM, Auyeung N, Rahmatian N, Klausner JF, Coker EN. Cobalt Ferrite in YSZ for Use as Reactive Material in Solar Thermochemical Water and Carbon Dioxide Splitting, Part II: Kinetic Modeling. JOM 2013;65:1682–93. doi:10.1007/s11837-013-0774-1.

[37] Qiu Y, Ma L, Li M, Cui D, Zhang S, Zeng D, et al. Copper and cobalt co-doped ferrites as effective agents for chemical looping CO2 splitting. Chem Eng J 2020;387. doi:10.1016/j.cej.2020.124150.

[38] Tong J, Jiang Q, Chen Z, Jiang Z, Li C. Two-step thermochemical cycles for CO_2 splitting on Zr-doped cobalt ferrite supported on silica. Sol Energy 2015;116:133–43. doi:10.1016/j.solener.2015.04.007.

[39] Huang J, Fu Y, Li S, Kong W, Zhang J, Sun Y. Cobalt-based ferrites as efficient redox materials for thermochemical two-step CO2-splitting: enhanced performance due to cation diffusion. Sustain Energy Fuels 2019;3:975–84. doi:10.1039/c8se00611c.

[40] Bhosale RR, Rashid S. Thermodynamic analysis of MgxFe3-xO4 redox CO2 conversion solar thermochemical cycle. Int J Energy Res 2022;46:923–36. doi:10.1002/er.7213.

[41] Hussein AMA, Burra KG, Bassioni G, Hammouda RM, Gupta AK. Production of CO from CO2 over mixed-metal oxides derived from layered-double-hydroxides. Appl Energy 2019;235:1183–91. doi:10.1016/j.apenergy.2018.11.040.

[42] Takalkar G, Bhosale RR, AlMomani F, Rashid S, Shakoor RA. Ni incorporation in MgFe2O4 for improved CO2-splitting activity during solar fuel production. J Mater Sci 2020;55:11086–94. doi:10.1007/s10853-020-04794-1.

[43] Shin H, Oh J, Lee J, Han S, Choi S. The Carbon Dioxide Decomposition Reaction with (NixCu1—x)Fe2O4 Solid Solution. Phys Stat Sol A 2002;3:741–5.

[44] Kodama T, Gokon N. Thermochemical cycles for high-temperature solar hydrogen production. Chem Rev 2007;107:4048–77.

[45] Chuayboon S, Abanades S, Rodat S. Solar chemical looping gasification of biomass with the ZnO/Zn redox system for syngas and zinc production in a continuously-fed solar reactor. Fuel 2018;215:66–79. doi:10.1016/j.fuel.2017.11.021.

[46] Steinfeld A. Solar hydrogen production via a two-step water-splitting thermochemical cycle based on Zn/ZnO redox reactions. Int J Hydrogen Energy 2002;27:611–9.

[47] Abanades S, Chambon M. CO2 dissociation and upgrading from two-step solar

thermochemical processes based on ZnO/Zn and SnO2/SnO redox pairs. Energy and Fuels 2010;24:6667–74. doi:10.1021/ef101092u.

[48] Levêque G, Abanades S, Jumas JC, Olivier-Fourcade J. Characterization of two-step tin-based redox system for thermochemical fuel production from solar-driven CO2 and H2O splitting cycle. Ind Eng Chem Res 2014;53:5668–77. doi:10.1021/ie500206u.

[49] Abanades S. CO 2 and H 2O reduction by solar thermochemical looping using SnO 2/SnO redox reactions: Thermogravimetric analysis. Int J Hydrogen Energy 2012;37:8223–31. doi:10.1016/j.ijhydene.2012.02.158.

[50] Gálvez ME, Frei A, Albisetti G, Lunardi G, Steinfeld A. Solar hydrogen production via a two-step thermochemical process based on MgO/Mg redox reactions-Thermodynamic and kinetic analyses. Int J Hydrogen Energy 2008;33:2880–90. doi:10.1016/j.ijhydene.2008.04.007.

[51] Halmann M, Frei A, Steinfeld A. VACUUM CARBOTHERMIC REDUCTION OF Al2O3, BeO, MgO-CaO, TiO2, ZrO2, HfO2þZrO2, SiO2, SiO2þFe2O3, AND GeO2 TO THE METALS. A THERMODYNAMIC STUDY. Miner Process Extr Metall Rev 2011;32:247–66. doi:10.1080/08827508.2010.530723.

[52] Steinfeld A, Brack M, Meier A, Weidenkaff A, Wuillemin D. A solar chemical reactor for co-production of zinc and synthesis gas. Energy 1998;23:803–14. doi:10.1016/S0360-5442(98)00026-7.

[53] Chueh WC, Falter C, Abbott M, Scipio D, Furler P, Haile SM, et al. High-Flux Solar-Driven Thermochemical Dissociation of CO_2 and H_2O using Nonstiochiometric Ceria. Science 2010;330:1797–801. doi:10.1126/science.1198374.

[54] Le Gal A, Abanades S, Flamant G. CO2 and H2O splitting for thermochemical production of solar fuels using nonstoichiometric ceria and ceria/zirconia solid solutions. Energy and Fuels 2011;25:4836–45. doi:10.1021/ef200972r.

[55] Rudisill SG, Venstrom LJ, Petkovich ND, Quan T, Hein N, Boman DB, et al. Enhanced oxidation kinetics in thermochemical cycling of CeO2 through

templated porosity. J Phys Chem C 2013;117:1692–700. doi:10.1021/jp309247c.

[56] Call F, Roeb M, Schmücker M, Bru H, Curulla-Ferre D, Sattler C, et al. Thermogravimetric Analysis of Zirconia-Doped Ceria for Thermochemical Production of Solar Fuel. Am J Anal Chem 2013;04:37–45. doi:10.4236/ajac.2013.410A1005.

[57] Call F, Roeb M, Schmücker M, Sattler C, Pitz Paal R. Ceria doped with zirconium and lanthanide oxides to enhance solar thermochemical production of fuels. J Phys Chem C 2015;119:6929–38. doi:10.1021/jp508959y.

[58] Bonk A, Maier AC, Schlupp MVF, Burnat D, Remhof A, Delmelle R, et al. The effect of dopants on the redox performance, microstructure and phase formation of ceria. J Power Sources 2015;300:261–71. doi:10.1016/j.jpowsour.2015.09.073.

[59] Zhao B, Huang C, Ran R, Wu X, Weng D. Two-step thermochemical looping using modified ceria-based materials for splitting CO2. J Mater Sci 2016;51:2299–306. doi:10.1007/s10853-015-9534-7.

[60] Zhu L, Lu Y, Li F. Reactivity of Ni, Cr and Zr doped ceria in CO2 splitting for CO production via two-step thermochemical cycle. Int J Hydrogen Energy 2018;43:13754–63. doi:10.1016/j.ijhydene.2018.02.015.

[61] Bhosale RR, Takalkar GD. Nanostructured co-precipitated Ce0.9Ln0.1O2 (Ln = La, Pr, Sm, Nd, Gd, Tb, Dy, or Er) for thermochemical conversion of CO2. Ceram Int 2018;44:16688–97. doi:10.1016/j.ceramint.2018.06.096.

[62] Takalkar GD, Bhosale RR, Kumar A, AlMomani F, Khraisheh M, Shakoor RA, et al. Transition metal doped ceria for solar thermochemical fuel production. Sol Energy 2018;172:204–11. doi:10.1016/j.solener.2018.03.022.

[63] Cheng Z, Sherman BJ, Lo CS. Carbon dioxide activation and dissociation on ceria (110): A density functional theory study. J Chem Phys 2013;138:14702. doi:10.1063/1.4773248.

[64] Venstrom LJ, De Smith RM, Hao Y, Haile SM, Davidson JH. Efficient Splitting of CO_2 in an Isothermal Redox Cycle Based on Ceria. Energy & Fuels

2014;28:2732–42. doi:10.1021/ef402492e.

[65] Hao Y, Jin J, Jin H. Thermodynamic Analysis of Isothermal CO2 Splitting and CO2-H2O Co-Splitting for Solar Fuel Production. Appl Therm Eng 2020;166:113600. doi:10.1016/j.applthermaleng.2019.04.010.

[66] Zhou G, Shah PR, Kim T, Fornasiero P, Gorte RJ. Oxidation entropies and enthalpies of ceria-zirconia solid solutions. Catal Today 2007;123:86–93. doi:10.1016/j.cattod.2007.01.013.

[67] Ramos-Fernandez E V., Shiju NR, Rothenberg G. Understanding the solar-driven reduction of CO 2 on doped ceria. RSC Adv 2014;4:16456–63. doi:10.1039/C4RA01242A.

[68] A. Cheikh, A. Madani, A. Touati, H. Boussetta, C. Monty, Ionic conductivity of zirconia based ceramics from single crystals to nanonstructured polycrystals, J. Eur. Ceram. Soc. 21 (2001) 1837–1841. https://doi.org/10.1016/S0955-2219(01)00126-1.

[69] Bhosale RR, Takalkar GD. Nanostructured co-precipitated Ce0.9Ln0.1O2 (Ln = La, Pr, Sm, Nd, Gd, Tb, Dy, or Er) for thermochemical conversion of CO2. Ceram Int 2018;44:16688–97. doi:10.1016/j.ceramint.2018.06.096.

[70] Jiang Q, Zhou G, Jiang Z, Li C. Thermochemical CO2 splitting reaction with CexM1-xO2-δ (M=Ti4+, Sn4+, Hf4+, Zr4+, La3+, Y3+ and Sm3+) solid solutions. Sol Energy 2014;99:55–66. doi:10.1016/j.solener.2013.10.021.

[71] Takalkar G, Bhosale R, AlMomani F, Rahul Bhosale CR. Evaluation of redox performance of silver and transition metal-doped ternary ceria oxides for thermochemical splitting of CO 2. Int J Energy Res 2019;43:3616–27. doi:10.1002/er.4509.

[72] Takalkar G, Bhosale RR, AlMomani F, Rashid S. Co-precipitation synthesized nanostructured Ce0.9Ln0.05Ag0.05O2−δ materials for solar thermochemical conversion of CO2 into fuels. J Mater Sci 2020;55:9748–61. doi:10.1007/s10853-020-04567-w.

[73] Bhosale RR, Kumar A, Almomani F, Ghosh U, Al-Muhtaseb S, Gupta R, et al. Assessment of CexZryHfzO2 based oxides as potential solar thermochemical CO2 splitting materials. Ceram Int 2016;42:9354–62. doi:10.1016/j.ceramint.2016.02.100.

[74] Takalkar G, Bhosale RR, AlMomani F. Thermochemical splitting of CO2 using Co-precipitation synthesized Ce0.75Zr0.2M0.05O2-Δ (M = Cr, Mn, Fe, CO, Ni, Zn) materials. Fuel 2019;256:115834. doi:10.1016/j.fuel.2019.115834.

[75] Kang M, Zhang J, Wang C, Wang F, Zhao N, Xiao F, et al. CO2 splitting via two step thermochemical reactions over doped ceria/zirconia solid solutions. RSC Adv 2013;3:18878–85. doi:10.1039/c3ra43742f.

[76] Kang M, Wu X, Zhang J, Zhao N, Wei W, Sun Y. Enhanced thermochemical CO2 splitting over Mg- and Ca-doped ceria/zirconia solid solutions. RSC Adv 2014;4:5583–90. doi:10.1039/c3ra45595e.

[77] Takalkar G, Bhosale RR, AlMomani F, Rashid S. Co-precipitation synthesized nanostructured Ce0.9Ln0.05Ag0.05O2−δ materials for solar thermochemical conversion of CO2 into fuels. J Mater Sci 2020. doi:10.1007/s10853-020-04567-w.

[78] Furler P, Scheffe J, Gorbar M, Moes L, Vogt U, Steinfeld A. Solar thermochemical CO2 splitting utilizing a reticulated porous ceria redox system. Energy and Fuels, vol. 26, 2012, p. 7051–9. doi:10.1021/ef3013757.

[79] Takalkar G, Bhosale RR, Rashid S, AlMomani F, Shakoor RA, Al Ashraf A. Application of Li-, Mg-, Ba-, Sr-, Ca-, and Sn-doped ceria for solar-driven thermochemical conversion of carbon dioxide. J Mater Sci 2020;55:11797–807. doi:10.1007/s10853-020-04875-1.

[80] Takalkar G, Bhosale RR. Investigation of Zr-doped ceria for solar thermochemical valorization of CO 2. Int J Energy Res 2020;44:12284–94. doi:10.1002/er.5205.

[81] Abanades S, Le Gal A. CO 2 splitting by thermo-chemical looping based on Zr xCe 1-xO 2 oxygen carriers for synthetic fuel generation. Fuel 2012;102:180–6.

doi:10.1016/j.fuel.2012.06.068.

[82] Bhalla AS, Guo R, Roy R. The perovskite structure - A review of its role in ceramic science and technology. Mater Res Innov 2000;4:3–26. doi:10.1007/s100190000062.

[83] Ellert G, Tsodikov M V, Novotortsev VM. Perovskite-type catalytic materials for environmental applications. Sci Technol Adv Mater 2015;16:36002, 1–13. doi:10.1088/1468-6996/16/3/036002org/10.1088/1468-6996/16/3/036002.

[84] Peña MA, Fierro JLG. Chemical structures and performance of perovskite oxides. Chem Rev 2001;101:1981–2017. doi:10.1021/cr980129f.

[85] Nair MM, Abanades S. Experimental screening of perovskite oxides as efficient redox materials for solar thermochemical CO 2 conversion. Sustain Energy Fuels 2018;2:843–54. doi:10.1039/C7SE00516D.

[86] Rodenbough PP, Chan S-W. Thermal oxygen exchange cycles in mixed manganese perovskites. Ceram Int 2018;44:1343–7. doi:10.1016/j.ceramint.2017.08.168.

[87] Lim HS, Kim Y, Kang D, Lee M, Jo A, Lee JW. Fundamental Aspects of Enhancing Low-Temperature CO2Splitting to CO on a Double La2NiFeO6Perovskite. ACS Catal 2021;11:12220–31. doi:10.1021/acscatal.1c03398.

[88] Grimaldi A. Investigation of SFNM-04 Perovskite Supported Composite Oxides for Chemical Looping CO2 Dissociation. 2021.

[89] Mulmi S, Chen H, Hassan A, Marco JF, Berry FJ, Sharif F, et al. Thermochemical CO2 splitting using double perovskite-type $Ba_2Ca_{0.66}Nb_{1.34-x}Fe_xO_{6-\delta}$. J Mater Chem A 2017;5:6874–83.

[90] S. Mulmi, A. Hassan, P. Pereira-Almao, V. Thangadurai, Detecting CO_2 at ppm level in synthetic air using mixed conducting double perovskite-type metal oxides, Sensors Actuators B Chem. 178 (2013) 598–605.

[91] S. Mulmi, V. Thangadurai, Preparation, Structure and CO2 Sensor Studies of

$BaCa_{0.33}Nb_{0.67-x}Fe_xO_{3-\delta}$, J. Electrochem. Soc. 160 (2013) B95–B101.

[92] W.H. Kan, T.T. Trinh, T. Fürstenhaupt, V. Thangadurai, Synthesis, rietveld refinement of crystal structure, electron diffraction, and electrical transport properties of Ba2(Ca1- x - YFe x Nb y)(Nb1- zFe z)O 6-δ double perovskites, Can. J. Chem. 89 (2011) 688–696. https://doi.org/10.1139/v11-058.

[93] S.S. Bhella, V. Thangadurai, Synthesis and characterization of carbon dioxide and boiling water stable proton conducting double perovskite-type metal oxides, J. Power Sources. 186 (2009) 311–319. https://doi.org/10.1016/j.jpowsour.2008.09.110.

[94] K.C. Liang, Y. Du, A.S. Nowick, Fast high-temperature proton transport in nonstoichiometric mixed perovskites, Solid State Ionics. 69 (1994) 117–120. https://doi.org/10.1016/0167-2738(94)90399-9.

Chapter 3 – THERMOCHEMICAL SPLITTING OF CARBON DIOXIDE BY LANTHANUM MANGANITES – UNDERSTANDING THE MECHANISTIC EFFECTS OF DOPING

3.1 Abstract

This review investigates the effect of different dopants on the oxygen evolution and carbon dioxide splitting abilities of the lanthanum manganites. Particular focus was placed on the lanthanide, alkaline earth metals, redox-active transition metal, and non-redox active Group 3 metals. The review suggests that a small ionic radius lanthanide on the A-site can increase the size discrepancy, leading to MnO_6 octahedral tilting and more facile Mn-O bond breaking. Doping the A-site with a divalent alkaline earth element can increase the valence of the transition metal, leading to greater reduction capabilities. A transition metal with one electron in the e_g orbital is the most effective for reduction while for oxidation, zero electrons in the high-energy e_g orbitals is optimal. Finally, doping of the B-site with metals such as gallium or aluminium aids in sintering resistance and allows reactivity to remain constant over multiple cycles. Higher reduction temperatures and moderate re-oxidation temperatures also promote higher fuel yields as does the active reduction of the perovskite under hydrogen, although the total energy implications of this is unknown. Far more is known about the mechanism of the reduction reaction than the oxidation reaction, therefore more research in this area is required.

This chapter is in a publishable format but has not yet been published. H. Kildahl is the first author, responsible for research and writing. Y. Ding and H. Cao are responsible for supervision and editing.

3.2 Introduction

The rapidly changing global energy matrix, with its shift away from fossil fuels for the production of energy and commodities, plus the recent initiatives towards a net-zero carbon energy future, brings in significant challenges that require new solutions. Both the transport and foundation industries, including the chemical sector, are hard-to-decarbonise due to their reliance on fossil fuels and limited opportunities for electrification. Therefore, a net-carbon neutral feedstock is required for the production of fuels and chemicals. Synthesis gas, a mixture of hydrogen and carbon monoxide, could be this feedstock, provided both components are produced without related emissions, such as using renewable electricity to electrolyse water. Synthesis gas has been upgraded into a large range of chemicals, plastics and fuels, including kerosene [1–6]. One method of producing carbon monoxide could be through the thermochemical splitting of carbon dioxide, acting as carbon capture and usage while upgrading low-grade thermal energy into high-grade chemical energy. The thermal energy required to power the cycle could be obtained from industrial waste heat or an electric heater powered by renewable energy [7–11].

The thermochemical splitting of CO_2 has high selectivity for CO production and energy conversion efficiency [12]. Many reviews have been written about decades of research into materials capable of thermochemical cycling such as ceria, CeO_2, or stoichiometric metal oxides such as Fe_2O_3, at high reduction temperatures, often above 1500 °C [13–23]. More recently, perovskites have been used as a new class of materials capable of converting CO_2 [24,25]. A perovskite is a material with the formula ABO_3, where A is a large 12-coordinate atom and B is a smaller cation which forms an oxygen anion octahedra. Twenty-seven elements can occupy the A-site, while thirty-five different

elements can be incorporated into the B-site, allowing the redox activity of the perovskite to be tuned to maximise yields and minimise reaction temperatures [26].

In a thermochemical cycle, a perovskite is first reduced at high temperatures or low oxygen partial pressures. The reduction reaction proceeds:

$$ABO_3 \rightarrow ABO_{3-\delta} + \frac{\delta}{2}O_2 \quad (3.1)$$

with δ equal to the degree of non-stoichiometry. This reduced perovskite can then be used to split a small molecule such as carbon dioxide leading to the re-oxidation of the perovskite and production of carbon monoxide.

$$ABO_{3-\delta} + \delta CO_2 \rightarrow ABO_3 + \delta CO \quad (3.2)$$

Since the original perovskite is re-formed, the material can be cycled to produce carbon monoxide from carbon dioxide on demand, with only the addition of heat. The perovskite that has been most researched is the lanthanum manganite family, the subject of this review. The non-stoichiometric properties of $LaMO_3$ (M = Cr, Mn, Fe, Co, Ni) were first discussed in a 1979 paper by Nakamura et al.[27]. These properties were then also found in $La_{1-x}Sr_xMO_3$ [28–31]. In the lanthanum manganite family of perovskites, the most common A-site elements are the trivalent lanthanides and the divalent alkaline earth metals, while the B-site is most commonly the first-row transition metals. The element which allows for the thermochemical activity of these perovskites is this redox-active transition metal.

This review focuses on the thermochemical splitting of carbon dioxide by the lanthanum manganite family of perovskites. Some seventy papers published on this topic since 1979 have been reviewed here. We reviewed and summarised these papers with an aim to understand the effect of the different elements on the reduction and oxidation reactions,

with a particular focus on the mechanisms of action behind these reactions. The structure of this review is as follows. The review first looks at the reduction reaction, followed by the oxidation reaction. In both the reduction and oxidation sections, the effect of various dopants on the mechanisms of action are examined. As shown in Figure 3.1, the focus will begin with the A-site of the perovskite, typically large elements that form a 12-coordinate cuboctahedral. Firstly, the alkaline earth metals, a bivalent group, are often used as dopants in the A-site. Secondly, the lanthanides, a trivalent group, is often the primary occupant of the A-site. Thirdly, the focus turns to the B-site, often composed of smaller atoms that form a 6-coordinate octahedral with oxygen. The transition metals are the redox-active elements, while the A-site and B-site dopants create a suitable structure for the activity of the transition metal to be expressed. Finally, the B-site is often doped either with a second transition metal or other metals, typically low valence group two or three metals. These four components, as highlighted in the figure, make up the basis of the perovskite.

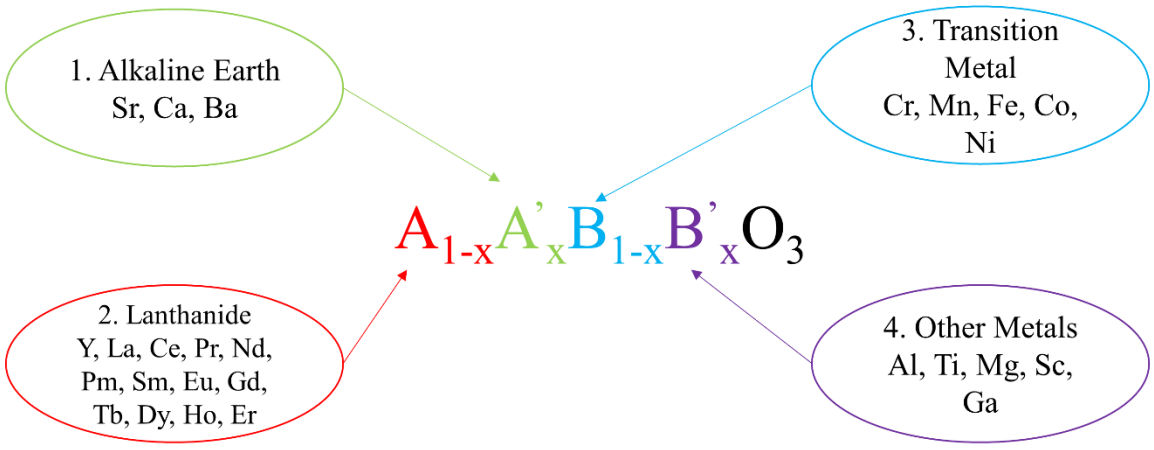

Figure 3.1. Components of the Lanthanum Manganite Perovskite Family

3.3 The Reduction Reaction

3.3.1 Alkaline Earth Metals

Reduction in the lanthanum manganites occurs *via* the incorporation of an electron by the transition metal manganese, reducing the manganese and allowing for the formation of an oxygen vacancy. The ease with which an oxygen vacancy is formed therefore relies on the breaking of the Mn-O bond and incorporation of an electron into the manganese electron shells. Based on the redox potentials, it can be seen that the reduction of Mn^{4+} to Mn^{3+} (1.0 V) occurs more easily than the reduction of Mn^{3+} to Mn^{2+} (1.51 V) [32]. One of the methods of increasing the number of Mn^{4+} atoms and therefore the oxygen evolution and reduction of the perovskite is the substitution or doping of a divalent alkaline earth metal in the A-site. The reason for this can be seen in Equations (3.3) and (3.4):

$$La^{3+}Mn^{3+}O_3^{2-} \rightarrow \ La^{3+}Mn^{(3-2\delta)+}O_{3-\delta}^{2-} + \frac{\delta}{2}O_2 \tag{3.3}$$

$$Sr^{2+}Mn^{4+}O_3^{2-} \ \rightarrow \ Sr^{2+}Mn^{(4-2\delta)+}O_{3-\delta}^{2-} + \frac{\delta}{2}O_2 \tag{3.4}$$

During the reduction of $LaMnO_3$ (Equation 3.3), a portion of the manganese atoms are being reduced from 3+ to 2+ in line with the non-stoichiometry of the perovskite. In $SrMnO_3$ (Equation 3.4), the strontium is in the 2+ state, meaning the manganese must accommodate the charge to maintain the neutrality of the unit cell, resulting in Mn^{4+}. During reduction, the Mn^{4+} is reduced to Mn^{3+}. $SrMnO_3$ is, therefore, more easily reduced than $LaMnO_3$, as evidenced by higher average oxygen evolution rates of 412 and 183 μmol/g, respectively and shown in Figure 3.2(a) [33–36]. In one study of $La_{1-x}Sr_xMnO_3$, where x = 0.35, 0.5 and 0.65, the oxygen evolution volumes were seen to increase as the strontium content increased, from 103 μmol/g for x =0.35 to 424 μmol/g at x = 0.65 [37].

For $La_{0.5}Sr_{0.5}MnO_3$ (x = 0.5) the average manganese oxidation state was found to decrease from +3.50 to +3.24 during reduction [38].

Another way that the alkaline earth elements increase the Mn^{4+} concentration is through charge disproportionation; Mn^{3+} ions are split into Mn^{2+} and Mn^{4+} ions while maintaining the overall charge [39]. Since Mn^{4+} is more favourably reduced than Mn^{3+}, charge disproportionation increases the extent of reduction. Dopants such as these alkaline earth elements can increase the extent of charge disproportionation compared with $LaMnO_3$, adding additional benefits than only through the charge balancing effect mentioned above [40,41].

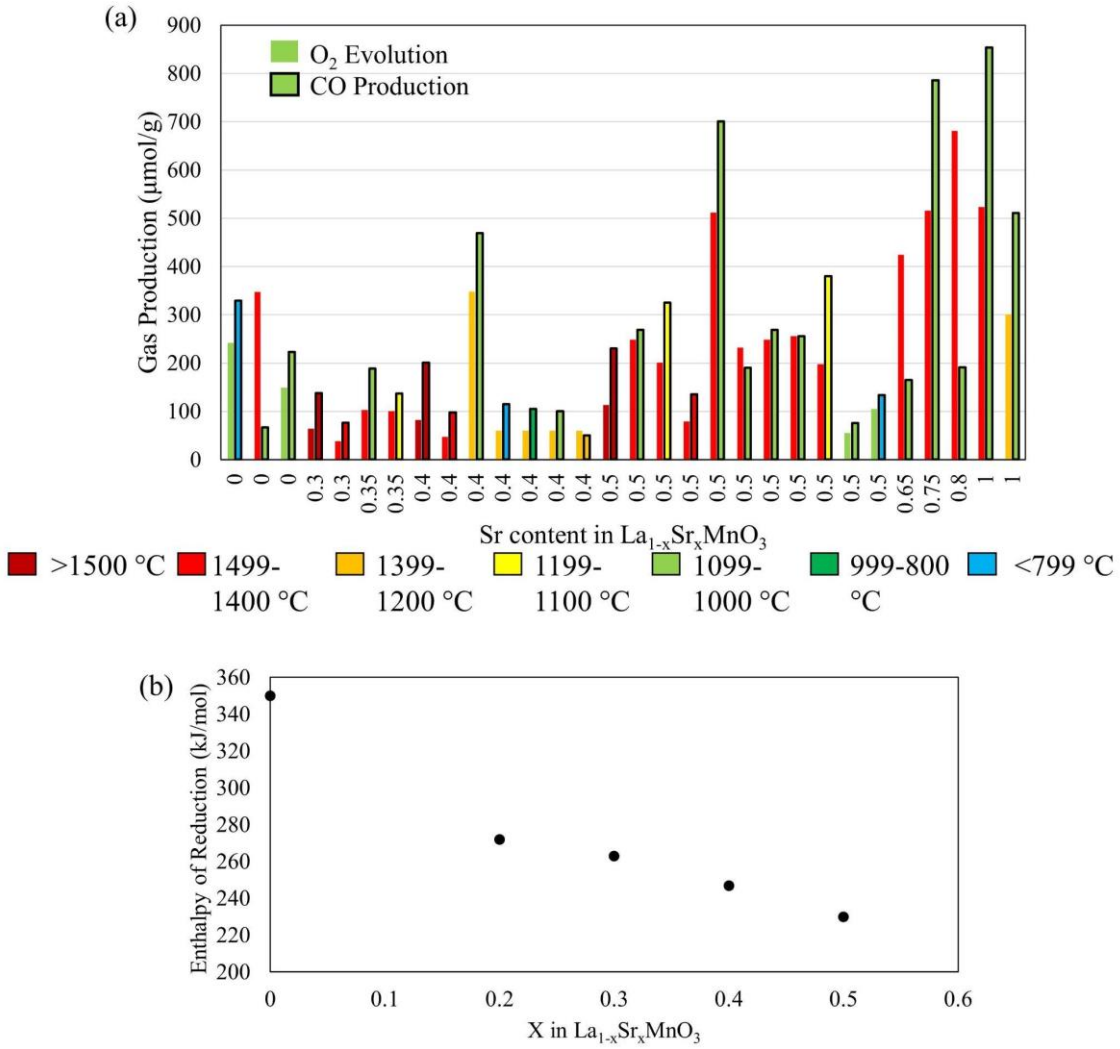

Figure 3.2. (a) Oxygen Evolution and Carbon Monoxide Production of $La_{1-x}Sr_xMnO_3$ with Varying Strontium Content, with Reduction and Oxidation Temperatures, Reduction under Ar/N_2 and Oxidation under 40-100 % CO_2 (data obtained from [33,34,37,42–49]) (b) The Effect of Strontium Content on the Enthalpy of Reduction in $La_{1-x}Sr_xMnO_3$, (data obtained from [50][51])

Doping with strontium also has the extra benefit of stabilising the reduced perovskite [52]. In $LaMnO_3$, the excess electron density formed by the creation of an oxygen vacancy is localised on the neighbouring manganese atoms, reducing Mn^{3+} to Mn^{2+}. In comparison, in $La_{0.6}Sr_{0.4}MnO_3$, more of the manganese atoms have a 4+ charge due to charge accommodation from the Sr^{2+} dopant, causing low energy manganese 3d orbitals to be unoccupied. These orbitals, together with the neighbouring oxygen 2p orbitals can accept the excess electron density from oxygen vacancy formation. The Mn-O bonds become partially covalent, and both the manganese and oxygen participate in the charge accommodation, resulting in greatly stabilised oxygen vacancies and increased oxygen evolution volumes.

Another benefit of doping with strontium is that the enthalpy of reduction decreases as strontium content increases. For example, the enthalpy of reduction is 350 kJ/mol for $LaMnO_3$ and 230 kJ/mol for $La_{0.5}Sr_{0.5}MnO_3$ [50], with no corresponding difference in entropy. There is indeed an almost linear relationship between enthalpy and strontium doping as seen in Figure 3.2(a). Importantly, for all materials the enthalpy of reduction increased as non-stoichiometry increased [50], showing it is more difficult to remove the second unit of oxygen than the first, which explains why the kinetics of the reduction reaction are seen to slow as the reaction progresses [53]. Despite the favourable enthalpies associated with strontium doping, the kinetics of the reaction are found to slow as strontium content increases. This is thought to be because of surface segregation, where

SrO forms on the surface of the material and inhibits the reaction [54]. There is therefore an important trade-off between yields and rate. However, the kinetics can be improved by increasing the reduction temperature. For example, $La_{0.5}Sr_{0.5}MnO_3$ reduced at 1400 °C produces 512 μmol/g at a rate of 130 μmol/min·g, while producing only 105 μmol/g at a rate of 40 μmol/min·g at 1000 °C [33].

Doping with calcium is particularly attractive because calcium is one of the cheapest and smallest A-site cations [55], reducing the cost of the perovskite and increasing the fuel production per gram due to a lower molecular weight than strontium. As calcium doping is increased from 20 % to 80 %, reduction begins at lower temperatures and oxygen evolution increases from 94 μmol/g for $La_{0.8}Ca_{0.2}MnO_3$ to 402 μmol/g for $La_{0.2}Ca_{0.8}MnO_3$ [56]. Additionally, calcium-doped materials can produce more oxygen during reduction than strontium-doped materials at the same doping concentration, for example, 315μmol/g for $La_{0.5}Ca_{0.5}MnO_3$ versus 201μmol/g for $La_{0.5}Sr_{0.5}MnO_3$, and as shown in Figure 3.2(b) [43]. Generally, at the same doping concentration, calcium doping releases more oxygen than strontium, which in turn releases more than barium. This correlates with the changes in the manganese oxidation state during reduction, changing from +3.50 in $La_{0.5}X_{0.5}MnO_3$ to +3.27, +3.31 and +3.32 for X = Ca, Sr and Ba, respectively, [57]. This corresponds to 0.23, 0.19 and 0.18 electrons exchanged during reduction per functional unit, respectively.

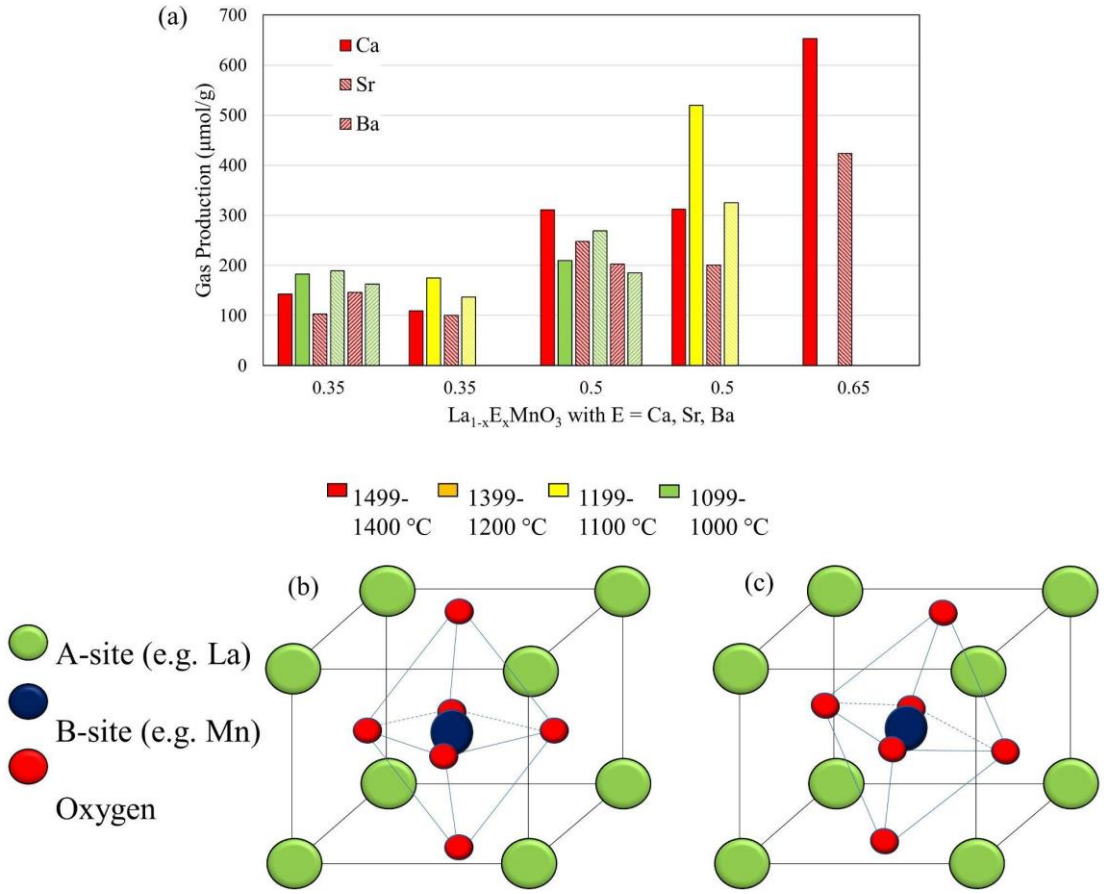

Figure 3.3.(a) Gas Production Volumes of $La_{1-x}E_xMnO_3$ with E = Ca, Sr, and Ba, Showing Different Dopant Concentrations and Reactions at Varying Temperatures. Column 1: Ca-doped Oxygen Evolution, Column 2: Ca-doped CO Production, Column 3: Sr-doped Oxygen Evolution, Column 4: Sr-doped CO Production, Column 5: Ba-doped Oxygen Evolution, Column 6: Ba-doped CO Production. Reduction under Ar and oxidation under 40-50 % CO_2 (data obtained from [37,50,51,58]) (b) Mn-O_6 Octahedra in Rhombohedral Crystal Structure (blue sphere: Mn, red spheres: O) (c) Tilted Mn-O_6 Octahedra in Octahedral Crystal Structure.

One of the main reasons for the difference in reduction extent between calcium and strontium-doped perovskites is a difference in the crystal structure; $La_{1-x}Sr_xMnO_3$ perovskites are rhombohedral, while $La_{1-x}Ca_xMnO_3$ perovskites are orthorhombic[43]. Another orthorhombic perovskite, $Sm_{0.5}Sr_{0.5}MnO_3$, has similar oxygen evolution properties to $La_{1-x}Ca_xMnO_3$, suggesting that the large reduction extent of $La_{1-x}Ca_xMnO_3$

could be due to a favourable crystal structure rather than any inherent superiority over strontium-doped perovskites. In the orthorhombic structure, there is a tilting of the Mn-O_6 octahedra (Figure 3.3 (b) & (c)). The Mn-O bond is formed by the overlap of the bonding e_g orbitals from the manganese with the 2pσ orbitals of the oxygen [44]. Tilting of this Mn-O_6 octahedral decreases the spatial overlap of these orbitals, weakening the bond and facilitating oxygen evolution. The radius of the cations present in the structure is also known to affect the titling of the Mn-O_6 octahedra, with smaller cations causing greater tilting. The ionic radii of the alkaline earth metals are Ca^{2+} = 1.34Å, Sr^{2+} = 1.44Å and Ba^{2+} = 1.61Å [57]. Since the radius of La^{3+} remains unchanged (1.17Å [59]), a calcium doped perovskite has the smallest average radius, causing larger tilting and explaining the greater reduction extent seen in Figure 3.2(b). Conversly, these perovskites in the rhombohedral structure are found to be extremely stable, with strong colombic interactions between the ions, making oxygen vacancy formation more difficult [62].

The perovskite $SrMnO_3$ provides more evidence that the crystal structure of a material is important for oxygen evolution. $SrMnO_3$ can be found with either a cubic or hexagonal crystal structure[60]. In the cubic structure, reduction begins at 425 °C while it begins at 1025 °C for the hexagonal material. This difference cannot be explained by differences in enthalpy alone; the difference in reduction enthalpies between the two crystal structures is only 6 kJ/mol. Instead, the cubic $SrMnO_{3-\delta}$ is stable while the hexagonal version is unstable. In the hexagonal structure, the Mn-O_6 octahedra share faces rather than sharing corners as in the cubic structure. After reduction, the hexagonal structure has face-sharing octahedra separated by planes with high oxygen vacancy concentrations, which is energetically unfavourable and as such requires higher temperatures for reduction. On the other hand, in the cubic structure, reduction forms a square pyramidal coordinated

manganese which is stable, energetically favourable and leads to larger non-stoichiometries.

Another explanation for the difference in oxygen evolution between Ca-, Sr- or Ba-doped perovskites is the critical radius per unit cell volume (R_{cu}) [53]. This parameter is the radius of an imaginary circle filling the space between two A-site cations and a B-site cation, divided by the unit cell volume. It was found that as R_{cu} increased, both oxygen evolution and oxygen evolution rate increased. Therefore the larger volumes produced by $La_{0.5}Ca_{0.5}MnO_3$ compared with $La_{0.5}Sr_{0.5}MnO_3$ and $La_{0.5}Ba_{0.5}MnO_3$ are explained by the larger R_{cu} of the calcium doped perovskite. This is likely because there is more space within the crystal structure for the facile diffusion of oxygen.

3.3.2 Lanthanides

Variation in the other A-site atom, the lanthanide, has also been studied. The lanthanides include neodymium, samarium, gadolinium, dysprosium and also yttrium, which have the same valence electron configuration as lanthanum [44]. Since all of these elements have a 3+ oxidation state, any changes in the reactivity of the perovskite must be due to the stability of the perovskite or the size of the lanthanide rather than due to changes in the manganese oxidation state. The ionic radii of the Ln^{3+} ions decrease with increasing atomic number due to lanthanide contraction [61]. This phenomenon is caused by the poor shielding of the 4f orbital electrons from the increasing nuclear charge, resulting in smaller ionic radii. The ionic radii of yttrium is the smallest of the A-site lanthanide dopants investigated, as shown in Figure 3.4. It can be seen that as the size of the lanthanide decreases, the oxygen evolution during reduction increases (shown by ×). One reason for this is that the decrease in radius leads to a decrease in the tolerance factor. The tolerance factor of a perovskite predicts the stability of the crystal structure. As the

tolerance factor decreases, there is a greater tilting of the Mn-O_6 octahedra [58]. Indeed, as the lanthanide radius decreases, the average angle of the O-Mn-O bonds increases proportionally, resulting in an increasingly tilted octahedra [62]. A lower tolerance factor is therefore correlated with an increase in oxygen evolution, likely due to the decreased overlap of the e_g and 2pσ orbitals from octahedral tilting as discussed above [44]. This is seen in practice; the largest A-site cation, $La_{0.5}Sr_{0.5}MnO_3$ has a tolerance factor of 0.996 and an oxygen evolution of 198 μmol/g, while the smallest A-site cation, $Y_{0.5}Sr_{0.5}MnO_3$ has a tolerance factor of 0.965 and an oxygen evolution of 481 μmol/g. This result was replicated by another research team who showed oxygen production of 248 and 551 μmol/g for the lanthanum and yttrium containing perovskites, respectively [45]. Interestingly, for all lanthanides presented here, calcium doped materials had higher oxygen evolutions than the strontium doped materials [44].

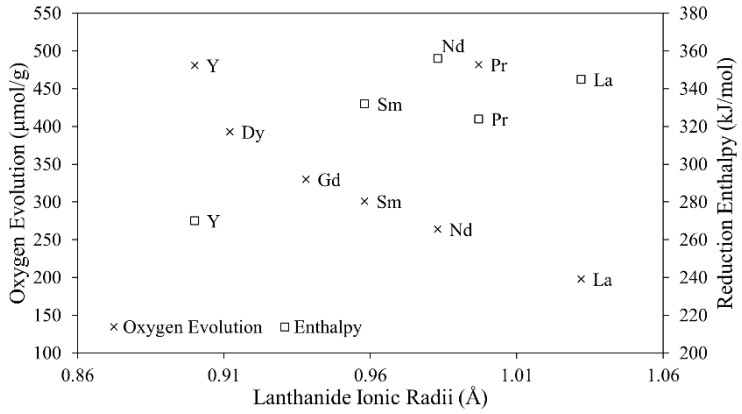

Figure 3.4. Effect of Lanthanide Ionic Radii on Oxygen Evolution ($La_{0.5}Ln_{0.5}MnO_3$) and Reduction Enthalpy ($LnMnO_3$) (data obtained from [59,63,64])

The non-stoichiometry (δ in $LnMnO_{3-\delta}$) of some lanthanides in $LnMnO_3$ was reported after reduction at 1000 °C[63]. Consistent with the results presented above, $YMnO_3$ had the highest degree of non-stoichiometry. This is expected since a larger degree of non-

stoichiometry means a deeper reduction has occurred, with resulting increases in oxygen evolution. Another explanation for the trends shown in Figure 3.4 is the enthalpy of reduction, (shown by □). As the enthalpy of reduction increases, the oxygen evolution predictably decreases, since more energy is required to reduce the perovskite. The only anomaly to the trends presented here are the praseodymium-based materials, with higher than expected oxygen evolution and lower than expected enthalpy given the ionic radius. Indeed, $Pr_{0.1}Sr_{0.9}MnO_3$ has a particularly high oxygen evolution of 1063 μmol/g during the first thermochemical cycle [64]. However, this material is particularly sensitive to sintering, with evolution decreasing to 200 μmol/g during the second cycle. Sintering occurs mainly by cationic diffusion of A and B-site elements and this is determined by powder morphology, the difference in ionic radii between the cations and the number of cation vacancies on the A-site [65].

Ceria, CeO_2, is one of the most researched thermochemical materials, therefore doping with cerium has also been attempted. Doping with 5% cerium in $LaMnO_3$ resulted in an increase in oxygen evolution from 452 μmol/g to 470 μmol/g [66]. This modest increase is present despite the fact that cerium is present in its 4+ oxidation state, reducing the average manganese charge through charge accommodation. This is thought to be compensated by the reduction of some Ce^{4+} atoms to Ce^{2+}. The doping of 30% cerium in $LaFeO_3$ led to an almost doubling of oxygen evolution, with a dramatically higher rate of evolution, presumably by the same mechanism [67].

3.3.3 Transition Metals

Shifting the focus to the B-site elements, manganese has been extensively studied. The impact of the manganese oxidation state and its effect on reactivity has been discussed above (Section 3.3.1), however, there are other important properties of Mn which affect

the perovskite reactivity. For example, the size of the manganese atom can change based on the charge and the distribution of electrons within the orbitals. Since manganese has six-coordinate bonding with oxygen to form a MnO_6 octahedron, its five d orbitals are split into three degenerate t_{2g} orbitals and two higher energy degenerate e_g orbitals (Figure 3.5(a)). Mn^{3+} has four d orbital electrons and as such can be found in either a high-spin or low-spin state. High-spin Mn^{3+} has one electron in each of its three t_{2g} orbitals and one electron in one of its e_g orbitals, denoted $t_{2g}^3e_g^1$ (Figure 3.5(b)). The energy required to place an electron in the higher energy e_g energy is lower than the energy required to place two alternate spin electrons in the same t_{2g} orbital due to the smaller bandgap. This configuration is called high-spin because it has a larger number of uncoupled electrons, in this case, four. Low-spin Mn^{3+} has four electrons in its three t_{2g} orbitals where two electrons occupy the same orbital, denoted $t_{2g}^4e_g^0$ (Figure 3.5(c)). In this case, the energy required to place two electrons in the same orbital is lower than that required to place an electron in the higher energy e_g orbital, since the bandgap is larger. The location of electrons within the orbitals affects the size of the ion. High-spin Mn^{3+} has a radius of 0.65 Å while low-spin is 0.58 Å, since the high-spin state has more orbitals containing an electron [68]. An Mn^{4+} ion is $t_{2g}^3e_g^0$ and has a radius of 0.54 Å, since the electrons are all uncoupled and therefore exhibit no repulsion, resulting in a smaller ion (Figure 3.5(d)). Since the tolerance factor is dependent on the size of the ions (Section 3.3.2), this results in a smaller tolerance factor when Mn is in the 4+ oxidation state. This explains the larger oxygen evolution volumes seen when more Mn^{4+} atoms are present, as seen with alkaline earth doping (Section 3.3.1).

The size of the bandgap between the t_{2g} and e_g orbitals is dependent on the ligands surrounding the transition metal. In reality, since oxide ions are mid-field ligands,

favouring neither the high spin or low spin state due to a median bandgap, Mn^{3+} is often found as a mixture of high-spin and low-spin states. For example, in $La_{1-x}Sr_xMnO_3$ over 60 % of Mn^{3+} atoms are in the high-spin state [68]. This is known because when strontium doping increases from 17.5 to 30 % the unit cell volume decreases by 1.5 % despite a 1.12 % increase in the A-site ionic radius (due to the larger radius of strontium compared with lanthanum), requiring a large decrease in the size of the B-site (from high-spin Mn^{3+} to Mn^{4+}) to achieve the overall volume contraction. Additionally, as strontium doping increases, the proportion of Mn^{4+} increases, decreasing the tolerance factor and increasing oxygen evolution.

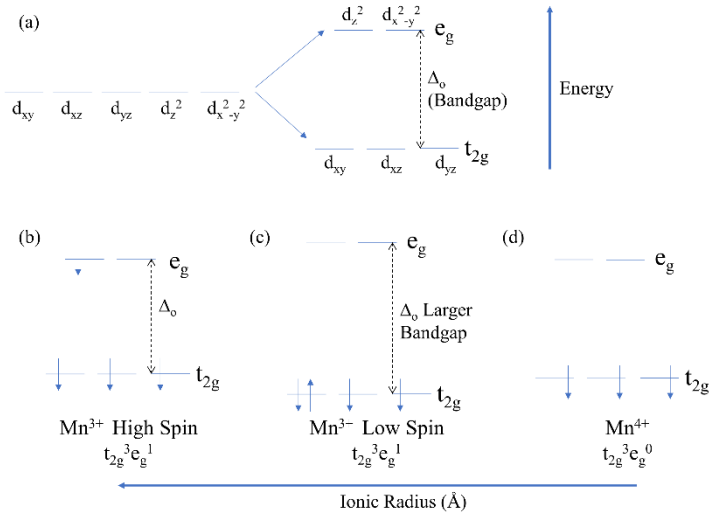

Figure 3.5. (a) Distribution of the Five Transition Metal d Orbitals when in an Octahedral Bonding Arrangement, Molecular Orbital Arrangement of (b) Mn^{3+} high spin, (c) Mn^{3+} low spin and (d) Mn^{4+}

There are four other first-row transition metals commonly used, namely chromium, iron, cobalt, and nickel, as either the sole transition metal or as a dopant. In the basic $LaTO_3$ perovskite the transition metal orbitals are as follows; $LaCrO_3$ is $t_{2g}^3e_g^0$, $LaMnO_3$ is $t_{2g}^3e_g^1$, $LaFeO_3$ is $t_{2g}^3e_g^2$, $LaCoO_3$ is $t_{2g}^5e_g^1$ and $LaNiO_3$ is $t_{2g}^6e_g^1$, shown in Figure 3.6(a) [69]. When these perovskites were used in the oxygen evolution reaction of an electrochemical

cell, the best performance was found when there was one electron present in the e_g orbital, such as Mn, Co, and Ni. When these materials were reduced in a thermochemical reaction, the highest oxygen evolution was seen for Mn, Co and Ni of 347, 665 and 362 µmol/g, respectively [34]. In comparison, $LaFeO_3$ and $LaCrO_3$, which have two and zero e_g electrons respectively, had very low oxygen evolution volumes around 30 µmol/g, and as seen in Figure 3.6(b). The occupancy of the e_g orbital also explains why $SrFeO_3$ has much higher oxygen evolution (750 µmol/g) than $LaFeO_3$; the Fe^{4+} found in $SrFeO_3$ has only one electron in its e_g orbitals [45].

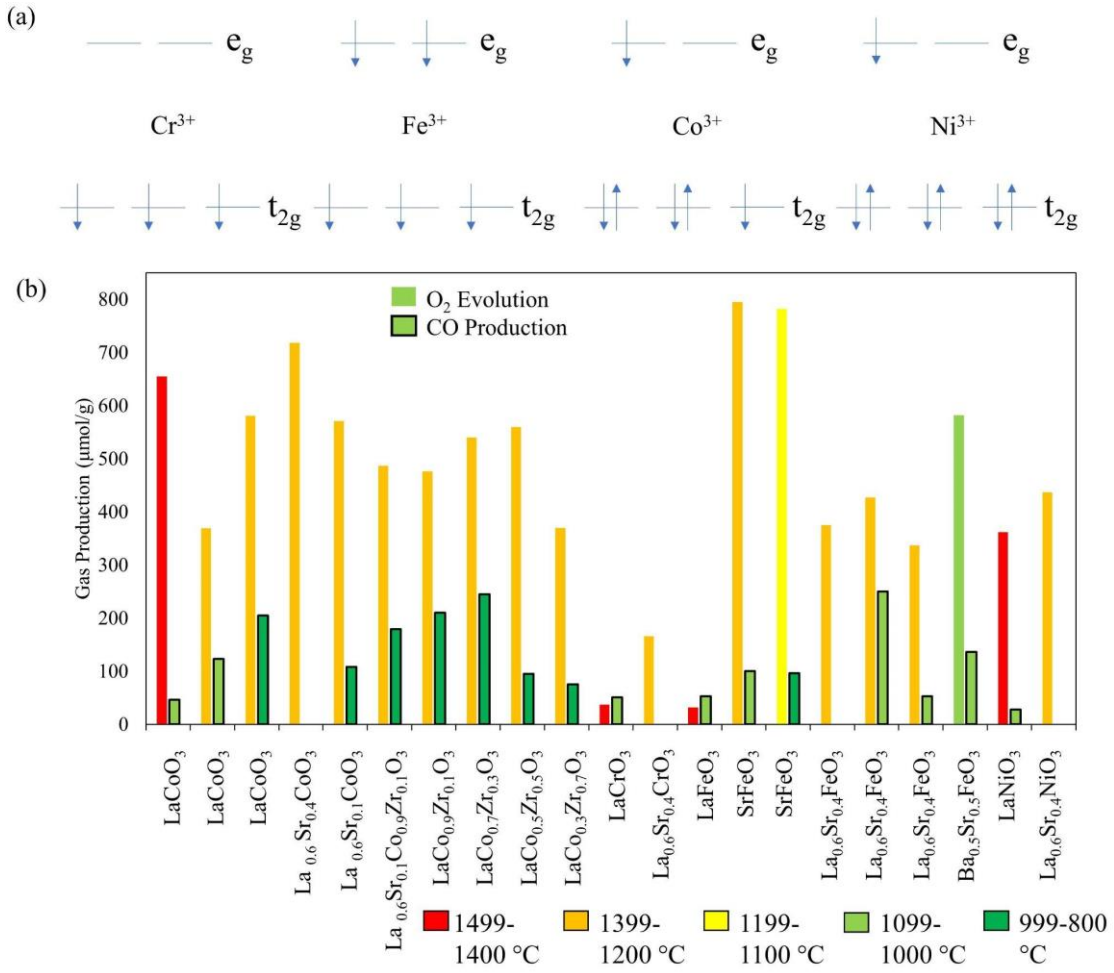

Figure 3.6. (a) Distribution of Transition Metal d Orbital Electrons into the e_g and t_{2g} orbitals in $LaTO_3$ (T = Cr, Fe, Co and Ni) (b) Oxygen Evolution and Carbon Monoxide Production with Variation in the

Transition Metal, Reduction under Ar/N_2 and Oxidation under 40-100 % CO_2 (data obtained from [34,42,45,49,70])

The reduction capacity of these perovskites can also be explained by the strength of the transition metal-oxygen bond. The strongest bond is Cr-O, followed by Mn-O, Fe-O, Co-O, and finally, the Ni-O bond requires the least energy to break [52]. This effect is demonstrated in $La_{0.1}Sr_{0.9}Mn_{1-x}Co_xO_3$, oxygen evolution increases as the concentration of cobalt increases, since the cobalt-oxygen bonds require less energy to break than the manganese-oxygen bonds, allowing oxygen vacancies to be formed more easily [71]. In $La_{0.8}Sr_{0.2}TO_3$, oxygen evolution volumes of 112 μmol/g and 732 μmol/g were seen when T is Mn and Co, respectively[38]. This finding was replicated by another group for $La_{0.3}Sr_{0.7}Co_{1-x}Mn_xO_3$, where increasing the manganese content from 10% to 20% decreases the maximum non-stoichiometry from 0.46 to 0.41 [72].

By the same mechanism of bond strength, doping $La_{0.6}Sr_{0.4}FeO_3$ with 20% cobalt increased oxygen yields from 425 μmol/g to 503 μmol/g [38]. The difference in reducibility between cobalt and iron is particularly noticeable when used as dopants. In $La_{0.5}Sr_{0.5}Mn_{0.5}T_{0.5}O_3$, oxygen evolution is found to be 538 μmol/g and 214 μmol/g when T is cobalt and iron, respectively [45]. Another explanation beyond metal-oxygen bond strength for the superiority of cobalt could be seen in the surface oxygen exchange coefficient (k^*) and oxide ion diffusivity (D^*), describing the ease with which oxygen moves through the material [73]. In $La_{1-x}Sr_xFe_{1-y}Co_yO_3$, as cobalt or strontium content increases, oxygen non-stoichiometry increased accompanied by increases in k^* and D^*, providing an easy method for assessing the reducibility of a material.

Table 3.1. Temperature Required for Various Reduction Reactions of Iron and Manganese (data obtained from [74])

Material	Fe^{4+} to Fe^{3+}	Fe^{3+} to Fe^{2+}	Mn^{4+} to Mn^{3+}	Mn^{3+} to Mn^{2+}
$La_{0.6}Sr_{0.4}FeO_3$	345 °C	>700 °C	-	-
$La_{0.6}Sr_{0.4}MnO_3$	-	-	422-499 °C	731 °C
$La_{0.6}Sr_{0.4}Fe_{0.8}Mn_{0.2}O_3$	285 °C	>700 °C	400-465 °C	690 °C

Another benefit from having two transition metals in the perovskite can be seen in Table 3.1. The mixed manganese and iron perovskite, $La_{0.6}Sr_{0.4}Fe_{0.8}Mn_{0.2}O_3$ was investigated along with its two single transition metal perovskites [74]. It can be seen from the table that in the two transition metal perovskites the temperature at which each reduction occurs is reduced, such as from 731 °C to 690 °C for Mn^{3+} to Mn^{2+}. This suggests that the presence of both transition metals in the perovskite structure allows for the more facile incorporation of electrons. The oxygen evolution of mixed transition metal perovskites is shown in Figure 3.7. As expected from the higher bond strength of chromium, all chromium containing perovskites have very low oxygen evolution volumes, with the evolution decreasing as chromium content increases [46]. Meanwhile, the highest yields come from cobalt and iron containing perovskites [38][45].

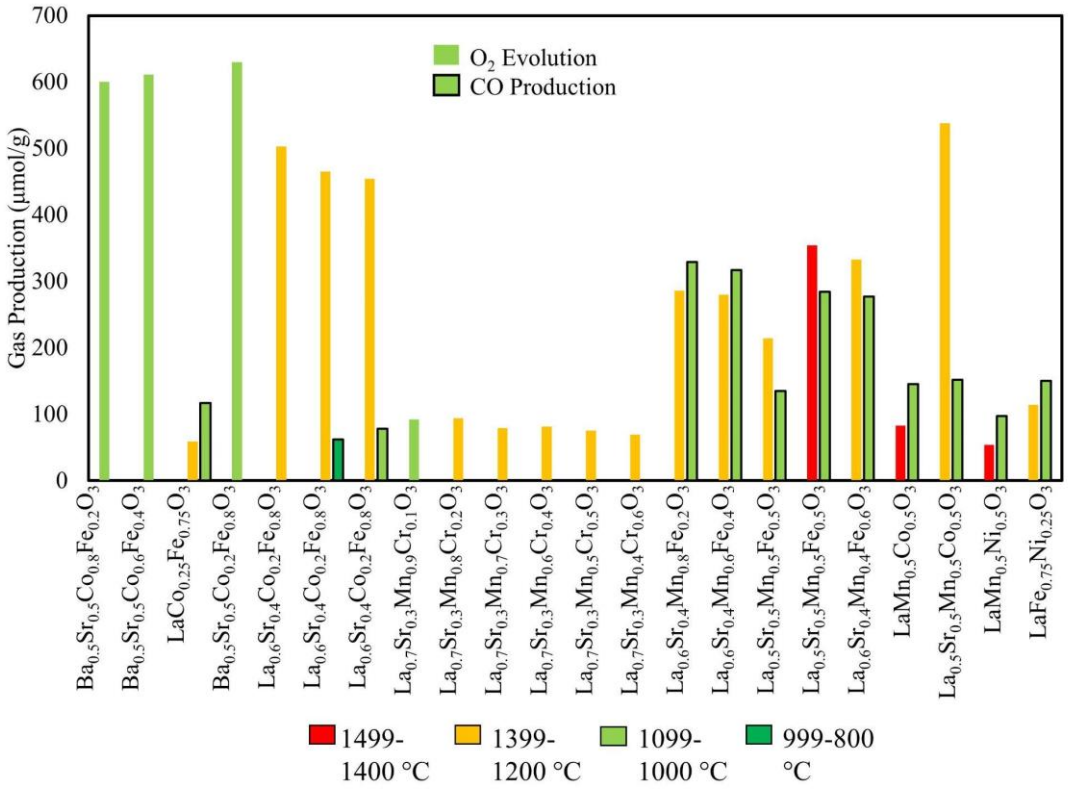

Figure 3.7. Oxygen Evolution and Carbon Monoxide Production of the Mixed Transition Metal Perovskites, when Reduced under Ar/N_2 and Oxidised under 10-50 % CO_2 (data obtained from [36,38,45,49,75,76])

3.3.4 Other B-site Metals

Non-redox metals such as aluminium and gallium have been doped on the B-site in an attempt to improve fuel yields, despite a decrease in the concentration of the redox-active metal. One of the mechanisms of increasing yields is through charge accommodation. Table 3.2 shows the oxygen evolution volumes for four $La_{0.5}Sr_{0.5}Mn_{1-x}B_xO_3$ materials and the correlating manganese oxidation state. It can be seen that doping with Al, Mg or Ga increases oxygen evolution with a concurrent increase in the Mn oxidation state before reduction, with a higher charge associated with higher yields [46]. Additionally,

increasing the gallium content in $La_{0.6}Ca_{0.4}Mn_{1-x}Ga_xO_3$ from 0 to 30 % increases oxygen evolution from around 200 μmol/g to over 320 μmol/g while also increasing the rate of oxygen evolution from 0.116 μmol/g/s to 0.175 μmol/g/s [77]. This increased rate was also seen with Al and Mg doping, likely due to better oxygen diffusivity [46]. Another method by which gallium doping increases oxygen yields is through changes in the thermodynamics of oxygen vacancy formation. Increasing gallium concentrations from 0 to 40 % in $La_{0.7}Sr_{0.3}Fe_{1-x}Ga_xO_3$ decreases the enthalpy and increases the entropy of oxygen vacancy resulting in more facile oxygen vacancy formation [47]. This is thought to be due to local lattice distortions near the gallium atoms because of the difference in covalency of the Ga-O and Fe-O bonds [78].

Table 3.2. Manganese Oxidation State and Oxygen Production Volumes of $La_{0.5}Sr_{0.5}Mn_{1-x}B_xO_3$ (B = Al, Mg & Ga) (data obtained from [46])

Material	Mn Oxidation State Before Reduction	Oxygen production (μmol/g)
$La_{0.5}Sr_{0.5}MnO_3$	+3.50	232
$La_{0.5}Sr_{0.5}Mn_{0.6}Al_{0.4}O_3$	+3.83	302
$La_{0.5}Sr_{0.5}Mn_{0.9}Mg_{0.1}O_3$	+3.67	269
$La_{0.5}Sr_{0.5}Mn_{0.8}Mg_{0.2}O_3$	+3.63	267

Another benefit of doping with these metals comes from a change in crystal structure. Doping of $LaCoO_3$ with gallium was found to change the crystal structure from rhombohedral to orthorhombic [79]. As discussed in Section 3.3.1, an orthorhombic crystal structure leads to tilting of the Co-O_6 octahedra, weakening the Co-O bond. The same is seen for doping with aluminium [80]. Another mechanism through which non-

redox active metals can increase oxygen yields is through an increased resistance to sintering at high temperatures. For example, doping with magnesium reduces the impact of sintering, resulting in smaller grain sizes over multiple cycles, due to the strength of the Mg-O bond, as demonstrated by the 2852 °C melting temperature of MgO [57]. The grain size of a perovskite is important because both the chemical bulk diffusion coefficient and the chemical surface exchange coefficient decrease with increasing grain size [81]. These properties influence the ability of oxygen to diffuse into and react with the perovskite. Therefore, smaller grain sizes are directly correlated with higher oxygen evolution volumes. Apart from doping with magnesium, another method of decreasing the grain size is through lower sintering temperature during perovskite synthesis, providing the temperature is still high enough to produce the perovskite. In $La_{0.5}Sr_{0.5}Fe_{0.8}Al_{0.2}O_3$, decreasing the sintering temperature from 1450 to 1150 °C decreased the grain size by more than a factor of fifteen, from 7 μm to 300nm [81].

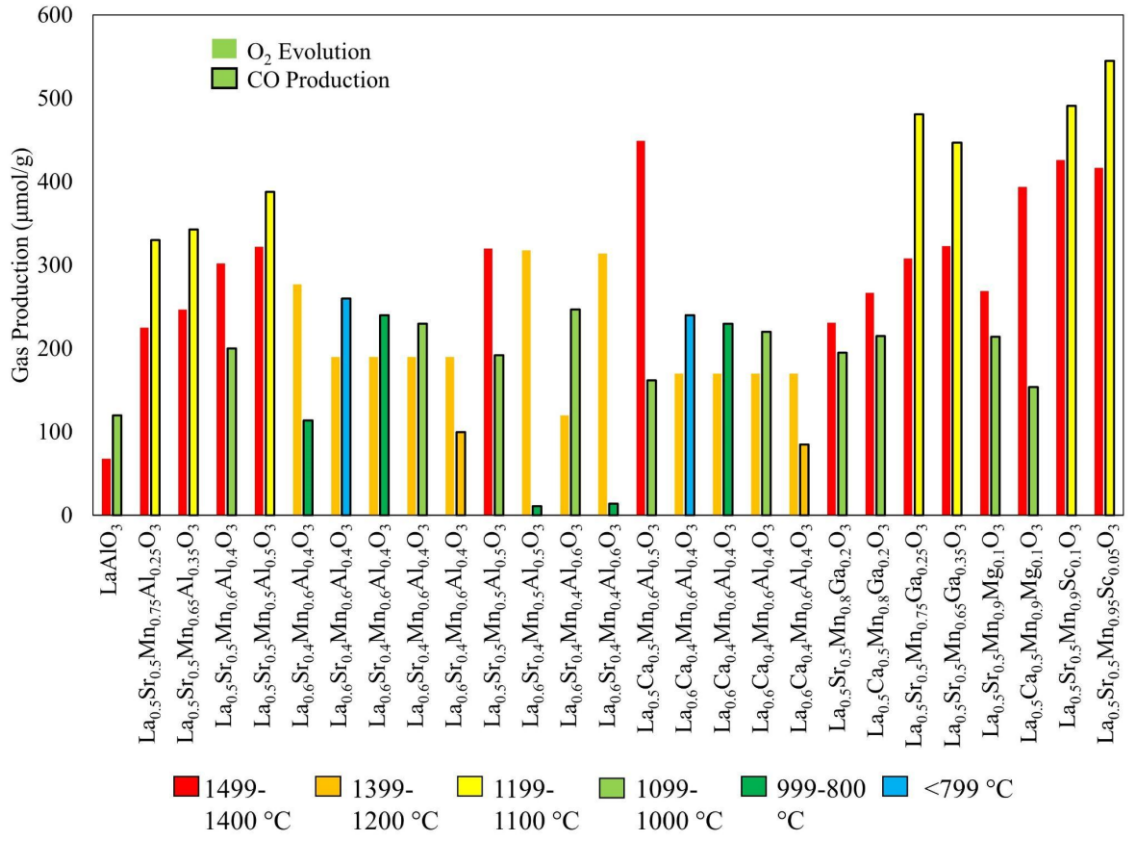

Figure 3.8. Doping of the B-site with Non-Redox Active Metals at Different Temperatures, with Oxygen Evolution and Carbon Monoxide Production when Reduced under Ar and Oxidised under 5-50 % CO_2 (data obtained from [34–36,46,47,76,79,80,82–84])

3.4 The Oxidation Reaction

Oxidation of this perovskite family in the presence of CO_2 leads to the splitting of CO_2 into CO, with incorporation of oxygen into the oxygen vacancies formed during reduction, re-forming the original perovskite. The mechanism of CO_2 decomposition was investigated by Fu *et al* on the surface of $LaMnO_3$ and can be seen in Figure 3.9 [85]. The process begins when a carbon dioxide molecule moves above an oxygen vacancy in the crystal structure (Figure 3.9(a)). The C-O bond of the oxygen closest to the oxygen vacancy begins to elongate, with a bond length of 1.34 Å compared with the 1.22 Å length of the other C-O bond (Figure 3.9(b)). The undercoordinated lattice manganese begins to

form a bond with this elongated oxygen while the carbon atom moves closer to a lattice oxygen and forms a tortuous carbonate structure (Figure 3.9(c)). As the oxygen moves downwards and fills the vacancy site, the remaining carbon monoxide relaxes towards the Mn before being released (Figure 3.9(d)).

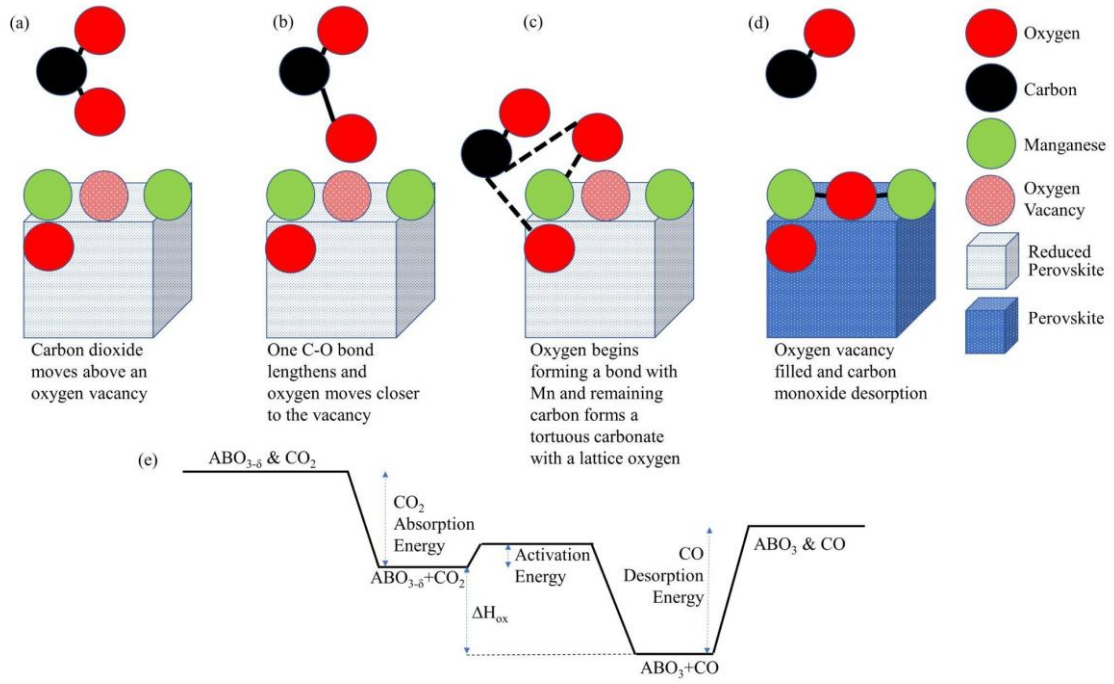

Figure 3.9. (a-d) Mechanism of Carbon Dioxide Splitting on Lanthanum Manganites, (e) Energy Changes during the CO_2 Splitting Reaction on the Perovskite Surface Showing the Absorption of CO_2 onto a Perovskite Surface with Oxygen Vacancies, Decomposition of CO_2 into CO and Filling of Oxygen Vacancies and the Desorption of CO from the Perovskite Surface

There are therefore three main steps to this reaction of $LaMnO_3$; (1) the adsorption of carbon dioxide onto the surface, (2) the breaking of the C-O bond and the energy released from the formation of the Mn-O bond, and (3) the desorption of the carbon monoxide. The energy of these three steps is shown in Figure 3.9(e). The rate-determining step is (2), which has an enthalpy of -72.5 kJ/mol and activation energy of 19 kJ/mol [85]. The

adsorption of carbon dioxide (1) releases 86.1 kJ/mol while the desorption of carbon monoxide requires 133 kJ/mol (3).

Similar to the reduction reaction, the effect of various elements in the A- and B-sites on oxidation will be investigated. However, the reaction temperatures also have an effect on the yield of the oxidation reaction and will be explored briefly here. It has been shown that yields are dependent on both reduction and oxidation temperatures, likely because the formation of more oxygen vacancies during reduction allows for the splitting of more carbon dioxide molecules. For example, in $SrMnO_3$, increasing the reduction temperature increases CO production, even with a constant oxidation temperature [33], as seen in Table 3.3. This was replicated with $Y_{0.5}Sr_{0.5}MnO_3$, where increasing reduction temperatures clearly lead to increased oxidation yields with a constant oxidation temperature of 900 °C [44]. While higher reduction temperatures are often optimal, the oxidation temperature is dependent on the competing factors of thermodynamics and diffusion. Since the oxidation reaction is exothermic, lower temperatures should favour carbon monoxide production. However, since the reaction is dependent on the diffusion of carbon dioxide from the bulk gas flow, higher temperatures increase diffusion within the material. This was seen for $La_{0.6}Sr_{0.4}MnO_3$, where oxidation was tested between 700 °C and 1100 °C, and the optimal was found to be 900 °C [56].

Table 3.3. The Effect of Reduction Temperature on Carbon Monoxide Yield

Material	Reduction Temperature (°C)	Oxygen evolution (μmol/g)	Oxidation Temperature (°C)	Carbon monoxide Production (μmol/g)	Reference
$SrMnO_3$	1400	532	1000	854	[33]
	1250	301	1000	511	
$Y_{0.5}Sr_{0.5}MnO_3$	1400	483	900	757	[44]
	1300	389	900	624	
	1200	258	900	418	

3.4.1 Alkaline Earth Metals

Unlike in the reduction reaction, the trends of doping with alkaline earth elements are less clear for oxidation. Doping with barium is ineffective, producing on average 183 μmol/g [53,57,76]. Doping with strontium produces on average 268 μmol/g, although there are some authors who published results as high as 854 μmol/g or as low as 50 μmol/g [33,47]. Indeed, doping $LaMnO_3$ with 12.5 % strontium doubles the activation energy of carbon dioxide splitting from 19 to 37.4 kJ/mol, suggesting that the reaction is less favourable [85]. Additionally, the energy released when carbon dioxide is adsorbed on the surface is 60.0 kJ/mol rather than 86.1 kJ/mol. Doping with calcium produces very similar results as strontium, producing 284 μmol/g of CO on average, although there are far less of the calcium-containing compounds to compare.

3.4.2 Lanthanides

Similar to the trend seen in the reduction reaction, as the size of the lanthanide in $Ln_{0.5}Sr_{0.5}MnO_3$ decreases, the carbon monoxide production generally increases. For example, in $Ln_{0.5}Sr_{0.5}MnO_3$, lanthanum (the largest lanthanide) produces 370 μmol/g while yttrium (the smallest lanthanide-like element) produces 571 μmol/g [44]. The only exception to this trend is samarium, which produces more CO than gadolinium, despite

having a larger ionic radius (0.958 Å and 0.938 Å, respectively) [59]. This correlation between ionic radius of the lanthanide and carbon monoxide production is likely due to the decrease in tolerance factor seen with smaller radii. This leads to a tilting of the MnO_6 octahedra, making the oxygen vacancies formed during reduction more accessible, and requiring less energy to reform the Mn-O bond.

3.4.3 Transition Metals

The impact of various transition metals on carbon monoxide yields can be studied via the activation energy (Ea) of carbon dioxide splitting. Lower activation energies suggest the reaction is more facile. It can be seen from Table 3.4 that doping with iron increases the Ea, while doping with chromium decreases the Ea, showing a thermodynamic favorability despite a stronger TM-O bond. Experimentally, doping $La_{0.6}Sr_{0.4}MnO_3$ with 30 % chromium almost doubles CO production [86]. The enthalpy of the reaction is also found to be lower for chromium containing materials [60]. This could be due to the fact the oxidising of Cr^{3+} to Cr^{4+} involves removing an electron from a lower energy t_{2g} orbital, while for Mn, Fe, Ni and Co, the change in oxidation state from 3+ to 4+ involves removing an electron from the higher energy e_g orbital.

The carbon monoxide yields have also been increased by reducing the perovskite under hydrogen. Hydrogen is a good reducing agent and leads to greater oxygen vacancy formation, resulting in greater CO_2 splitting. For example, $La_{0.75}Sr_{0.25}CoO_3$ was reduced at 500 °C under hydrogen then oxidised at 850 °C producing 4032 μmol/g of CO, higher than any other reaction found in the literature [87]. In addition to higher yields, reducing under hydrogen reduces both the reduction and oxidation temperatures, leading to significant energy savings (from 1400 °C to 500 °C). However, the energy required for

the manufacturing of hydrogen must be considered when evaluating the suitability of this technique.

Table 3.4. Activation Energy of Carbon Dioxide Splitting for various Transition Metal Doped Perovskites (data obtained from [85])

Material	Activation Energy (kJ/mol)
$La_{0.625}Sr_{0.375}MnO_3$	68.65
$La_{0.625}Sr_{0.375}Mn_{0.5}Fe_{0.5}O_3$	75.70
$La_{0.625}Sr_{0.375}Mn_{0.5}Cr_{0.5}O_3$	54.59

3.4.4 Other B-site Metals

As was seen in the reduction reaction, doping the B-site with non-redox active metals can improve yields. The carbon monoxide production of these materials can be seen in Figure 3.8. Generally, gallium performs better than aluminium and magnesium, with the maximum yield of 513 μmol/g seen with 20% gallium doping of $La_{0.6}Ca_{0.4}MnO_3$ [77]. The highest yield for aluminium doped materials was seen with 50 % doping of $La_{0.5}Sr_{0.5}MnO_3$, producing 388 μmol/g [84], while for the same material, doping with 10% magnesium produced 214 μmol/g [46]. This trend does not follow that seen in reduction, where doping with Al leads to a larger increase in the manganese oxidation state than magnesium and gallium, releasing more oxygen. Doping with a very small amount of scandium produces the highest CO yield of any non-redox active metal. $La_{0.5}Sr_{0.5}MnO_3$ doped with only 5% scandium produces 545 μmol/g [84].

3.4.5 Supported Perovskites

Another way to increase carbon monoxide yields is through the incorporation of supports to limit the detrimental effect of sintering during repeated cycling [67,88,89].

$La_{0.75}Sr_{0.25}FeO_3$ was supported on CeO_2, ZrO_2, Al_2O_3, SiO_2, TiO_2 and SiC in a 1:3 weight ratio [88]. All perovskites were reduced under hydrogen, explaining the high CO yields seen even in the unsupported control of 690 μmol/g. The most effective supports are SiO_2 (1700 $\mu mol/g_{perovskite}$) and ZrO_2 (1350 $\mu mol/g_{perovskite}$), while Al_2O_3 decreases the yield to 490 $\mu mol/g_{perovskite}$. Interestingly, using a 1:1 weight ratio of SiO_2 produces only 380 $\mu mol/g_{perovskite}$, suggesting the weight ratio is vital. The supports are thought to increase yields through two mechanisms: increasing gas diffusion through the material and adding resistance to sintering. However, if the weight of the supported perovskite is considered, the best yield is 425 μmol/g of material rather than 1700 $\mu mol/g_{perovskite}$. This brings the yield in line with many reported so far or found in Table 3.5. Additionally, once a similar perovskite $La_{0.7}Sr_{0.3}FeO_3$ was also supported in a 1:3 ratio with SiO_2 but reduction was performed under argon rather than hydrogen, the yield was 112 $\mu mol/g_{perovskite}$, showing no improvement [67]. Therefore, the only real benefit of supports is in maintaining the yields over multiple cycles through decreased sintering. Another important factor in the decision to use a support is the increased heating and energy costs encountered due to the greater total weight of the supported perovskite. Therefore, if the main benefit arises from sintering resistance, adding a non-redox active metal such as magnesium or gallium may be a cheaper alternative.

Table 3.5. Thermochemical Conversion Results from the Lanthanum Manganite Family of Perovskites

Material	Crystal Structure	Oxygen Evolution (µmol/g)	Reduction Temperature (°C)	Reduction Gas	Carbon Monoxide Production (µmol/g)	Oxidation Temperature (°C)	Oxidation Gas	Reference
$La_{1-x}Sr_xMnO_3$								
$SrMnO_3$	-	523	1400	N_2	854	1000	CO_2 /air	[33]
$SrMnO_3$	-	301	1250	N_2	511	1000	CO_2 /air	[33]
$La_{0.9}Sr_{0.1}MnO_3$	Rhombohedral (*R3c*)	22	1400	Ar	-	-	-	[50]
$La_{0.9}Sr_{0.1}MnO_3$	Orthorhombic (*Pnma*)	-	800	16 % CO/ 84 % CO_2	106	800	CO_2	[54]
$La_{0.9}Sr_{0.1}MnO_3$	-	177	1400	Ar	114	1000	50 % CO_2 in Ar	[90]
$La_{0.8}Sr_{0.2}MnO_3$	Rhombohedral (*R3c*)	58	1400	Ar	-	-	-	[50]
$La_{0.8}Sr_{0.2}MnO_3$	Rhombohedral (*R3c*)	112	1400	Ar	-	-	-	[38]
$La_{0.8}Sr_{0.2}MnO_3$	Orthorhombic (*Pnma*)	-	800	16 % CO/ 84 % CO_2	246	800	CO_2	[54]
$La_{0.8}Sr_{0.2}MnO_3$	-	233	1400	Ar	161	1000	50 % CO_2 in Ar	[90]
$La_{0.7}Sr_{0.3}MnO_3$	Rhombohedral (*R3c*)	64	1500	N_2	138	1500	1 atm CO_2	[48]
$La_{0.7}Sr_{0.3}MnO_3$	Rhombohedral (*R3c*)	38	1400	N_2	76	1400	1 atm CO_2	[48]
$La_{0.7}Sr_{0.3}MnO_3$	Rhombohedral (*R3c*)	136	1400	Ar	-	-	-	[50]
$La_{0.7}Sr_{0.3}MnO_3$	Orthorhombic (*Pnma*)	-	800	16 % CO/ 84 % CO_2	320	800	CO_2	[54]
$La_{0.7}Sr_{0.3}MnO_3$	-	473	1400	Ar	163	1000	50 % CO_2 in Ar	[90]
$La_{0.65}Sr_{0.35}MnO_3$	Rhombohedral (*R3c*)	103	1400	Ar	189	1050	50 % CO_2 in Ar	[37]
$La_{0.65}Sr_{0.35}MnO_3$	Rhombohedral (*R3c*)	166	1400	Ar	-	-	-	[38]

Material	Crystal Structure	Oxygen Evolution (μmol/g)	Reduction Temperature (°C)	Reduction Gas	Carbon Monoxide Production (μmol/g)	Oxidation Temperature (°C)	Oxidation Gas	Reference
$La_{0.65}Sr_{0.35}MnO_3$	Rhombohedral (*R3c*)	100	1400	Ar	137	1100	40 % CO_2 in Ar	[43]
$La_{0.6}Sr_{0.4}MnO_3$	Rhombohedral (*R3c*)	82	1500	N_2	201	1500	1 atm CO_2	[48]
$La_{0.6}Sr_{0.4}MnO_3$	Rhombohedral (*R3c*)	47	1400	N_2	98	1400	1 atm CO_2	[48]
$La_{0.6}Sr_{0.4}MnO_3$	Rhombohedral (*R3c*)	196	1400	Ar	-	-	-	[50]
$La_{0.6}Sr_{0.4}MnO_3$	Tetragonal & Orthorhombic	348	1350	N_2	469	1000	CO_2	[49]
$La_{0.6}Sr_{0.4}MnO_3$	Orthorhombic	126	1300	Ar	-	-	-	[35]
$La_{0.6}Sr_{0.4}MnO_3$	-	131	1300	Ar	-	-	-	[42]
$La_{0.6}Sr_{0.4}MnO_3$	Hexagonal	222	1250	Ar	-	900	5% CO_2 in He	[83]
$La_{0.6}Sr_{0.4}MnO_3$	-	60	1240	Ar	115	640	CO_2	[47]
$La_{0.6}Sr_{0.4}MnO_3$	-	60	1240	Ar	105	840	CO_2	[47]
$La_{0.6}Sr_{0.4}MnO_3$	-	60	1240	Ar	100	1040	CO_2	[47]
$La_{0.6}Sr_{0.4}MnO_3$	-	60	1240	Ar	50	1240	CO_2	[47]
$La_{0.6}Sr_{0.4}MnO_3$	Rhombohedral (*R3c*)	-	800	16 % CO/ 84 % CO_2	485	800	CO_2	[54]
$La_{0.6}Sr_{0.4}MnO_3$	-	544	1400	Ar	285	1000	50 % CO_2 in Ar	[90]
$La_{0.5}Sr_{0.5}MnO_3$	Tetragonal (*I4/mcm*)	113	1500	N_2	230	1500	1 atm CO_2	[48]
$La_{0.5}Sr_{0.5}MnO_3$	Tetragonal (*I4/mcm*)	248	1400	Ar	269	1050	50 % CO_2 in Ar	[37]
$La_{0.5}Sr_{0.5}MnO_3$	Rhombohedral (*R3c*)	298	1400	Ar	-	-	-	[38]
$La_{0.5}Sr_{0.5}MnO_3$	Rhombohedral (*R3c*)	298	1400	Ar	-	-	-	[38]

Material	Crystal Structure	Oxygen Evolution (μmol/g)	Reduction Temperature (°C)	Reduction Gas	Carbon Monoxide Production (μmol/g)	Oxidation Temperature (°C)	Oxidation Gas	Reference
$La_{0.5}Sr_{0.5}MnO_3$	Rhombohedral (*R3c*)	201	1400	Ar	325	1100	40 % CO_2 in Ar	[43]
$La_{0.5}Sr_{0.5}MnO_3$	Tetragonal (*I4/mcm*)	79	1400	N_2	135	1400	1 atm CO_2	[48]
$La_{0.5}Sr_{0.5}MnO_3$	-	512	1400	N_2	701	1000	CO_2 /air	[33]
$La_{0.5}Sr_{0.5}MnO_3$	Cubic (*Pm3̲m*)	232	1400	Ar	190	1050	50 % CO_2 in Ar	[46]
$La_{0.5}Sr_{0.5}MnO_3$	-	248	1400	Ar	269	1050	50 % CO_2 in Ar	[45]
$La_{0.5}Sr_{0.5}MnO_3$	-	256	1400	Ar	256	1050	50 % CO_2 in Ar	[76]
$La_{0.5}Sr_{0.5}MnO_3$	Rhombohedral (*R3c*)	198	1400	Ar	380	1100	40 % CO_2 in Ar	[44]
$La_{0.5}Sr_{0.5}MnO_3$	-	55	1000	N_2	76	1000	CO_2 /air	[33]
$La_{0.5}Sr_{0.5}MnO_3$	-	105	1000	N_2	134	700	CO_2 /air	[33]
$La_{0.5}Sr_{0.5}MnO_3$	-	248	1400	Ar	275	1050	50 % CO_2 in Ar	[53]
$La_{0.5}Sr_{0.5}MnO_3$	-	591	1400	Ar	338	1000	50 % CO_2 in Ar	[90]
$La_{0.5}Sr_{0.5}MnO_3$	-	992	900	10% CH_4 in N_2	1813	900	50 % CO_2 in N_2	[91]
$La_{0.5}Sr_{0.5}MnO_3$	-	-	1400	Ar	185	900	50 % CO_2 in Ar	[92]
$La_{0.5}Sr_{0.5}MnO_3$	-	-	1400	Ar	236	1050	50 % CO_2 in Ar	[92]
$La_{0.5}Sr_{0.5}MnO_3$	-	-	1400	Ar	243	1200	50 % CO_2 in Ar	[92]
$La_{0.35}Sr_{0.65}MnO_3$	Tetragonal (*I4/mcm*)	424	1400	Ar	165	1050	50 % CO_2 in Ar	[37]
$La_{0.4}Sr_{0.6}MnO_3$	-	610	1400	Ar	309	1000	50 % CO_2 in Ar	[90]
$La_{0.3}Sr_{0.7}MnO_3$	-	648	1400	Ar	424	1000	50 % CO_2 in Ar	[90]
$La_{0.25}Sr_{0.75}MnO_3$	-	516	1400	N_2	786	1000	CO_2 /air	[33]

Material	Crystal Structure	Oxygen Evolution (µmol/g)	Reduction Temperature (°C)	Reduction Gas	Carbon Monoxide Production (µmol/g)	Oxidation Temperature (°C)	Oxidation Gas	Reference
$La_{0.2}Sr_{0.8}MnO_3$	Cubic (*Pm3̲m*)	681	1400	Ar	191	1050	50 % CO_2 in Ar	[37]
$La_{0.2}Sr_{0.8}MnO_3$	-	801	1400	Ar	295	1000	50 % CO_2 in Ar	[90]
$La_{0.1}Sr_{0.9}MnO_3$	-	1476	1400	Ar	64.7	1000	50 % CO_2 in Ar	[90]
$La_{1-x}Ca_xMnO_3$								
$La_{0.8}Ca_{0.2}MnO_3$	Orthorhombic (*Pnma*)	94	1300	Ar	-	-	-	[56]
$La_{0.65}Ca_{0.35}MnO_3$	Orthorhombic (*Pnma*)	143	1400	Ar	183	1050	50 % CO_2 in Ar	[57]
$La_{0.65}Ca_{0.35}MnO_3$	Orthorhombic (*Pnma*)	109	1400	Ar	175	1100	40 % CO_2 in Ar	[43]
$La_{0.6}Ca_{0.4}MnO_3$	Orthorhombic (*Pnma*)	167	1300	Ar	-	-	-	[56]
$La_{0.6}Ca_{0.4}MnO_3$	Orthorhombic (*Pnma*)	167	1300	Ar	-	-	-	[56]
$La_{0.6}Ca_{0.4}MnO_3$	Orthorhombic (*Pnma*)	167	1300	Ar	-	-	-	[56]
$La_{0.6}Ca_{0.4}MnO_3$	Orthorhombic (*Pnma*)	167	1300	Ar	-	-	-	[56]
$La_{0.6}Ca_{0.4}MnO_3$	Orthorhombic (*Pnma*)	167	1300	Ar	-	-	-	[56]
$La_{0.6}Ca_{04}MnO_3$	Orthorhombic	167	1300	Ar	-	-	-	[35]
$La_{0.5}Ca_{0.5}MnO_3$	Orthorhombic (*Pnma*)	311	1400	Ar	210	1050	50 % CO_2 in Ar	[57]
$La_{0.5}Ca_{0.5}MnO_3$	Cubic (*Pm3̲m*)	325	1400	Ar	175	1050	50 % CO_2 in Ar	[46]
$La_{0.5}Ca_{0.5}MnO_3$	-	314	1400	Ar	210	1050	50 % CO_2 in Ar	[76]
$La_{0.5}Ca_{0.5}MnO_3$	Orthorhombic (*Pnma*)	312	1400	Ar	520	1100	40 % CO_2 in Ar	[44]
$La_{0.5}Ca_{0.5}MnO_3$	Orthorhombic (*Pnma*)	315	1400	Ar	525	1100	40 % CO_2 in Ar	[43]
$La_{0.5}Ca_{0.5}MnO_3$	-	311	1400	Ar	212	1050	50 % CO_2 in Ar	[53]

Material	Crystal Structure	Oxygen Evolution (μmol/g)	Reduction Temperature (°C)	Reduction Gas	Carbon Monoxide Production (μmol/g)	Oxidation Temperature (°C)	Oxidation Gas	Reference
$La_{0.5}Ca_{0.5}MnO_3$	-	840	900	10% CH_4 in N_2	1422	900	50 % CO_2 in N_2	[91]
$La_{0.4}Ca_{0.6}MnO_3$	Orthorhombic (*Pnma*)	224	1300	Ar	-	-	-	[56]
$La_{0.35}Ca_{0.65}MnO_3$	Orthorhombic (*Pnma*)	653	1400	Ar	350	1100	40 % CO_2 in Ar	[43]
$La_{0.2}Ca_{0.8}MnO_3$	Orthorhombic (*Pnma*)	402	1300	Ar	-	-	-	[56]
$CaMnO_3$	-	4122	900	10% CH_4 in N_2	0	900	50 % CO_2 in N_2	[91]
$La_{1-x}Ba_xMnO_3$								
$La_{0.65}Ba_{0.35}MnO_3$	Rhombohedral (*R3c*)	146	1400	Ar	163	1050	50 % CO_2 in Ar	[57]
$La_{0.6}Ba_{0.4}MnO_3$	Orthorhombic	113	1300	Ar	-	-	-	[35]
$La_{0.5}Ba_{0.5}MnO_3$	Cubic (*Pm$\underline{3}$m*)	203	1400	Ar	185	1050	50 % CO_2 in Ar	[57]
$La_{0.5}Ba_{0.5}MnO_3$	-	287	1400	Ar	197	1050	50 % in CO_2	[76]
$La_{0.5}Ba_{0.5}MnO_3$	-	204	1400	Ar	186	1050	50 % CO_2 in Ar	[53]
$Ln_{1-x}(Sr, Ca)_xMnO_3$								
$Y_{0.5}Sr_{0.5}MnO_3$	Orthorhombic (*Pnma*)	551	1400	Ar	112	1050	50 % CO_2 in Ar	[57],[45]
$Y_{0.5}Sr_{0.5}MnO_3$	Orthorhombic (*Pnma*)	481	1400	Ar	757	900	40 % CO_2 in Ar	[44]
$Y_{0.5}Sr_{0.5}MnO_3$	-	539	1400	Ar	151	1050	50 % CO_2 in Ar	[76]
$Y_{0.5}Sr_{0.5}MnO_3$	-	550	1400	Ar	113	1050	50 % CO_2 in Ar	[54]
$Y_{0.5}Sr_{0.5}MnO_3$	Orthorhombic (*Pnma*)	389	1300	Ar	624	900	40 % CO_2 in Ar	[44]
$Y_{0.5}Sr_{0.5}MnO_3$	Orthorhombic (*Pnma*)	258	1200	Ar	418	900	40 % CO_2 in Ar	[44]
$Y_{0.5}Sr_{0.5}MnO_3$	-	1362	900	10% CH_4 in N_2	2458	900	50 % CO_2 in N_2	[91]

Material	Crystal Structure	Oxygen Evolution (μmol/g)	Reduction Temperature (°C)	Reduction Gas	Carbon Monoxide Production (μmol/g)	Oxidation Temperature (°C)	Oxidation Gas	Reference
$Y_{0.5}Ca_{0.5}MnO_3$	Orthorhombic (*Pnma*)	573	1400	Ar	670	1100	40 % CO_2 in Ar	[44]
$LaMnO_3$	-	347	1400	Ar	67	1000	50 % CO_2 in Ar	[34]
$LaMnO_3$	-	104	1350	N_2	-	-	-	[36]
$LaMnO_3$	Orthorhombic	76	1300	Ar	-	-	-	[35]
$LaMnO_3$	-	242	1000	N_2	329	700	CO_2 /air	[33]
$LaMnO_3$	-	149	1000	N_2	223	1000	CO_2 /air	[33]
$La_{0.95}Ce_{0.05}MnO_3$	-	470	480	CO in He	-	-	-	[66]
$La_{0.9}Ce_{0.1}MnO_3$	-	451	480	CO in He	-	-	-	[66]
$Pr_{0.9}Sr_{0.1}MnO_3$	-	206	1400	Ar	272	1000	CO_2 in Ar	[64]
$Pr_{0.8}Sr_{0.2}MnO_3$	-	243	1400	Ar	299	1000	CO_2 in Ar	[64]
$Pr_{0.7}Sr_{0.3}MnO_3$	-	256	1400	Ar	336	1000	CO_2 in Ar	[64]
$Pr_{0.6}Sr_{0.4}MnO_3$	-	285	1400	Ar	362	1000	CO_2 in Ar	[64]
$Pr_{0.5}Sr_{0.5}MnO_3$	-	482	1400	Ar	299	1000	CO_2 in Ar	[64]
$Pr_{0.4}Sr_{0.6}MnO_3$	-	376	1400	Ar	573	1000	CO_2 in Ar	[64]
$Pr_{0.3}Sr_{0.7}MnO_3$	-	665	1400	Ar	367	1000	CO_2 in Ar	[64]
$Pr_{0.2}Sr_{0.8}MnO_3$	-	838	1400	Ar	637	1000	CO_2 in Ar	[64]
$Pr_{0.1}Sr_{0.9}MnO_3$	-	1062	1400	Ar	324	1000	CO_2 in Ar	[64]
$Nd_{0.5}Sr_{0.5}MnO_3$	Orthorhombic (*Imma*)	264	1400	Ar	390	1100	40 % CO_2 in Ar	[44]
$Nd_{0.5}Ca_{0.5}MnO_3$	Orthorhombic (*Pnma*)	343	1400	Ar	530	1100	40 % CO_2 in Ar	[44]

Material	Crystal Structure	Oxygen Evolution (μmol/g)	Reduction Temperature (°C)	Reduction Gas	Carbon Monoxide Production (μmol/g)	Oxidation Temperature (°C)	Oxidation Gas	Reference
$Sm_{0.5}Sr_{0.5}MnO_3$	Orthorhombic (*Pnma*)	301	1400	Ar	540	1100	40 % CO_2 in Ar	[44]
$Sm_{0.5}Ca_{0.5}MnO_3$	Orthorhombic (*Pnma*)	361	1400	Ar	580	1100	40 % CO_2 in Ar	[44]
$Gd_{0.5}Sr_{0.5}MnO_3$	Orthorhombic (*Pnma*)	330	1400	Ar	480	1100	40 % CO_2 in Ar	[44]
$Gd_{0.5}Ca_{0.5}MnO_3$	Orthorhombic (*Pnma*)	404	1400	Ar	620	1100	40 % CO_2 in Ar	[44]
$Dy_{0.5}Sr_{0.5}MnO_3$	Orthorhombic (*Pnma*)	393	1400	Ar	560	1100	40 % CO_2 in Ar	[44]
$Dy_{0.5}Ca_{0.5}MnO_3$	Orthorhombic (*Pnma*)	493	1400	Ar	560	1100	40 % CO_2 in Ar	[44]
$La_{1-x}(Sr,Ca)_xTMO_3$								
$LaCoO_3$	-	655	1400	Ar	46	1000	50 % CO_2 in Ar	[34]
$LaCoO_3$	Rhombohedral	369	1300	Ar	123	1050	50 % CO_2 in Ar	[45]
$LaCoO_3$	Rhombohedral (*R3c*)	581	1300	Ar	205	800	CO_2 in Ar	[70]
$La_{0.6}Sr_{0.4}CoO_3$	-	718	1300	Ar	-	-	-	[42]
$La_{0.9}Sr_{0.1}CoO_3$	Hexagonal (*R3m*)	571	1300	Ar	108	800	CO_2 in Ar	[70]
$La_{0.2}Ca_{0.8}CoO_3$	Rhombohedral	1213	1300	Ar	-	-	-	[93]
$La_{0.4}Ca_{0.6}CoO_3$	Rhombohedral	1050	1300	Ar	-	-	-	[93]
$La_{0.6}Ca_{0.4}CoO_3$	Rhombohedral	850	1300	Ar	-	-	-	[93]
$La_{0.8}Ca_{0.2}CoO_3$	Rhombohedral	715	1300	Ar	-	-	-	[93]
$La_{0.9}Sr_{0.1}Co_{0.9}Zr_{0.1}O_3$	Hexagonal (*R3m*)	487	1300	Ar	179	800	CO_2 in Ar	[70]
$LaCo_{0.9}Zr_{0.1}O_3$	Rhombohedral (*R3c*)	476	1300	Ar	210	800	CO_2 in Ar	[70]
$LaCo_{0.7}Zr_{0.3}O_3$	Rhombohedral (*R3c*)	540	1300	Ar	245	800	CO_2 in Ar	[70]

Material	Crystal Structure	Oxygen Evolution (μmol/g)	Reduction Temperature (°C)	Reduction Gas	Carbon Monoxide Production (μmol/g)	Oxidation Temperature (°C)	Oxidation Gas	Reference
$LaCo_{0.5}Zr_{0.5}O_3$	Rhombohedral (*R3c*)	560	1300	Ar	95	800	CO_2 in Ar	[70]
$LaCo_{0.3}Zr_{0.7}O_3$	Rhombohedral (*R3c*)	370	1300	Ar	75	800	CO_2 in Ar	[70]
$LaCrO_3$	-	37	1400	Ar	51	1000	50 % CO_2 in Ar	[34]
$La_{0.6}Sr_{0.4}CrO_3$	-	166	1300	Ar	-	-	-	[42]
$LaFeO_3$	-	32	1400	Ar	53	1000	50 % CO_2 in Ar	[34]
$SrFeO_3$	-	795	1200	Ar	100	1050	50 % CO_2 in Ar	[45]
$SrFeO_3$	-	782	1100	Ar	96	800	50 % CO_2 in Ar	[45]
$La_{0.6}Sr_{0.4}FeO_3$	-	375	1300	Ar	-	-	-	[42]
$La_{0.6}Sr_{0.4}FeO_3$	Rhombohedral & Tetragonal	427	1350	N_2	250	1000	CO_2	[49]
$La_{0.6}Sr_{0.4}FeO_3$	Rhombohedral & Tetragonal	-	1000	5 % H_2 in N_2	-	-	-	[49]
$La_{0.6}Sr_{0.4}FeO_3$	-	337	1200	Ar	53	1050	50 % CO_2 in Ar	[45]
$Ba_{0.5}Sr_{0.5}FeO_3$	-	582	1000	Ar	136	1050	50 % CO_2 in Ar	[45]
$LaNiO_3$	-	362	1400	Ar	28	1000	50 % CO_2 in Ar	[34]
$La_{0.6}Sr_{0.4}NiO_3$	-	437	1300	Ar	-	-	-	[42]
$Ba_{0.5}Sr_{0.5}Co_{0.8}Fe_{0.2}O_3$	Cubic ($Pm\underline{3}m$)	600	1000	Ar	-	-	-	[38]
$Ba_{0.5}Sr_{0.5}Co_{0.6}Fe_{0.4}O_3$	Cubic ($Pm\underline{3}m$)	611	1000	Ar	-	-	-	[38]
$LaCo_{0.25}Fe_{0.75}O_3$	Rhombohedral	59	1300	Ar	117	1050	50 % CO_2 in Ar	[45]
$Ba_{0.5}Sr_{0.5}Co_{0.2}Fe_{0.8}O_3$	Cubic ($Pm\underline{3}m$)	630	1000	Ar	-	-	-	[38]

Material	Crystal Structure	Oxygen Evolution (μmol/g)	Reduction Temperature (°C)	Reduction Gas	Carbon Monoxide Production (μmol/g)	Oxidation Temperature (°C)	Oxidation Gas	Reference
$La_{0.6}Sr_{0.4}Co_{0.2}Fe_{0.8}O_3$	Rhombohedral (*R3c*)	503	1200	Ar	-	-	-	[38]
$La_{0.6}Sr_{0.4}Co_{0.2}Fe_{0.8}O_3$	-	465	1200	Ar	62	800	50 % CO_2 in Ar	[45]
$La_{0.6}Sr_{0.4}Co_{0.2}Fe_{0.8}O_3$	-	454	1200	Ar	78	1050	50 % CO_2 in Ar	[45]
$La_{0.7}Sr_{0.3}Mn_{0.9}Cr_{0.1}O_3$	Rhombohedral (*R3c*)	92	1350	N_2	-	-	-	[36]
$La_{0.7}Sr_{0.3}Mn_{0.8}Cr_{0.2}O_3$	Rhombohedral (*R3c*)	94	1350	N_2	-	-	-	[36]
$La_{0.7}Sr_{0.3}Mn_{0.7}Cr_{0.3}O_3$	Rhombohedral (*R3c*)	79	1350	N_2	-	-	-	[36]
$La_{0.7}Sr_{0.3}Mn_{0.6}Cr_{0.4}O_3$	Rhombohedral (*R3c*)	81	1350	N_2	-	-	-	[36]
$La_{0.7}Sr_{0.3}Mn_{0.5}Cr_{0.5}O_3$	Rhombohedral (*R3c*)	75	1350	N_2	-	-	-	[36]
$La_{0.7}Sr_{0.3}Mn_{0.4}Cr_{0.6}O_3$	Rhombohedral (*R3c*)	69	1350	N_2	-	-	-	[36]
$La_{0.5}Sr_{0.5}Mn_{0.6}Cr_{0.4}O_3$	Cubic ($Pm\underline{3}m$)	215	1400	Ar	134	1050	50 % CO_2 in Ar	[46]
$La_{0.5}Ca_{0.5}Mn_{0.6}Cr_{0.4}O_3$	Cubic ($Pm\underline{3}m$)	249	1400	Ar	111	1050	50 % CO_2 in Ar	[46]
$La_{0.6}Sr_{0.4}Mn_{0.8}Fe_{0.2}O_3$	Tetragonal & Orthorhombic	286	1350	N_2	329	1000	CO_2	[49]
$La_{0.6}Sr_{0.4}Mn_{0.8}Fe_{0.2}O_3$	Tetragonal & Orthorhombic	-	1000	5 % H_2 in N_2	-	-	-	[49]
$La_{0.6}Sr_{0.4}Mn_{0.6}Fe_{0.4}O_3$	Rhombohedral	280	1350	N_2	317	1000	CO_2	[49]
$La_{0.6}Sr_{0.4}Mn_{0.6}Fe_{0.4}O_3$	Rhombohedral	-	1000	5 % H_2 in N_2	-	-	-	[49]
$La_{0.5}Sr_{0.5}Mn_{0.5}Fe_{0.5}O_3$	-	214	1300	Ar	135	1050	50 % CO_2 in Ar	[45]
$La_{0.5}Sr_{0.5}Mn_{0.5}Fe_{0.5}O_3$	-	354	1400	Ar	284	1050	50 % CO_2 in Ar	[76]
$La_{0.6}Sr_{0.4}Mn_{0.4}Fe_{0.6}O_3$	Rhombohedral	333	1350	N_2	277	1000	CO_2	[49]

Material	Crystal Structure	Oxygen Evolution (μmol/g)	Reduction Temperature (°C)	Reduction Gas	Carbon Monoxide Production (μmol/g)	Oxidation Temperature (°C)	Oxidation Gas	Reference
$La_{0.6}Sr_{0.4}Mn_{0.4}Fe_{0.6}O_3$	Rhombohedral	-	1000	5 % H_2 in N_2	-	-	-	[49]
$LaMn_{0.5}Co_{0.5}O_3$	Rhombohedral	83	1400	Ar	145	1050	50 % CO_2 in Ar	[45]
$LaMn_{0.5}Co_{0.5}O_3$	-	-	1400	Ar	181	900	50 % CO_2 in Ar	[92]
$LaMn_{0.5}Co_{0.5}O_3$	-	-	1400	Ar	286	1050	50 % CO_2 in Ar	[92]
$LaMn_{0.5}Co_{0.5}O_3$	-	-	1400	Ar	281	1200	50 % CO_2 in Ar	[92]
$La_{0.5}Sr_{0.5}Mn_{.5}Co_{0.5}O_3$	-	538	1300	Ar	152	1050	50 % CO_2 in Ar	[45]
$LaMn_{0.5}Ni_{0.5}O_3$	Rhombohedral	54	1400	Ar	97	1050	50 % CO_2 in Ar	[45]
$LaFe_{0.75}Ni_{0.25}O_3$	Rhombohedral	114	1300	Ar	150	1050	50 % CO_2 in Ar	[45]
$LaCo_{0.5}Fe_{0.25}Mn_{0.25}O_3$	Orthorhombic	1130	600	10 % H_2 in He	660	600	10 % CO_2 in He	[75]
$LaFe_{0.5}Co_{0.25}Mn_{0.25}O_3$	Orthorhombic	1790	600	10 % H_2 in He	570	600	10 % CO_2 in He	[75]
$LaMn_{0.5}Co_{0.25}Fe_{0.25}O_3$	Orthorhombic	2170	600	10 % H_2 in He	815	600	10 % CO_2 in He	[75]
$LaM_{1-x}B_xO_3$								
$LaAlO_3$	-	68	1400	Ar	120	1000	50 % CO_2 in Ar	[34]
$La_{0.9}Sr_{0.1}Mn_{0.9}Al_{0.1}O_3$	-	52	1350	N_2	-	-	-	[36]
$La_{0.8}Sr_{0.2}Mn_{0.8}Al_{0.2}O_3$	-	75	1350	N_2	-	-	-	[36]
$La_{0.7}Sr_{0.3}Mn_{0.7}Al_{0.3}O_3$	-	98	1350	N_2	-	-	-	[36]
$La_{0.7}Sr_{0.3}Mn_{0.3}Al_{0.7}O_3$	Trigonal (*R3m*) & Hexagonal (P_{6_3}/mmc)	150	1350	N_2	-	-	-	[36]
$La_{0.5}Sr_{0.5}Mn_{0.75}Al_{0.25}O_3$	Rhombohedral (*R3c*)	225	1400	Ar	330	1100	40 % CO_2 in Ar	[84]

Material	Crystal Structure	Oxygen Evolution (μmol/g)	Reduction Temperature (°C)	Reduction Gas	Carbon Monoxide Production (μmol/g)	Oxidation Temperature (°C)	Oxidation Gas	Reference
$La_{0.5}Sr_{0.5}Mn_{0.65}Al_{0.35}O_3$	Rhombohedral (*R3c*)	247	1400	Ar	343	1100	40 % CO_2 in Ar	[84]
$La_{0.5}Sr_{0.5}Mn_{0.6}Al_{0.4}O_3$	Cubic (*Pm$\underline{3}$m*)	302	1400	Ar	200	1050	50 % CO_2 in Ar	[46]
$La_{0.5}Sr_{0.5}Mn_{0.5}Al_{0.5}O_3$	Cubic (*Pm$\underline{3}$m*) & Orthorhombic (*Pbam*)	358	1350	N_2	-	-	-	[36]
$La_{0.5}Sr_{0.5}Mn_{0.5}Al_{0.5}O_3$	Rhombohedral (*R3c*)	322	1400	Ar	388	1100	40 % CO_2 in Ar	[84]
$La_{0.4}Sr_{0.6}Mn_{0.6}Al_{0.4}O_3$	Cubic (*Pm$\underline{3}$m*) & Orthorhombic (*Pbam*)	491	1350	N_2	-	-	-	[36]
$La_{0.4}Sr_{0.6}Mn_{0.6}Al_{0.4}O_3$	-	-	1350	He	286	1000	40 % CO_2 in He	[82]
$La_{0.3}Sr_{0.7}Mn_{0.7}Al_{0.3}O_3$	Cubic (*Pm$\underline{3}$m*) & Orthorhombic (*Pbam*)	633	1350	N_2	-	-	-	[36]
$La_{0.6}Sr_{0.4}Mn_{0.8}Al_{0.2}O_3$	Hexagonal	239	1250	Ar	-	900	5% CO_2 in He	[83]
$La_{0.6}Sr_{0.4}Mn_{0.6}Al_{0.4}O_3$	-	310	1380	Ar	-	-	CO_2	[47]
$La_{0.6}Sr_{0.4}Mn_{0.6}Al_{0.4}O_3$	-	96	1350	N_2	-	-	-	[36]
$La_{0.6}Sr_{0.4}Mn_{0.6}Al_{0.4}O_3$	-	-	1350	He	294	1000	40 % CO_2 in He	[82]
$La_{0.6}Sr_{0.4}Mn_{0.6}Al_{0.4}O_3$	-	275	1330	Ar	-	-	CO_2	[47]
$La_{0.6}Sr_{0.4}Mn_{0.6}Al_{0.4}O_3$	-	220	1280	Ar	-	-	CO_2	[47]
$La_{0.6}Sr_{0.4}Mn_{0.6}Al_{0.4}O_3$	Hexagonal	277	1250	Ar	114	900	5% CO_2 in He	[83]
$La_{0.6}Sr_{0.4}Mn_{0.6}Al_{0.4}O_3$	-	190	1240	Ar	260	640	CO_2	[47]
$La_{0.6}Sr_{0.4}Mn_{0.6}Al_{0.4}O_3$	-	190	1240	Ar	240	840	CO_2	[47]
$La_{0.6}Sr_{0.4}Mn_{0.6}Al_{0.4}O_3$	-	190	1240	Ar	230	1040	CO_2	[47]

Material	Crystal Structure	Oxygen Evolution (μmol/g)	Reduction Temperature (°C)	Reduction Gas	Carbon Monoxide Production (μmol/g)	Oxidation Temperature (°C)	Oxidation Gas	Reference
$La_{0.6}Sr_{0.4}Mn_{0.6}Al_{0.4}O_3$	-	190	1240	Ar	100	1240	CO_2	[47]
$La_{0.5}Sr_{0.5}Mn_{0.5}Al_{0.5}O_3$	-	320	1400	Ar	192	1050	50 % in CO_2	[76]
$La_{0.6}Sr_{0.4}Mn_{0.5}Al_{0.5}O_3$	Hexagonal	318	1250	Ar	11	900	5% CO_2 in He	[83]
$La_{0.6}Sr_{0.4}Mn_{0.4}Al_{0.6}O_3$	Cubic (*Pm*$\underline{3}$*m*)	325	1350	N_2	-	-	-	[36]
$La_{0.6}Sr_{0.4}Mn_{0.4}Al_{0.6}O_3$	-	120	1350	He	247	1000	40 % CO_2 in He	[82]
$La_{0.6}Sr_{0.4}Mn_{0.4}Al_{0.6}O_3$	Hexagonal	314	1250	Ar	14	900	5% CO_2 in He	[83]
$La_{0.6}Sr_{0.4}Mn_{0.2}Al_{0.8}O_3$	Hexagonal	292	1250	Ar	-	900	5% CO_2 in He	[83]
$La_{0.5}Ca_{0.5}Mn_{0.6}Al_{0.4}O_3$	Cubic (*Pm*$\underline{3}$*m*)	449	1400	Ar	162	1050	50 % CO_2 in Ar	[46]
$La_{0.6}Ca_{0.4}Mn_{0.6}Al_{0.4}O_3$	-	315	1380	Ar	-	-	CO_2	[47]
$La_{0.6}Ca_{0.4}Mn_{0.6}Al_{0.4}O_3$	-	260	1330	Ar	-	-	CO_2	[47]
$La_{0.6}Ca_{0.4}Mn_{0.6}Al_{0.4}O_3$	-	210	1280	Ar	-	-	CO_2	[47]
$La_{0.6}Ca_{0.4}Mn_{0.6}Al_{0.4}O_3$	-	170	1240	Ar	240	640	CO_2	[47]
$La_{0.6}Ca_{0.4}Mn_{0.6}Al_{0.4}O_3$	-	170	1240	Ar	230	840	CO_2	[47]
$La_{0.6}Ca_{0.4}Mn_{0.6}Al_{0.4}O_3$	-	170	1240	Ar	220	1040	CO_2	[47]
$La_{0.6}Ca_{0.4}Mn_{0.6}Al_{0.4}O_3$	-	170	1240	Ar	85	1240	CO_2	[47]
$La_{0.6}Ca_{0.4}Mn_{0.8}Al_{0.2}O_3$	Orthorhombic	184	1300	Ar	-	-	-	[35]
$La_{0.8}Ca_{0.2}Mn_{0.6}Al_{0.4}O_3$	Orthorhombic (*Pnma*)	175	1400	Ar	-	-	-	[80]
$La_{0.6}Ca_{0.4}Mn_{0.5}Al_{0.5}O_3$	Orthorhombic (*Pnma*)	220	1400	Ar	-	-	-	[80]
$La_{0.4}Ca_{0.6}Mn_{0.4}Al_{0.6}O_3$	Orthorhombic (*Pnma*)	260	1400	Ar	-	-	-	[80]

Material	Crystal Structure	Oxygen Evolution (μmol/g)	Reduction Temperature (°C)	Reduction Gas	Carbon Monoxide Production (μmol/g)	Oxidation Temperature (°C)	Oxidation Gas	Reference
$La_{0.2}Ca_{0.8}Mn_{0.2}Al_{0.8}O_3$	Orthorhombic (*Pnma*)	420	1400	Ar	-	-	-	[80]
$La_{0.6}Ca_{0.4}Mn_{0.8}Ga_{0.2}O_3$	Orthorhombic	212	1300	Ar	-	-	-	[35]
$La_{0.6}Ca_{0.4}Mn_{0.8}Ga_{0.2}O_3$	Orthorhombic (*Pnma*)	307	1350	Ar	513	1050	50 CO_2 in Ar	[77]
$La_{0.5}Sr_{0.5}Mn_{0.8}Ga_{0.2}O_3$	Cubic (*Pm$\underline{3}$m*)	231	1400	Ar	195	1050	50 % CO_2 in Ar	[46]
$La_{0.5}Sr_{0.5}Mn_{0.75}Ga_{0.25}O_3$	Rhombohedral (*R3c*)	308	1400	Ar	481	1100	40 % CO_2 in Ar	[84]
$La_{0.5}Sr_{0.5}Mn_{0.65}Ga_{0.35}O_3$	Rhombohedral (*R3c*)	323	1400	Ar	447	1100	40 % CO_2 in Ar	[84]
$La_{0.5}Ca_{0.5}Mn_{0.8}Ga_{0.2}O_3$	Cubic (*Pm$\underline{3}$m*)	267	1400	Ar	215	1050	50 % CO_2 in Ar	[46]
$La_{0.5}Sr_{0.5}Mn_{0.9}Mg_{0.1}O_3$	Cubic (*Pm$\underline{3}$m*)	269	1400	Ar	214	1050	50 % CO_2 in Ar	[46]
$La_{0.5}Ca_{0.5}Mn_{0.9}Mg_{0.1}O_3$	Cubic (*Pm$\underline{3}$m*)	394	1400	Ar	154	1050	50 % CO_2 in Ar	[46]
$La_{0.5}Sr_{0.5}Mn_{0.9}Sc_{0.1}O_3$	Rhombohedral (*R3c*)	426	1400	Ar	491	1100	40 % CO_2 in Ar	[84]
$La_{0.5}Sr_{0.5}Mn_{0.95}Sc_{0.05}O_3$	Rhombohedral (*R3c*)	417	1400	Ar	545	1100	40 % CO_2 in Ar	[84]
$LaCo_{0.5}Ga_{0.5}O_3$	Orthorhombic (*Pbnm*) & Rhombohedral (*R3c*)	270	1350	Ar	-	-	-	[79]
$LaCo_{0.5}Ga_{0.5}O_3$	Orthorhombic (*Pbnm*) & Rhombohedral (*R3c*)	270	1350	Ar	-	-	-	[79]
$LaCo_{0.6}Ga_{0.4}O_3$	Orthorhombic (*Pbnm*) & Rhombohedral (*R3c*)	320	1350	Ar	-	-	-	[79]
Supported Perovskites								
$La_{0.75}Sr_{0.25}FeO_3$	Orthorhombic	2210	950	10 % H_2 in He	690	950	10 % CO_2 in He	[89]
$La_{0.75}Sr_{0.25}FeO_3$ / CeO_2 (1:3)	Orthorhombic	1720	950	10 % H_2 in He	1100	950	10 % CO_2 in He	[89]

Material	Crystal Structure	Oxygen Evolution (μmol/g)	Reduction Temperature (°C)	Reduction Gas	Carbon Monoxide Production (μmol/g)	Oxidation Temperature (°C)	Oxidation Gas	Reference
$La_{0.75}Sr_{0.25}FeO_3$ /ZrO_2 (1:3)	Orthorhombic	2040	950	10 % H_2 in He	1350	950	10 % CO_2 in He	[89]
$La_{0.75}Sr_{0.25}FeO_3$ / Al_2O_3 (1:3)	Orthorhombic	2920	950	10 % H_2 in He	490	950	10 % CO_2 in He	[89]
$La_{0.75}Sr_{0.25}FeO_3$ / SiO_2 (1:3)	Orthorhombic	3690	950	10 % H_2 in He	1700	950	10 % CO_2 in He	[89]
$La_{0.75}Sr_{0.25}FeO_3$ / TiO_2 (1:3)	Orthorhombic	2180	950	10 % H_2 in He	850	950	10 % CO_2 in He	[89]
$La_{0.75}Sr_{0.25}FeO_3$ / SiC (1:3)	Orthorhombic	2910	950	10 % H_2 in He	1200	950	10 % CO_2 in He	[88]
$La_{0.75}Sr_{0.25}FeO_3$ / SiO_2 (1:1)	Orthorhombic	1250	950	10 % H_2 in He	380	950	10 % CO_2 in He	[88]
$La_{0.75}Sr_{0.25}FeO_3$ / SiO_2 (3:1)	Orthorhombic	1540	950	10 % H_2 in He	530	950	10 % CO_2 in He	[88]
$LaFeO_3$ /SiO_2 (1:3)	Orthorhombic	96	1300	Ar	80	1100	CO_2	[67]
$SrFeO_3$ /SiO_2 (1:3)	Orthorhombic	64	1300	Ar	68	1100	CO_2	[67]
$La_{0.7}Sr_{0.3}FeO_3$ /SiO_2 (1:3)	Orthorhombic	256	1300	Ar	112	1100	CO_2	[67]
$La_{0.7}Ce_{0.3}FeO_3$ /SiO_2 (1:3)	Orthorhombic	188	1300	Ar	128	1100	CO_2	[67]
$LaFe_{0.9}Co_{0.1}O_3$ /SiO_2 (1:3)	Orthorhombic	148	1300	Ar	88	1100	CO_2	[67]
$LaFe_{0.7}Co_{0.3}O_3$ /SiO_2 (1:3)	Orthorhombic	216	1300	Ar	240	1100	CO_2	[67]
$LaFe_{0.7}Co_{0.3}O_3$ /SiO_2 (1:3)	Orthorhombic	64	1200	Ar	16	1100	CO_2	[67]
$LaFe_{0.7}Co_{0.3}O_3$ /SiO_2 (1:3)	Orthorhombic	252	1400	Ar	152	1100	CO_2	[67]
$LaFe_{0.5}Co_{0.5}O_3$ /SiO_2 (1:3)	Orthorhombic	272	1300	Ar	256	1100	CO_2	[67]
$LaFe_{0.7}Mn_{0.3}O_3$ /SiO_2 (1:3)	Orthorhombic	276	1300	Ar	210	1100	CO_2	[67]

3.5 Concluding Remarks

This review provides an overview of the research conducted on the lanthanum manganite perovskite family and their use in the thermochemical splitting of carbon dioxide into carbon monoxide. Far more is known about the mechanism of action of reduction at the various scales, electronic, orbital, molecular and structural, than is known for oxidation. A few potential approaches to effectively increase the reactivity are:

- increasing the oxidation state of the transition metal by doping with lower valence elements.
- one electron in the transition metals' e_g orbitals before reduction and zero electrons in these orbitals before oxidation.
- a large size mismatch between elements to increase the tilting of the TMO_6 octahedra, facilitating the breaking or formation of the TM-O bond.
- the addition of non-redox active metals to increase the resistance to sintering, improving cycling.

This review also provides a summary of the many lanthanum manganites in the literature, as summarised in Table 3.5. This can serve as a reference for those wishing to understand the research that has already been undertaken in this field and should allow for new combinations of elements to be trialled, based upon the factors summarised above. The table also demonstrates the wide range of experimental conditions applied in the literature. The research base would benefit from consistency of conditions and reporting methods. Further research should focus on understanding the mechanism of the oxidation reaction, which should uncover new ways to increase the carbon monoxide yields and increase overall cycling efficiency. Finally, methods of decreasing the reduction and oxidation temperatures should be researched as a way of reducing the energy consumption and therefore costs per cycle, and to minimise degradation due to sintering during repeated cycling.

3.6 References

[1] Marxer D, Furler P, Scheffe J, Geerlings H, Falter C, Batteiger V, et al. Demonstration of the Entire Production Chain to Renewable Kerosene via Solar Thermochemical Splitting of H_2O and CO_2. Energy and Fuels 2015;29:3241–50.

[2] Fischer F, Tropsch H. Process for the production of paraffin-hydrocarbons with more than one carbon atom. U.S Patent 1746464, 1930.

[3] Tountas AA, Peng X, Tavasoli A V, Duchesne PN, Dingle TL, Dong Y, et al. Towards Solar Methanol: Past, Present, and Future. Adv Sci 2019;6. doi:10.1002/advs.201801903.

[4] Pregger T, Schiller G, Cebulla F, Dietrich R, Maier S, Thess A, et al. Renewable Synthetic Fuels. Energies 2020;13:1–36.

[5] Mallapragada DS, Singh NR, Curteanu V, Agrawal R. Sun-to-fuel assessment of routes for fixing CO_2 as liquid fuel. Ind Eng Chem Res 2013;52:5136–44.

[6] Patterson BD, Mo F, Borgschulte A, Hillestad M, Joos F, Kristiansen T, et al. Renewable CO2 recycling and synthetic fuel production in a marine environment. Proc Natl Acad Sci U S A 2019;116:12212–9. doi:10.1073/pnas.1902335116.

[7] McKenna RC, Norman JB. Spatial modelling of industrial heat loads and recovery potentials in the UK. Energy Policy 2010;38:5878–91.

[8] Brueckner S, Miró L, Cabeza LF, Pehnt M, Laevemann E. Methods to estimate the industrial waste heat potential of regions - A categorization and literature review. Renew Sustain Energy Rev 2014;38:164–71. doi:10.1016/j.rser.2014.04.078.

[9] Papapetrou M, Kosmadakis G, Cipollina A, La Commare U, Micale G. Industrial waste heat: Estimation of the technically available resource in the EU per industrial sector, temperature level and country. Appl Therm Eng 2018;138:207–16. doi:10.1016/j.applthermaleng.2018.04.043.

[10] Kosmadakis G. Estimating the potential of industrial (high-temperature) heat pumps for exploiting waste heat in EU industries. Appl Therm Eng 2019;156:287–98.

[11] Broberg Viklund S, Johansson MT. Technologies for utilization of industrial excess heat: Potentials for energy recovery and CO2 emission reduction. Energy Convers

Manag 2014;77:369–79. doi:10.1016/j.enconman.2013.09.052.

[12] Marxer D, Furler P, Takacs M, Steinfeld A. Solar thermochemical splitting of CO2 into separate streams of CO and O2 with high selectivity, stability, conversion, and efficiency. Energy Environ Sci 2017;10:1142–9. doi:10.1039/c6ee03776c.

[13] Scheffe JR, Steinfeld A. Oxygen exchange materials for solar thermochemical splitting of H_2O and CO_2: A review. Mater Today 2014;17:341–8. doi:10.1016/j.mattod.2014.04.025.

[14] Kodama T, Gokon N. Thermochemical cycles for high-temperature solar hydrogen production. Chem Rev 2007;107:4048–77.

[15] Voitic G, Hacker V. Recent advancements in chemical looping water splitting for the production of hydrogen. RSC Adv 2016;6:98267–96. doi:10.1039/c6ra21180a.

[16] Safari F, Dincer I. A review and comparative evaluation of thermochemical water splitting cycles for hydrogen production. Energy Convers Manag 2020;205:112182. doi:10.1016/j.enconman.2019.112182.

[17] Prieto C, Cooper P, Fernández AI, Cabeza LF. Review of technology: Thermochemical energy storage for concentrated solar power plants. Renew Sustain Energy Rev 2016;60:909–29. doi:10.1016/j.rser.2015.12.364.

[18] Carrillo AJ, Joségonzaíez-Aguilar J, Romero M, Coronado JM, González-Aguilar J, Romero M, et al. Solar Energy on Demand: A Review on High Temperature Thermochemical Heat Storage Systems and Materials. Chem Rev 2019;119:4777–816. doi:10.1021/acs.chemrev.8b00315.

[19] André L, Abanades S, Flamant G. Screening of thermochemical systems based on solid-gas reversible reactions for high temperature solar thermal energy storage. Renew Sustain Energy Rev 2016;64:703–15. doi:10.1016/j.rser.2016.06.043.

[20] Steinfeld A. Solar thermochemical production of hydrogen - A review. Sol Energy 2005;78:603–15. doi:10.1016/j.solener.2003.12.012.

[21] Pardo P, Deydier A, Anxionnaz-Minvielle Z, Rougé S, Cabassud M, Cognet P. A review on high temperature thermochemical heat energy storage. Renew Sustain Energy Rev 2014;32:591–610. doi:10.1016/j.rser.2013.12.014.

[22] Hu J, Galvita V V., Poelman H, Marin GB. Advanced chemical looping materials for CO_2 utilization: A review. Materials (Basel) 2018;11:1187, 1–32. doi:10.3390/ma11071187.

[23] Luo M, Yi Y, Wang S, Wang Z, Du M, Pan J, et al. Review of hydrogen production using chemical-looping technology. Renew Sustain Energy Rev 2018;81:3186–214. doi:10.1016/j.rser.2017.07.007.

[24] Orfila M, Linares M, Molina R, Botas JÁ, Sanz R, Marugán J. Perovskite materials for hydrogen production by thermochemical water splitting. Int J Hydrogen Energy 2016;41:19329–38. doi:10.1016/J.IJHYDENE.2016.07.041.

[25] Kubicek M, Bork AH, Rupp JLM. Perovskite oxides-a review on a versatile material class for solar-to-fuel conversion processes. J Mater Chem A 2017;5:11983–2000. doi:10.1039/c7ta00987a.

[26] Ishihara T. Perovskite Oxide Solid Oxide Fuel Cells. New York: Springer; 2009.

[27] Nakamura T, Petzow G, Gauckler LJ. Stability of the perovskite phase LaBO3 (B = V, Cr, Mn, Fe, Co, Ni) in reducing atmosphere I. Experimental results. Mater Res Bull 1979;14:649–59. doi:10.1016/0025-5408(79)90048-5.

[28] Mizusaki J, Sasamoto T, Cannon W, Kent Bowen H. Electronic Conductivity, Seebeck Coefficient, and Defect Structure of LaFe03. J Am Ceram Soc 1982;65:363–8.

[29] Ishigaki T, Yamauchi S, Mizusaki J, Fueki K, Naito H, Adachi T. Diffusion of oxide ions in LaFeO3 single crystal. J Solid State Chem 1984;55:50–3. doi:10.1016/0022-4596(84)90246-9.

[30] Mizusaki J, Yamauchi S, Fueki K, Ishikawa A. Nonstoichiometry of the perovskite-type oxide La1-xSrxCrO3-δ. Solid State Ionics 1984;12:119–24. doi:10.1016/0167-2738(84)90138-3.

[31] Matsuura T. Single-Crystal Growth of Perovskite-Type La1- xSrxMO3 (M=Fe, Co) Solid Solutions. Jpn J Appl Phys 1984;23:1172–5. doi:10.7868/s0002337x15100048.

[32] Yamaguchi KS, Sawyer DT. The Redox Chemistry of Manganese(III) and -(IV) Complexes. Isr J Chem 1985;25:164–76.

[33] Riaz A, Kreider P, Kremer F, Tabassum H, Yeoh JS, Lipiński WL, et al. Electrospun

Manganese-Based Perovskites as Efficient Oxygen Exchange Redox Materials for Improved Solar Thermochemical CO 2 Splitting. ACS Appl Energy Mater 2019;2:2494–505. doi:10.1021/acsaem.8b01994.

[34] Takalkar G, Bhosale RR, AlMomani F, Kumar A, Banu A, Ashok A, et al. Thermochemical splitting of CO2 using solution combustion synthesized LaMO3 (where, M = Co, Fe, Mn, Ni, Al, Cr, Sr). Appl Surf Sci 2020;509:144908. doi:10.1016/j.apsusc.2019.144908.

[35] Wang L, Al-Mamun M, Zhong YL, Jiang L, Liu P, Wang Y, et al. Ca 2+ and Ga 3+ doped LaMnO 3 perovskite as a highly efficient and stable catalyst for two-step thermochemical water splitting. Sustain Energy Fuels 2017;1:1013–7. doi:10.1039/C6SE00097E.

[36] Gokon N, Hara K, Sugiyama Y, Bellan S, Kodama T, Hyun-seok C. Thermochemical two-step water splitting cycle using perovskite oxides based on LaSrMnO3 redox system for solar H2 production. Thermochim Acta 2019;680:178374. doi:10.1016/j.tca.2019.178374.

[37] Demont A, Abanades S. High redox activity of Sr-substituted lanthanum manganite perovskites for two-step thermochemical dissociation of CO2. RSC Adv 2014;4:54885–91. doi:10.1039/c4ra10578h.

[38] Demont A, Abanades S, Beche E. Investigation of perovskite structures as oxygen-exchange redox materials for hydrogen production from thermochemical two-step water-splitting cycles. J Phys Chem C 2014;118:12682–92. doi:10.1021/jp5034849.

[39] R. Raffaelle, H. U. Anderson, D. M. Sparlin and PEP. Transport Anomalies in the High-Temperature Hopping Conductivity and Thermopower of Sr-doped La(Cr,Mn)O3. Phys Rev B - Condens Matter Mater Phys 1991;43:7991–9.

[40] Bucher E, Sitte W, Caraman GB, Cherepanov VA, Aksenova T V., Ananyev M V. Defect equilibria and partial molar properties of (La,Sr)(Co,Fe)O3-δ. Solid State Ionics 2006;177:3109–15. doi:10.1016/j.ssi.2006.07.062.

[41] Yasuda I, Hishinuma M. Electrical conductivity and chemical diffusion coefficient of strontium-doped lanthanum manganites. J Solid State Chem 1996;123:382–90. doi:10.1006/jssc.1996.0193.

[42] Wang L, Al-Mamun M, Zhong YL, Liu P, Wang Y, Yang HG, et al. Enhanced Thermochemical Water Splitting through Formation of Oxygen Vacancy in La 0.6 Sr 0.4 BO 3− δ (B=Cr, Mn, Fe, Co, and Ni) Perovskites. Chempluschem 2018;83:924–8. doi:10.1002/cplu.201800178.

[43] Dey S, Naidu BS, Govindaraj A, Rao CNR. Noteworthy performance of La1-xCaxMnO3 perovskites in generating H2 and CO by the thermochemical splitting of H2O and CO2. Phys Chem Chem Phys 2015;17:122–5. doi:10.1039/c4cp04578e.

[44] Dey S, Naidu BS, Rao CNR. Ln 0.5 A 0.5 MnO 3 (Ln=Lanthanide, A= Ca, Sr) Perovskites Exhibiting Remarkable Performance in the Thermochemical Generation of CO and H 2 from CO 2 and H 2 O. Chem - A Eur J 2015;21:7077–81. doi:10.1002/chem.201500442.

[45] Nair MM, Abanades S. Experimental screening of perovskite oxides as efficient redox materials for solar thermochemical CO 2 conversion. Sustain Energy Fuels 2018;2:843–54. doi:10.1039/C7SE00516D.

[46] Jouannaux J, Haeussler A, Drobek M, Ayral A, Abanades S, Julbe A. Lanthanum manganite perovskite ceramic powders for CO2 splitting: Influence of Pechini synthesis parameters on sinterability and reactivity. Ceram Int 2019;45:15636–48. doi:10.1016/j.ceramint.2019.05.075.

[47] Cooper T, Scheffe JR, Galvez ME, Jacot R, Patzke G, Steinfeld A. Lanthanum Manganite Perovskites with Ca/Sr A-site and Al B-site Doping as Effective Oxygen Exchange Materials for Solar Thermochemical Fuel Production. Energy Technol 2015;3:1130–42.

[48] Dey S, Rao CNR. Splitting of CO 2 by Manganite Perovskites to Generate CO by Solar Isothermal Redox Cycling. ACS Energy Lett 2016;1:237–43. doi:10.1021/acsenergylett.6b00122.

[49] Luciani G, Landi G, Aronne A, Di Benedetto A. Partial substitution of B cation in La0.6Sr0.4MnO3 perovskites: A promising strategy to improve the redox properties useful for solar thermochemical water and carbon dioxide splitting. Sol Energy 2018;171:1–7. doi:10.1016/j.solener.2018.06.058.

[50] Yang C-K, Yamazaki Y, Aydin A, Haile SM. Thermodynamic and kinetic assessments of strontium-doped lanthanum manganite perovskites for two-step thermochemical water splitting. J Mater Chem A 2014;2:13612–23. doi:10.1039/C4TA02694B.

[51] Bork AH, Povoden-Karadeniz E, Rupp JLM. Modeling Thermochemical Solar-to-Fuel Conversion: CALPHAD for Thermodynamic Assessment Studies of Perovskites, Exemplified for (La,Sr)MnO3. Adv Energy Mater 2017;7:1601086. doi:10.1002/aenm.201601086.

[52] Deml AM, Stevanović V, Muhich CL, Musgrave CB, O'Hayre R. Oxide enthalpy of formation and band gap energy as accurate descriptors of oxygen vacancy formation energetics. Energy Environ Sci 2014;7:1996–2004. doi:10.1039/c3ee43874k.

[53] Nair MM, Abanades S. Correlating oxygen mobility with thermochemical CO 2 - splitting efficiency in A-site substituted manganite perovskites. Sustain Energy Fuels 2021;5:4570–4. doi:10.1039/D1SE00950H.

[54] Kim Y, Jeong SJ, Koo B, Lee S, Kwak NW, Jung W. Study of the surface reaction kinetics of (La,Sr)MnO3-δ oxygen carriers for solar thermochemical fuel production. J Mater Chem A 2018;6:13082–9. doi:10.1039/c8ta01939h.

[55] Babiniec S, Coker E, Miller J, Ambrosini A. Doped calcium manganites for advanced high- temperature thermochemical energy storage. Int J ENERGY Res 2015;40:280–4. doi:10.1002/er.

[56] Wang L, Al-Mamun M, Liu P, Zhong YL, Wang Y, Yang HG, et al. Enhanced Thermochemical H2 Production on Ca-Doped Lanthanum Manganite Perovskites Through Optimizing the Dopant Level and Re-oxidation Temperature. Acta Metall Sin English Lett 2018;31:431–9.

[57] Demont A, Abanades S. Solar thermochemical conversion of CO2 into fuel via two-step redox cycling of non-stoichiometric Mn-containing perovskite oxides. J Mater Chem A 2015;3:3536–46. doi:10.1039/c4ta06655c.

[58] Li Z, Yang M, Park JS, Wei SH, Berry JJ, Zhu K. Stabilizing Perovskite Structures by Tuning Tolerance Factor: Formation of Formamidinium and Cesium Lead Iodide Solid-State Alloys. Chem Mater 2016;28:284–92. doi:10.1021/acs.chemmater.5b04107.

[59] Shannon RD. Revised Effective Ionic Radii and Systematic Studies of Interatomic Distances in Halides and Chalcogenides. Acta Crystallogr 1976;A32:751–67.

[60] Bakken E, Norby T, Stølen S. Redox energetics of perovskite-related oxides. J Mater Chem 2002;12:317–23. doi:10.1039/b106422n.

[61] Douglas BE. The lanthanide contraction. J Chem Educ 1954;31:598–9. doi:10.1021/ed031p598.

[62] Woodward PM, Vogt T, Cox DE, Arulraj A, Rao CNR, Karen P, et al. Influence of Cation Size on the Structural Features of Ln1/2A1/2MnO3Perovskites at Room Temperature. Chem Mater 1998;10:3652–65. doi:10.1021/cm980397u.

[63] Atsumi T, Ohgushi T, Namikata H, Kamegashira N. Oxygen nonstoichiometry of LnMnO3-δ (Ln = La, Pr, Nd, Sm and Y). J Alloys Compd 1997;252:67–70. doi:10.1016/S0925-8388(96)02610-2.

[64] Takalkar G, Bhosale RR. Solar thermocatalytic conversion of CO2 using PrxSr(1−x)MnO3−Δ perovskites. Fuel 2019;254:115624. doi:10.1016/j.fuel.2019.115624.

[65] Aruna ST, Muthuraman M, Patil KC. Combustion synthesis and properties of strontium substituted lanthanum manganites La1−xSrxMnO3 (0 ≤ x ≤ 0.3). J Mater Chem 1997;7:2499–503. doi:10.1039/a703901h.

[66] Royer S, Alamdari H, Duprez D, Kaliaguine S. Oxygen storage capacity of La1-xA′xBO 3 perovskites (with A′ = Sr, Ce; B = Co, Mn) - Relation with catalytic activity in the CH4 oxidation reaction. Appl Catal B Environ 2005;58:273–88. doi:10.1016/j.apcatb.2004.12.010.

[67] Jiang Q, Tong J, Zhou G, Jiang Z, Li Z, Li C. Thermochemical CO_2 splitting reaction with supported $La_xA_{1-x}Fe_yB_{1-y}O_3$ (A=Sr, Ce, B=Co, Mn; 0≤x, y≤1) perovskite oxides. Sol Energy 2014;103:425–37. doi:10.1016/j.solener.2014.02.033.

[68] Belous A, V'yunov O, Pashkova E, Yanchevskii O, Tovstolytkin A, Pogorelyi A. Effects of Chemical Composition and Sintering Temperature on the Structure of La 1 –

x Sr x MnO 3 ± g Solid Solutions. Inorg Mater 2003;39:161–70. doi:10.1023/A.

[69] Suntivich J, May KJ, Gasteiger HA, Goodenough JB, Shao-Horn Y. A perovskite oxide optimized for oxygen evolution catalysis from molecular orbital principles. Science 2011;334:1383–5. doi:10.1126/science.1212858.

[70] Wang L, Ma T, Dai S, Ren T, Chang Z, Dou L, et al. Experimental study on the high performance of Zr doped LaCoO3 for solar thermochemical CO production. Chem Eng J 2020;389:124426. doi:10.1016/j.cej.2020.124426.

[71] Ambrosini A, Garino T, Nenoff TM. Synthesis and characterization of the double-substituted perovskites LaxSr1-xCo1-yMnyO3-δ for use in high-temperature oxygen separations. Solid State Ionics 2006;177:2275–9. doi:10.1016/j.ssi.2006.05.023.

[72] Babiniec SM, Coker EN, Miller JE, Ambrosini A. Investigation of LaxSr1-xCoyM1-yO3-δ (M=Mn, Fe) perovskite materials as thermochemical energy storage media. Sol Energy 2015;118:451–9. doi:10.1016/j.solener.2015.05.040.

[73] Budiman RA, Bagarinao KD, Ishiyama T, Kishimoto H, Yamaji K, Horita T, et al. Influence of Sr and Co deficiency on the transport properties and oxygen reduction reaction of La0.6Sr0.4Co0.2Fe0.8O3-δ. Solid State Ionics 2020;348:115285. doi:10.1016/j.ssi.2020.115285.

[74] Duranti L, Natali Sora I, Zurlo F, Luisetto I, Licoccia S, Di Bartolomeo E. The role of manganese substitution on the redox behavior of La0.6Sr0.4Fe0.8Mn0.2O3-δ. J Eur Ceram Soc 2020;40:4076–83. doi:10.1016/j.jeurceramsoc.2020.04.017.

[75] Ramos AE, Maiti D, Daza YA, Kuhn JN, Bhethanabotla VR. Co, Fe, and Mn in La-perovskite oxides for low temperature thermochemical CO2 conversion. Catal Today 2019;338:52–9.

[76] Nair MM, Abanades S. Insights into the Redox Performance of Non-stoichiometric Lanthanum Manganite Perovskites for Solar Thermochemical CO 2 Splitting. ChemistrySelect 2016;1:4449–57. doi:10.1002/slct.201601171.

[77] Liu X, Wang T, Gao K, Meng X, Xu Q, Song C, et al. Ca- And Ga-Doped LaMnO3for Solar Thermochemical CO2Splitting with High Fuel Yield and Cycle Stability. ACS Appl Energy Mater 2021;2021. doi:10.1021/acsaem.1c01274.

[78] Patrakeev M V., Mitberg EB, Lakhtin AA, Leonidov IA, Kozhevnikov VL, Kharton V

V., et al. Oxygen nonstoichiometry, conductivity, and Seebeck coefficient of La0.3Sr0.7Fe1-xGaxO 2.65+δ perovskites. J Solid State Chem 2002;167:203–13. doi:10.1006/jssc.2002.9644.

[79] Chen Z, Jiang Q, Cheng F, Tong J, Yang M, Jiang Z, et al. Sr- and Co-doped LaGaO 3−δ with high O 2 and H 2 yields in solar thermochemical water splitting. J Mater Chem A 2019;7:6099–112. doi:10.1039/C8TA11957K.

[80] Wang L, Al-Mamun M, Liu P, Wang Y, Yang HG, Zhao H. La1-xCaxMn1-yAlyO3 perovskites as efficient catalysts for two-step thermochemical water splitting in conjunction with exceptional hydrogen yields. Cuihua Xuebao/Chinese J Catal 2017;38:1079–86. doi:10.1016/S1872-2067(17)62820-1.

[81] Sowjanya C, Mandal R, Pratihar SK. Grain size dependent electrical conductivity, chemical surface exchange and bulk diffusion coefficient of La0.5Sr0.5Al0.2Fe0.8O3-δ. J Alloys Compd 2020;818:152831. doi:10.1016/j.jallcom.2019.152831.

[82] McDaniel AH, Miller EC, Arifin D, Ambrosini A, Coker EN, O'Hayre R, et al. Sr- and Mn-doped LaAlO3-δ for solar thermochemical H 2 and CO production. Energy Environ Sci 2013;6:2424–8. doi:10.1039/c3ee41372a.

[83] Sastre D, Carrillo AJ, Serrano DP, Pizarro P, Coronado JM. Exploring the Redox Behavior of La0.6Sr0.4Mn1−xAlxO3 Perovskites for CO2−Splitting in Thermochemical Cycles. Top Catal 2017;60:1108–18. doi:10.1007/s11244−017−0790−4.

[84] Dey S, Naidu BS, Rao CNR. Beneficial effects of substituting trivalent ions in the B-site of La 0.5 Sr 0.5 Mn 1−x A x O 3 (A = Al, Ga, Sc) on the thermochemical generation of CO and H 2 from CO 2 and H 2 O. Dalt Trans 2016;45:2430–5. doi:10.1039/C5DT04822B.

[85] Fu M, Wang L, Ma T, Ma H, Xu H, Li X. Mechanism of CO production around oxygen vacancy of LaMnO3: An efficient and rapid evaluation of the doping effect on the kinetics and thermodynamic driving force of CO2-splitting. J Mater Chem A 2020;8:1709–16. doi:10.1039/c9ta09764c.

[86] Carrillo AJ, Bork AH, Moser T, Sediva E, Hood ZD, Rupp JLM. Modifying La0.6Sr0.4MnO3 Perovskites with Cr Incorporation for Fast Isothermal CO2-Splitting

Kinetics in Solar-Driven Thermochemical Cycles. Adv Energy Mater 2019;9:1–13. doi:10.1002/aenm.201803886.

[87] Daza YA, Kent RA, Yung MM, Kuhn JN. Carbon dioxide conversion by reverse water-gas shift chemical looping on perovskite-type oxides. Ind Eng Chem Res 2014;53:5828–37. doi:10.1021/ie5002185.

[88] Hare BJ, Maiti D, Daza YA, Bhethanabotla VR, Kuhn JN. Enhanced CO2 Conversion to CO by Silica-Supported Perovskite Oxides at Low Temperatures. ACS Catal 2018;8:3021–9. doi:10.1021/acscatal.7b03941.

[89] Hare BJ, Maiti D, Ramani S, Ramos AE, Bhethanabotla VR, Kuhn JN. Thermochemical conversion of carbon dioxide by reverse water-gas shift chemical looping using supported perovskite oxides. Catal Today 2018;323:225–32.

[90] Takalkar G, Bhosale RR, AlMomani F, Rashid S, Qiblawey H, Saleh Saad MA, et al. Thermochemical splitting of CO2 using solution combustion synthesized lanthanum–strontium–manganese perovskites. Fuel 2021;285:119154. doi:10.1016/j.fuel.2020.119154.

[91] Shrestha P, Nair MM, Mahinpey N. Isothermal redox cycling of A- and B-site substituted manganite-based perovskites for CO2 conversion. Can J Chem Eng 2021:1–11. doi:10.1002/cjce.24019.

[92] Muraleedharan Nair M, Abanades S. Solid-State Reoxidation Kinetics of A/B-Site Substituted LaMnO 3 During Solar Thermochemical CO 2 Conversion. Energy Technol 2021;9:2000885. doi:10.1002/ente.202000885.

[93] Wang L, Al-Mamun M, Liu P, Wang Y, Yang HG, Zhao H. Notable hydrogen production on LaxCa1-xCoO3 perovskites via two-step thermochemical water splitting. J Mater Sci 2018;53:6796–806. doi:10.1007/s10853-018-2004-2.

Chapter 4 – CARBON DIOXIDE DECOMPOSITION THROUGH GAS EXCHANGE IN BARIUM CALCIUM IRON NIOBATES

4.1 Abstract

A number of metal oxides and perovskites are capable of being reduced at high temperatures and then re-oxidised in the presence of CO_2 or H_2O to form CO or H_2. Barium calcium iron niobates have been found to be redox-active in this way. The redox activity of these perovskites was explored, and the chemical and physical stability was investigated using EDX and SEM imaging, respectively. The most promising, $Ba_2Ca_{0.66}Nb_{0.34}FeO_{6-\delta}$ (BCNF1), showed mass changes of 0.45% after five cycles of reduction with N_2 and re-oxidation with 10% CO_2. BCNF1 is chemically stable as it shows no changes in XRD and no evidence of sintering, although cracking of the pellets was observed after re-oxidation. The low enthalpy of re-oxidation of BCNF1 coupled with the high and sustained mass change makes this perovskite suitable for chemical looping use for energy storage and conversion systems.

This chapter has been published in Catalysis Today as an article of the same name. H. Kildahl is the first author of the paper, responsible for the experimental work completed, data analysis undertaken and the production of a full draft. The co-authors are responsible for the supervision, conceptualisation and/or editing. The citation for this article is

H. Kildahl, Z. Li, H. Cao, P. Slater, Y. Ding, Carbon dioxide decomposition through gas exchange in barium calcium iron niobates, Catal. Today. 364 (2021) 211–219. https://doi.org/10.1016/j.cattod.2020.05.024.

4.2 Introduction

With the shift towards a 100% renewable future well underway, there are still areas where gains in efficiency and minimisation of losses can be made. One of these areas is industrial waste heat. There are many industries which require heat such as chemicals, food and drink, textiles, and metal processing. The 28 members of the European Union required 1820 TWh of energy as heat across all industries in 2018, which amounts to around 70% of total energy consumption by industry [1]. More than 48% of this heat is over 500 °C with up to 28% hotter than 1000 °C. The iron and steel industries are particularly attractive for waste heat recovery or usage since the temperatures can be up to 2000 °C [2]. Industrial-scale demonstrations have been built to store the waste heat as thermal energy for reuse in industrial/domestic heating [3]. A recently proposed novel concept of exploiting this waste heat is to use a thermochemical cycle where changes in temperature are used to decompose small molecules such as CO_2 or H_2O into CO and H_2 [4]. Carbon monoxide and hydrogen can be used as syngas for the Fischer-Tropsch process, to produce essential chemicals without the need for crude oil [5], or as a fuel in a fuel cell device. The iron and steel industries also have high CO_2 emissions, such as 1.89 tonnes of CO_2 per tonne of product produced in a blast furnace [6]. Therefore, both heat and increased CO_2 concentrations could be found in these industries, which would be ideal for the implementation of a thermochemical material and help to reduce direct emissions. CO production from carbon dioxide by a thermochemical cycle was found to be more than 2.5 times more efficient than algae-based biomass conversions when using waste heat from industry [7].

A thermochemical cycle works through the addition of heat, causing reduction of the material. Oxygen is released from the material resulting in the formation of oxygen vacancies throughout the structure (Equation 4.1). Upon the addition of CO_2 or H_2O, the material is re-oxidised, often at a lower temperature, and the oxygen vacancies are filled while CO or H_2 is released

(Equation 4.2). As can be seen from Equations (4.1) and (4.2), fuel production is increased with an increase in the oxygen non-stoichiometry, δ. Therefore, the efficiency and fuel production yields can be increased by aiding the diffusion of gases throughout the material. If oxygen is lost throughout the material rather than only on the surface, more oxygen vacancies can be formed. This greater level of reduction leads to deeper oxidation as there are more oxygen vacancies to be filled. This leads to a greater decomposition of CO_2 or H_2O and therefore greater fuel production. The diffusion of gases within the material can be aided by increases in porosity or surface area to volume ratio.

$$MO_y \rightarrow MO_{y-\delta} + \frac{\delta}{2} O_2 \tag{4.1}$$

$$MO_{y-\delta} + \delta CO_2 \rightarrow MO_y + \delta CO \tag{4.2}$$

The two main classes of materials capable of undergoing a thermochemical cycle are simple metal oxides or mixed metal oxides, such as perovskites. Of the simple metal oxides, the most researched is ceria (cerium oxide) which can split both carbon dioxide and water with good yields; however, it requires high temperatures such as 1400 °C for reduction and 900 °C for oxidation [8]. Ceria is a non-stoichiometric oxygen carrier meaning that less than one mole of oxygen is released per mole of ceria. Other metal oxides include volatile metal oxides and iron oxides. Volatile metal oxides are stoichiometric oxygen carriers and have melting temperatures of the pure metal lower than the reduction temperature of the metal oxide. For example, ZnO has a reduction temperature of 2000 °C but a melting temperature of 420 °C, meaning that the gaseous zinc must be quenched quickly to avoid recombination with oxygen [9]. Pure iron oxide (Fe_3O_4) can be reduced at 2200 °C; however, it can be oxidised easily by water at 175 °C [10].

Perovskites are non-stoichiometric mixed metal oxides with an ideal formula of ABO_3. The most researched perovskite for thermochemical cycles is the $La_{1-x}Sr_xMnO_3$ family, which can be reduced at about 1400 °C and oxidised at around 900 °C with up to ten times higher fuel yields than ceria [11]. $Ba_2Ca_{0.66}Nb_{1.34-x}Fe_xO_6$ (x = 0, 0.34, 0.66 and 1) is a double perovskite-type and can be reduced and made to decompose CO_2 at 700 °C [12]. This paper will investigate the barium calcium iron niobate perovskite family for their ability to split carbon dioxide at 700 °C. The redox activity of these materials will be measured predominantly by mass change during the thermochemical cycles along with tracking of changes to the crystal structure and surface morphology during the reaction.

4.3 Experimental

4.3.1 Material Synthesis

$Ba_2Ca_{0.66}Nb_{1.34-x}Fe_xO_6$ perovskites were synthesised through a solid-state reaction as performed previously [12]. Four perovskites were synthesised by varying the concentrations of niobium and iron in the B-site while maintaining the concentration of calcium in the B-site and barium in the A-site. The four perovskites tested are $Ba_2Ca_{0.66}Nb_{1.34}O_{6-\delta}$ (x = 0, named BCNF0), $Ba_2Ca_{0.66}NbFe_{0.34}O_{6-\delta}$ (x = 0.34, named BCNF0.34), $Ba_2Ca_{0.66}Nb_{0.68}Fe_{0.66}O_{6-\delta}$ (x = 0.66, named BCNF0.66) and $Ba_2Ca_{0.66}Nb_{0.34}FeO_{6-\delta}$ (x = 1, named BCNF1). Stoichiometric ratios of the precursors ($BaCO_3$ (Alfa Aesar, 99%), $CaCO_3$ (Alfa Aesar, 99.5%), Nb_2O_5 (Alfa Aesar, 99.5%), Fe_2O_3 (J.T.Baker, 99%)) were mixed in a ball mill (Fritsch Pulverisette) at 350 rpm for 30 minutes. The resulting powder was calcined in air at 1000 °C for 12 hours (Carbolite, HTF18/27) before ball milling again. The powder was pressed into 13mm diameter pellets with isostatic pressure of 120 MPa (Lloyd Instruments, LS100Plus) and sintered at 1400 °C for 24 hours.

4.3.2 Material Characterisation

X-ray diffraction (XRD) was performed on a Bruker d8 Advance X-ray Diffractometer with Cu Kα radiation (λ=1.54 Å) over the 2θ range between 10° and 80° with a step size of 0.02° and 3 seconds per step. The pellets were measured whole, rather than as a powder. Lattice parameters were calculated by solving the least-squares of 2θ, using Bragg's Law and the plane spacing equation. Scanning electron microscopy (SEM) (Hitachi TM3030) with energy dispersive X-ray (EDX) was used to investigate the surface structure of the pellets and the composition of the surface layers. Helium Pycnometry (Accupyc II 1340) was used to determine the density and porosity of the perovskite pellets. Microcomputer tomography (Micro CT) (Bruker SkyScan 2211) was used to visualise the 3D structure of the pellets to investigate gas exchange.

4.3.3 Temperature Programmed Experiments

The perovskites were tested for catalytic ability in a tubular furnace with controlled gas flows (Elite Thermal Systems Ltd TSH15/50/450). The pellets were inserted into the furnace, and the furnace was heated to 700 °C with a nitrogen flow of 50 ml/min. The pellets were reduced for 24 hours before being weighed and characterised with SEM, EDX and XRD. The pellets were heated again to 700 °C with a 10% CO_2/90% N_2 flow of 50 ml/min and left to react for 24 hours. The pellets were weighed again, and characterisation with SEM, EDX and XRD was repeated. Simultaneous thermal analysis (Linseis STA PT1600/800) was used to calculate the enthalpy of the CO_2 reaction. The experimental flowchart is shown in Figure 4.1(a). Thermal cycling was performed by alternating 24 hours of reduction under nitrogen at 700 °C with 24 hours of oxidation under 10 % CO_2 / 90 % N_2 at 700 °C for five cycles (for a total of 10 days). After each step of the cycle, the pellets were cooled to room temperature and weighed.

4.4 Results and Discussion

4.4.1 Material Characterisation

Characterisation of the as-prepared perovskites was undertaken to confirm their phase formation. The as-prepared pellets can be seen in Figure 4.1(b). The iron-containing perovskites (BCNF1 (1), BCNF0.66 (2) and BCNF0.34 (3)) are black while BCNF0 (4) which contains no iron is white. Helium Pycnometry (Table 4.1) shows an increase in density with increasing niobium content due to the higher molecular weight of niobium compared to iron. Porosity also generally increases with increasing niobium content, and it can be seen in Figure 4.1(b) that the BCNF0 pellets are slightly larger than the iron-containing pellets (BCNF0.34, BCNF0.66 and BCNF1), despite being made in the same mould, indicating less shrinkage on sintering. This correlates with the much higher pore volume in BCNF0. This agrees with the literature where doping with larger atomic radii elements results in greater porosity [13].

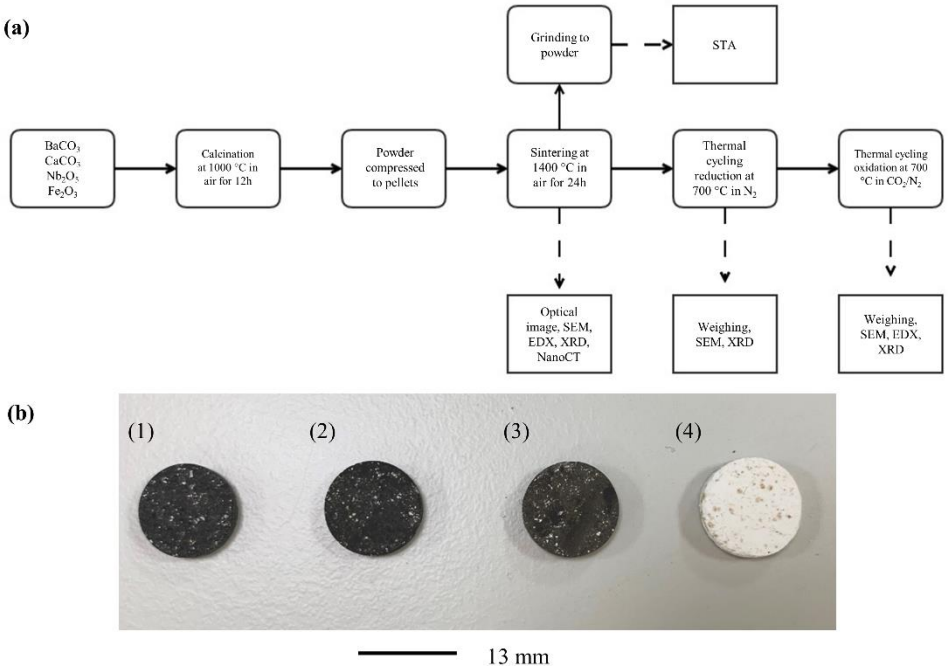

Figure 4.1. (a) Experimental Workflow, (b) Visual Representation of the As-synthesised Pellets, (1) BCNF1, (2) BCNF0.66, (3) BCNF0.34 and (4) BCNF0

Table 4.1. Helium Pycnometry Results showing Density, Pore Volume and Porosity

Sample	Mass (g)	Density (g/cm^3)	Pore volume (cm^3/g)	Porosity (%)
BCNF1	0.472	6.1003	0.1687	50.70
BCNF0.66	0.462	6.2382	0.2512	61.04
BCNF0.34	0.468	6.3966	0.2278	59.31
BCNF0	0.441	6.6309	0.3231	68.18

SEM images with x1000 magnification of the as-prepared perovskites can be seen in Figure 4.2. The as-prepared BCNF0 perovskite without iron (a) had an average grain size of around 10μm with no grains larger than 20μm and pores of around 1μm. BCNF0 had the smallest variation in grain sizes of any of the perovskites. The BCNF0.34 perovskite (d) had an average grain size below 5μm with a high density of pores. The as-prepared BCNF0.66 perovskite (g) had larger grains than BCNF0 or BCNF0.34 with an average size of around 20μm and a few large pores around 8μm. The grain sizes in the as-prepared BCNF1 (j), the perovskite with the most iron, are not distinguishable.

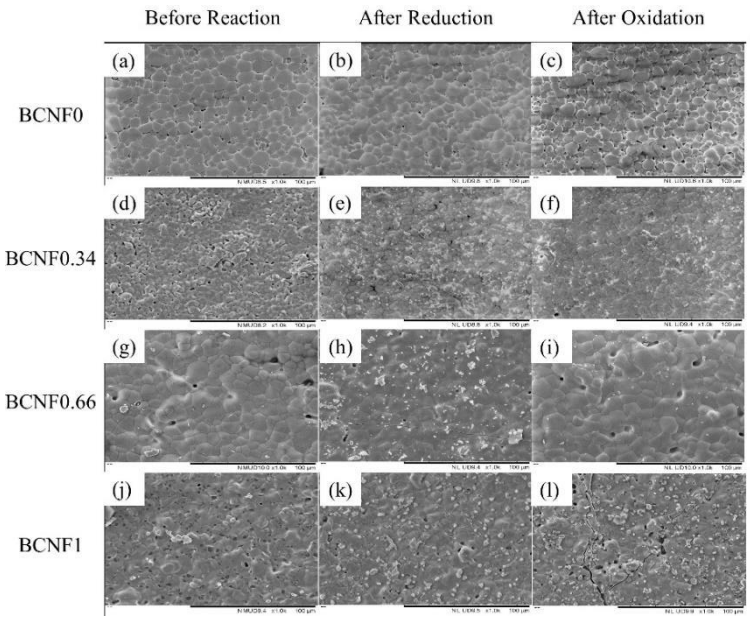

Figure 4.2. SEM Images of As-prepared, After Reduction and After Re-oxidation of BCNF0, BCNF0.34, BCNF0.66 and BCNF1

The Micro CT scans of the four perovskites are shown in Figure 4.3, where blue represents areas of lower density and orange represents areas of higher density. It can be seen that the core of the pellets has a higher density than the outer edges of the pellets, which likely occurred during the high-pressure moulding of the pellets. Additionally, the faces of the pellets are textured rather than smooth, showing that the surface is porous, as was seen in the SEM images and confirmed by helium pycnometry.

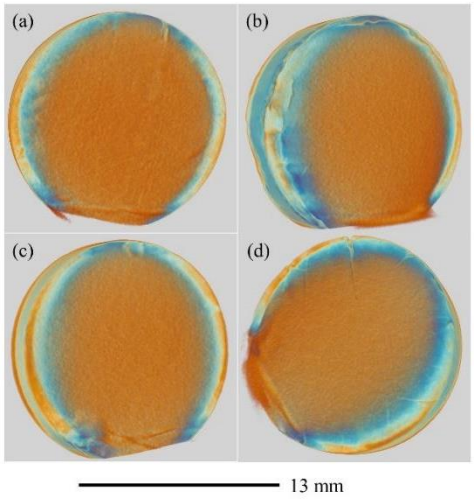

Figure 4.3. Micro Computer Tomography Reconstructed Images of (a) BCNF0, (b) BCNF0.34, (c) BCNF0.66, and (d) BCNF1.

XRD data of the as-prepared perovskites (Figure 4.4) shows that all perovskites had a double-perovskite type face centred cubic structure with an $Fm\bar{3}m$ space group. The average lattice parameters and miller indexing can be seen in Table 4.2. The perovskites synthesised here showed similar XRD patterns and crystal structures as other barium calcium iron niobates synthesised in the literature [12,14,15], with some variations in relative intensities of peaks, which may relate to some preferred orientation of the crystallites within the pellets. None of the impurities seen in the literature on these compounds could be identified here, including $BaCO_3$, Fe_2C, C and Fe_3O_4 [15], supporting the purity of the samples in the present study. It can be seen that there is a splitting of the peaks of BCNF0.34 and even more so for BCNF0,

possibly suggesting a deviation from the ideal cubic structure.

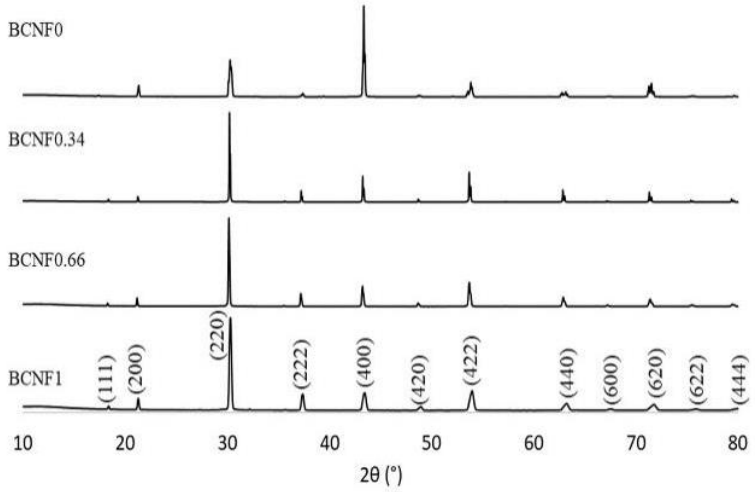

Figure 4.4. X-ray Diffraction Patterns of As-synthesised BCNF1, BCNF0.66, BCNF0.34 and BCNF0.

Table 4.2. Indexed XRD data for BCNF1, BCNF0.66, BCNF0.34 and BCNF0 with d Spacing and Intensity

			BCNF1		BCNF0.66		BCNF0.34		BCNF0	
h	k	l	d(Å)	I(%)	d(Å)	I(%)	d(Å)	I(%)	d(Å)	I(%)
1	1	1	4.831	7	4.852	5	4.831	4	5.089	2
2	0	0	4.174	15	4.198	11	4.182	6	4.166	13
2	2	0	2.950	100	2.962	100	2.958	100	2.952	41
2	2	2	2.404	19	2.417	16	2.414	13	2.404	5
4	0	0	2.081	21	2.092	24	2.091	29	2.086	100
4	2	0	1.861	6	1.870	5	1.869	4	1.862	2
4	2	2	1.699	23	1.706	28	1.706	34	1.702	17
4	4	0	1.470	10	1.477	11	1.478	14	1.472	6
6	0	0	1.385	4	1.392	3	1.393	2	1.388	2
6	2	0	1.314	8	1.321	9	1.319	6	1.318	16
6	2	2	1.253	4	1.259	5	1.260	2	1.258	2
4	4	4	1.201	4	1.205	4	1.207	4	1.203	2

a = 8.344Å a = 8.377Å a = 8.366Å a = 8.345Å

The double-perovskite type crystal structures can be seen in Figure 4.5, with calcium, niobium and iron occupying the B-sites and barium occupying the A-sites. The EDX scans in Figure 4.6 of as-prepared BCNF0, BCNF0.34 and BCNF0.66 show an even distribution of all elements, which suggests a uniform sample. On the other hand, BCNF1 shows small clumps of calcium with many areas containing no calcium at all. Since XRD analysis shows that the correct perovskite was synthesised, it can be suggested that the calcium seen in lumps on the surface of the perovskite does not represent the spread of elements within the whole pellet. There are many small patches of around 4μm on the surface, which through EDX analysis are seen to contain high concentrations of calcium. The $CaCO_3$ starting material had a powder size less than 5μm and so these patches are highly likely to be unreacted $CaCO_3$ starting material.

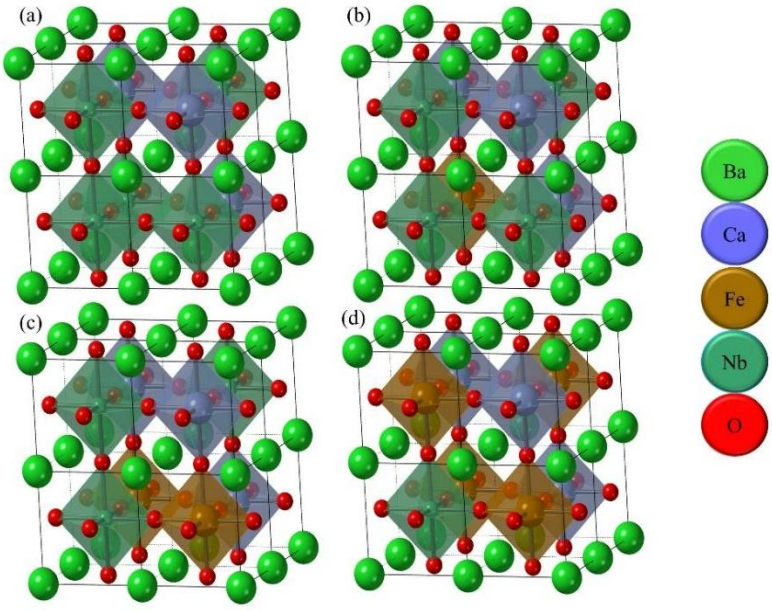

Figure 4.5. Crystal Structures of (a) BCNF0, (b) BCNF0.34, (c) BCNF0.66 and (d) BCNF1

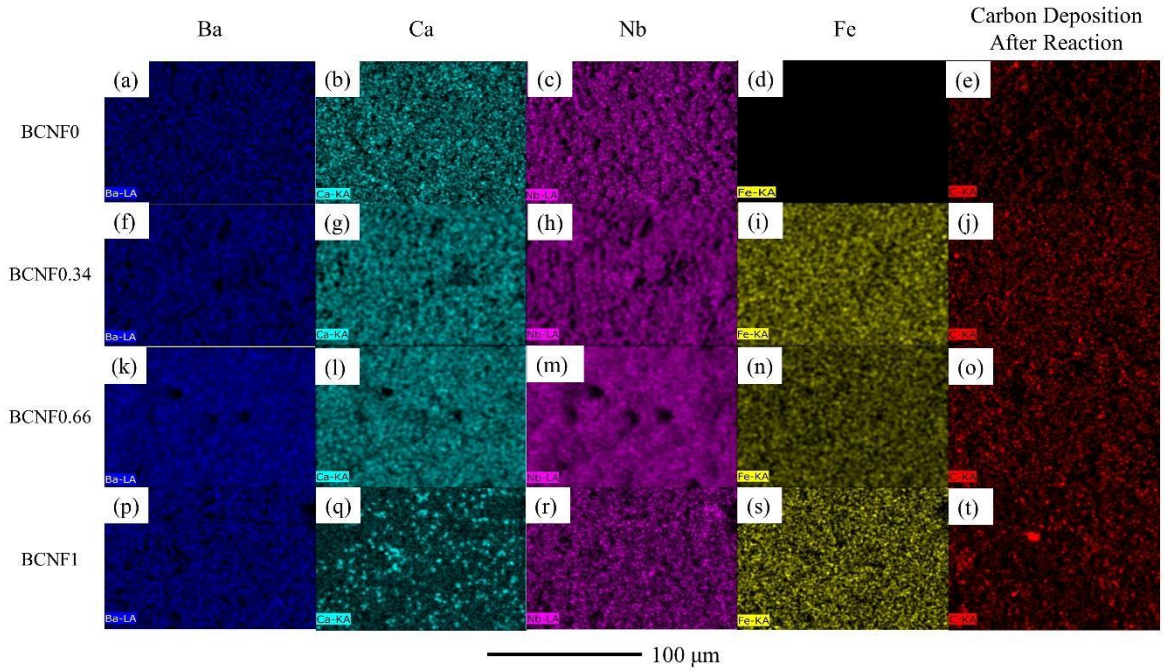

Figure 4.6. EDX Scans of As-synthesised BCNF1, BCNF0.66, BCNF0.34 and BCNF0

4.4.2 Reduction and Oxidation

The average mass change during reduction and reoxidation of the perovskites in the tubular furnace at 700 °C can be seen in Figure 4.7, and error bars showing one standard deviation are shown in red. Firstly, BCNF0 showed no mass change during reduction or re-oxidation, supporting that iron is needed for reduction or oxidation. This finding has also been confirmed in the literature [12]. BCNF0.34 and BCNF0.66 lost 0.28 and 0.21 % mass during reduction respectively; however, both showed no mass gain during re-oxidation. In fact, BCNF0.34 showed a minimal amount of mass loss during re-oxidation, perhaps since nitrogen was used during the reduction step and 90 % nitrogen with 10 % carbon dioxide was used during re-oxidation. This could suggest that a higher concentration of carbon dioxide is necessary for the re-oxidation of BCNF0.34 and BCNF0.66. The 10% carbon dioxide mixture used for re-oxidation was chosen to mimic flue gases from iron and steel processing industries. The peak splitting seen in the XRD plots before reduction appears to correlate with thermochemical activity, with increased peak splitting related to low mass changes.

BCNF1 showed the highest mass loss during reduction, 1.14 %. This high level of reduction suggests that oxygen vacancies are forming easily, likely due to the high iron content, allowing more oxygen vacancies to form. Re-oxidation of BCNF1 with 10 % carbon dioxide resulted in a 0.2 % increase in mass. It is common that perovskites are not completely re-oxidised during the re-oxidation reaction [16–19]. This suggests that not all oxygen vacancies formed during reduction are filled during the re-oxidation step. This could be due to the low carbon dioxide content (10 %) which could mean that carbon dioxide was not coming into contact with the oxygen vacancies in the material. Secondly, the low extent of re-oxidation could be due to the high density of the pellets, as seen in the Micro CT images in Figure 4.3, particularly in the core of the pellet, meaning that gas exchange was likely not possible within the pellet but rather just on the surface. Reactivity of the four perovskites had an inverse relationship with porosity, suggesting that gas exchange was not the limiting factor but rather the material itself, particularly in the case of BCNF0. It is likely however, that increasing the porosity of BCNF1 would increase its reactivity. It must be noted that the position in the tubular furnace is not linked to the extent of reduction or oxidation for any of the perovskites.

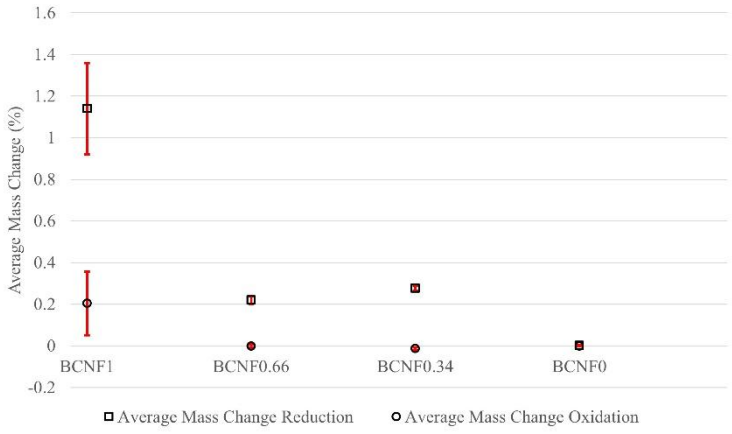

Figure 4.7. Average Mass Change of the Four Perovskites During Reduction and Reoxidation

The difference in the reactivities of the four perovskites can be partially explained by the enthalpy of oxidation calculated from STA measurements (Table 4.3). A negative enthalpy of

oxidation suggests an exothermic reaction while a positive enthalpy suggests an endothermic reaction. The enthalpy of the oxidation reaction for BCNF1 is -45 J/g, which is very small compared to the energy required to raise the perovskite to the reaction temperature of 700 °C, which is around 2570 J/g. This energy likely incorporates the enthalpy of reduction and the energy required to heat the perovskite. This energy requirement is likely much higher for BCNF1 because it contains more iron and can therefore form more oxygen vacancies. Part of this large enthalpy could be rearrangement within the crystal structure to allow oxygen to move from within the material to the surface of the material. This would allow more oxygen to be released during the reduction step; this was observed in the experimental studies. In order to elucidate the effect reduction is playing on the magnitude of this energy, future research using STA will maintain the perovskite at 700 °C while cycling between nitrogen and carbon dioxide atmospheres in order to separate the enthalpy of reduction. However, the low enthalpy of re-oxidation of BCNF1 means that when the perovskite is kept at 700 °C, the energy required to cycle between the oxidation and reduction reactions is very small, which should lead to a high level of energy storage with very little energy lost to the reaction. Since the enthalpy of oxidation for BCNF1 is exothermic, this suggests that the products (the oxidised perovskite and carbon monoxide) are more stable than the reactants (the reduces perovskite with oxygen vacancies and carbon dioxide) and therefore the oxidation reaction is energetically favourable. However, the enthalpy of oxidation for BCNF0.66 and BCNF0.34 are only around -1J/g, likely the difference in stability is not large enough to make the reaction favourable. BCNF0 has an endothermic reaction enthalpy, meaning the products are less stable than the reactants and therefore the reaction is less favourable. The enthalpy results also explain the fact that compounds similar to BCNF0 are unable to split carbon dioxide in the literature [12,14,15,20–23].

Table 4.3. Enthalpy Calculations of the Perovskites Calculated from Simultaneous Thermal Analysis.

Perovskite	Energy to heat from 25 to 750 °C (J/g)	Enthalpy of oxidation (J/g)
BCNF1	2570.89	-45.11
BCNF0.66	2046.13	-1.04
BCNF0.34	1337.06	-1.11
BCNF0	458.85	0.14

EDX analysis (Figure 4.6) of the pellets after oxidation in 10% CO_2 were used to visualise carbon deposition on the surface of the pellets. BCNF0 (e) clearly shows the least carbon deposition on its surface compared to the other three perovskites. This small amount of carbon on the surface could be due to the carbonate salts used in the synthesis of the perovskite, suggesting that the carbonate was not completely reacted during calcining and sintering. Moving from BCNF0.33 (j) to BCNF0.66 (o) and BCNF1 (t) there is an increase in the size of the carbon deposition particles, with large patches forming in BCNF1. Given that there was no mass gain during re-oxidation for BCNF0.34 and BCNF0.66, this carbon deposition could again be due to improper removal of carbonate salts during synthesis or very minimal surface deposition. The large clumps of carbon deposition on BCNF1 are not likely to be from the carbonate salts since it does not present this way in any other perovskite. This suggests that some of the CO_2 has been split into carbon on the surface of BCNF1, showing the high activity of this phase for CO_2 reduction.

4.4.3 Perovskite stability

XRD scans (Figure 4.8) of the perovskites as-prepared, after reduction and after re-oxidation were taken to investigate the chemical stability of the perovskites throughout the cycle. For BCNF0 (1), it can be seen that there were very little changes throughout the cycle, as expected from the lack of redox activity in this material. BCNF0.34 (2), BCNF0.66 (3) also showed no change in XRD pattern throughout the cycle, showing that they are stable at 700 °C and under

a 10 % CO_2 flow. BCNF1 showed a slight broadening of peaks after reduction, consistent with either decreased particle size or increased strain on the crystal lattice. The formation of oxygen vacancies, local lattice defects, are known to increase the strain, so this peak broadening could be evidence of oxygen vacancy formation [24]. In agreement with previous research, the BCNF1 perovskite did not show evidence of carbon deposition after re-oxidation (4c), usually visible as a small peak after the (422) reflection at around 55° [15]. A small peak appeared around 29° after oxidation, although again this isn't consistent with carbon deposition. In previous research, this carbon peak was only seen after re-oxidation with pure CO_2 while the reaction with 2000ppm CO_2 did not show a carbon peak.

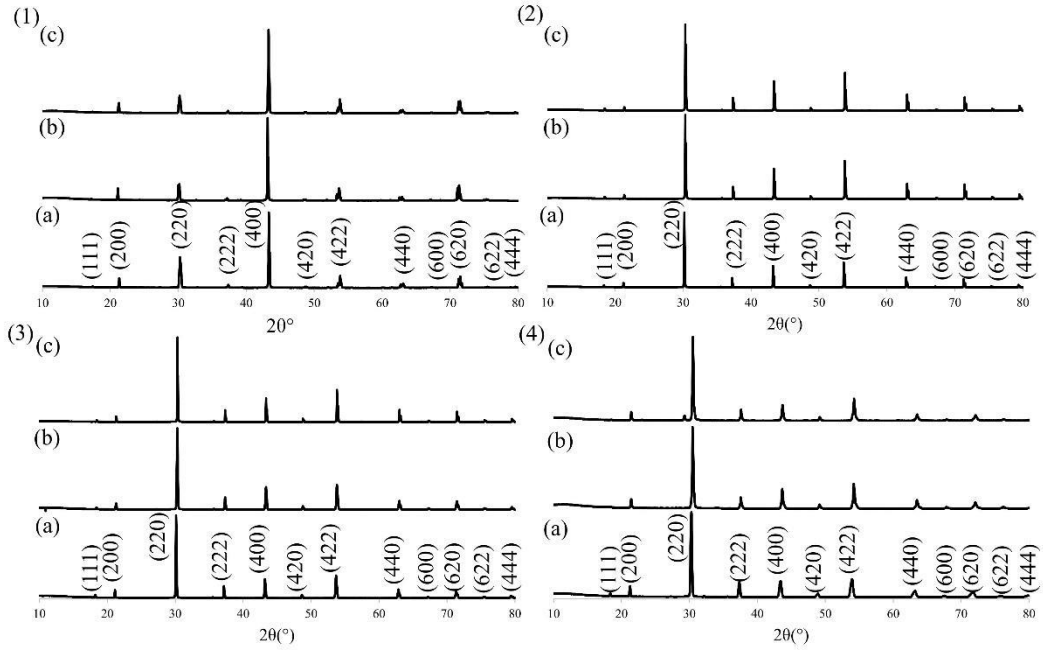

Figure 4.8. XRD Scans of (1) BCNF0, (2) BCNF0.34, (3) BCNF0.66 and (4) BCNF1 with (a) As-prepared, (b) After Reduction and (c) After Re-oxidation

SEM images (Figure 4.2) were taken of the as-prepared perovskites, after reduction and after re-oxidation to assess the structural stability of the perovskites. In BCNF0, after reduction (b) the average grain size had decreased from around 10μm to less than 10μm and fewer pores were visible. There was also less definition between the grain boundaries. After re-oxidation

(c) the definition of the grain boundaries has increased, the grain size has grown to larger than 10μm, and there are more pores visible, most around 3μm. This suggests that sintering has occurred due to the increase in grain size. In BCNF0.34 after reduction (e), the average pore size had increased from less than 5μm to around 10μm, and fewer pores are present, suggesting sintering has occurred. Additionally, there is a small amount of deposition on the surface which appears to have a high concentration of calcium through EDX analysis (Figure 4.6 (g)). After re-oxidation (f), there are markedly fewer pores and less deposition on the surface, suggesting the calcium-containing deposits were reacted or incorporated into the structure. The average grain size remains unchanged through the re-oxidation step. The as-prepared BCNF0.66 (g) perovskite had larger grains than BCNF0 or BCNF0.34. After reduction (h), the grain boundaries are less pronounced, and the pore sizes have decreased from around 8μm to just a few microns. Overall, the grains are roughly the same size as the as-prepared sample; however, there is again some solid deposition. After re-oxidation (i), there is an increase in grain size, with some of the larger grains above 30μm and an increase in the number and size of pores. There is also a significant decrease in deposition on the surface, as seen in BCNF0.34 after re-oxidation. After reduction of BCNF1 (k), the perovskite again has indistinguishable grain sizes, a few pores and deposition on the surface. After re-oxidation (l), a large crack can be seen running the length of the scanned area and upon visual observation, many large cracks had appeared over the surface of the pellet. The cracking of the pellet suggests significant volume changes during the redox process; however, the cracks may help gas diffusion and penetration in later cycles.

Figure 4.9 shows the mass change observed through five cycles of reduction in 100% N_2 and re-oxidation in 10% CO_2/90% N_2 for BCNF1. It can be seen that although the mass gain in the first re-oxidation cycle was only 0.2 %, from the second cycle, the mass changes stabilise at around 0.45 %. This increase in the reactivity of the CO_2 splitting reaction between the first

and second cycle is likely due to morphological changes since no changes were seen in the XRD after the first cycle. Figure 4.2 shows that the pellet had cracks on the surface after the first cycle, which could have led to a larger surface area for the reaction to occur, resulting in a larger mass change in the second cycle. The lower mass change for the 3rd re-oxidation and 4th reduction is accompanied by a much higher standard deviation between the pellets, perhaps suggesting some human or mechanical error during weighing. This is likely the case because the mass change returns to 0.45% after these two points, making error more likely. However, the sustained mass change of 0.45 % is extremely promising in terms of potential applications of this material. This mass change can be converted to oxygen evolution and carbon monoxide production volumes, giving an average over five cycles of 140 μmol of O_2 per gram of perovskite and 160 μmol of CO per gram. This fuel yield is higher than many ceria-based materials [8]. In industrial applications it is likely that a thousand or more cycles would be required, therefore although BCNF1 shows promise during five cycles, future research should focus on prolonged cycling.

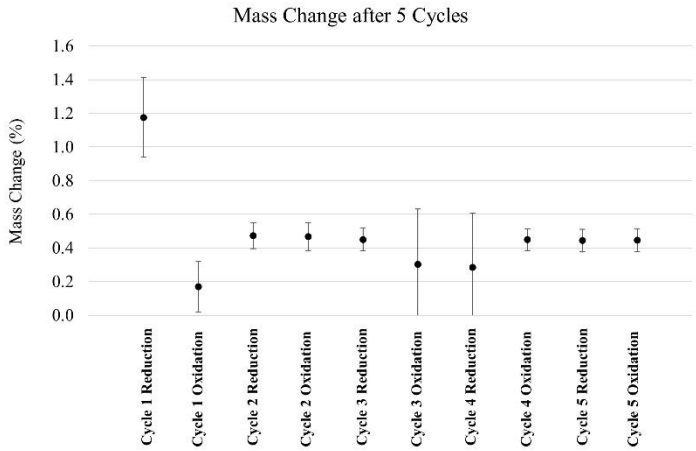

Figure 4.9. Mass Change of BCNF1 during Five Cycles of Reduction and Reoxidation

4.5 Conclusion

The results presented here show that for the barium calcium iron niobate family of perovskites, the higher the iron content, the more successful for chemical looping and the decomposition of carbon dioxide. BCNF1, $Ba_2Ca_{0.66}Nb_{0.34}FeO_{6-\delta}$, showed an exceptionally high mass loss during reduction of 1.14%, equal to the loss of 0.34 moles of oxygen. The sustained mass change of 0.45 % after five cycles suggests this material could be suitable for use in chemical looping energy storage applications. More importantly, the low enthalpy change of oxidation of BCNF1 suggests that very little energy would be lost cycling the material, meaning more of the energy input can be regained.

4.6 References

[1] G. Kosmadakis, Estimating the potential of industrial (high-temperature) heat pumps for exploiting waste heat in EU industries, Appl. Therm. Eng. 156 (2019) 287–298.

[2] R.C. McKenna, J.B. Norman, Spatial modelling of industrial heat loads and recovery potentials in the UK, Energy Policy. 38 (2010) 5878–5891.

[3] H. Fang, J. Xia, K. Zhu, Y. Su, Y. Jiang, Industrial waste heat utilization for low temperature district heating, Energy Policy. 62 (2013) 236–246.

[4] Y. Ding, H. Cao, P. Slater, Y. Li, S. Du, Energy Generation, WO/2019/158948, 2019.

[5] D. Marxer, P. Furler, J. Scheffe, H. Geerlings, C. Falter, V. Batteiger, A. Sizmann, A. Steinfeld, Demonstration of the Entire Production Chain to Renewable Kerosene via Solar Thermochemical Splitting of H_2O and CO_2, Energy and Fuels. 29 (2015) 3241–3250.

[6] N. Pardo, J.A. Moya, Prospective scenarios on energy efficiency and CO_2 emissions in the European Iron & Steel industry, Energy. 54 (2013) 113–128.

[7] D.S. Mallapragada, N.R. Singh, V. Curteanu, R. Agrawal, Sun-to-fuel assessment of routes for fixing CO_2 as liquid fuel, Ind. Eng. Chem. Res. 52 (2013) 5136–5144.

[8] R.R. Bhosale, G. Takalkar, P. Sutar, A. Kumar, F. AlMomani, M. Khraisheh, A decade of ceria based solar thermochemical H_2O/CO_2 splitting cycle, Int. J. Hydrogen Energy. In Press (2018) 1–27.

[9] A. Steinfeld, Solar hydrogen production via a two-step water-splitting thermochemical cycle

based on Zn/ZnO redox reactions, Int. J. Hydrogen Energy. 27 (2002) 611–619.

[10] T. Kodama, N. Gokon, Thermochemical cycles for high-temperature solar hydrogen production, Chem. Rev. 107 (2007) 4048–4077.

[11] J.R. Scheffe, D. Weibel, A. Steinfeld, Lanthanum-strontium-manganese perovskites as redox materials for solar thermochemical splitting of H_2O and CO_2, Energy and Fuels. 27 (2013) 4250–4257. https://doi.org/10.1021/ef301923h.

[12] S. Mulmi, H. Chen, A. Hassan, J.F. Marco, F.J. Berry, F. Sharif, P.R. Slater, E.P.L. Roberts, S. Adams, V. Thangadurai, Thermochemical CO2 splitting using double perovskite-type $Ba_2Ca_{0.66}Nb_{1.34-x}Fe_xO_{6-\delta}$, J. Mater. Chem. A. 5 (2017) 6874–6883.

[13] T. Tsuji, Y. Ohashi, Y. Yamamura, Effect of ionic radius on electrical conductivity of doped $SmAlO_3$ perovskite oxide, Solid State Ionics. (2002).

[14] S. Mulmi, V. Thangadurai, Preparation, Structure and CO2 Sensor Studies of $BaCa_{0.33}Nb_{0.67-x}Fe_xO_{3-\delta}$, J. Electrochem. Soc. 160 (2013) B95–B101.

[15] S. Mulmi, Greenhouse Gas Detection Using Metal Oxides: Experiments and Challenges, 2016.

[16] R.D. Barcellos, M.D. Sanders, J. Tong, A.H. McDaniel, R.P. O'Hayre, $BaCe_{0.25}Mn_{0.75}O_{3-\delta}$ promising perovskite-type oxide for solar thermochemical hydrogen production, Energy Environ. Sci. 11 (2018) 3256–3265.

[17] A.E. Ramos, D. Maiti, Y.A. Daza, J.N. Kuhn, V.R. Bhethanabotla, Co, Fe, and Mn in La-perovskite oxides for low temperature thermochemical CO2 conversion, Catal. Today. 338 (2019) 52–59.

[18] B.J. Hare, D. Maiti, S. Ramani, A.E. Ramos, V.R. Bhethanabotla, J.N. Kuhn, Thermochemical conversion of carbon dioxide by reverse water-gas shift chemical looping using supported perovskite oxides, Catal. Today. 323 (2018) 225–232.

[19] L. Wang, M. Al-Mamun, P. Liu, Y.L. Zhong, Y. Wang, H.G. Yang, H. Zhao, Enhanced Thermochemical H_2 Production on Ca-Doped Lanthanum Manganite Perovskites Through Optimizing the Dopant Level and Re-oxidation Temperature, Acta Metall. Sin. English Lett. 31 (2018) 431–439.

[20] S. Mulmi, A. Hassan, P. Pereira-Almao, V. Thangadurai, Detecting CO_2 at ppm level in synthetic air using mixed conducting double perovskite-type metal oxides, Sensors Actuators B Chem. 178 (2013) 598–605.

[21] S. Mulmi, R. Kannan, V. Thangadurai, CO_2 and SO_2 tolerant Fe-doped metal oxides for solid state gas sensors, Solid State Ionics. 262 (2014) 274–278.

[22] S. Mulmi, R. Kannan, V. Thangadurai, Mixed Ion and Electron Conducting Ceramics for Gas Sensors, ECS Trans. 58 (2014) 31–36.

[23] R. Kannan, S. Mulmi, V. Thangadurai, Synthesis and characterization of perovskite-type $BaMg_{0.33}Nb_{0.67-x}Fe_xO_{3-\delta}$ for potential high temperature CO2 sensors application, J. Mater. Chem. A. 1 (2013) 6874.

[24] K.-B. Le-Van, G.-Z. Tang, X.-X. Ma, S.-Q. Jiang, Influence of Grinding Particle Size on Structure and Electrical Properties of La 0.67 Sr 0.33 MnO 3-δ Compound, Mater. Manuf. Process. 31 (2016) 880-886. https://doi.org/10.1080/10426914.2015.1004700.

Chapter 5 – THERMOCHEMICAL SPLITTING OF CARBON DIOXIDE ON $Ba_2Ca_{0.66}Nb_{0.34}FeO_6$ AT MODERATE TEMPERATURES: THE INFLUENCES OF REDUCTION AND OXIDATION CONDITIONS AND CO_2 DIFFUSION

5.1 Abstract

We report our recent findings that $Ba_2Ca_{0.66}Nb_{0.34}FeO_6$ can split CO_2 at moderate temperatures achievable by current large scale concentrated solar plants. This provides a thermochemical route for synthesis gas production from carbon monoxide and water via water-gas shift reaction. The synthesis gas can be upgraded into chemicals and fuels to aid in the decarbonisation of the transport and chemical sectors. We investigated the conditions of the reduction and oxidation reactions to improve carbon monoxide yields. An increase in the oxidation temperature from 700 to 800 °C increased CO yields from 58 to 447 μmol/g. The reaction depth increased as the temperature was increased, showing improved permeability to CO_2. Product yields were increased further by reacting over the perovskite as a powder rather than a pellet, increasing CO yields to 727 μmol/g. Over 10 thermal cycles, the pellets saw a decrease in yield, stabilising around 250 μmol/g, whereas the powder stabilised at 630 μmol/g. These results bring the yields of this perovskite in-line with the most successful thermochemical materials for fuel production.

This chapter is in a publishable format but has not yet been published. H. Kildahl is the first author, responsible for research and writing. Y. Ding and H. Cao are responsible for supervision and editing.

5.2 Introduction

The urgent need to reduce the human drivers of climate change has been unequivocally outlined in the newest assessment report by the International Panel on Climate Change (IPCC) [1]. To limit warming to below 1.5 °C by the end of the century, the remaining global carbon budget could be as little as 300 Gt CO_{2eq}. Indeed, only one of the pathways outlined in the report would meet this target, requiring net carbon neutrality on a global scale before 2055. The so-called hard-to-decarbonise sectors, including aviation, freight, and the chemicals industry, are unlikely to reach this net-zero target by electrification or efficiency improvements alone [2–5]. One solution could be the conversion of a carbon-neutral starting material into the fuels and chemicals required. This could be synthesis gas, a mixture of carbon monoxide and hydrogen that can be upgraded *via* the Fischer Tropsch process into chemical building blocks, and higher order olefins, including kerosene [6–14]. A thermochemical cycle allows for the splitting of carbon dioxide into carbon monoxide at temperatures between 700 and 1500 °C. The most researched materials capable of thermochemical cycles are ceria (cerium oxide) and the lanthanum strontium manganites, a perovskite family [15–27]. However, both these materials require between 1200 and 1500 °C to operate.

A thermochemical cycle consists of two basic reactions, making a redox reaction. During reduction, oxygen vacancies are formed within the material, oxygen gas is released, and the material is reduced. During the oxidation reaction, carbon dioxide is introduced to the reduced perovskite and is reduced into carbon monoxide, filling the oxygen vacancies, and oxidising the perovskite. This cycle is repeated. Many methods have been employed to improve fuel yields and therefore overall thermal efficiency. Doping has been used extensively both in metal oxide and perovskite-based thermochemical conversion systems and many reviews have been published on this subject [28–36]. Doping will therefore not be the focus of this paper, instead the conditions of both the reduction and oxidation reactions will be optimised.

The reduction temperature has been shown to have an effect on oxygen evolution yields and carbon monoxide production in the later oxidation reaction. $LaCo_{0.7}Zr_{0.3}O_3$, a perovskite, was reduced at temperatures between 1000 °C and 1400 °C [37]. As the reduction temperature increased, oxygen evolution and carbon monoxide production generally increased, up to a maxima. Maximum oxygen evolution is seen at 1300 °C due to sintering occurring at 1400 °C. Another material, $SrMnO_3$ was reduced at 1250 °C or 1400 °C and re-oxidised at 1000 °C [38]. Reducing at 1250 °C resulted in a 0.8 % mass change whereas reduction at 1400 °C produced a 2.4 % mass change, showing that a relatively small change in temperature can have a large effect on the reduction extent of this material. The introduction of 25 % La into the A site, forming $Sr_{0.75}La_{0.25}MnO_3$, minimises the effect of reduction temperature; mass change at 1250 °C was 0.5 % while at 1400 °C this change was 1.1 %. This shows that the optimum reduction temperature is highly specific to each material and should be investigated in each case to improve yields. This was replicated with $Y_{0.5}Sr_{0.5}MnO_3$ which was reduced at 1200 °C, 1300 °C and 1400 °C and re-oxidised at 900 °C [39]. Not only did higher temperatures release more oxygen, 483 μmol/g vs 258 μmol/g at 1400 °C and 1200 °C, respectively, but the deeper reduction translated to higher CO production, 757 μmol/g vs 418 μmol/g.

The time allowed for the reduction reaction can also have an effect on the fuel yields. $La_{0.6}Sr_{0.4}Cr_{0.8}Co_{0.2}O_3$ was reduced at 1000 °C for one hour or four hours before being re-oxidised at 800 °C [40]. The short reduction produced 10 μmol/g of carbon monoxide while the longer reduction led to a production of 63 μmol/g. No longer reduction times than four hours were researched, meaning that the optimum time could be greater than four hours for this material.

The oxidation temperature is perhaps more important than the reduction temperature since typically carbon monoxide yields are prioritised. $LaCo_{0.7}Zr_{0.3}O_3$ was oxidised at temperatures between 800 °C and 1300 °C [37]. It was found that 800 °C produced the most carbon

monoxide and that generally, as the temperature increased, the fuel production decreased. For example, 1680 μmol/g of carbon monoxide was produced at 800 °C, whereas only 150 μmol/g was produced at 1300 °C. Another material which was investigated for the optimal oxidation temperature is $La_{0.5}Sr_{0.5}MnO_3$ [17]. The perovskite was reduced at 1400 °C and re-oxidised at 900 °C, 1050 °C, 1200 °C and 1400 °C. For the first cycle, 1050 °C produced the most CO (269 μmol/g) and retained this activity into the second thermal cycle, producing 215 μmol/g. In this research, 1400 °C caused sintering and poor carbon monoxide yields, whereas 900 °C was too low to produce high fuel yields. This demonstrates again that optimum reaction conditions are specific to each material and large improvements in yield can be achieved through small changes in conditions.

This work is focused on $Ba_2Ca_{0.66}Nb_{0.34}FeO_6$ (BCNF1), a double perovskite type material which was found to be the most promising material from our previous research [41]. This research aims to improve the carbon monoxide yields of this material by optimising the reduction and oxidation reaction conditions. We will show that the yields of CO produced by this perovskite are in-line with the most successful thermochemical materials at 700-800 °C. Such mild temperature conditions could be realistically achieved by the current concentrated solar plants.

5.3 Methodology

5.3.1 Material Synthesis

$Ba_2Ca_{0.66}Nb_{0.34}FeO_6$ was synthesised using a solid-state reaction from a stoichiometric combination of the precursor materials, as demonstrated previously [42]. These starting materials were $BaCO_3$ (Alfa Aesar, 99%), $CaCO_3$ (Alfa Aesar, 99%), Nb_2O_5 (Alfa Aesar, 99.5%) and Fe_2O_3 (J.T Baker, 99%) and were used as received without further purification. The powder mixture was ground using a mortar and pestle before being calcined in air at 1000

°C for 12 hours (Carbolite, HTF18/27). The calcined material was ground to a fine powder before being pressed into 10mm diameter pellets with an isostatic pressure of 120 MPa for 1 minute (Lloyd Instruments, LS100Plus). The 0.5g pellets were sintered at 1400 °C for 24 hours before characterisation and thermochemical cycling experiments.

5.3.2 Material Characterisation

Before the thermochemical conversion experiments were performed, the synthesised pellets were characterised so that any changes after the experiment could be easily observed. Whole pellets were characterised using X-Ray Diffraction (XRD) on a Bruker d8 Advance X-ray Diffractometer with Cu Kα radiation (λ=1.54 Å) over the 2θ range between 10° and 80° with a step size of 0.02° and 3 seconds per step. Morphological features of the pellets were examined using Scanning Electron Microscopy (SEM) (Hitachi TM3030) with Energy Dispersive X-ray Spectroscopy (EDX). Porosity and density of the pellets were investigated using helium pycnometry (Accupyc II 1340).

5.3.3 Reduction Temperature and Time

The as-synthesised pellets produced as described above were inserted into a tubular furnace (Elite Thermal Systems Ltd TSH15/50/450). The pellets were heated to the reduction temperature and reduced for 24 hours under nitrogen at 50 ml/min. The long reduction times of 24 hours were chosen to ensure that the largest extent of reduction could be realised. The reduction temperatures investigated were 600 °C, 700 °C, 800 °C and 900 °C. The mass change was recorded, and the pellets were recharacterized by XRD, SEM, EDX and helium pycnometry to find the optimum reduction conditions. Next, the reduction time was investigated by performing the reduction reaction on fresh pellets for 6, 12, 18, 24 and 36 hours at the optimum temperature. All other parameters were kept constant for this set of experiments.

5.3.4 Oxidation Temperature

As-synthesised pellets were reduced at 700 °C under nitrogen for 24 hours, based upon the best temperature for reduction as determined by the previous set of experiments. The pellets were weighed before being oxidised at 600 °C, 650 °C, 700 °C, 750 °C or 800 °C under 100 % CO_2 at 50 ml/min for 24 hours. The pellets were weighed again, before being examined with SEM, EDX and helium pycnometry.

5.3.5 Oxidation Kinetics

A fresh batch of 10mm pellets were synthesised and reduced for 24 hours at 700 °C. The pellets were weighed, heated to 800 °C and allowed to spend 1, 3, 6, 9, 12, 15, 18, 21 or 24 hours at 800 °C under CO_2 before being cooled to room temperature and reweighed to determine CO production from different oxidation durations. This allows the kinetics of the oxidation reaction to be investigated.

5.3.6 Material Shape/Form

Four different shapes/forms of material were investigated: 10 mm diameter pellets, 5 mm diameter pellets, 1g and 500mg of powder in a ceramic boat, to investigate the effect of superficial surface area on diffusion. The pellets were synthesised as above, using corresponding pellet dies. The powders were produced in the same way as described above, however after calcining the powder was ground in the mortar and pestle before being sintered in a ceramic crucible. The powder properties were investigated using the QICPIC Particle Size Analyser. The materials were reduced at 700 °C under nitrogen for 24 hours in the tubular furnace, weighed and oxidised under CO_2 at 800 °C for 24 hours before being characterised.

5.3.7 Thermal Cycling

A new batch of pellets and powder was synthesised as above. The 10mm pellets and 1g of powder in a ceramic boat were thermally cycled ten times between reduction at 700 °C,

weighed and re-oxidation at 800 °C under CO_2 before being weighed again. This allows the cyclability of the material to be tested under the optimal reaction conditions as determined in the previous experiments above.

5.4 Results and Discussion

5.4.1 Reduction Reaction

The as-synthesised BCNF1 was reduced at different temperatures between 600 and 900 °C to find the optimum reduction temperature. Figure 5.1(a) shows the result of these reduction reactions, with 700 °C clearly being the optimum among the temperatures tested with an oxygen evolution of 95 μmol/g. The reduction reaction is endothermic and therefore, thermodynamically, higher temperatures should give higher yields. The lower result from the reaction at 900 °C is therefore likely due to sintering of the pellet hindering gas diffusion through the pellets. This was confirmed by SEM, where, as seen in Figure 5.2(b), the pellet reacting at 900 °C shows much larger grains and fewer pores. The pellets reduced at 800 °C showed an anomalously low oxygen evolution of 2 μmol/g, therefore this experiment was repeated with a fresh batch of pellets. The same result was obtained, suggesting a change is taking place in the pellets when reduced under nitrogen at 800 °C. The SEM results show no difference between the 800 °C reduction and the 600 or 700 °C reduction, however, XRD Figure 5.2(a) shows an increase in the peak at 54 °, which correlates with the (422) plane. Crystallite orientation in the (422) plane has been shown to be correlated with poor thermochemical activity in these materials, with this orientation likely hindering oxygen vacancy formation [41].

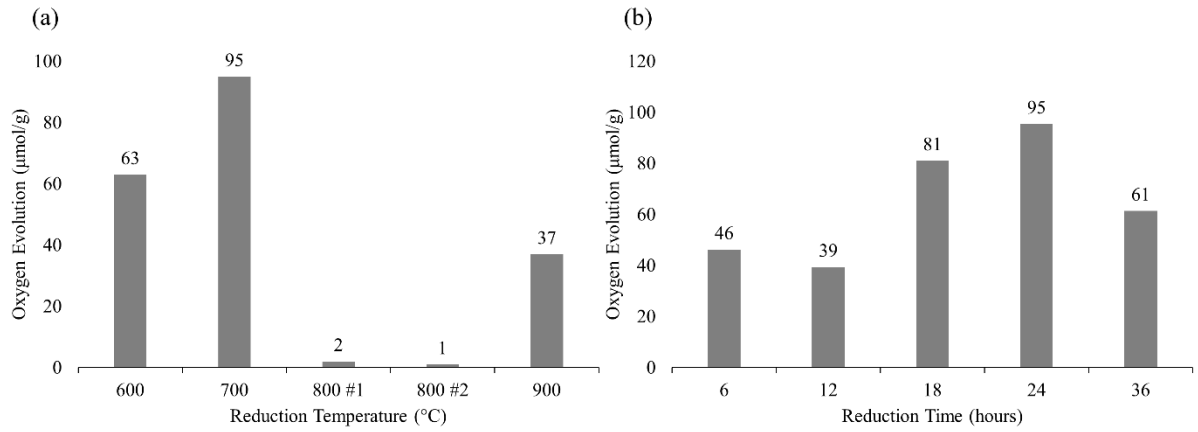

Figure 5.1. (a) Oxygen Evolution from the Reduction Reaction Performed between 600-900 °C for 24 hours. The Reduction Reaction at 800 °C was repeated due to the Lower than Expected Result. (b) Oxygen Evolution from the Reduction Reaction reformed at 700 °C for between 6 and 36 hours.

Figure 5.1(b) shows the oxygen evolution for the reduction reaction performed at 700 °C for between 6 and 36 hours, with each duration performed on a fresh set of pellets. The optimum time is 24 hours, although 18 hours produces only about 15% less oxygen despite only requiring 75% of the time and therefore approximately 75% of the thermal energy to maintain the temperature. However, the 24-hour duration was used for the remainder of the experiments due to restrictions in lab access, although in an industrial setting 18 hours may be the optimum due to decreased heating costs.

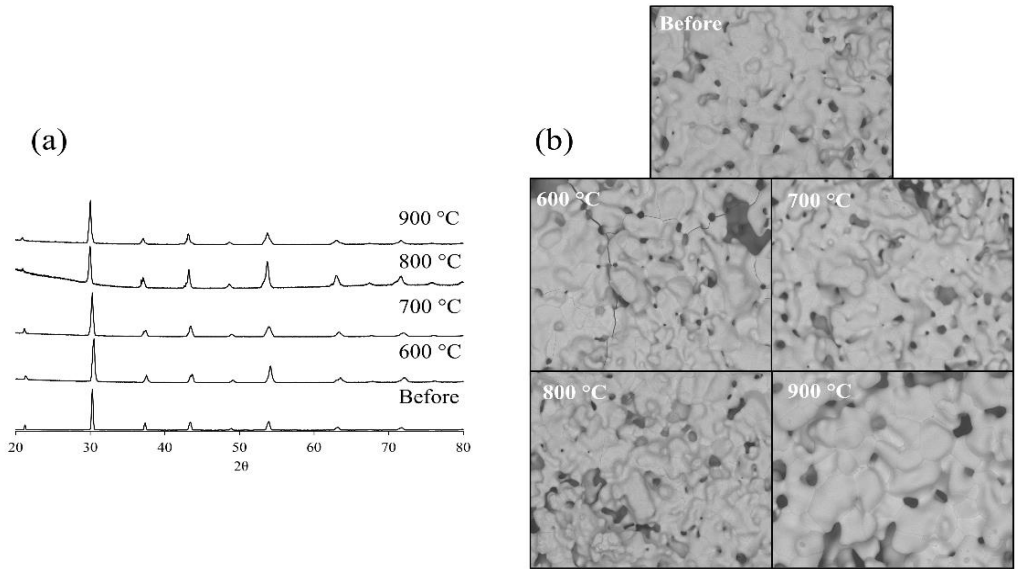

Figure 5.2. (a) XRD Plots and (b) SEM images of the Perovskite Pellets Before Reduction and After Reduction at Different Temperatures.

5.4.2 Oxidation Reaction

The oxidation temperature was varied between 600 and 800 °C. From Figure 5.3 it can be seen that there are two trends relating to carbon monoxide production. Carbon monoxide yields decrease from 85 μmol/g to 58 μmol/g as the temperature increases from 600 to 700 °C, respectively. This is likely due to the fact that the oxidation reaction is exothermic, meaning lower temperatures shift the equilibrium to the right, favouring the carbon dioxide splitting reaction. However, once the temperature exceeds 750 °C, another mechanism begins to play a role and carbon monoxide production increases to 447 μmol/g at 800 °C, namely the diffusion of the carbon dioxide gas within the pellet, which is discussed below.

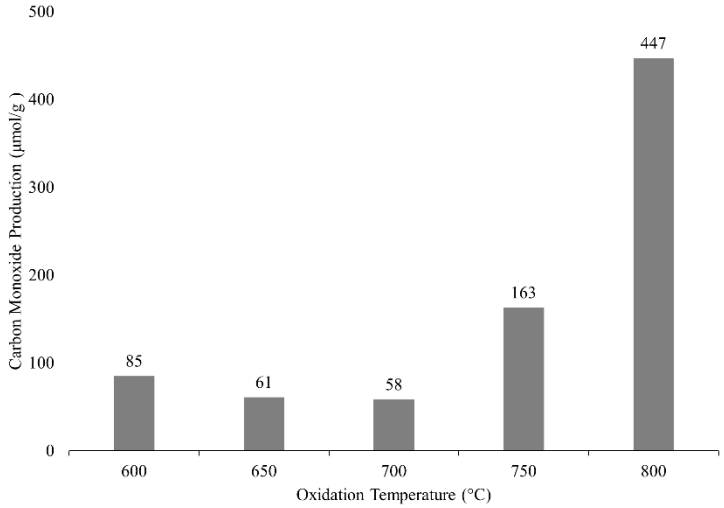

Figure 5.3. Carbon Monoxide Production from the Oxidation Reaction Performed between 600-800 °C for 24 Hours

5.4.2.1 Diffusion Effect

Focusing on the diffusion aspect of the oxidation reaction, carbon monoxide has a higher binary diffusion coefficient than carbon dioxide, meaning it can move more quickly through the pores of the pellet than carbon dioxide. Therefore, carbon dioxide diffusion into the pellet is likely the rate-limiting diffusion process and shall be investigated here. Given that there is the absence of a total pressure gradient between the inside and outside of the pores, gas in the bulk fluid must first diffuse into the pores through partial pressure difference for the reaction to occur.

The type of diffusion can be estimated by the relation between the mean free path (λ) and the pore radius (r_a)[43].

$$Type\ of\ diffusion = \frac{\lambda}{2 * r_a} \tag{5.1}$$

The pore radius can be estimated from measurements of pore diameter from SEM images (See Section 5.4.1, Figure 2(a)) and the mean free path, λ, of carbon dioxide can be calculated with:

$$\lambda\ (m) = \frac{4 *\ 10^3}{p} \tag{5.2}$$

Where p is the total pressure of the system in pascal. In this case the pressure is atmospheric pressure, i.e., 101325 Pa. Therefore $\lambda =$ 0.0395 μm and at all temperatures the mean free path of carbon dioxide is smaller than the average pore diameter found in the pellets. When $\lambda/(2 * r_a) \leq 0.01$ diffusion inside the pore is controlled by normal diffusion, where the diffusion rate depends on the collision frequency between molecules, is independent of pore radius and is described by Fick's Law. When $\lambda/(2 * r_a) \geq 10$, diffusion inside the pores is named Knudsen diffusion, where collisions occur between molecules and the pore walls while collisions between molecules have little impact. The values of $\lambda/(2 * r_a)$ for the pellets used in the oxidation reactions can be found in Table 5.1. Between 600 and 700 °C, the value of $\lambda/(2 * r_a)$ is between these two extremes and both normal and Knudsen diffusion plays a role. At 750 and 800 °C, only normal diffusion plays a role, as measured by the binary diffusion coefficient.

Table 5.1. Pore Diameter, $\lambda/(2 * r_a)$, and Type of Diffusion Present in 10mm Pellets Oxidised between 600 and 800 °C.

Oxidation temperature (°C)	**Pore diameter (μm)**	$\lambda/(2 * r_a)$	**Type of Diffusion**
600	3.153	0.0125	Knudsen & Normal
650	3.245	0.0122	Knudsen & Normal
700	2.954	0.0134	Knudsen & Normal
750	6.927	0.0057	Normal
800	4.235	0.0093	Normal

The total diffusion (D_{CO2}) can then be written as:

$$D_{CO2} = \frac{1}{\left(\frac{1}{D_k}\right) + \left(\frac{1}{D_{CO2-CO}}\right)} \quad (5.3)$$

Where D_k is the Knudsen diffusion coefficient and D_{CO2-CO} is the binary diffusion coefficient of CO into CO_2, which is equal to 1.57 cm^2/s at 822 °C [44].

The Knudsen diffusion coefficient can be calculated by:

$$D_k = 9.7 * 10^3 * r_a * \sqrt{T/M} \quad (5.4)$$

Where *T* is the absolute temperature in Kelvin and *M* is the molecular weight of the diffusing component. The effective diffusion coefficient can then be calculated using:

$$D_{eCO2} = D_{CO2} * \varepsilon/\tau \quad (5.5)$$

Where ε is the porosity, measured by helium pycnometry and τ is the tortuosity, calculated to be between 1.94 and 2.11 for the 600 and 800 °C pellets, respectively. Figure 5.4 shows the effective diffusion coefficient plotted against carbon monoxide production for each oxidation temperature. It can be seen that the effective diffusion coefficient decreases as oxidation temperature increases. This was an unexpected result, since faster diffusion should lead to higher carbon monoxide yields. One explanation could be that when the effective diffusion coefficient is lower, a larger proportion of carbon dioxide molecules are travelling slowly enough for the C-O bond to begin breaking when the molecule comes into contact with an oxygen vacancy in the perovskite. When the coefficient is higher, fewer CO_2 molecules are travelling slowly enough for the carbon dioxide splitting reaction to occur and the carbon monoxide production is therefore lower. Another explanation could be that ionic conductivity increased as temperature increased, resulting in more facile oxygen vacancy migration, allowing oxygen vacancies to move to the surface of particles where contact with CO_2 occurs.

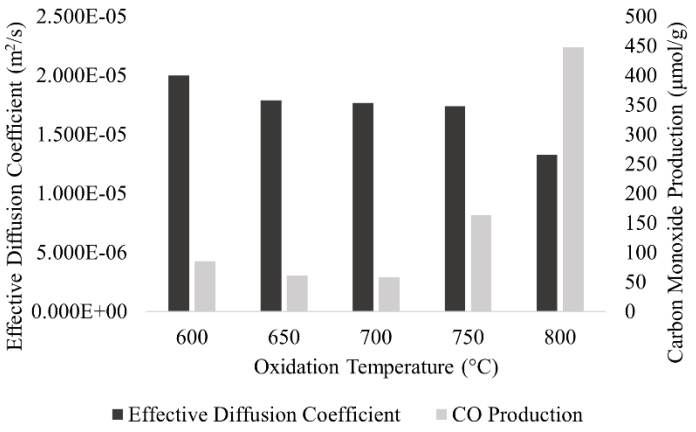

Figure 5.4. Effective Diffusion Coefficient plotted against Carbon Monoxide Production at Oxidation Temperatures between 600 and 800 °C.

5.4.2.2 Reaction Extent

Since diffusion has been shown to play a large role in the CO production capabilities of the pellets, SEM and EDX were used to investigate the reaction extent within the pellets. Pellets which had undergone a full redox cycle were broken to expose the inner surface of the pellet. EDX was then used to visualise the carbon present within the pellet, as seen in Figure 5.5. It can be seen that carbon is present on the outer surface of the pellets but only until a certain depth, showing that the diffusion of carbon dioxide into the pellet only reaches this depth. This reaction depth was measured to be between 38 µm and 147 µm depending on the reaction temperature. There was a correlation between reaction depth and carbon monoxide production, with deeper reaction depths leading to higher yields. This reaction depth could be extrapolated to calculate the volume of pellet involved in the reaction. The percentage of the pellet involved in the reaction can then be calculated using Equation 6. Figure 5.6 shows the percentage of the pellet involved in the reaction plotted against the carbon monoxide production, and unsurprisingly, it can be seen that the more of the pellet involved in the reaction, the greater the CO yields. For the pellet oxidised at 800 °C, the reaction depth was at least as deep as the area imaged by EDX and as such the percentage reacted is greater than or equal to 20.6 %. It

is therefore clear that a 10mm pellet is not the optimum shape for maximum carbon monoxide yields as not all of the perovskite is participating in the reaction. This will be investigated further in Section 5.4.3.

$$Percentage\ of\ Pellet\ Reacted = \frac{Volume\ of\ Pellet\ Involved\ in\ Reaction}{Total\ volume\ of\ Pellet} * 100\ \#(6)$$

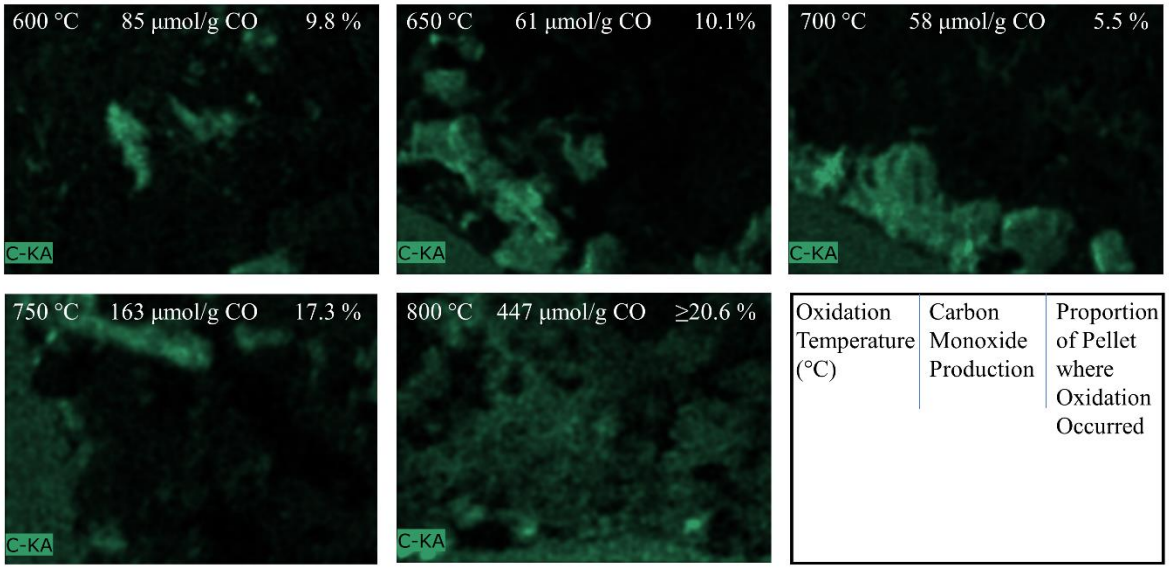

Figure 5.5. Elemental Analysis from EDX showing the presence of carbon.

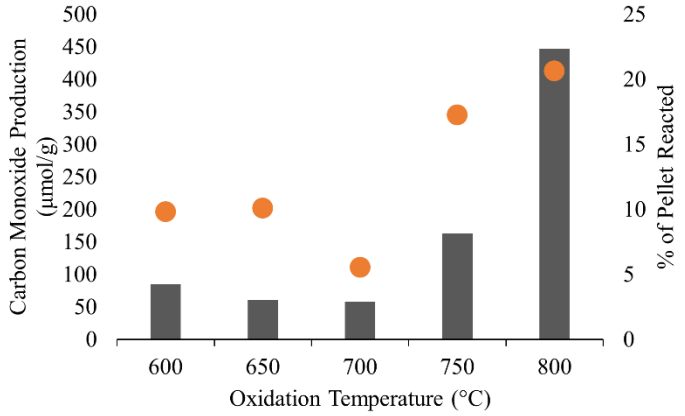

Figure 5.6. Carbon Monoxide Production plotted Against the Percentage of the Pellets Involved in the Oxidation Reaction at Different Oxidation Temperatures.

5.4.2.3 Oxidation Kinetics

The oxidation reaction was performed on fresh pellets reduced at 700 °C for 24 hours. The pellet was allowed to heat up to 800 °C under CO_2 and reacted for 1, 3, 6, 9, 12, 15, 18, 21 or

24 hours before being cooled to room temperature. The carbon monoxide production for each oxidation duration is shown in Figure 5.7(a). It can be seen that no reaction occurred during the first three hours, with the oxidation reaction starting somewhere between three and six hours. Generally, the carbon monoxide production increases as the oxidation duration increases, with 499 μmol/g of CO produced after 24 hours. From the carbon monoxide production, the solid-state conversion as a function of time was calculated, taking the CO production at 24 hours as 100% conversion (relative conversion), and is shown in Figure 5.7(b). It can be seen that there is an almost linear relationship between conversion and time.

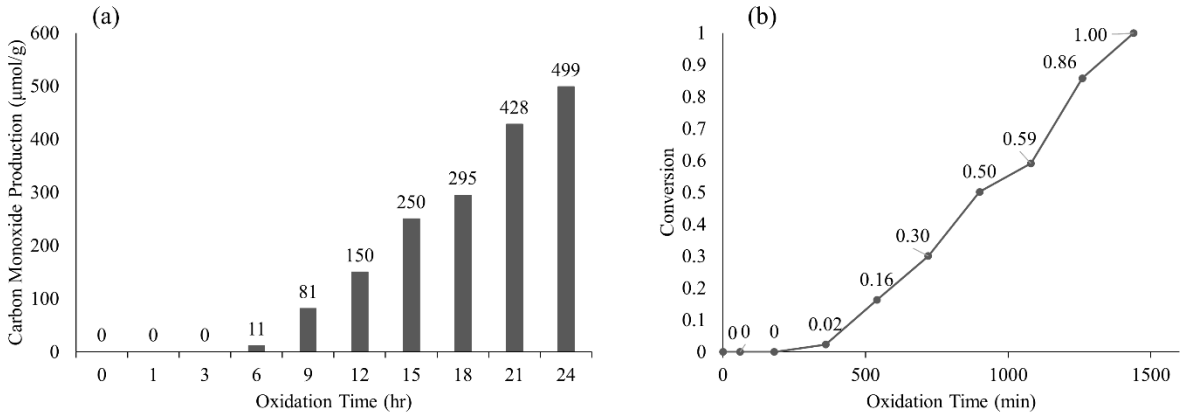

Figure 5.7. (a) Carbon Monoxide Production of BCNF1 Pellets between 1 and 24 Hours of Oxidation, (b) Conversion of Carbon Dioxide to Carbon Monoxide over Various Time Domains between 1 and 24 Hours.

5.4.3 Material Shape/Form

Since it was shown in Section 5.4.2.2 that not all of the pellet volume was involved in the oxidation reaction, different material shapes/forms were investigated including the original 10mm diameter pellet, a 5mm diameter pellet, and 0.5g or 1g of powder in a ceramic boat. It was found through image analysis that more than 90% of the powder was between 65 and 450 μm in diameter with an average sphericity of 83 %. These four shapes/forms were reduced at 700 °C for 24 hours then oxidised at 800 °C for 24 hours. The results can be seen in Figure 5.8. Firstly, the 5mm pellet performed poorly compared to the 10mm pellet, producing 255 μmol/g

of CO, likely due to the smaller surface area to volume ratio. Both powder weights resulted in exceptionally high results of around 720 μmol/g, suggesting that this approaches the upper limit of the perovskite when all of the material is able to take part in the reaction. The results also show that CO production is not dependent on the oxygen evolution in the first cycle, since both powder weights had the same CO production despite the 1g of powder producing half the oxygen of the 0.5g powder. Both the 10mm pellet and the 1g of powder were re-synthesised to be used in thermal cycling.

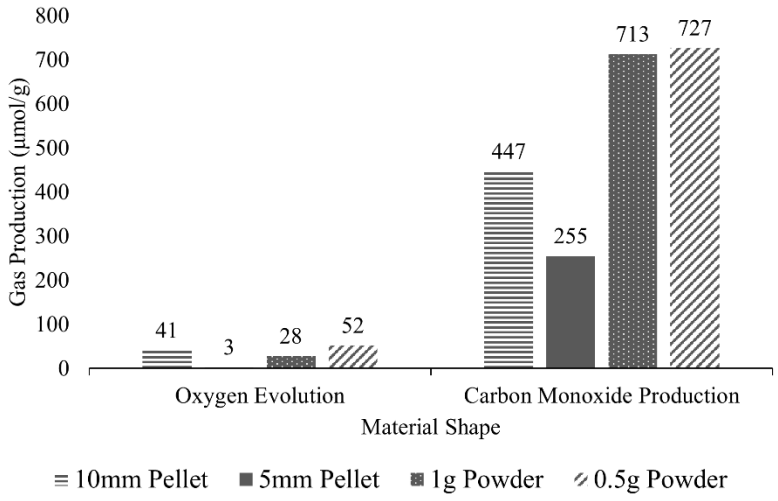

Figure 5.8. Reduction Reaction at 700 °C for 24 Hours and Oxidation Reaction at 800 °C for 24 Hours for different Shape of Material, 10mm Pellet, 5mm Pellet, 1g of Powder in a Ceramic Boat and 0.5g of Powder in a Ceramic Boat.

5.4.4 Thermal Cycling

The thermal cycling results of the 10mm pellet and 1g powder are shown in Figure 5.9(a) and (b) respectively. There are two main trends visible for the 10 mm pellet. Firstly, CO production drops from around 400 μmol/g in the first cycle to around 250 μmol/g in the second cycle but then remains constant until the 8th cycle. Secondly, the oxygen evolution increases steadily from 42 μmol/g to 127 μmol/g from the 1st to 7th cycles respectively before decreasing slightly, suggesting that changes in the morphology during cycling may be beneficial for oxygen

vacancy formation, but not for CO_2 splitting. The ratio of carbon monoxide production to oxygen evolution stabilises around 2. Since the formation of one mole of oxygen gas creates two moles of oxygen vacancies in the perovskite structure, two moles of carbon monoxide can be formed, giving a ratio of 2. This shows that for the 10mm pellet, all oxygen vacancies formed during reduction are filled during oxidation with CO_2. Looking at the results of the 1g powder in Figure 5.9(b), it can be seen that both oxygen evolution and carbon monoxide production increase throughout the ten cycles, with CO production and oxygen evolution stabilising around 620 μmol/g and 430 μmol/g, respectively. This is much higher per gram than the 10mm pellets, suggesting that the powder is more suitable for repeated thermal cycling. However, the carbon monoxide to oxygen production ratio of the powder stabilises around 1.5, suggesting that only 75 % of oxygen vacancies formed during reduction are filled during oxidation, perhaps suggesting that the oxidation reaction is not at the optimum conditions for filling oxygen vacancies in the powder.

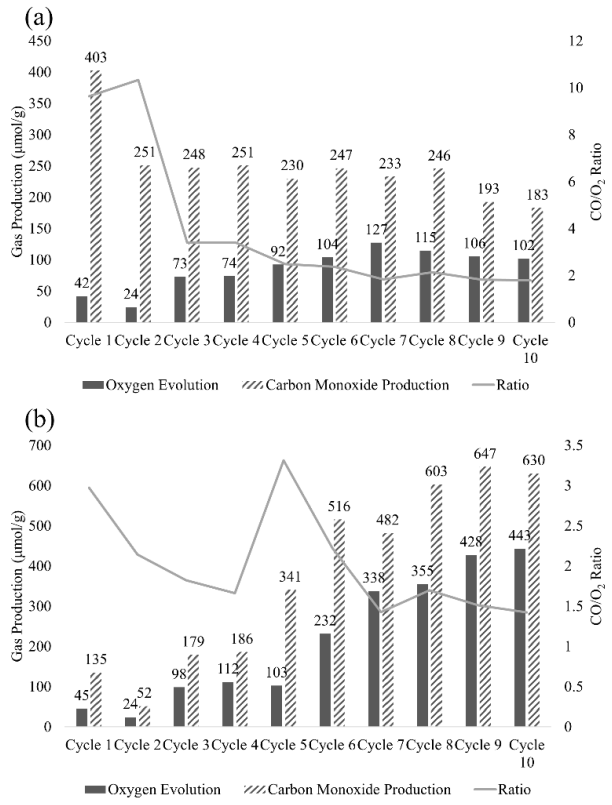

Figure 5.9. Thermal Cycling of BCNF1 over 10 Cycles for (a) 10mm Pellets, (b) 1g Powder

The reason for the higher powder yields can be explained by looking at the SEM images of pellets and powder after 10 cycles (Figure 5.10 (c, d & e)). It can be seen that the powder has a larger surface area than the pellets, both on a macroscopic (Figure 5.10 (d)) and microscopic level Figure 5.10 (e). On the other hand, the pellet is found to undergo sintering between the first and fifth cycles, with a large decrease in porosity and a concurrent increase in grain size, likely leading to much lower permeability to CO_2. By the tenth cycle, calcium is found to be deposited on the surface of the pellet. This is not seen in the powder.

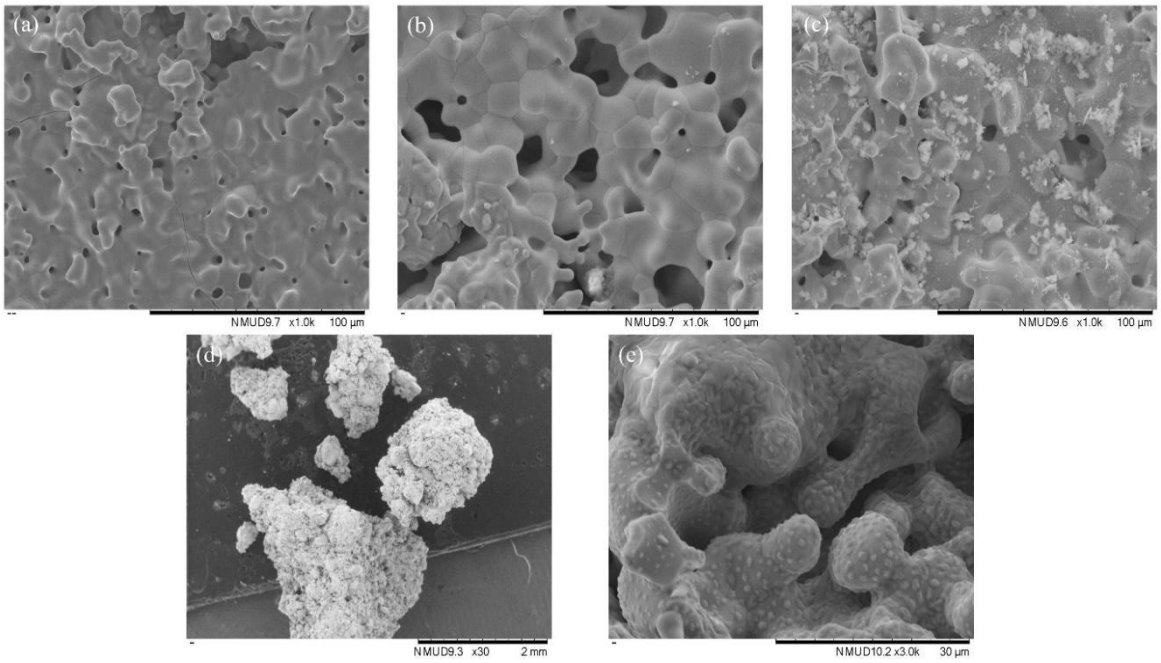

Figure 5.10. SEM Images of BCNF1 (a) 10mm Pellet before Thermal Cycling, (b) 10mm Pellet after 5 Cycles, (c) 10mm Pellet after 10 Cycles, (d) Powder after 10 Cycles at 30x Magnification, (e) Powder after 10 Cycles at 3000x Magnification

Given the success of the powder, 18g of BCNF1 powder was reacted under optimum conditions, namely 700 °C reduction for 24 hours followed by 800 °C oxidation for 24 hours. This larger sample of powder was found to release 132 µmol/g of oxygen and 859 µmol/g of carbon monoxide. Therefore, optimising the reaction conditions has increased CO yields from

160 μmol/g to 859 μmol/g, a greater than five-fold increase. This is more effective than many dopants or supports used in the literature to improve yields.

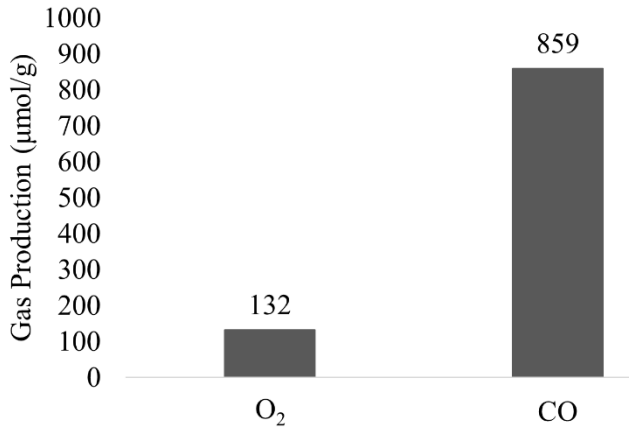

Figure 5.11. Oxygen Evolution and Carbon Monoxide Production of 18g of BCNF1 Reacted in a Ceramic Boat under Optimum Conditions.

5.5 Conclusions

This research aims to uncover the optimum conditions for the thermochemical splitting of CO_2 using $Ba_2Ca_{0.66}Nb_{0.34}FeO_6$. It was found that for the reduction reaction under nitrogen, the optimum is the reaction at 700 °C for 24 hours, although when heating costs and energy use are considered, 18 hours may be preferable. The oxidation reaction was found to be optimal at 800 °C, producing 447 μmol/g , with CO production decreasing between 600 °C and 700 °C before increasing from 700 °C to 800 °C, due to the competing factors of thermodynamics and gas diffusion. The oxidation reaction is exothermic, therefore lower temperatures shift the equilibrium towards carbon monoxide production, while between 600 and 700 °C diffusion occurs *via* Knudsen and normal diffusion. Above 750 °C, diffusion occurs only via molecular diffusion, where the diffusion rate is independent of pore size. EDX analysis showed that only a small outer volume of the pellets is taking part in the oxidation reaction, such as around 17 % at 750 °C, meaning the pellet shape was suboptimal for efficient gas exchange throughout the whole pellet. Meanwhile, 0.5 g or 1 g of perovskite powder in a small ceramic boat

produced around 720 μmol/g of CO, suggesting that more of the perovskite is able to participate in the reaction. The powder of BCNF1 was found to be thermally stable after ten cycles of reduction and oxidation, with carbon monoxide yields increasing throughout the cycles up to 630 μmol/g. This brings the carbon monoxide yields of this material in line with the most successful thermochemical materials, the lanthanum strontium manganites and ceria. In conclusion, the CO yields of this perovskite have been substantially increased, improving its suitability for the repeated production of carbon monoxide from carbon dioxide and acting as a source of negative carbon emissions.

5.6 References

[1] Intergovernmental Panel on Climate Change, Climate Change 2021: The Physical Science Basis. Contribution of Working Group I to the Sixth Assessment Report of the Intergovernmental Panel on Climate Change, 2021.

[2] IRENA, Reaching zero with renewables: Eliminating CO2 emissions from industry and transport in line with the 1.5^0C climate goal, (2020) 216. https://www.irena.org/publications/2020/Sep/Reaching-Zero-with-Renewables.

[3] S. Gota, C. Huizenga, K. Peet, N. Medimorec, S. Bakker, Decarbonising transport to achieve Paris Agreement targets, Energy Effic. (2018) 1–24. https://doi.org/10.1007/s12053-018-9671-3.

[4] G. Abdulkareem-Alsultan, N. Asikin-Mijan, Y.H. Taufiq-Yap, Sustainable Development for Energy, Power, and Propulsion, in: Green Energy Technol., 2021: pp. 505–522. https://doi.org/10.1007/978-981-15-5667-8_20.

[5] E. Worrell, L. Price, M. Neelis, C. Galitsky, Z. Nan, World Best Practice Energy Intensity Values for Selected Industrial Sectors, Lawrence Berkeley Natl. Lab. (2007) 51. https://escholarship.org/uc/item/77n9d4sp.

[6] H. Kirsch, N. Lochmahr, C. Staudt, P. Pfeifer, R. Dittmeyer, Production of CO2-neutral liquid fuels by integrating Fischer-Tropsch synthesis and hydrocracking in a single micro-structured reactor: Performance evaluation of different configurations by factorial design experiments, Chem. Eng. J. 393 (2020) 124553.

https://doi.org/10.1016/j.cej.2020.124553.

[7] N. Monnerie, P.G. Gan, M. Roeb, C. Sattler, Methanol production using hydrogen from concentrated solar energy, Int. J. Hydrogen Energy. (2020). https://doi.org/10.1016/j.ijhydene.2019.12.200.

[8] F. Lin, M. Rothensteiner, I. Alxneit, J.A. Van Bokhoven, A. Wokaun, First demonstration of direct hydrocarbon fuel production from water and carbon dioxide by solar-driven thermochemical cycles using rhodium-ceria, Energy Environ. Sci. 9 (2016) 2400–2409. https://doi.org/10.1039/c6ee00862c.

[9] M. Ali, H.M. Koo, S. Kasipandi, G.Y. Han, J.W. Bae, Direct synthesis of liquid fuels and aromatics from syngas over mesoporous FeZrOx catalyst mixed with Mo/ferrierite, Fuel. 264 (2020) 116851. https://doi.org/10.1016/j.fuel.2019.116851.

[10] D. Marxer, P. Furler, J. Scheffe, H. Geerlings, C. Falter, V. Batteiger, A. Sizmann, A. Steinfeld, Demonstration of the Entire Production Chain to Renewable Kerosene via Solar Thermochemical Splitting of H_2O and CO_2, Energy and Fuels. 29 (2015) 3241–3250.

[11] F. Fischer, H. Tropsch, Process for the production of paraffin-hydrocarbons with more than one carbon atom, U.S Patent 1746464, 1930.

[12] M. Marchese, E. Giglio, M. Santarelli, A. Lanzini, Energy performance of Power-to-Liquid applications integrating biogas upgrading, reverse water gas shift, solid oxide electrolysis and Fischer-Tropsch technologies, Energy Convers. Manag. X. 6 (2020) 100041. https://doi.org/10.1016/j.ecmx.2020.100041.

[13] S. Mehariya, A. Iovine, P. Casella, D. Musmarra, A. Figoli, T. Marino, N. Sharma, A. Molino, Fischer–Tropsch synthesis of syngas to liquid hydrocarbons, INC, 2020. https://doi.org/10.1016/b978-0-12-815936-1.00007-1.

[14] H. Mahmoudi, H. Jahangiri, O. Doustdar, N. Akbari, J. Wood, A. Tsolakis, M.L. Wyszynski, Maximizing paraffin to olefin ratio employing simulated nitrogen-rich syngas via Fischer-Tropsch process over Co3O4/SiO2 catalysts, Fuel Process. Technol. 208 (2020) 106477. https://doi.org/10.1016/j.fuproc.2020.106477.

[15] R.J. Panlener, R.N. Blumenthal, J.E. Garnier, A thermodynamic study of nonstoichiometric cerium dioxide, J. Phys. Chem. Solids. 36 (1975) 1213–1222.

https://doi.org/10.1016/0022-3697(76)90017-2.

[16] B. Zhao, C. Huang, R. Ran, X. Wu, D. Weng, Two-step thermochemical looping using modified ceria-based materials for splitting CO2, J. Mater. Sci. 51 (2016) 2299–2306. https://doi.org/10.1007/s10853-015-9534-7.

[17] A. Demont, S. Abanades, High redox activity of Sr-substituted lanthanum manganite perovskites for two-step thermochemical dissociation of CO2, RSC Adv. 4 (2014) 54885–54891. https://doi.org/10.1039/c4ra10578h.

[18] A. Demont, S. Abanades, Solar thermochemical conversion of CO2 into fuel via two-step redox cycling of non-stoichiometric Mn-containing perovskite oxides, J. Mater. Chem. A. 3 (2015) 3536–3546. https://doi.org/10.1039/c4ta06655c.

[19] I.S. Metcalfe, B. Ray, C. Dejoie, W. Hu, C. de Leeuwe, C. Dueso, F.R. García-García, C.M. Mak, E.I. Papaioannou, C.R. Thompson, J.S.O. Evans, Overcoming chemical equilibrium limitations using a thermodynamically reversible chemical reactor, Nat. Chem. 11 (2019) 638–643. https://doi.org/10.1038/s41557-019-0273-2.

[20] E. V. Ramos-Fernandez, N.R. Shiju, G. Rothenberg, Understanding the solar-driven reduction of CO 2 on doped ceria, RSC Adv. 4 (2014) 16456–16463. https://doi.org/10.1039/C4RA01242A.

[21] T. Kodama, N. Gokon, Thermochemical cycles for high-temperature solar hydrogen production, Chem. Rev. 107 (2007) 4048–4077.

[22] M. Kubicek, A.H. Bork, J.L.M. Rupp, Perovskite oxides-a review on a versatile material class for solar-to-fuel conversion processes, J. Mater. Chem. A. 5 (2017) 11983–12000. https://doi.org/10.1039/c7ta00987a.

[23] J.R. Scheffe, A. Steinfeld, Oxygen exchange materials for solar thermochemical splitting of H_2O and CO_2: A review, Mater. Today. 17 (2014) 341–348. https://doi.org/10.1016/j.mattod.2014.04.025.

[24] R.R. Bhosale, G. Takalkar, P. Sutar, A. Kumar, F. AlMomani, M. Khraisheh, A decade of ceria based solar thermochemical H2O/CO2 splitting cycle, Int. J. Hydrogen Energy. 44 (2018) 34–60.

[25] W.C. Chueh, S.M. Haile, A thermochemical study of ceria: Exploiting an old material for new modes of energy conversion and CO_2 mitigation, Philos. Trans. R. Soc. A. 368

(2010) 3269–3294. https://doi.org/10.1098/rsta.2010.0114.

[26] M.M. Nair, S. Abanades, Experimental screening of perovskite oxides as efficient redox materials for solar thermochemical CO 2 conversion, Sustain. Energy Fuels. 2 (2018) 843–854. https://doi.org/10.1039/C7SE00516D.

[27] S. Dey, B.S. Naidu, A. Govindaraj, C.N.R. Rao, Noteworthy performance of La1-xCaxMnO3 perovskites in generating H2 and CO by the thermochemical splitting of H2O and CO2, Phys. Chem. Chem. Phys. 17 (2015) 122–125. https://doi.org/10.1039/c4cp04578e.

[28] A. Bonk, A.C. Maier, M.V.F. Schlupp, D. Burnat, A. Remhof, R. Delmelle, A. Steinfeld, U.F. Vogt, The effect of dopants on the redox performance, microstructure and phase formation of ceria, J. Power Sources. 300 (2015) 261–271. https://doi.org/10.1016/j.jpowsour.2015.09.073.

[29] G. Takalkar, R.R. Bhosale, F. AlMomani, A. Kumar, A. Banu, A. Ashok, S. Rashid, M. Khraisheh, A. Shakoor, A. al Ashraf, Thermochemical splitting of CO2 using solution combustion synthesized LaMO3 (where, M = Co, Fe, Mn, Ni, Al, Cr, Sr), Appl. Surf. Sci. 509 (2020) 144908. https://doi.org/10.1016/j.apsusc.2019.144908.

[30] G. Takalkar, R.R. Bhosale, F. AlMomani, S. Rashid, Co-precipitation synthesized nanostructured Ce0.9Ln0.05Ag0.05O2−δ materials for solar thermochemical conversion of CO2 into fuels, J. Mater. Sci. (2020). https://doi.org/10.1007/s10853-020-04567-w.

[31] A.J. Carrillo, A.H. Bork, T. Moser, E. Sediva, Z.D. Hood, J.L.M. Rupp, Modifying La0.6Sr0.4MnO3 Perovskites with Cr Incorporation for Fast Isothermal CO2-Splitting Kinetics in Solar-Driven Thermochemical Cycles, Adv. Energy Mater. 9 (2019) 1–13. https://doi.org/10.1002/aenm.201803886.

[32] A.H. Bork, M. Kubicek, M. Struzik, J.L.M. Rupp, Perovskite La0.6Sr0.4Cr1-xCoxO3-δ solid solutions for solar-thermochemical fuel production: Strategies to lower the operation temperature, J. Mater. Chem. A. 3 (2015) 15546–15557. https://doi.org/10.1039/c5ta02519b.

[33] Q. Jiang, J. Tong, G. Zhou, Z. Jiang, Z. Li, C. Li, Thermochemical CO_2 splitting reaction with supported $La_xA_{1-x}Fe_yB_{1-y}O_3$ (A=Sr, Ce, B=Co, Mn; $0 \leq x, y \leq 1$) perovskite

oxides, Sol. Energy. 103 (2014) 425–437. https://doi.org/10.1016/j.solener.2014.02.033.

[34] H. Kildahl, Z. Jiang, A. Palacios, C. Song, X. Zhang, H. Zheng, H. Cao, Z. He, X. Liu, L. Wang, L. Tong, Y. Li, Y. Xuan, Y. Ding, Thermal and Thermochemical Energy Conversion and Storage, in: 2020: pp. 257–301. https://doi.org/10.1021/bk-2020-1364.ch010.

[35] P. Shrestha, M.M. Nair, N. Mahinpey, Isothermal redox cycling of A- and B-site substituted manganite-based perovskites for CO2 conversion, Can. J. Chem. Eng. (2021) 1–11. https://doi.org/10.1002/cjce.24019.

[36] X. Liu, T. Wang, K. Gao, X. Meng, Q. Xu, C. Song, Z. Zhu, H. Zheng, Y. Hao, Y. Xuan, Ca- And Ga-Doped LaMnO3for Solar Thermochemical CO2Splitting with High Fuel Yield and Cycle Stability, ACS Appl. Energy Mater. 2021 (2021). https://doi.org/10.1021/acsaem.1c01274.

[37] L. Wang, T. Ma, S. Dai, T. Ren, Z. Chang, L. Dou, M. Fu, X. Li, Experimental study on the high performance of Zr doped LaCoO3 for solar thermochemical CO production, Chem. Eng. J. 389 (2020) 124426. https://doi.org/10.1016/j.cej.2020.124426.

[38] A. Riaz, P. Kreider, F. Kremer, H. Tabassum, J.S. Yeoh, W.L. Lipiński, A. Lowe, W. Lipiński, A. Lowe, Electrospun Manganese-Based Perovskites as Efficient Oxygen Exchange Redox Materials for Improved Solar Thermochemical CO 2 Splitting, ACS Appl. Energy Mater. 2 (2019) 2494–2505. https://doi.org/10.1021/acsaem.8b01994.

[39] S. Dey, B.S. Naidu, C.N.R. Rao, Ln 0.5 A 0.5 MnO 3 (Ln=Lanthanide, A= Ca, Sr) Perovskites Exhibiting Remarkable Performance in the Thermochemical Generation of CO and H 2 from CO 2 and H 2 O, Chem. - A Eur. J. 21 (2015) 7077–7081. https://doi.org/10.1002/chem.201500442.

[40] A.H. Bork, M. Kubicek, M. Struzik, J.L.M. Rupp, Perovskite La0.6Sr0.4Cr1-xCoxO3-δ solid solutions for solar-thermochemical fuel production: Strategies to lower the operation temperature, J. Mater. Chem. A. 3 (2015) 15546–15557. https://doi.org/10.1039/c5ta02519b.

[41] H. Kildahl, Z. Li, H. Cao, P. Slater, Y. Ding, Carbon dioxide decomposition through

gas exchange in barium calcium iron niobates, Catal. Today. 364 (2021) 211–219. https://doi.org/10.1016/j.cattod.2020.05.024.

[42] S. Mulmi, H. Chen, A. Hassan, J.F. Marco, F.J. Berry, F. Sharif, P.R. Slater, E.P.L. Roberts, S. Adams, V. Thangadurai, Thermochemical CO2 splitting using double perovskite-type $Ba_2Ca_{0.66}Nb_{1.34-x}Fe_xO_{6-\delta}$, J. Mater. Chem. A. 5 (2017) 6874–6883.

[43] S. Li, Chemical Reaction and Transport Phenomena in Heterogeneous System, in: Chem. React. Eng., Elsevier, 2017: pp. 265–310. https://doi.org/10.1016/B978-0-12-410416-7.00006-9.

[44] L. Kleiminger, T. Li, K. Li, G.H. Kelsall, Syngas (CO-H2) production using high temperature micro-tubular solid oxide electrolysers, Electrochim. Acta. 179 (2015) 565–577. https://doi.org/10.1016/j.electacta.2015.07.062.

Chapter 6 – CARBON MONOXIDE PRODUCTION BY THERMOCHEMICAL CO_2 SPLITTING – A TECHNO-ECONOMIC ASSESSMENT

6.1 Abstract

This research presents the splitting of CO_2 by $Ba_2Ca_{0.66}Nb_{0.34}FeO_6$ (BCNF1) at the 100g scale in a purpose built reactor and the techno-economic assessment of the industrial scale up of a carbon monoxide production facility based upon this perovskite. BCNF1 was found to convert 10.1 % of carbon dioxide (CO_2) to carbon monoxide (CO) with 100% selectivity at 800 °C, which was sustained for five thermochemical cycles showing little sign of degradation. This oxidation reaction was found to proceed *via* a zero-order reaction mechanism at 800 °C, with an activation energy of 46.6 kJ/mol. This activation energy for CO_2 splitting is lower than all bar one of the perovskites investigated in the literature, explaining the lower oxidation temperature required and higher CO yields of this material. Economic evaluation of an industrial scale-up system based on this data suggested profitability despite high sensitivity to electricity prices, as expected. At an electricity price of $0.15 per kWh, a 150 m^3/hr plant would produce CO at $0.26 per kg, and at $0.15 per kg at the average industrial US electricity price of $0.068/kWh. This is significantly cheaper than reported costs of electrochemically produced CO in the literature. As electricity prices fall due to abundant renewables, larger production volumes become optimal, with $1.3 million a year profits for a 500 m^3/hr plant at $0.05/kWh.

This chapter is in a publishable format but has not yet been published. H. Kildahl is the first author, responsible for research and writing. Y. Ding and H. Cao are responsible for supervision and editing. L. Wang and L. Tong are responsible for validation.

6.2 Introduction

The chemical industry is responsible for almost 5% of global energy use and produces over 1.7 Gt of CO_2 each year [1]. The majority of the feedstocks are obtained from oil and gas and only 3% renewable electricity is used. Decarbonisation of the chemical industry will require electrification, a circular economy, particularly for products like plastics, and carbon capture if crude oil continues to be used as a feedstock. Another option is a low carbon feedstock, allowing for the production of the same materials without the embedded carbon emissions. Carbon monoxide, both on its own and in combination with hydrogen as synthesis gas, could be this feedstock. Carbon monoxide is already widely used in the chemical sector as a reactant and research has demonstrated the production of a large number of chemicals from carbon monoxide including; acetic acid, formic acid, and precursors of polyurethane and polycarbonate plastics [2]. The production of other chemicals and fuels *via* the Fischer-Tropsch route has also been demonstrated including, methane, ethanol and higher order fuels such as kerosene [3,4]. The production of these fuels could also aid in the decarbonisation of other hard-to-decarbonise sectors such as shipping and freight.

The realisation of this decarbonisation relies on the production of net-carbon neutral carbon monoxide. Currently the production of carbon monoxide relies on the gasification of coal, steam reforming of natural gas, and partial oxidation of hydrocarbons, all of which are carbon intensive [5]. One low carbon solution for the production of carbon monoxide is the electrolysis of carbon dioxide. Many different electrolysis methods have been proposed, although most suffer from a low technology readiness level (TRL) of 1-4 [2]. High temperature solid oxide electrolysis cells (HTSOEC) are approaching commercialisation, with temperatures between 700 and 900 °C required. It is estimated that current HTSOEC can produce carbon monoxide at $0.38 per kg with an electricity price of $0.068 per kWh [6]. Low temperature electrolysis (LTSOEC) is expected to cost $0.44 per kg with an electricity price of $0.03 per kWh [7].

This research looks at an alternative method of net-carbon neutral carbon monoxide production, namely the thermochemical splitting of CO_2. Many materials are capable of undergoing a thermochemical cycle to split small molecules such as water or carbon dioxide. Several perovskites, materials with the formula ABO_3, have been found to have high carbon monoxide yields, as seen in Table 6.1. The particularly high yields of $Ba_2Ca_{0.66}Nb_{0.34}FeO_6$ (BCNF1) found in the authors' previous research suggest that this may be an optimal material to scale up. Not only are the yields higher, but the reaction also occurs at a lower temperature.

This paper first aims to investigate the activation energy of the CO_2 splitting reaction on BCNF1 to understand the higher yields. The first experimental scale up of BCNF1 will then be investigated at the 100g scale in a purpose built reactor. This will allow the conversion of carbon dioxide to carbon monoxide to be calculated. The conversion will allow a techno-economic assessment to be performed for a BCNF1 based industrial carbon monoxide plant. The economic feasibility and cost of carbon monoxide production in $ per kg will then be evaluated.

Table 6.1. Carbon Monoxide Yields of Several Perovskites Undergoing Thermochemical Cycles

Perovskite	Carbon Monoxide Yield (μmol/g)	Reduction/Oxidation Temperature (°C)	Reference
$La_{0.6}Sr_{0.4}MnO_3$	469	1350/1000	[8]
$La_{0.5}Ca_{0.5}MnO_3$	525	1400/1100	[9]
$Y_{0.5}Sr_{0.5}MnO_3$	757	1400/900	[10]
$Pr_{0.2}Sr_{0.8}MnO_3$	637	1400/1000	[11]
$Sm_{0.5}Ca_{0.5}MnO_3$	580	1400/1100	[10]
$La_{0.6}Ca_{0.4}Mn_{0.8}Ga_{0.2}O_3$	515	1350/1050	[12]
$La_{0.5}Sr_{0.5}Mn_{0.95}Sc_{0.05}O_3$	545	1400/1100	[13]

$Ba_2Ca_{0.66}Nb_{0.34}FeO_6$	859	700/800	Authors' Previous Research

6.3 Methodology

6.3.1 Perovskite Synthesis

$Ba_2Ca_{0.66}Nb_{0.34}FeO_6$ (BCNF1) was synthesised by mixing stoichiometric quantities of the precursors $BaCO_3$ (Alfa Aesar, 99%), $CaCO_3$ (Alfa Aesar, 99%), Nb_2O_5 (Alfa Aesar, 99.5%) and Fe_2O_3 (J.T Baker, 99%) [14]. The solid state reaction was performed by grinding the powders in a mortar and pestle to ensure a well-mixed powder was formed. This powder was calcined in air at 1000 °C for 12 hours before being ground again to a fine powder. In the following experiments, the perovskite was used as both a powder and as 10mm pellets. To create the powder, the fine powder after calcining was sintered at 1400 °C for 24 hours, while for the pellets the calcined powder was compressed into 10mm pellets with an isostatic pressure of 120 MPa for 1 minute (Lloyd Instruments, LS100Plus), before sintering in the same way.

6.3.2 Kinetics

Kinetics experiments were performed on 10mm pellets in a tubular furnace (Elite Thermal Systems Ltd TSH15/50/450). Fifty-four pellets were used, with two pellets per experimental condition. All pellets were reduced at 700 °C for 24 hours under nitrogen. The oxidation reaction was performed at 800 °C, 750 °C and 700 °C for 1, 3, 6, 9, 12, 15, 18, 21, or 24 hours with the addition of carbon dioxide. The mass of each pellet before reduction, after reduction and after oxidation was recorded and the corresponding gas production calculated. The activation energy was calculated from this kinetic data.

6.3.3 Lab-Based Scale Up

100g of perovskite powder was synthesised as above. The parent compounds were mixed, then split into four portions of 25g, each in a ceramic cup, for calcining and sintering. A purpose built rig was constructed, allowing the powder to reside in a 1" diameter reactor, as seen in Figure 6.1. During reduction at 700 °C for 24 hours, nitrogen gas was passed through the reactor at 40 ml/min. The temperature was increased to 800 °C, the optimum oxidation temperature, and the gas flow was changed to carbon dioxide at 40 ml/min. This was repeated for five full thermochemical cycles. During the first cycle, the gas leaving the reactor was collected in gas collection bags every hour between hour 0 and hour 11. For cycles two to five, a gas sample was collected every hour between hours 12 and 23. These gas samples were used for gas chromatography (GC).

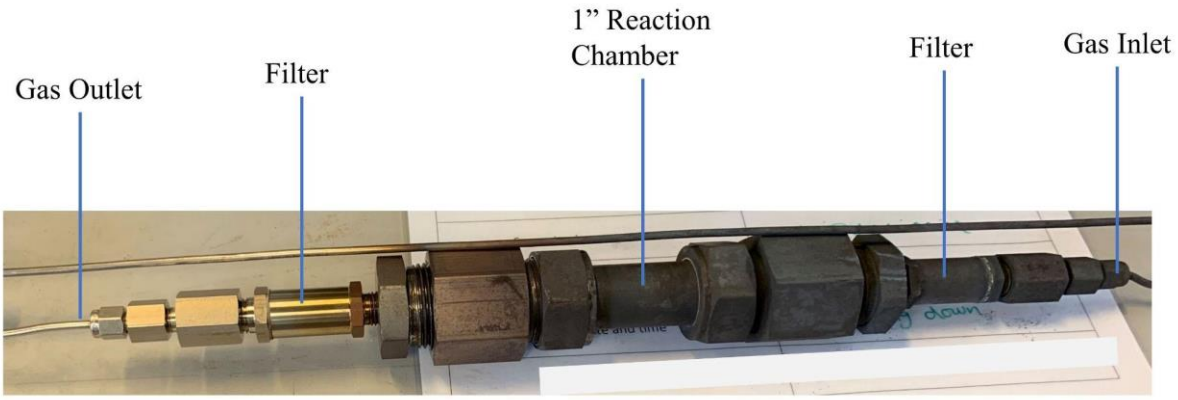

Figure 6.1 Image of the 100g Scale-Up rig with 1" reactor

6.3.4 Gas Chromatography

A Thermo Fischer Scientific Trace 1300 Gas Chromatograph with a direct gas injection valve and a fused silica PLOT column (Restek RT-Q-BOND) was used to separate carbon dioxide and carbon monoxide in the reaction gas. First, calibration curves were obtained by injecting 0.5, 1.0, 15, 2.0 and 2.5 ml of each gas standard (carbon dioxide, carbon monoxide and nitrogen) to find the relationship between gas volume and peak area. The calibration curves

can be found in the supplementary information (Supplementary Figure 6.1). To analyse the reaction gas, 1 ml of gas was injected into the GC, with a split ratio of 50 and helium carrier gas. The peak area of carbon monoxide and carbon dioxide can then be used to calculate the conversion of the carbon dioxide splitting reaction by BCNF1.

6.4 Results & Discussion

6.4.1 Kinetics

Figure 6.2(a) shows the carbon monoxide yields of BCNF1 at different oxidation temperatures over time. It can clearly be seen that 800 °C is the optimal temperature of the three due to significantly higher CO production over all time domains. As the temperature decreases so does carbon monoxide production. The maximum CO production of 498 μmol/g (800 °C, 24 hours) was used as a baseline to calculate the conversion (*Xa*) at each point, shown in Figure 6.2(b). Plotting *ln(ln(1-Xa))* against *ln(t)*, where *t* is the time in seconds, gives a Hancock & Sharpe plot (Figure 6.3). The slope of the plot, *m* (inset of Figure 6.3), gives information about the type of mechanism of redox reactions, for example, when m is below one the reaction is diffusion controlled. Since for all oxidation temperatures *m* is greater than one, the reaction is phase boundary controlled. A linear best fit method of different phase-boundary controlled mechanisms was therefore applied to understand more about the oxidation reaction. The various models that were tested can be seen in Supplementary Table 6.1.

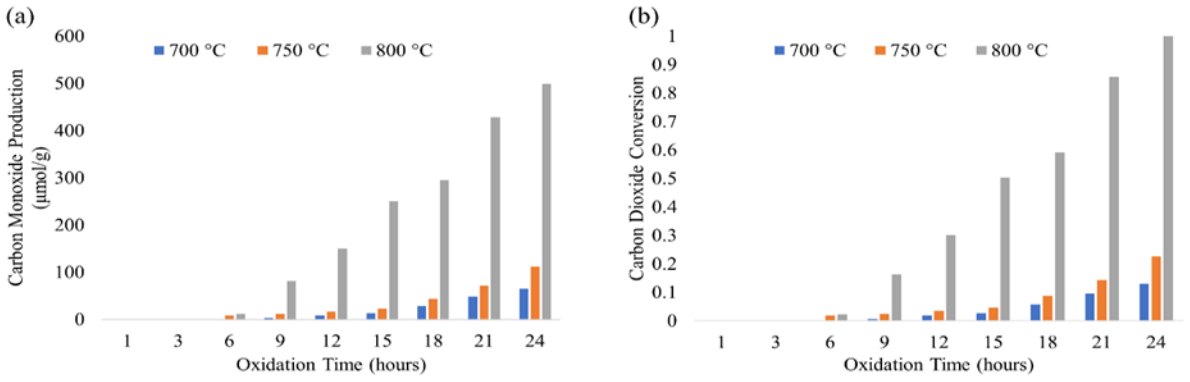

Figure 6.2. (a) Carbon Monoxide Production at 700 °C, 750 °C and 800 °C between 1 and 24 hours, (b) Carbon Dioxide Conversion at 700 °C, 750 °C, and 800 °C between 1 and 24 hours relative to maximum conversion (800 °C, 24 hours)

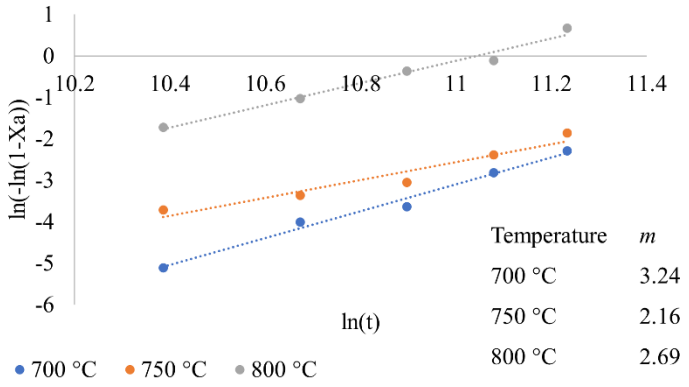

Figure 6.3. Hancock & Sharp plot, obtained by plotting ln(-ln(1-Xa)) against ln(t), where Xa is the conversion and t is the time in seconds

The reaction at 800 °C was found to have best fit with a zero order model (R^2 = 0.9905), suggesting that the splitting of carbon dioxide into carbon monoxide at this temperature depends only on time and not on the concentration of carbon dioxide, non-stoichiometry of the perovskite or conversion extent. This is very favourable as at this temperature the splitting reaction will occur at its maximum rate no matter how far along the reaction is. Best fit for the reaction at 700 °C was found with an Avrami-Erofeyev 4 model (R^2 = 0.9912), where conversion is low at the beginning and end of the time period but speeds up during the middle of the time period. The reaction occurs at the same rate in all directions and the rate of conversion does not depend on the extent of conversion. Best fit could not be found in the models tested for the reaction at 750 °C. Therefore, for the purposes of creating an Arrhenius plot, the reaction at 750 °C was taken to be a 50/50 mix of a zero order reaction and Avrami-Erofeyev 4. Figure 6.4(a) shows the rate constant at each temperature, as obtained from the models discussed above.

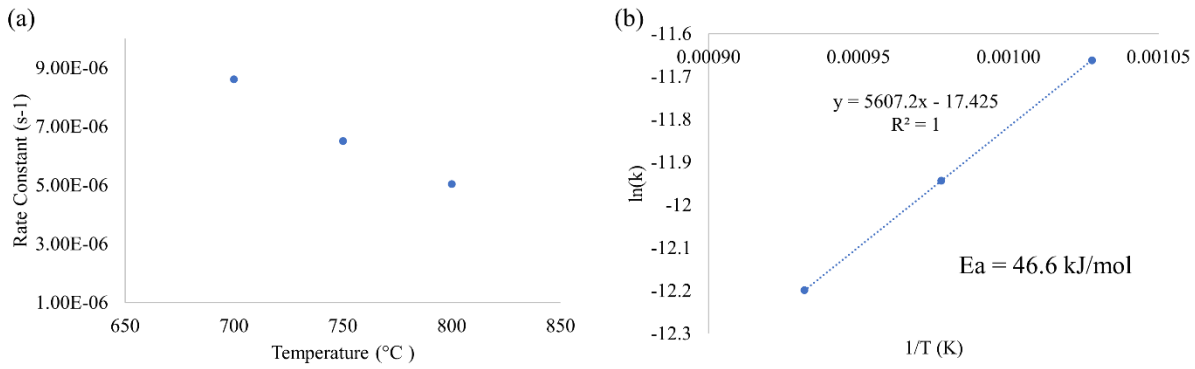

Figure 6.4.(a) Rate constants at Various Oxidation Temperatures, (b) Arrhenius plot

The Arrhenius plot for the oxidation reaction is shown in Figure 6.4(b) and gives an activation energy (Ea) of 46.6 kJ/mol. This is compared with the oxidation reaction of similar materials in Table 6.2. It can be seen that the activation energy of BCNF1 is lower than all lanthanum manganites (LSMO) studied except for $La_{0.625}Ca_{0.375}Mn_{0.5}Cr_{0.5}O_3$, suggesting the CO_2 splitting reaction is more favourable with BCNF1 than for most LSMO [15]. This is demonstrated by the temperature required for the oxidation reaction, which is 800 °C in this work and at least 1050 °C for LSMOs. When compared with barium magnesium iron niobates, an increase in the iron content decreases the activation energy. $BaMg_{0.33}Nb_{0.5}Fe_{0.17}O_3$ has a higher Ea than BCNF1 while $BaMg_{0.33}Nb_{0.34}Fe_{0.33}O_3$ has almost half the Ea of BCNF1, suggesting the CO_2 splitting reaction on this perovskite is more favourable than BCNF1 [16]. However, given that LSMO is often considered the industry standard, the lower activation energy of BCNF1 is extremely promising and partially explains the higher carbon monoxide yields seen from this material. The low activation energy of the oxidation reaction with BCNF1 suggests that this material may be favourable for industrial scale-up.

Table 6.2. Activation Energy of the Perovskite Oxidation Reaction under Carbon Dioxide

Material	Activation Energy (kJ/mol)	Reference
$Ba_2Ca_{0.66}Nb_{0.34}FeO_6$	46.62	This work

$BaMg_{0.33}Nb_{0.67}O_3$	92.60	[16]
$BaMg_{0.33}Nb_{0.5}Fe_{0.17}O_3$	69.50	[16]
$BaMg_{0.33}Nb_{0.34}Fe_{0.33}O_3$	24.10	[16]
$La_{0.625}Ca_{0.375}MnO_3$	54.78	[15]
$La_{0.625}Sr_{0.375}MnO_3$	68.65	[15]
$La_{0.625}Ca_{0.375}Mn_{0.5}Al_{0.5}O_3$	92.23	[15]
$La_{0.625}Sr_{0.375}Mn_{0.5}Al_{0.5}O_3$	78.11	[15]
$La_{0.625}Ca_{0.375}Mn_{0.5}Cr_{0.5}O_3$	43.37	[15]
$La_{0.625}Sr_{0.375}Mn_{0.5}Cr_{0.5}O_3$	54.59	[15]
$La_{0.625}Ca_{0.375}Mn_{0.5}Fe_{0.5}O_3$	75.59	[15]
$La_{0.625}Sr_{0.375}Mn_{0.5}Fe_{0.5}O_3$	75.70	[15]
$La_{0.625}Ca_{0.375}Mn_{0.5}Ga_{0.5}O_3$	90.36	[15]
$La_{0.625}Sr_{0.375}Mn_{0,5}Ga_{0.5}O_3$	74.49	[15]

6.4.2 100g Scale-Up

The results from the purpose-built reactor containing 100g of BCNF1 are shown in Figure 6.5. During cycle 1 (Figure 6.5(a)), the gas was changed from nitrogen to carbon dioxide and the temperature was then allowed to equilibrate at 800 °C. The first gas sample was then taken (Hour 0) and was found to contain nitrogen, showing that not all of the nitrogen had been displaced from the furnace. Nitrogen and carbon monoxide have similar retention times in the column used in the GC analysis, with nitrogen being eluded a fraction earlier. This means that the conversion at the beginning of this cycle, as determined by relative peak areas, includes both nitrogen and carbon monoxide. Between hour 0 and hour 5, the peak was seen to shift to longer retention times, suggesting the displacement of nitrogen by carbon dioxide and carbon monoxide. As seen in Figure 6.2(a), the oxidation reaction was found to begin between 6 and 9 hours. This is consistent with what is seen here, with a large increase in conversion occurring between hours 7 and 8. Most importantly, no other peaks were seen on the GC spectra, showing that the splitting of CO_2 by BCNF1 is 100% selective towards carbon monoxide.

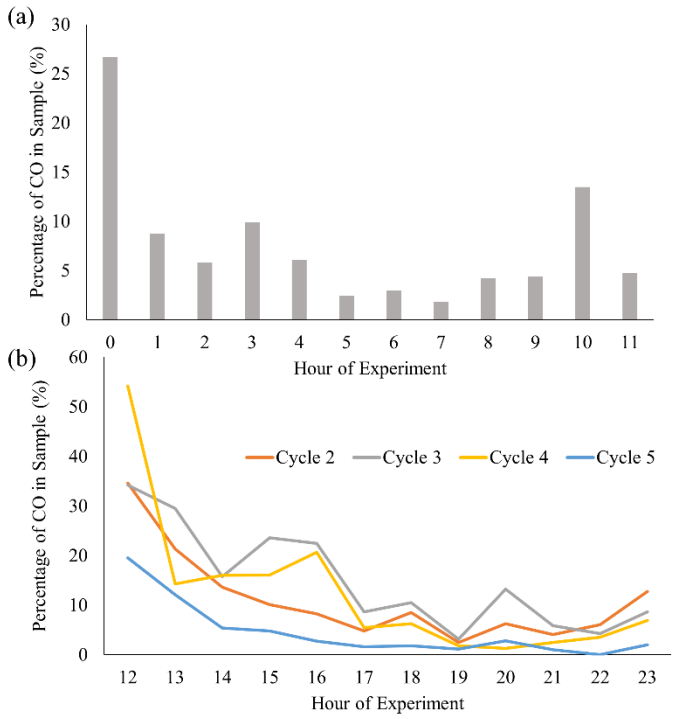

Figure 6.5. CO_2 Conversion to CO in (a) Cycle 1 between 0 and 11 hours, (b) Cycles 2-5 between 12 and 23 hours

Looking at cycles 2-5 (Figure 6.5(b)), there is some variation between the cycles, but the overall trend remains the same. Exceptionally high carbon dioxide conversions are seen at hour 12, with between 54 and 19% of the gas analysed found to be carbon monoxide depending on the cycle. Conversion generally decreased between hour 13 and hour 18, with the lowest conversions seen consistently at hour 19. Conversion continues at a lower rate between 19 and 22 hours, with an uptick in conversion seen at hour 23. An average conversion of 10.1 % was achieved between 12 and 23 hours in cycles 2 to 5. This shows the advantage of reacting the perovskite powder in a packed bed, rather than as 10mm pellets which were found to have a conversion of 1.4 %. The packed bed allows the carbon dioxide to come into contact with a greater surface area of perovskite and suggests that in an industrial setting, a fluidised bed may produce even higher conversions due to extreme solid and gas mixing [17].

6.4.3 Industrial Plant Scale-Up

The conversion data was used to perform a techno-economic assessment of an industrial CO production plant based on BCNF1. Three scenarios were analysed. In the first scenario (S1), the heater size was determined by the power needed to heat from room temperature to the reduction temperature (700 °C) at 5 °C/min with enough BCNF1 to produce 100 m^3/hr of CO. This gives a heater power requirement of 1.2 MW. The second scenario (S2) is where the heater power is estimated based on 100 m^3/hr of CO production but for heating between the reduction (700 °C) and oxidation (800 °C) temperatures at 5 °C/min only. In this scenario a 0.2 MW heater is needed, with additional heating requirements for the first cycle to heat from room temperature to 700 °C likely being needed. The final scenario (S3) is based on a 150 m^3/hr CO production with heater power calculated in the same way as the second scenario. This would require a heater with a 0.3 MW power rating. Some parameters of the three scenarios can be found in Table 6.3. Several assumptions were made in this calculation which can be found in the Supplementary Information. The specific heat capacity of BCNF1 was taken to be 0.7 kJ/kgK, based on data from similar perovskites [18–22]. The system operates continuously, the reduction and oxidation each occurring for 24 hours.

Table 6.3. Three Scenarios of the Scale-Up of a BCNF1 based Facility for the Production of CO

Scenario	1	2	3
CO Production	100 m^3/hr	100 m^3/hr	150 m^3/hr
Heater Power Calculated from	20-700 °C at 5 °C/min	700-800 °C at 5 °C/min	700-800 °C at 5 °C/min
Heater Power	1.2 MW	0.2 MW	0.3 MW
Mass of BCNF1 Needed	17,132 kg	17,132 kg	25,698 kg
Minimum Volume of Reactor	4.3 m^3	4.3 m^3	6.4 m^3
Cost of Raw Materials	$115,422	$115,422	$173,134
Total Cost of Producing Perovskite	$121,764	$121,764	$182,646

Cost of First Cycle Starting from Room Temperature	$4,100	$1,436	$2,154
Electricity Cost of Subsequent Cycles	$3,257	$593	$865
Tonnes of CO per Year	510	510	765
Cost per Tonne of CO Produced	$1,221	$270	$264
Energy Intensity	21.7 MJ/kg	5.1 MJ/kg	4.9 MJ/kg
Electricity Intensity	7.75 kWh/kg	1.41 kWh/kg	1.37 kWh/kg

Both scenarios 2 and 3 are profitable on a yearly basis, producing carbon monoxide at a cost of $270 and $264 per tonne, respectively. The market price of carbon monoxide is around $600 [23]. Indeed, both scenarios are profitable up to electricity prices of $0.39 per kWh, allowing for short term fluctuations in electricity prices. The higher hourly CO production of Scenario 3 compared to Scenario 2 (150 m^3/hr compared to 100 m^3/hr), leads to more efficient CO production, requiring 0.2 MJ less energy per kg of CO produced. On the other hand, scenario 1 is not profitable at an electricity price of $0.15 per kWh, producing CO at a cost of $1221 per tonne, due to the larger electricity needs of such a high-powered heater, as demonstrated by the drastically higher energy and electricity intensity compared to Scenarios 2 and 3. Indeed, Scenario 1 is only profitable with electricity prices of $0.07/kWh and lower, which while not unreasonable given the price of renewables, still makes Scenario 1 unfavourable.

The yearly carbon monoxide sales, expenditure and profit or loss for each scenario have been calculated and can be seen in Figure 6.6(a). Figure 6.6(b) shows the effect of electricity prices on the yearly profit or loss. It can be seen that the higher the electricity usage, the greater effect electricity prices have, as seen by the steeper slope for scenario 3 compared to scenario 2. For scenarios 2 and 3, profits increase as electricity prices decrease below $0.15/kWh.

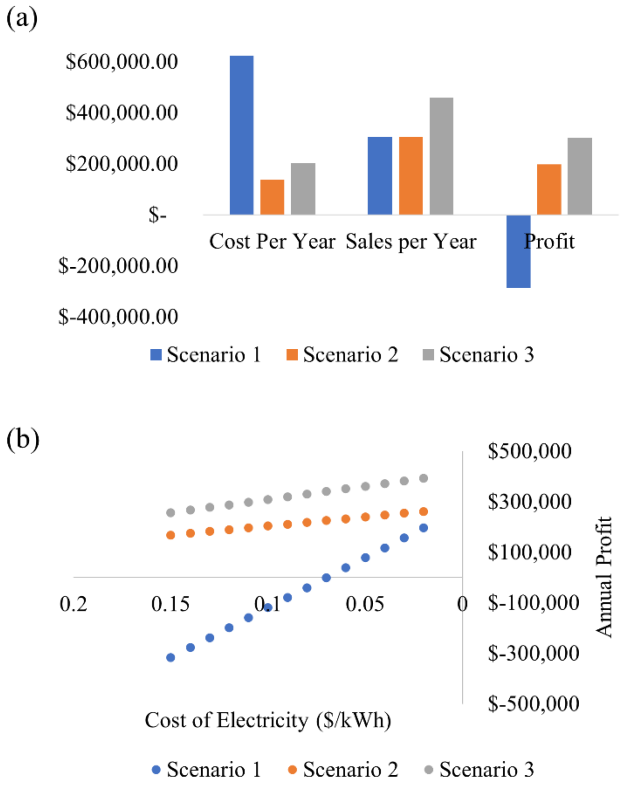

Figure 6.6(a) Annual Costs, Sales and Profits for Three Scenarios, (b) Effect of Electricity Prices on Profits in the Three Scenarios

This relationship shows that as electricity costs continue to fall due to the widespread implementation of solar and wind, larger production volumes will become more and more profitable. For example, increasing carbon monoxide production by 50 m^3/hr requires an extra 0.1MW of heater power, 8500 kg of perovskite, and $60,000 of capital expenditure but produces an extra 255 tonnes of CO a year, $152,000 of sales and $103,000 of profit at an electricity price of $0.15 per kWh. However, if electricity prices were $0.05 per kWh, increasing production by 50 m^3/hr would create an extra $136,000 of profit. In this case, producing 500 m^3/hr of CO would create profits of $1.36 million. Therefore, this technology is highly scalable and sensitive to electricity prices. Costs could be reduced further by acting as demand response, using cheap electricity from the grid when demand is low. Other methods of increasing profits could be to separate the oxygen produced during reduction from the nitrogen reducing gas, selling the oxygen at around $40 per tonne [24]. Another revenue stream

that is likely to become increasingly important is carbon credits, the value of each tonne of CO_2 removed from the atmosphere. According to the World Bank, 21.5 % of global greenhouse gas emissions are covered by emissions trading schemes or carbon taxes, with prices ranging from $20 to $130 per tonne, and the EU emissions trading scheme priced at $50 per tonne [25].

Table 6.4. Cost of CO Production per kg for Different Technologies with Variable Electricity Price (HTSOEC = High Temperature Solid Oxide Electrolysis Cell, LTSOEC = Low Temperature Solid Oxide Electrolysis Cell, TC-BCNF1 = Thermochemical Cycle of BCNF1, S3= Scenario 3)

Technology	Electricity Price ($/kWh)	CO Production Cost ($/kg)	Reference
HTSOEC	0.068	0.38	[6]
LTSOEC	0.03	0.44	[7]
TC-BCNF1 (S3)	0.15	0.26	This Work
TC-BCNF1 (S3)	0.068	0.15	This Work
TC-BCNF1 (S3)	0.03	0.10	This Work

Table 6.4 shows the cost of carbon monoxide production for different technologies in the literature and the electricity prices the simulation was calculated at. Given that the electricity price in other research is much lower than the $0.15/kWh used here, the CO production of S3 was recalculated at these lower electricity prices to allow for easier comparison. It can be seen that even at higher electricity prices, the thermochemical splitting of CO_2 by BCNF1 (TC-BCNF1) is far cheaper than either high temperature or low temperature solid oxide electrolyte cells, likely due to the smaller number of components in the system.

6.5 Conclusion

This paper demonstrates the successful lab-scale demonstration of $Ba_2Ca_{0.66}Nb_{0.34}FeO_6$ in a 100g system for the splitting of carbon dioxide into carbon monoxide. The mechanism of this reaction was found to proceed *via* a zero order mechanism at 800 °C, showing that at this

temperature CO_2 splitting is dependent only on time. Meanwhile, at 700 °C this reaction proceeds *via* an Avrami-Erofeyev 4 mechanism, where CO production follows an s-shaped curve. The activation energy of this CO_2 splitting reaction was found to be 46.62 kJ/mol, lower than the industry standard perovskite, the lanthanum manganites. The favorability of the reaction with BCNF1 compared with LSMO is demonstrated by the lower oxidation temperature required for this reaction, 800 °C against over 1050 °C. The 100g reactor investigated here was able to split 10.1 % of CO_2 into CO, as calculated from GC. This conversion was used for a techno-economic assessment of an industrial CO production facility, which can be profitable with electricity prices as high as $0.39 per kWh. All scenarios investigated were found to be sensitive to electricity prices, with lower electricity prices favouring larger reactors and production volumes. For example, at $0.05 per kWh a 150 m^3/hr system would have yearly profits of $406,000, while a 500 m^3/hr system would give profits of $1.36 million a year. Finally, at an electricity price of $0.15 per kWh, BCNF1 can produce carbon monoxide at a price of $0.26 per kg, far lower than reported for electrochemical systems.

6.6 References

[1] IRENA. Reaching zero with renewables: Eliminating CO2 emissions from industry and transport in line with the 1.5^0C climate goal 2020:216.

[2] Küngas R. Review—Electrochemical CO 2 Reduction for CO Production: Comparison of Low- and High-Temperature Electrolysis Technologies . J Electrochem Soc 2020;167:044508. doi:10.1149/1945-7111/ab7099.

[3] Hanaoka T, Miyazawa T, Shimura K, Hirata S. Jet fuel synthesis from Fischer-Tropsch product under mild hydrocracking conditions using Pt-loaded catalysts. Chem Eng J 2015;263:178–85. doi:10.1016/j.cej.2014.11.042.

[4] Panzone C, Philippe R, Chappaz A, Fongarland P, Bengaouer A. Power-to-Liquid catalytic CO2 valorization into fuels and chemicals: Focus on the Fischer-Tropsch

route. J CO2 Util 2020;38:314–47. doi:10.1016/j.jcou.2020.02.009.

[5] Küngas R. Review—Electrochemical CO 2 Reduction for CO Production: Comparison of Low- and High-Temperature Electrolysis Technologies . J Electrochem Soc 2020;167:044508. doi:10.1149/1945-7111/ab7099.

[6] Huang Z, Grim RG, Schaidle JA, Tao L. The economic outlook for converting CO2and electrons to molecules. Energy Environ Sci 2021;14:3664–78. doi:10.1039/d0ee03525d.

[7] Shin H, Hansen K., Jiao F. Techno-economic assessment of low-temperature carbon dioxide electrolysis. Nat Sustain 2021;4:911–9.

[8] Luciani G, Landi G, Aronne A, Di Benedetto A. Partial substitution of B cation in La0.6Sr0.4MnO3 perovskites: A promising strategy to improve the redox properties useful for solar thermochemical water and carbon dioxide splitting. Sol Energy 2018;171:1–7. doi:10.1016/j.solener.2018.06.058.

[9] Dey S, Naidu BS, Govindaraj A, Rao CNR. Noteworthy performance of La1-xCaxMnO3 perovskites in generating H2 and CO by the thermochemical splitting of H2O and CO2. Phys Chem Chem Phys 2015;17:122–5. doi:10.1039/c4cp04578e.

[10] Dey S, Naidu BS, Rao CNR. Ln 0.5 A 0.5 MnO 3 (Ln=Lanthanide, A= Ca, Sr) Perovskites Exhibiting Remarkable Performance in the Thermochemical Generation of CO and H 2 from CO 2 and H 2 O. Chem - A Eur J 2015;21:7077–81. doi:10.1002/chem.201500442.

[11] Takalkar G, Bhosale RR, AlMomani F. Thermochemical splitting of CO2 using Co-precipitation synthesized Ce0.75Zr0.2M0.05O2-Δ (M = Cr, Mn, Fe, CO, Ni, Zn) materials. Fuel 2019;256:115834. doi:10.1016/j.fuel.2019.115834.

[12] Liu X, Wang T, Gao K, Meng X, Xu Q, Song C, et al. Ca- And Ga-Doped LaMnO3for Solar Thermochemical CO2Splitting with High Fuel Yield and Cycle Stability. ACS Appl Energy Mater 2021;2021. doi:10.1021/acsaem.1c01274.

[13] Dey S, Naidu BS, Rao CNR. Beneficial effects of substituting trivalent ions in the B−site of La 0.5 Sr 0.5 Mn 1−x A x O 3 (A = Al, Ga, Sc) on the thermochemical generation of CO and H 2 from CO 2 and H 2 O. Dalt Trans 2016;45:2430–5.

doi:10.1039/C5DT04822B.

[14] Mulmi S, Chen H, Hassan A, Marco JF, Berry FJ, Sharif F, et al. Thermochemical CO2 splitting using double perovskite-type $Ba_2Ca_{0.66}Nb_{1.34-x}Fe_xO_{6-\delta}$. J Mater Chem A 2017;5:6874–83.

[15] Fu M, Wang L, Ma T, Ma H, Xu H, Li X. Mechanism of CO production around oxygen vacancy of LaMnO3: An efficient and rapid evaluation of the doping effect on the kinetics and thermodynamic driving force of CO2-splitting. J Mater Chem A 2020;8:1709–16. doi:10.1039/c9ta09764c.

[16] Kannan R, Mulmi S, Thangadurai V. Synthesis and characterization of perovskite-type $BaMg_{0.33}$ $Nb_{0.67-x}$ Fe_x $O_{3-\delta}$ for potential high temperature CO2 sensors application. J Mater Chem A 2013;1:6874.

[17] Mirmohamadsadeghi S, Karimi K. Recovery of silica from rice straw and husk. Elsevier B.V.; 2020. doi:10.1016/B978-0-444-64321-6.00021-5.

[18] Guyot F, Richet P, Courtial P, Gillet P. High-temperature heat capacity and phase transitions of CaTiO3 perovskite. Phys Chem Miner 1993;20:141–6. doi:10.1007/BF00200116.

[19] Mastronardo E, Qian X, Coronado JM, Haile S. Fe-doped CaMnO3 for thermochemical heat storage application. AIP Conf Proc 2019;2126. doi:10.1063/1.5117754.

[20] Manzoor S, Ahmed A, Rashid A, Ahmad S, Shaheen S. Study of Magnetothermal Properties of Strontium Doped Lanthanum Manganite Nanoparticles for Hyperthermia Applications. IEEE Trans Magn 2013;49:3504–3407. doi:10.1016/j.jmmm.2013.07.045.

[21] Kim D, Zink BL, Hellman F, Coey JMD. Critical behavior of La0.75Sr0.25MnO3. Phys Rev B - Condens Matter Mater Phys 2002;65:1–7. doi:10.1103/PhysRevB.65.214424.

[22] Povoden E, Chen M, Grundy AN, Ivas T, Gauckler LJ. Thermodynamic assessment of the La-Cr-O system. J Phase Equilibria Diffus 2009;30:12–27. doi:10.1007/s11669-008-9463-0.

[23] Jouny M, Luc W, Jiao F. General Techno-Economic Analysis of CO2 Electrolysis

Systems. Ind Eng Chem Res 2018;57:2165–77. doi:10.1021/acs.iecr.7b03514.

[24] Dorris CC, Lu E, Park S, Toro FH. High-Purity Oxygen Production Using Mixed Ionic-Electronic Conducting Sorbents. Sr Des Reports 2016.

[25] Bank W. Carbon Pricing Dashboard 2021. https://carbonpricingdashboard.worldbank.org/map_data (accessed December 30, 2021).

6.7 Supplementary Information

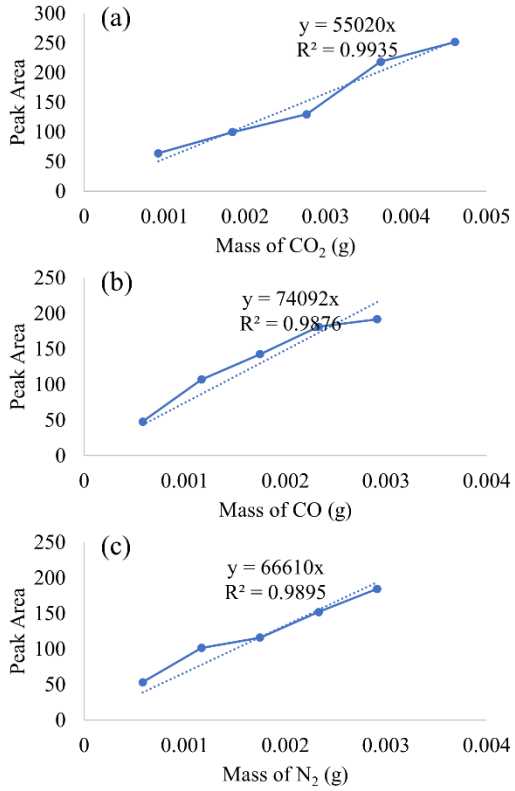

Supplementary Figure 6.1. Gas Chromatography Calibration Curves for (a) CO_2, (b) CO, (c) N_2

Supplementary Table 6.1 Phase-Boundary Controlled Models Against which the Experimental Results were Tested for Best Fit.

Model	Equation (kt =)
0 Order	Xa
1st Order	ln(1-Xa)
2nd Order	[1/(1-Xa)]-1

3rd Order	$(1/2)[(1-Xa)^{-2}-1]$
Power Law 2	$Xa^{1/2}$
Power Law 3	$Xa^{1/3}$
Power Law 4	$Xa^{1/4}$
Avrami-Erofeyev 2 (2D NGM)	$[\ln(1-Xa)]^{1/2}$
Avrami-Erofeyev 3	$[\ln(1-Xa)]^{1/3}$
Avrami-Erofeyev 4	$[\ln(1-Xa)]^{1/4}$
Prout Tompkins	$\ln[Xa/(1-Xa)]$
2D SCM	$1-(1-Xa)^{1/2}$
3D SCM	$1-(1-Xa)^{1/3}$
1D Diffusion	Xa^2
2D Diffusion	$[(1-Xa)\ln(1-Xa)]+Xa$
3D Jander's Diffusion	$[1-(1-Xa)^{1/3}]^2$
3D Ginstling Diffusion	$1-(2/3)Xa-(1-Xa)^{2/3}$
3D NGM	$[\ln(1-Xa)]^{2/3}$

Assumptions in the Scale-Up Calculations:

- The specific heat capacity of BCNF is 0.7 kJ/kgK
- The efficiency of an electric heater is 85 %
- The estimated holding power of a heater is:
    - 40 % of max power at 800 °C
    - 35 % of max power at 700 °C
- Carbon dioxide is obtained for $40/tonne
- Recouperation of unreacted CO_2 is 90%
- Nitrogen is obtained for $\$0.30/m^3$
- Recouperation of nitrogen is 90 %
- The market price of carbon monoxide is $600 per tonne

- The price of electricity is $0.15/kWh

Chapter 7 – THERMOCHEMICAL SECTOR COUPLING WITH BLAST FURNACE – BASIC OXYGEN FURNACE STEEL PRODUCTION FOR COST EFFECTIVE DECARBONISATION

7.1 Abstract

The production of iron and steel releases 9 % of global emissions and is considered a hard-to-decarbonise sector due to the inherent carbon-intensive nature of the blast furnace (BF), which produces 70 % of the iron used for steelmaking. Many options for the decarbonisation of the sector have been suggested such as shifting toward direct reduced iron and electric arc furnaces which suffer from low technology readiness levels, extremely high capital expenditure and billions in stranded assets from the then redundant BFs. We present here a decarbonisation strategy that makes use of existing BFs through coupling with a thermochemical cycle (TC-BF-BOF). A double perovskite, $Ba_2Ca_{0.66}Nb_{0.34}FeO_6$, is proposed for the thermochemical splitting of CO_2, which was recently found to be a good candidate due to its low reaction temperatures, high CO yields and 100% selectivity towards CO when compared to other TC materials. Expensive and energy intensive coke is replaced by carbon monoxide produced directly from the CO_2 emissions of the plant and other sources. In this way, carbon could be recycled in the process. Implementation of this coupling technology in the UK BFs would reduce steel sector emissions by 88 %. Within five years, implementation of the TC-BF-BOF would give total savings of £1.28 billion while reducing UK-wide emissions by 2.9 %. Finally, through cost reduction, this system would increase the cost-competitiveness of UK steel on the global market.

This chapter is in a publishable format but has not yet been published. H. Kildahl is the first author, responsible for research and writing. Y. Ding is responsible for supervision and editing. L. Wang and L. Tong are responsible for validation.

7.2 Introduction

The iron and steel sector is a major greenhouse gas emitter, releasing up to 9% of global CO_2 emissions [1]. Steel is firmly in the category of hard-to-decarbonise sectors due to the inherent carbon intensive nature of its production. Indeed, more carbon dioxide is released on a weight basis than steel produced, with 1.89 tonnes of CO_2 released for every tonne of steel produced. The main reason for this is the use of coking coal as an energy source and structural support, making up a 74% share of the total energy feedstock and accounting for 15% of the total global coal consumption [2]. Nevertheless, the sector must achieve 54 % or 90 % emissions reductions by 2050 to limit warming to 2 °C and 1.5 °C, respectively [1]. If the currently operational assets are run for their natural 40 year lifetimes, it would constitute entrenched emissions of 65 Gt of CO_{2eq}. On an annual basis the steel industry uses 2 billion tonnes of iron ore, a billion tonnes of metallurgical coal, 575 million tonnes of recycled steel and 32EJ of final energy to produce 1.7 billion tonnes of crude steel [1,2]. There are currently two main methods of steel production, the blast furnace-basic oxygen furnace (BF-BOF) route accounting for 71% of production, and natural gas based direct reduction of iron followed by an electric arc furnace (DRI-EAF) making up the other 29 % [1]. The BF-BOF route will be discussed in detail below but generally both methods consist of two parts. Firstly, iron ore is reduced to metallic iron in the BF or DRI before being converted to steel by reducing the carbon content in the metal in the BOF or EAF.

There are a few technologies that are being researched to decarbonise the steel industry [3]. The first option is to close down the old BF-BOFs and replace them with DRI-EAFs. If the EAF is powered by renewable electricity, it has the potential to save 1.5 Gt of CO_2 emissions annually [1]. However, a DRI-EAF plant costs between $1.1 and $1.7 billion to build [4], which combined with the stranded assets of the old BF-BOF plant, makes this switch economically unfeasible in the short time periods needed to meet the Paris Climate Agreement [5]. A second

option is to increase scrap recycling. Steel is already one of the most recycled materials, with an 84 % recycling rate in 2017 [1]. In 2019, 32 % of all inputs were scrap [3]. Scrap recycling results in a 90% reduction of CO_2 emissions and 70 % energy savings compared with virgin iron ore in a BF-BOF. Additionally, each tonne of scrap steel reused displaces 1400kg of iron ore, 740kg of coal and 120kg of limestone [2]. The proportion of scrap steel in the input can be up to 100% in an EAF while 20-25 % is currently the maximum input for a BF-BOF. It is expected that the share of scrap in inputs could increase to 46 % by 2050 and although this is not sufficient to decarbonise the sector alone, it could result in significant CO_2 emission reductions. Another decarbonisation option is to use hydrogen for the direct reduction of iron (HDRI), followed by EAF [2]. If renewable electricity is used to power an electrolyser to make green hydrogen, this could dramatically reduce emissions. However, this requires new DRI plants to be built to replace BF-BOFs and has a Technological Readiness Level (TRL) of 5-7, meaning the technology has been demonstrated but is not industrially operational. It has been estimated that a carbon price of \$67/tCO_{2eq} would be needed to enable HDRI to produce steel at the same price as a traditional blast furnace, provided there is sufficient low-cost renewable electricity [1]. Additionally, reducing iron with hydrogen is less efficient at lower temperatures than carbon monoxide, with the reduction from Fe_2O_3 to Fe_3O_4 occurring more readily under CO [6]. Conversely, the reduction of Fe_3O_4 to Fe at higher temperatures occurs more readily under hydrogen. Modelling suggests that hydrogen-based DRI could reduce emissions in the EU steel industry by 35 % at current grid emission levels while requiring 3.72 MWh per tonne of liquid steel produced [7]. For reference BF-BOF uses 3.48 MWh/t. The cost of hydrogen production remains prohibitive.

A related technology is natural gas DRI with carbon capture, use and storage (CCUS), which also has a TRL of 5-7. Although several methods of CCUS have been demonstrated and a few industrial CCUS facilities are operational, the cost is expected to be \$100 per tonne of CO_2 for

capture and $160 per tonne for transport and storage by 2030, with costs falling moderately by 2050 [3]. Given the extremely high emissions from iron and steel facilities, large CCUS plants would be required but emissions reductions are estimated to be between 20-80 %. Finally, another proposed solution is iron ore electrolysis, which has a TRL of 6. This technique is already used on a large scale for the manufacture of aluminium, so the technology has been proven on an industrial scale [8]. Optimisation of the electrodes and electrolyte are needed for the efficient reduction of iron.

In summary, steel production accounts for 9 % of global CO_2 emissions and must be rapidly decarbonised to limit warming to 1.5 °C. Seventy percent of existing iron and steel facilities rely on the extremely energy intensive and emission heavy BF-BOF route. Most of the current methods of decarbonising this sector rely on the phase-out of these BF-BOF plants and the implementation of lower carbon methods such as EAF and DRI plants. This will be extremely costly. This paper proposes another way to decarbonise the sector, namely by coupling a thermochemical carbon monoxide plant with a BF-BOF facility creating a closed carbon loop for the production of steel. The existing BF-BOF technology will first be examined to determine the optimal coupling. A basic description of the sector coupling will then be proposed, with expected emissions reduction and cost estimates. Finally, the superiority of this technology compared with existing decarbonisation solutions will be discussed.

7.3 Blast Furnace – Basic Oxygen Furnace

Modern blast furnaces can produce 10,000 tonnes of hot metal a day in furnaces as large as 15 metres in diameter and 35 metres tall [9]. The top of the furnace is around 200 °C while the bottom can reach temperatures in excess of 1600 °C [10]. Iron ore and coke are added to the furnace in layers. Air or oxygen enriched air, also called the blast, is injected at the bottom of the furnace, having been preheated to 1100-1350 °C by regenerative heat exchangers known as hot stoves [9]. This hot blast provides most of the heat needed in the furnace. The hot blast

reacts with the layers of coke, producing large volumes of carbon monoxide (CO) which rise through the furnace, reducing the iron ore and transferring heat to the material higher up in the furnace. Once the iron ore has been reduced to metallic iron, the liquid metal collects lower in the furnace to be tapped, or removed, from the furnace. Iron ore is often impure; therefore, limestone and other additives are used to separate these impurities from the liquid metal. For example, limestone removes sulphur from FeS to give metallic iron and CaS [10]. The CaS, having a lower density than metallic iron, rises in the furnace and forms a layer of molten slag which also contains other impurities such as SiO_2, Al_2O_3, MgO and CaO. The slag is tapped from the furnace at 1650 °C, and up to 65 % of this heat can be recuperated [11]. Around 0.275 tonnes of slag are produced per tonne of steel produced. The blast gas, mixing with carbon monoxide and carbon dioxide in the furnace, rises to the top of the furnace and is known as top gas. This top gas leaves the furnace at around 200-300 °C and has a lower heating value of 3-4 MJ per Nm^3, much of which is recovered by regenerative heat exchangers [9]. This heat, along with additional heat obtained through the combustion of this top gas is used to heat the blast to over 1100 °C, as discussed above.

Attention will now be paid to the material flows in the BF. Modern steel production *via* the BF-BOF route uses 1,370 kg of iron ore, 780 kg of metallurgical coal, 270 kg of limestone, and 125 kg of recycled steel to produce 1,000 kg of crude steel [2]. The blast requires 1500 kg of air which is fed into the bottom of the furnace via tuyeres (nozzles) [10]. The metallurgical coal must be treated before it can be used in the BF, being heated to 1250 °C for 12 hours using heat obtained from the top gas and the coke oven gas (COG). COG is the gas released from the pre-treatment of the coal once it has been quenched and cleaned. Typically, COG contains 60% H_2, 24% CH_4, 6% CO, 6% N_2, and 4% CO_2 [9]. COG is also used in the BF, since hydrogen and carbon monoxide are excellent reducing agents of iron ore. Once treated, the coke has a few main uses in a BF [9]. Firstly, the coke is a major energy source for the BF, with 95% of

the total energy being supplied from combustion of coke in the BF and making up 20-40 % of total costs. Secondly the coke reacts with oxygen to produce carbon monoxide, a good reducing agent for iron ore, then reacts with the carbon dioxide produced in the reduction to form more carbon monoxide according to the Boudouard reaction. The coke also adds carbon to the metallic iron. Finally, the coke acts as a support for the layers of iron ore and aids in gas movement through the furnace. Other reducing agents can also be injected in a blast furnace to reduce the amount of coke needed, such as pulverised coal (cheaper than metallurgical coal), hydrocarbons, waste plastics and biomass. Additionally, natural gas can replace some coke due to its decomposition to carbon monoxide and hydrogen, providing it has a methane content above 80 % [9]. There is an accepted minimum theoretical fuel value of 465 kg per tonne of hot metal produced, with modern BF coming close to this with 500 kg per tonne.

There are four main reactions occurring in a BF regarding the reduction of iron ore [9]. Iron ore is predominantly made of Fe_2O_3. There are two reaction occurring below 570 °C:

$$3Fe_2O_3 + CO \rightarrow 2Fe_3O_4 + CO_2 \quad (7.1)$$

$$\Delta H_{843K} = -30.050\text{kJ}$$

$$Fe_3O_4 + 4CO \rightarrow Fe + 4CO_2 \quad (7.2)$$

$$\Delta H_{843K} = -44.478\text{kJ}$$

Once the remaining iron ore has started to drop lower in the furnace and the temperature increases above 570 °C, the following two reactions become dominant:

$$Fe_3O_4 + CO \rightarrow 3FeO + CO_2 \quad (7.3)$$

$$\Delta H_{1073K} = +9.707\text{kJ}$$

$$FeO + CO \rightarrow Fe + CO_2 \quad (7.4)$$

$$\Delta H_{1273K} = -15.653\text{kJ}, \Delta H_{1473K} = -16.484\text{kJ}$$

The reduction of FeO (Equation 4) requires a CO concentration of at least 70 %. The so-called pig iron is tapped from the BF and injected into the BOF. Scrap metal may also be charged in

the BOF up to 25-30 % by weight [10]. No heat must be added to the BOF, instead when oxygen is blown through the molten metal, the carbon in the iron (often FeC) reacts, forming carbon monoxide and carbon dioxide while releasing heat. This reaction increases the temperature to 1650 °C. The oxygen must be a minimum of 99.9 % pure to allow for a large range of steel products to be made [12]. A total of 50-60 Nm^3 of oxygen per tonne of liquid steel (tls) is blown through a lance above the hot metal for 15 to 20 minutes, also called the blow. The steel will be tapped from the furnace every 40 minutes. Basic Oxygen Furnace Gas (BOF Gas) exits the furnace at around 1600 °C and 100 Nm^3/tls is produced, containing carbon dioxide and carbon monoxide. This BOF Gas has a heating value of around 8.8 MJ/Nm^3 [13], of which over 90 % can be recovered as heat and chemical energy [12]. However, the gas will also contain dust, up to 20 kg/tls, made up predominantly of iron oxide and lime. A slag will also form in a BOF, containing carbon, silicone, sulphur and phosphorus. Slag-forming agents are added at the beginning of the blow such as lime and dolomite, as the fast formation of the slag is needed for the removal of impurities.

7.4 Thermochemical Cycle

A thermochemical cycle consists of a reduction and oxidation reaction (redox). Many materials are capable of undergoing a thermochemical cycle, however $Ba_2Ca_{0.66}Nb_{0.34}FeO_6$ (BCNF1) will be used here due to its superior properties including high yields, low reaction temperatures, 100% selectivity towards CO, and a low activation energy of the oxidation reaction. BCNF1 is a double perovskite material. When BCNF1 is reduced at 700 °C under nitrogen, oxygen is lost from the crystal structure, forming oxygen vacancies, and releasing oxygen gas.

$$Ba_2Ca_{0.66}Nb_{0.34}FeO_6 \rightarrow Ba_2Ca_{0.66}Nb_{0.34}FeO_{6-\delta} + \frac{\delta}{2}O_2 \quad (7.5)$$

Where δ is equal to the degree of non-stoichiometry. The oxidation reaction occurs at 800 °C under carbon dioxide, causing the CO_2 to be split to CO, reincorporating the oxygen in the lattice by filling the oxygen vacancies, and reforming the original perovskite.

$$Ba_2Ca_{0.66}Nb_{0.34}FeO_{6-\delta} + \delta CO_2 \; 800\,°C \rightarrow Ba_2Ca_{0.66}Nb_{0.34}FeO_6 + \delta CO \qquad (7.6)$$

This allows the cycle of reduction and oxidation to be repeated, splitting CO_2. BCNF1 has been found to convert 10.1 % of CO_2 to CO over five cycles. The scale-up to an industrial carbon monoxide production facility was calculated. Producing 150 m^3/hr of CO would require 5700 kWh of electricity with an 85 % efficient electric heater. This plant could produce carbon monoxide at a cost of £0.19 per kg at an electricity price of £0.11/kWh. At an electricity price of £0.05 (the average US industrial electricity price), carbon monoxide would cost £0.11 per kg.

7.5 Thermochemical Blast Furnace-Basic Oxygen Furnace Coupling (TC-BF-BOF)

There exists a significant opportunity for sector coupling. The main reducing agent in a BF is carbon monoxide (currently obtained from the reaction of coke with air), with an output of large volumes of carbon dioxide responsible for the significant emissions of the system. The BOF requires large quantities of oxygen and releases carbon monoxide and carbon dioxide in the BOF Gas. Both the BOF Gas and BF top gas contain significant amounts of thermal energy. The BCNF1 thermochemical cycle has inputs of heat and carbon dioxide and outputs of carbon monoxide and oxygen. The TC-BF-BOF system proposed here is composed of two thermochemical reactors for the simultaneous production of oxygen and carbon monoxide. In one reactor the BCNF1 will be reduced, producing an oxygen stream. In the second reactor, reduced BCNF1 will be oxidised under CO_2, creating a CO stream. Once the reactions have proceeded to their optimum point, or in other words the maximum non-stoichiometry has been reached in the first reactor and all oxygen vacancies have been filled in the second reactor, the

gas flows in each reactor will be switched. The newly reduced BCNF1 in the first reactor will now produce CO and the second reactor will now undergo reduction.

7.5.1 Mass Flows

The TC-BF-BOF system is depicted in Figure 7.1, showing the mass flows of the system for the production of 1 tonne of liquid steel.

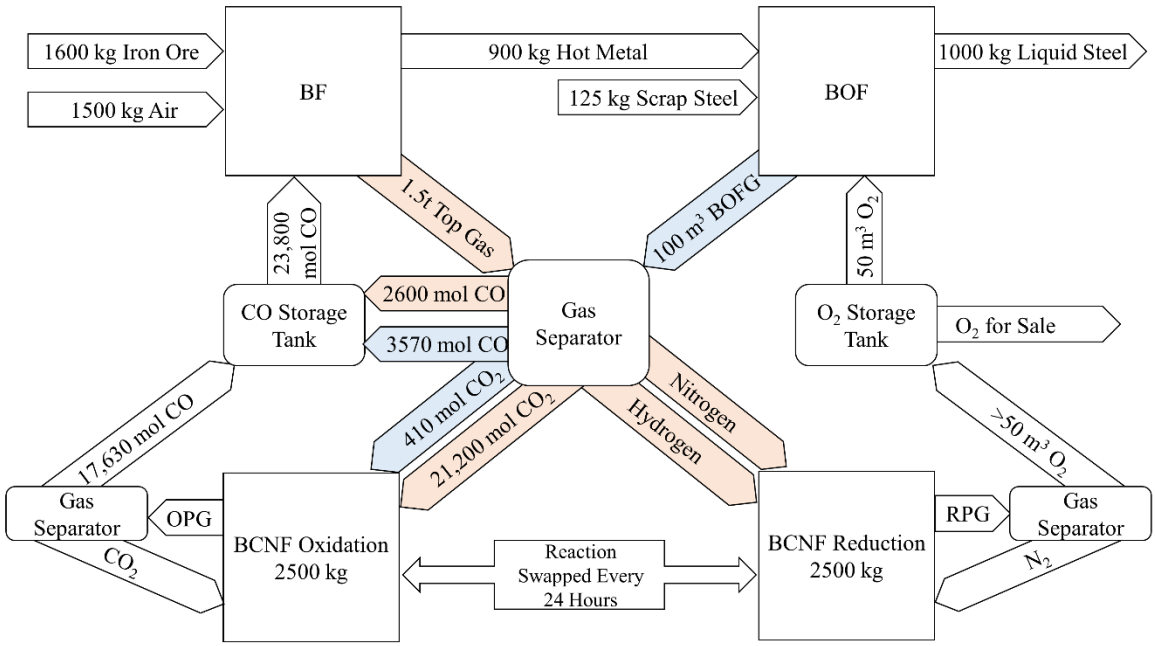

Figure 7.1. The TC-BF-BOF System with Mass Flows for the Production of 1 Tonne of Liquid Steel.

The production of 1 tonne of liquid steel in the TC-BF-BOF system occurs as follows:

- If the reduction of iron ore to metallic iron occurs via reactions (1) and (2), for every mole of Fe_2O_3, three moles of CO are needed. If the reduction proceeds via (1), (3) and (4), two moles of CO are needed. Therefore, an approximation is made in the calculation of stoichiometric quantities needed, where 2.5 moles of CO are needed per mole of Fe_2O_3. This equals 23,800 moles of CO/tls.
- The CO is injected into the BF via the tuyeres, with 1500 kg/tls of hot air-based blast.

- The iron ore is estimated to have 95 % Fe_2O_3 and 5 % impurities, and 1.599 tonnes of iron ore are needed per tls [7]. 125 kg of recycled steel is added to the hot metal in the BOF.
- The usual slag-forming agents are used at the same rates as a typical BF-BOF.
- BF top gas is typically produced at a rate of 2.5-3.5 tonnes/tls and contains 20-30 % CO, 20-25 % CO_2 and 2-6 % H_2 with the remainder being nitrogen [14]. The hydrogen content comes from the humidity in the blast furnace and the water content of the iron ore [15]. In the TC-BF, an estimated 1.5 tonnes/tls of top gas is produced, containing 5 % CO, 45 % CO_2, 2 % H_2 and 48 % N_2 due to the absence of coke and the stoichiometric volume of CO added.
- The BF top gas is separated into its constituent components. The CO is stored in the CO storage tank until it is needed, the CO_2 is added to the BCNF reactor undergoing oxidation and the nitrogen and small volume of hydrogen are added to the BCNF reactor undergoing reduction. The addition of hydrogen in the reduction step has been found to improve reduction extent and oxygen yields in similar materials [16–18].
- 50 m^3/tls of oxygen are blown into the BOF, producing BOF gas at 100 m^3/tls which contains 90 % CO and 10 % CO_2 [12][19]. The BOF gas is separated, with the CO stored in the CO storage tank and the CO_2 being added to the BCNF reactor undergoing oxidation.
- Oxygen is blown into the BOF via a lance for 15-20 minutes, with liquid steel and slag being tapped every 40 minutes [12].
- CO_2 is injected into the BCNF oxidation reactor, where 10.1 % is converted to CO with each pass. The oxidation product gas (OPG) therefore contains 10.1 % CO and 89.9 % CO_2. The CO is separated out and stored in the CO storage tank and the unreacted CO_2 is injected back into the BCNF oxidation reactor.

- The CO produced by the thermochemical cycle is enough to replace 90 % of the coke in the BF, with the remaining 10% being supplied by biomass based charcoal or recycled plastics to give a solid source of carbon for the Boudouard reaction. Theoretically, 100 % of the injected coke can be replaced by charcoal at a rate of 200 kg per tonne of hot metal (thm), reducing CO_2 emissions by 40 % and reducing slag volumes and sulphur content [13]. However, the biomass must be injected via the tuyeres rather than top loading, due to the lower mechanical strength and higher proportion of volatiles than coke. Waste plastics can also be used as a solid carbon source at a rate of 70 kg/thm.
- The nitrogen and a small volume of hydrogen obtained from the top gas are injected into the BCNF reduction reactor, where the hydrogen actively reduces the BCNF to form water and the nitrogen provides the low oxygen concentration necessary to passively reduce the BCNF. The reduction product gas (RPG) therefore contains nitrogen, oxygen, and water. The small volume of water is condensed out, the oxygen is stored in the O_2 storage tank, and the nitrogen is recycled to be used again during reduction, or released into the atmosphere.
- When the rate of oxygen evolution from the reduction reactor and carbon monoxide evolution from the oxidation reactor decreases after 24 hours, the reaction conditions and gas flows will be switched so that the reduced material now undergoes oxidation, and the oxidised material now undergoes reduction.
- One kg of BCNF produces 5.8 moles of CO in 24 hours, as determined experimentally.
- The TC-BF-BOF system would reduce CO_2 emissions by 94% compared to a typical BF-BOF, with the only emissions arising from the biomass-based charcoal since all carbon monoxide is produced from carbon dioxide.

- Coke typically acts as a structural backbone in the BF, helping to ensure even gas flows throughout the iron ore. Research is needed to understand the impact of coke removal on the structural stability of the BF. Blast furnaces have been operated with 180kg natural gas and 256 kg coke/thm, with coke rates decreasing when the natural gas is heated before injection via the tuyeres [20].

7.5.2 Energy Flows

The energy flows of the TC-BF-BOF system are shown in Figure 7.2 and are described below.

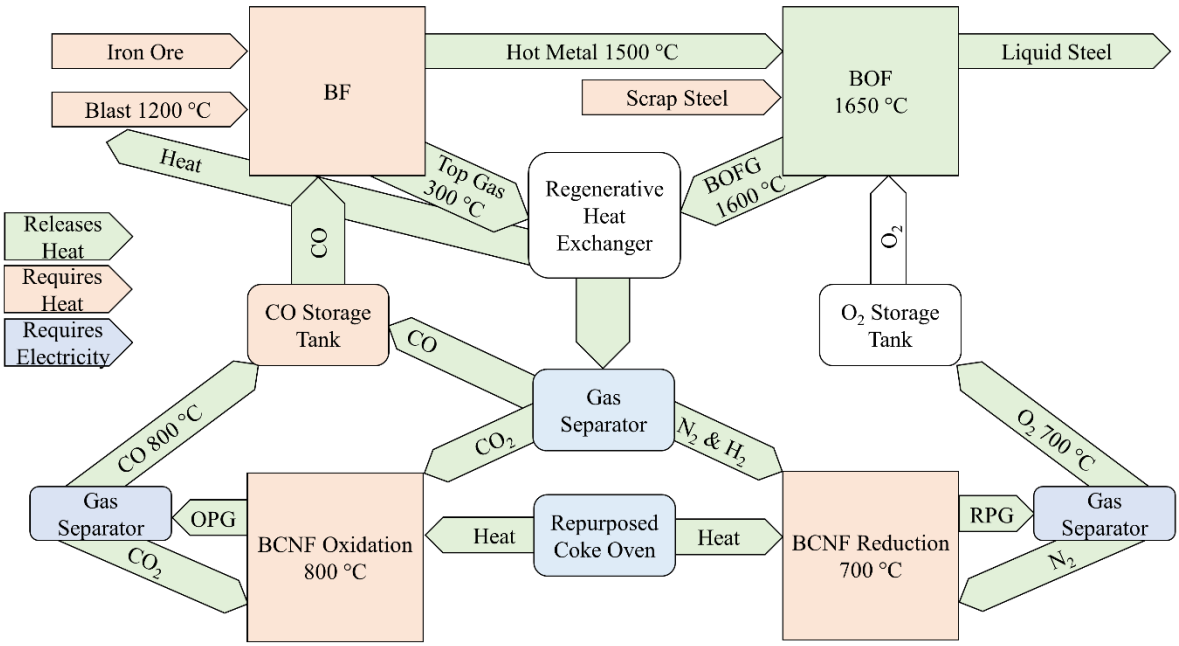

Figure 7.2. The TC-BF-BOF System with Energy Flows for the Production of 1 Tonne of Liquid Steel.

- Removing coke from the BF decreases the energy available to heat the BF to the required temperature. Usually, the reaction between coke and oxygen is exothermic, releasing heat. The 10 % biomass based charcoal will help in this, but additional heating, likely from electric heaters, may be needed to reach the required temperatures. The iron ore could be preheated to aid in this.
- The blast will be preheated from the top gas and BOF gas, as in a normal BF-BOF. BF top gas and BOF gas contain 2.7 GJ/tls [9] and 0.8 GJ/tls [13], respectively, if 90% of

the energy is recovered using the regenerative heat exchangers already in use in a BF-BOF [12]. This heat will be transferred from these gases before they are fed into the gas separator.

- The COG, BF top gas and BOF gas are usually combusted after the thermal energy has been extracted to produce electricity needed for the BF-BOF. Given that COG does not exist in the TC-BF-BOF system and that top gas and BOF gas are now entirely recycled by the TC reactors, this electricity production is no longer possible. Electricity must therefore be imported.
- The carbon monoxide leaving the TC reactor is at a temperature of 800 °C, decreasing the heating requirements for a blast at 1200 °C. This may require the temperatures in the CO storage tank to be maintained at around 800 °C. This could be achieved by heat transfer from the oxygen produced in the reduction reactor since oxygen does not need to be heated before introduction into the BOF.
- The BOF does not require any extra heat or fuels since heat is generated by the reaction between oxygen and iron carbide (FeC).
- Liquid steel leaves the BOF at above 1500 °C. Once the steel has been cast into its final shape, some heat could be recuperated for use in the TC-BF-BOF.
- The coke oven would no longer be needed for coke preparation, saving 1.1 GJ/tls of primary energy [21]. 2.2 GJ/tls is needed to power the TC reactors. This means the electricity and electric heaters previously used to heat coal to 1250 °C for 12 hours could be repurposed to maintain the temperature in the TC reactors and to heat the BCNF1 from the reduction temperature of 700 °C to the oxidation temperature of 800 °C when the reaction conditions are being switched over. Therefore, an extra 1.1 GJ/tls of electricity used to power an electric heater is likely to be necessary to run the TC reactors.

- If the electricity needed to power the electric heaters and gas separators is procured from renewable sources, this would not add to the emissions of the TC-BF-BOF. The cost of this electricity, plus the electricity needed to power the gas separators, is more than accounted for in the savings from replacing the coke in the system.

7.6 Decarbonisation of the UK Steel Industry

The TC-BF-BOF system proposed above could be used to decarbonise the UK steel industry. The UK currently has five steel producing companies; Tata Steel and British Steel which operate BF-BOFs, and British Steel, Liberty Steels and Outokumpu which operate EAFs [22]. Six million tonnes of steel products are made via the BF-BOF route out of the 7.65 million tonnes produced in the UK annually. BF-BOFs in the UK therefore account for around 94 % of total emissions of the UK Steel sector based on an emissions intensity of 1.89 tCO_{2eq}/tls for the BF-BOF route and 0.44 tCO_{2eq}/tls for the EAF route [23,24]. EAFs can be more easily decarbonised with the use of renewable electricity and/or 100 % recycled steel. On the other hand, decarbonising a BF-BOF is far more difficult due to the inherent carbon intensive nature of the process. Their decarbonisation is crucial for the UK to reach its net-zero emissions goal by 2050.

Tata Steel and British Steel both produce around three million tonnes of steel a year at their Port Talbot and Scunthorpe sites, respectively. Due to the similar production values, the same TC-BF-BOF system can be used in both cases, as described hereafter. 42,500 tonnes of BCNF1 would be required to produce the 124 million moles a day of carbon monoxide necessary to displace 90 % of the coke, with the remaining 10 % displaced by a solid carbon source such as biomass-based charcoal. The BCNF1 would be split into ten reactors that are 15m tall and 9.5m in diameter, with five reactors undergoing reduction and five undergoing oxidation at any one time. The raw materials to produce the required amount of BCNF1 would cost £210 million, which may need to be replaced every 5-10 years based on current estimates. In addition to the

CO, these reactors would produce 1.3 million m^3 of oxygen a day, of which 420,000 m^3 would be required in the BOF. This excess oxygen production could generate £35,000/day. Additionally, the displacement of 90 % of the coke by CO would save £187 million a year [25]. The energy requirements to power the TC cycle are 3.6 TJ per reactor for a full cycle of reduction and oxidation over 48 hours. The reduction reaction uses 85 % of this energy due to the high endothermic enthalpy of reduction of 620 kJ/kg, while the enthalpy of oxidation is exothermic and therefore releases energy (-45.1 kJ/kg [26]). The implementation of the TC-BF-BOF system requires an additional 2.2 GJ/tls, where a typical BF-BOF requires between 19.8 and 31.2 GJ/tls [9]. The now redundant coke oven could be repurposed, producing 1.1 GJ/tls of heat. As discussed above, there are large amounts of energy in the top gas and BOF gas. If 90 % of this energy is recovered *via* the regenerative heat exchangers already in use, this equals 3.5 GJ/tls, higher than the energy use of the TC system. Alternatively, if the TC reactors were exclusively powered by electricity, it would require 607kWh/tls, costing around £42/tls. This is drastically lower than HDRI which requires 3.72 MWh/tls [7]. If this was taken from the UK grid electricity, which has an emissions factor of 212 gCO_{2eq}/kWh, this would produce 129 $kgCO_{2eq}$/tls, equal to 6.9 % of current emissions per tonne of liquid steel. Both financially and environmentally, using as high a share of renewable electricity as possible is beneficial.

Most importantly, implementation of the TC-BF-BOF system would reduce emissions from 5.7 million tonnes CO_{2eq} per site to 340,000 tonnes CO_{2eq}. Even if no improvements in emissions were seen from the EAF plants in operation, implementation of this system would reduce UK steel emissions by 88 % and the share of emissions from BFs would decrease from 94 % to 48 %. Currently, the Steel industry emits 12 million tonnes of CO_{2eq} of the total 369 million tonnes CO_{2eq} of the UK as a whole, meaning steel represents almost 3.3 % of UK emissions. Implementing the TC-BF-BOF system at the Tata Steel and British Steel plants

would decrease the steel-based share of UK emissions to 0.38 %. Therefore a 2.9 % reduction in UK emissions can be realised with £720 million in capital expenditure, with ongoing expenditure of £400 million every 5-10 years to replace the spent BCNF1 material once activity has dropped. Additionally, there are significant operational expenditure reductions achieved from the implementation of this system, due primarily to the displacement of expensive metallurgical coal. The capital expenditure would be entirely repaid from these savings in 22 months, with total savings of £1.28 billion after 5 years. The possible small increase in electricity consumption on implementation of this system would be easily absorbed in these savings. This system would also decrease the price of steel production, increasing the competitiveness of UK steel on the global market.

7.7 Advantages of the TC-BF-BOF System

The TC-BF-BOF system proposed here has several advantages over other methods to decarbonise the iron and steel sector. Firstly, since this system makes use of existing BF-BOFs, which make up 70 % of steel production, this method prevents the formation of stranded assets. Given that the global switch to a net-zero economy is likely to create stranded assets in multiple sectors incompatible with net-zero, any system which minimises stranded assets while achieving drastic emissions reductions should be prioritised. Furthermore, the continued operation of BF-BOFs globally would ensure the preservation of highly-skilled jobs and could create new jobs for the management and operation of the TC reactors. Secondly, the emissions reductions are evident as soon as the TC-BF-BOF retrofit is installed, rather than waiting years for a new DRI-EAF to be built or for decarbonisation of the grid for emissions reductions to be realised. This system operates a nearly perfect closed carbon loop, where any CO_2 produced in the BF or BOF is fed into the TC reactors to be split into more carbon monoxide for use in the BF. Additionally, the system provides an additional, albeit small, income in the form of selling the extra oxygen produced in the TC reactors, equal to around £13 million a year each for the

UKs two BF-BOF plants. Another important factor is that since the TC-BF-BOF is economically viable and saves over £600 million per plant over five years, the cost of producing steel is lower than with a traditional BF-BOF. UK steel has historically been expensive on the global scale so this should allow UK steel to become more competitive. In addition to cheaper steel production, the steel produced could also be considered carbon-neutral steel, which is likely to fetch a premium as companies and governments try to reduce operational and entrenched emissions in a wide range of sectors. The emissions intensity of steel created via TC-BF-BOF could be up to four times lower than a DRI-EAF plant. Most importantly, implementation of the TC-BF-BOF system does not exclude other efforts to decarbonise the sector such as efficiency improvements, the use of renewable electricity, increased scrap recycling or methods of improving the DRI-EAF route. Indeed, to maximise sector-wide emissions reduction, the majority of scrap steel should be used in EAFs (where 100% scrap can be used) with the remaining scrap being used in the TC-BF-BOF.

7.8 Conclusions

This research demonstrated the concept of coupling a thermochemical cycle to a BF-BOF to form an integrated TC-BF-BOF system. This system could replace 90 % of typical coke use with carbon monoxide produced from the TC while the remaining 10 % would be replaced by a biomass-based charcoal to provide solid carbon for the Boudouard reaction between CO_2 and carbon. For each tonne of liquid steel produced per day, 5000 kg of BCNF1 would be required, split into two reactors, one undergoing reduction and the other oxidation. BCNF1 is an ideal TC material due to its low reaction temperatures, high CO yields and 100% selectivity towards CO compared to other TC materials. The addition of this system would add 2.2 GJ/tls of energy requirement, where a typical BF-BOF uses 19.8-31.2 GJ/tls, and 3.5 GJ/tls of energy can be recovered from the BF top gas and BOF gas. Six of 7.65 million tonnes of steel in the UK are produced via the BF-BOF route. Implementation of this system in the two BF-BOF steel plants

in the UK could reduce steel sector emissions by 88 %. This would require a capital investment of £720 million, which would be repaid in 22 months through the displacement of expensive metallurgical coal and sales of excess oxygen not required in the BOF. Within five years, implementation of the TC-BF-BOF would give total savings of £1.28 billion while reducing UK emissions by 2.9 %. Finally, through cost reduction, this system would increase the cost-competitiveness of UK steel on the global market.

7.9 References

[1] IRENA, Reaching zero with renewables: Eliminating CO2 emissions from industry and transport in line with the 1.5^{0}C climate goal, (2020) 216. https://www.irena.org/publications/2020/Sep/Reaching-Zero-with-Renewables.

[2] World Steel Association, Steel and Raw materials, 15 (2011) 710–739. http://www.worldsteel.org/dms/internetDocumentList/fact-sheets/Fact-sheet_Raw-materials2011/document/Fact sheet_Raw materials2011.pdf.

[3] S. Managi, S. Kaneko, Iron and Steel Industry, 2020. https://doi.org/10.4337/9781849803434.00015.

[4] M. Moggridge, ArcelorMittal plans DRI-EAF plants for Bremen and Eisenhuttenstadt, Steel Times Int. (2021).

[5] United Nations, The Paris Agreement, 2015. https://doi.org/10.4324/9789276082569-2.

[6] M.N. Abu Tahari, F. Salleh, T.S. Tengku Saharuddin, N. Dzakaria, A. Samsuri, M.W. Mohamed Hisham, M.A. Yarmo, Influence of hydrogen and various carbon monoxide concentrations on reduction behavior of iron oxide at low temperature, Int. J. Hydrogen Energy. 44 (2019) 20751–20759. https://doi.org/10.1016/j.ijhydene.2018.09.186.

[7] A. Bhaskar, M. Assadi, H.N. Somehsaraei, Decarbonization of the iron and steel industry with direct reduction of iron ore with green hydrogen, Energies. 13 (2020) 1–23. https://doi.org/10.3390/en13030758.

[8] J. Haraldsson, M.T. Johansson, Review of measures for improved energy efficiency in

production-related processes in the aluminium industry – From electrolysis to recycling, Renew. Sustain. Energy Rev. 93 (2018) 525–548. https://doi.org/10.1016/j.rser.2018.05.043.

[9] Y. Yang, K. Raipala, L. Holappa, Ironmaking, Elsevier Ltd., 2014. https://doi.org/10.1016/B978-0-08-096988-6.00017-1.

[10] W.F. Hosford, Modern Steel Making, Iron Steel. (2012) 11–24. https://doi.org/10.1017/cbo9781139086233.004.

[11] M. Barati, S. Esfahani, T.A. Utigard, Energy recovery from high temperature slags, Energy. 36 (2011) 5440–5449. https://doi.org/10.1016/j.energy.2011.07.007.

[12] A. Ghosh, A. Chatterjee, Ironmaking and Steelmaking: Theory and Practice, 2008. https://books.google.com/books?hl=en&lr=&id=7_GcmB4i_dsC&oi=fnd&pg=PA2&dq=+BOOK+Iron+making+and+steelmaking:+theory+and+practice&ots=vG47-o5X26&sig=I0EJjnIIaP1HRebThKvf8wGkWLM%0Ahttps://books.google.co.in/books/about/Ironmaking_and_Steelmaking.html?id=7_G.

[13] H. Ahmed, New trends in the application of carbon-bearing materials in blast furnace iron-making, Minerals. 8 (2018) 1–20. https://doi.org/10.3390/min8120561.

[14] M. Huth, A. Heilos, Fuel flexibility in gas turbine systems: Impact on burner design and performance, Woodhead Publishing Limited, 2013. https://doi.org/10.1533/9780857096067.3.635.

[15] L. Song, L. Xiaojie, L. Qing, Z. Xusheng, Q. Yana, Study on the appropriate production parameters of a gas-injection blast furnace, High Temp. Mater. Process. 39 (2020) 10–25. https://doi.org/10.1515/htmp-2020-0005.

[16] A.E. Ramos, D. Maiti, Y.A. Daza, J.N. Kuhn, V.R. Bhethanabotla, Co, Fe, and Mn in La-perovskite oxides for low temperature thermochemical CO2 conversion, Catal. Today. 338 (2019) 52–59.

[17] B.J. Hare, D. Maiti, Y.A. Daza, V.R. Bhethanabotla, J.N. Kuhn, Enhanced CO2 Conversion to CO by Silica-Supported Perovskite Oxides at Low Temperatures, ACS Catal. 8 (2018) 3021–3029. https://doi.org/10.1021/acscatal.7b03941.

[18] B.J. Hare, D. Maiti, S. Ramani, A.E. Ramos, V.R. Bhethanabotla, J.N. Kuhn, Thermochemical conversion of carbon dioxide by reverse water-gas shift chemical

looping using supported perovskite oxides, Catal. Today. 323 (2018) 225–232.

[19] J. Nutting, E. Wondris, Basic Oxygen Steelmaking, Britannica. (2019). https://www.britannica.com/technology/steel/Basic-oxygen-steelmaking.

[20] M. Jampani, J. Gibson, P.C. Pistorius, Increased Use of Natural Gas in Blast Furnace Ironmaking: Mass and Energy Balance Calculations, Metall. Mater. Trans. B Process Metall. Mater. Process. Sci. 50 (2019) 1290–1299. https://doi.org/10.1007/s11663-019-01538-8.

[21] E. Worrell, L. Price, M. Neelis, C. Galitsky, Z. Nan, World Best Practice Energy Intensity Values for Selected Industrial Sectors, Lawrence Berkeley Natl. Lab. (2007) 51. https://escholarship.org/uc/item/77n9d4sp.

[22] MakeUK, UK Steel, Make UK. (2022). https://www.makeuk.org/about/uk-steel.

[23] UK Steel, Future carbon pricing, briefing for BEIS Select Committee, (2020).

[24] EVRAZ, EVRAZ Canadian Steel: Low Carbon Footprint, (2016). http://d3n8a8pro7vhmx.cloudfront.net/erinweir/mailings/195/attachments/original/Cleaner_Steel_November_2016.pdf.

[25] D. Gielen, D. Saygin, E. Taibi, J. Birat, Renewables-based decarbonization and relocation of iron and steel making: A case study, J. Ind. Ecol. 24 (2020) 1113–1125. https://doi.org/10.1111/jiec.12997.

[26] H. Kildahl, Z. Li, H. Cao, P. Slater, Y. Ding, Carbon dioxide decomposition through gas exchange in barium calcium iron niobates, Catal. Today. 364 (2021) 211–219. https://doi.org/10.1016/j.cattod.2020.05.024.

Chapter 8 – CONCLUSIONS AND RECOMMENDATIONS FOR FUTURE RESEARCH

8.1 Conclusions

Synthetic fuel provides a cheaper method of decarbonisation of the hard-to-decarbonise sectors through the use of a carbon-neutral drop-in fuel. Many fuels and commodity chemicals can be synthesised via a Fischer Tropsch synthesis from carbon monoxide or synthesis gas (CO and H_2). Therefore, a cost-effective method of producing carbon-neutral CO is needed. A thermochemical cycle can produce carbon monoxide from carbon dioxide using renewable electricity powering an electric heater, industrial waste heat, or concentrated solar power. An ideal thermochemical material has several key properties including low reaction temperatures, a small temperature change between reduction and oxidation, resistance to sintering, and high CO yields during repeated cycling. Among the most successful thermochemical materials are the lanthanum strontium manganites, a perovskite family. Several factors have been found that increase the fuel production of this family. Firstly, increasing the oxidation state of the transition metal by doping with lower valence elements. Secondly, having one electron in the transition metals' e_g orbitals before reduction and zero electrons in these orbitals before oxidation. Thirdly, a large size mismatch between A- and B-site elements to increase the tilting of the TMO_6 octahedra, facilitating the breaking or formation of the TM-O bond. Finally, the addition of non-redox active metals to the B-site to increase the resistance to sintering, improving cyclability.

The barium calcium iron niobates are a new family of perovskites capable of splitting carbon dioxide. This thesis initially focuses on ways of increasing the fuel production of this family. It was found that the higher the iron content, the higher the mass change during thermal cycling. BCNF1 showed 1.14 % mass loss during reduction, equal to the loss of 0.34 moles of oxygen.

This material had sustained mass change of 0.45 % after five cycles, producing 160 μmol/g of CO. More importantly, the low enthalpy of oxidation of BCNF1 is promising, releasing -45 kJ/kg of perovskite. Research therefore continued with the BCNF1 formulation. Optimisation of the reaction conditions can increase the energy-to-fuel efficiency of the cycle. Increasing the oxidation reaction temperature from 700 °C to 800 °C increased the CO yield from 58 μmol/g to 447 μmol/g. This is due to the competing factors of thermodynamics and gas diffusion. The oxidation reaction is exothermic, therefore lower temperatures shift the equilibrium towards carbon monoxide production, while increasing the temperature increases gas diffusion, shifting the type of diffusion from Knudsen diffusion at 700 °C and below to normal diffusion above 750 °C, where the diffusion rate is independent of pore size. However, it was found that only a small percentage of the perovskite pellet was involved in the oxidation reaction, meaning gas exchange throughout the pellet was suboptimal. Reacting over the perovskite as a powder increases carbon monoxide yields to 720 μmol/g. This powder was found to be thermally stable over 10 cycles, producing 630 μmol/g of CO. Finally, reacting 18g of the powder increased yields to 859 μmol/g, making BCNF1 one of the most successful thermochemical materials in the literature.

In order to investigate the CO_2 conversion extent, a 100g of BCNF1 powder lab-scale demonstration was built. Firstly, the oxidation kinetics were investigated, and it was found that at 800 °C, oxidation proceeds *via* a zero order mechanism, suggesting that at this temperature oxidation is dependent only on time. The activation energy of this CO_2 splitting reaction was found to be 46.62 kJ/mol, lower than most lanthanum strontium manganites reported in the literature, as demonstrated by the lower reaction temperatures of BCNF1. 100g of BCNF1 was able to split 10.1 % of CO_2 to CO at 800 °C. The techno-economic assessment found that the production of carbon monoxide by a BCNF1-based industrial thermochemical plant is profitable with electricity prices up to $0.39/kWh. Under all scenarios investigated, the plant

was found to be sensitive to electricity prices. As the electricity price drops, larger reactors with greater hourly production volumes are favoured. At an electricity price of $0.15 per kWh, BCNF1 can produce carbon monoxide at a price of $0.26 per kg, far lower than reported for electrochemical systems and the market price of CO.

Finally, the sector coupling between a BCNF1-based thermochemical CO production facility and a BF-BOF plant for the production of steel was presented. The TC-BF-BOF system is ideal because the inputs of the BF-BOF are the outputs of the TC while the inputs of the TC are the outputs of the BF-BOF. This system creates a closed carbon loop for the production of low carbon steel. The addition of the TC reactors would require an additional 2.2 GJ/tls of energy on top of the 19.8-31.2 GJ/tls currently needed, however 3.5 GJ/tls can be recovered from the BF-BOF gases to help power the TC reactors. If this system was used for the 6.0 million tonnes of steel produced via the BF-BOF route in the UK, it would reduce total steel sector emissions by 88 %. With £720 million of capital investment, UK-wide emissions would fall 2.9 %. This investment would be repaid in 22 months, with £1.28 billion in savings after five years due to the replacement of expensive metallurgical coal. Through cost reduction, this system would increase the cost-competitiveness of UK steel on the global market.

In conclusion BCNF1 is an ideal thermochemical material due to its low reaction temperatures, high CO yields and 100% selectivity towards CO compared to other thermochemical materials. A BCNF1-based TC could aid in the decarbonisation of the aviation, shipping, freight, and chemical sectors through the production of carbon neutral fuels from carbon monoxide upgrading. The use of a carbon-neutral drop-in fuel reduces investment requirements and limits the risk of stranded assets. There is also a unique opportunity for the decarbonisation of the iron and steel sector through coupling with a TC, allowing for cost effective emissions reductions without the need for fleet renewal. To conclude, a BCNF1-based thermochemical

cycle can aid in the race to net-zero through the decarbonisation of the hard-to-decarbonise sectors.

8.2 Recommendations for Future Research

In order to bring a BCNF1-based thermochemical carbon monoxide production plant to market, the following further research should be undertaken:

- Firstly, based on the results of the LSMO review in Chapter 3, doping of BCNF1 with other elements may increase carbon monoxide yields. The most successful dopants are Sr and Y in the A-site and Mn in the B-site [1–6]. A perovskite with iron and manganese in the B-site is promising, particularly for reduction, where the incorporation of manganese leads to a lowering of the enthalpy of reduction [7–9]. A significant proportion of the energy required for a thermochemical cycle of BCNF1 comes from the enthalpy of reduction (Chapter 6), therefore methods of lowering this are likely to increase energy to fuel efficiency.
- Secondly, the influence of reducing BCNF1 under a small volume of hydrogen should be investigated. During coupling with steel manufacturing, the reducing gas could include between 2-5 % hydrogen in nitrogen since hydrogen is produced by the splitting of water in the BF. As reported in Chapters 2 and 3, active reduction of other thermochemical materials under hydrogen leads to greatly improved oxygen evolution volumes, which also translate into higher carbon monoxide yields [10–12]. Of particular importance is understanding if active reduction under H_2 leads to a decrease in the enthalpy of reduction or if lower reaction temperatures can be used. Both of these factors would lead to increased energy to fuel efficiencies and lower reduction temperatures could reduce the risk of sintering with repeated cycling.
- Thirdly, the 100g scale BCNF1 reactor should be cycled repeatedly to understand the CO yields and CO_2 conversion rates after 100 and even 1000 cycles. This will allow

the susceptibility to sintering during long-term cycling to be understood. If BCNF1 is able to produce CO at a reasonable yield for 1000 cycles, a CO production facility would require replacement of the BCNF1 every 5.5 years, or 11 years if 2000 cycles are possible. The economics of the system depend on how often the BCNF1 must be replaced.

- Given that the BCNF1 must be replaced every so often once yields decrease, research should also be conducted on the recycling of the spent BCNF1. If this system was used to replace a large proportion of fuels globally, this would result in an extremely large volume of spent perovskite, likely causing environmental damage. A small volume of research has already been conducted on the recycling of the perovskites used in thin film solar cells [13]. For thermochemical BCNF1 this could include complete decommissioning, or regeneration by reversing the effects of sintering, namely pore shrinking and grain growth.
- In order to assess the suitability of BCNF1 for industrial CO production, investigations at the pilot-plant scale should be performed, likely with hundreds of kilos of BCNF1. If the pilot plant is configured as a fluidised bed, the increased solid-gas interactions could lead to increased carbon monoxide yields and CO_2 conversion. This could be a cost-effective way of improving yields and should increase the efficiency of the system.
- Finally modelling should be undertaken to understand why BCNF1 is able to operate at much lower temperatures than other thermochemical materials. Particular attention should be paid to the mechanism of action of the oxidation reaction as this may provide information about other ways to increase CO yields.

8.3 References

[1] G. Luciani, G. Landi, A. Aronne, A. Di Benedetto, Partial substitution of B cation in La0.6Sr0.4MnO3 perovskites: A promising strategy to improve the redox properties useful for solar thermochemical water and carbon dioxide splitting, Sol. Energy. 171

(2018) 1–7. https://doi.org/10.1016/j.solener.2018.06.058.

[2] S. Dey, B.S. Naidu, A. Govindaraj, C.N.R. Rao, Noteworthy performance of La1-xCaxMnO3 perovskites in generating H2 and CO by the thermochemical splitting of H2O and CO2, Phys. Chem. Chem. Phys. 17 (2015) 122–125. https://doi.org/10.1039/c4cp04578e.

[3] S. Dey, B.S. Naidu, C.N.R. Rao, Ln 0.5 A 0.5 MnO 3 (Ln=Lanthanide, A= Ca, Sr) Perovskites Exhibiting Remarkable Performance in the Thermochemical Generation of CO and H 2 from CO 2 and H 2 O, Chem. - A Eur. J. 21 (2015) 7077–7081. https://doi.org/10.1002/chem.201500442.

[4] G. Takalkar, R.R. Bhosale, F. AlMomani, Thermochemical splitting of CO2 using Co-precipitation synthesized Ce0.75Zr0.2M0.05O2-Δ (M = Cr, Mn, Fe, CO, Ni, Zn) materials, Fuel. 256 (2019) 115834. https://doi.org/10.1016/j.fuel.2019.115834.

[5] X. Liu, T. Wang, K. Gao, X. Meng, Q. Xu, C. Song, Z. Zhu, H. Zheng, Y. Hao, Y. Xuan, Ca- And Ga-Doped LaMnO3for Solar Thermochemical CO2Splitting with High Fuel Yield and Cycle Stability, ACS Appl. Energy Mater. 2021 (2021). https://doi.org/10.1021/acsaem.1c01274.

[6] S. Dey, B.S. Naidu, C.N.R. Rao, Beneficial effects of substituting trivalent ions in the B−site of La 0.5 Sr 0.5 Mn 1−x A x O 3 (A = Al, Ga, Sc) on the thermochemical generation of CO and H 2 from CO 2 and H 2 O, Dalt. Trans. 45 (2016) 2430–2435. https://doi.org/10.1039/C5DT04822B.

[7] A.J. Carrillo, D.P. Serrano, P. Pizarro, J.M. Coronado, Manganese oxide-based thermochemical energy storage: Modulating temperatures of redox cycles by Fe-Cu co-doping, J. Energy Storage. 5 (2016) 169–176. https://doi.org/10.1016/j.est.2015.12.005.

[8] L. André, S. Abanades, L. Cassayre, High-temperature thermochemical energy storage based on redox reactions using Co-Fe and Mn-Fe mixed metal oxides, J. Solid State Chem. 253 (2017) 6–14. https://doi.org/10.1016/j.jssc.2017.05.015.

[9] T. Block, M. Schmücker, Metal oxides for thermochemical energy storage: A comparison of several metal oxide systems, Sol. Energy. 126 (2016) 195–207.

https://doi.org/10.1016/j.solener.2015.12.032.

[10] A.E. Ramos, D. Maiti, Y.A. Daza, J.N. Kuhn, V.R. Bhethanabotla, Co, Fe, and Mn in La-perovskite oxides for low temperature thermochemical CO2 conversion, Catal. Today. 338 (2019) 52–59.

[11] B.J. Hare, D. Maiti, S. Ramani, A.E. Ramos, V.R. Bhethanabotla, J.N. Kuhn, Thermochemical conversion of carbon dioxide by reverse water-gas shift chemical looping using supported perovskite oxides, Catal. Today. 323 (2018) 225–232.

[12] Y. Qiu, L. Ma, M. Li, D. Cui, S. Zhang, D. Zeng, R. Xiao, Copper and cobalt co-doped ferrites as effective agents for chemical looping CO2 splitting, Chem. Eng. J. 387 (2020). https://doi.org/10.1016/j.cej.2020.124150.

[13] P. Chhillar, B.P. Dhamaniya, V. Dutta, S.K. Pathak, Recycling of Perovskite Films: Route toward Cost-Efficient and Environment-Friendly Perovskite Technology, ACS Omega. 4 (2019) 11880–11887. https://doi.org/10.1021/acsomega.9b01053.